



HAL
open science

NEAT : a spatial telescope to detect nearby exoplanets using astrometry

Antoine Crouzier

► **To cite this version:**

Antoine Crouzier. NEAT : a spatial telescope to detect nearby exoplanets using astrometry. Astrophysics [astro-ph]. Université de Grenoble, 2014. English. NNT : 2014GRENY053 . tel-01362947

HAL Id: tel-01362947

<https://theses.hal.science/tel-01362947v1>

Submitted on 9 Sep 2016

HAL is a multi-disciplinary open access archive for the deposit and dissemination of scientific research documents, whether they are published or not. The documents may come from teaching and research institutions in France or abroad, or from public or private research centers.

L'archive ouverte pluridisciplinaire **HAL**, est destinée au dépôt et à la diffusion de documents scientifiques de niveau recherche, publiés ou non, émanant des établissements d'enseignement et de recherche français ou étrangers, des laboratoires publics ou privés.

THÈSE

Pour obtenir le grade de

DOCTEUR DE L'UNIVERSITÉ DE GRENOBLE

Spécialité : **Astronomie & Astrophysique**

Arrêté ministériel : 7 août 2006

Présentée par

Antoine Cruzier

Thèse dirigée par **Fabien Malbet**

préparée au sein de l'**Institut de Planétologie et d'Astrophysique de Grenoble**
et de l'**Ecole Doctorale de Physique de Grenoble**

NEAT: un télescope spatial pour détecter des exoplanètes proches par astrométrie.

NEAT: a spatial telescope to detect nearby exoplanets using astrometry

Thèse soutenue publiquement le **17 décembre 2014**,
devant le jury composé de :

Dr. Xavier Delfosse

Astronome, Institut de Planétologie et d'Astrophysique de Grenoble, Président

Prof. Olivier Guyon

Professeur, University of Arizona, Rapporteur

Prof. Didier Queloz

Professeur, University of Cambridge, Rapporteur

Prof. Paul Kamoun

Professeur, Thalès Aliena Space, Examineur

Dr. Nicolas Guerinou

Docteur ingénieur, Office National d'Etudes et de Recherches Aérospatiales, Examineur

Ing. Jean-Michel Le Duigou

Ingénieur, Centre National d'Etudes Spatiales, Examineur

Dr. Fabien Malbet

Directeur de recherche CNRS, Institut de Planétologie et d'Astrophysique de Grenoble, Directeur de thèse



Contents

Acknowledgements	5
I Introduction	7
1 Context	7
1.1 The beginning of a new field: exoplanetology	8
1.2 Exoplanet detection and characterization techniques	11
1.3 Understanding planetary formation and searching for life outside of the Solar System	18
2 Space borne missions and ground based instruments for exoplanet science	19
2.1 Transits	19
2.2 Radial velocities	20
2.3 Imaging, coronagraphy and nulling interferometry	21
2.4 The case for μas astrometry	21
3 Astrometry, exoplanets and NEAT	24
3.1 Historical presentation of Astrometry	24
3.2 The recent developments	26
3.3 Exoplanet detection using astrometry	27
4 My contribution in the context of NEAT	33
4.1 NEAT mission: science case and optimization	33
4.2 NEAT lab demo	34
II NEAT mission	35
1 Presentation of NEAT	35
1.1 Principle of the pointed differential astrometric measure	36
1.2 Single epoch astrometric accuracy of NEAT	37
1.3 How NEAT reaches μas accuracy?	38
1.4 Error budget	41
2 Optimization of the number of visits per target	42
2.1 Description of the model	42
2.2 Numerical results	45
2.3 Discussion	46
3 Construction of the catalog of NEAT targets and references	47
3.1 The NEAT catalogs	47
3.2 Creation of the NEAT columns	49
4 Statistical analysis of the NEAT catalogs	49
4.1 Availability of reference stars	49
4.2 Astrometric signal in HZ versus stellar mass	50
4.3 Crossmatch with already known exoplanets	51
5 Allocation strategies and science yields	54

6	Conclusion	57
III NEAT lab demo: concept, specifications, design and test results		58
1	Foreword	58
2	High level specifications and concept	59
3	Specifications	61
	3.1 Mechanical supports and environment	62
	3.2 Detector/pixel specifications	62
	3.3 Pseudo stars specifications	63
	3.4 Metrology specifications	63
4	Critical design constraints	64
	4.1 Nyquist sampling of pseudo stars and pupil size	64
	4.2 Photometric relations	64
5	Design	71
	5.1 Overview	72
	5.2 Sub-systems	72
	5.3 Baffles	80
	5.4 Parameters and components summary	80
6	Compliance and tests	83
	6.1 Photometric budgets	83
	6.2 Diffraction limited PSF	83
	6.3 Safe operation of the CCD: temperature and critical pressure	86
	6.4 Mechanical and thermal stability	88
	6.5 Individual components tests	89
	6.6 CCD calibration results	89
	6.7 Compliance table	97
IV NEAT lab demo: data analysis methods and simulations		102
1	Introduction	102
2	Data analysis: methods	104
	2.1 Overview	104
	2.2 Dark and flat fields	104
	2.3 Metrology	106
	2.4 Pseudo stars	112
3	Results on simulated data	114
	3.1 Metrology	114
	3.2 Pseudo stars	117
V NEAT lab demo: results and conclusions		119
1	Result on actual data	119
	1.1 Dark and flat fields	120
	1.2 Metrology	125
	1.3 Pseudo stars	130
2	Conclusions on the data analysis	142
	2.1 Metrology	142
	2.2 Flat fields	142
	2.3 Stray light	143
	2.4 Centroids (plus corrections from flat and metrology)	143
VI Conclusions and perspectives		146

1	The NEAT/Theia mission concepts and the science case for μ as astrometry	146
1.1	Results for the science case	146
1.2	The new mission concept: Theia	147
1.3	Future use of the catalog of targets and references	147
1.4	Improvements on the catalogs of targets and references and yield simulator	148
1.5	Near and mid-term perspectives in exoplanetology	149
2	The NEAT lab demo	150
2.1	General feedback on the project and teamwork aspects	150
2.2	Possible improvements for the NEAT lab demo	151
2.3	Lessons learned for the NEAT lab demo	154
2.4	Future applications of the NEAT demo experiment	156
3	After my PhD...	157
	APPENDICES	158
	A Animations	158
	B Analysis of JPL data	160
1	Flat fields	160
2	Metrology	161
3	Pseudo stars	163
	C Table of reference documents	165
	D Components references	166
	E NEAT demo user manual	167
1	Folder naming convention	167
2	The work environment	167
3	Reminder: list of operations	169
4	The data cube creation routine: from row data to fits files	174
4.1	Introduction	174
4.2	createFitsCubes.m: list of operations	175
5	Python example command file	177
6	Tutorial: mounting directories with SSH tunnel manager and Macfusion	179
7	Metrology switch configuration	180
	F NEAT memo: Creation and exploitation of the NEAT catalog	182
	G Tests on individual components	217
	H Size of the diffraction spot and Nyquist sampling	228
	I Coherent and incoherent stray light	230
	Glossary	232
	Bibliography	235

Acknowledgements

First of all I thank my PhD advisor Fabien Malbet for his continuous support throughout the 3 years of my PhD. From the dynamic weekly meetings during the first year that got the neat lab demonstration experiment (neat-demo) on good tracks to the final stage when he helped me to take control over the experiment, his management has been critical for a good unfolding of my PhD.

I acknowledge the labex OSUG@2020 and CNES (Centre National d'Etudes Spatiales) for financing the neat-demo experiment and CNES and TAS (Thales Alenia Space) for funding my PhD.

I also thank Arianne Lançon, for putting me in contact with Fabien Malbet, which helped me to find a thesis in very good agreement with my personal interests.



I am very grateful to all the people that contributed to the neat-demo: without many of them the latter simply would not have been possible. Most of the neat-demo team is from IPAG (Institut de Planétologie et d'Astrophysique de Grenoble): Pierre Kern, François Henault, Eric Stadler, Noel Ventura, Guillermo Martin, Alain Delboulbé, Olivier Preis, Philippe Feautrier, Sylvain Lafrasse. We also had many students that contributed to the neat-lab demo though their internships. So I give my thanks to Etienne Behar, Morgan Saint-Pe, Jan Dupont and Sandra Potin as well.

I thank in particular the people from the CEA (Commissariat à l'Energie Atomique et aux Energies Alternatives), who have designed and made the readout electronics of the camera, a crucial part of the neat lab demonstration. Their team was composed of Christophe Cara, Modeste Donati and Eric Doumayrou. I give special thanks to Alain Léger from the IAS (Institut d'Astrophysique Spatiale) which has supported us from the very beginning and throughout our progress, in regard to various aspects of the experiment.

I am especially grateful to Mike Shao, Bijan Nemati, Chengxing Zhai, Inseob Hahn and Debra Shimoda for hosting me into their team during my two month visit at JPL and taking the time to answer many of my questions. During these two months, my work with them on the VESTA experiment (very similar to our neat-demo one) brought me invaluable experience.

I also thank the administration and IT support from IPAG, and in particular Laurence Platel, for the continuous support with the administrative hurdles and for defending me against our sometime merciless and grumpy IT support team.

And last but not least, I thank mom and dad for their support, Faustine Cantaloube for the penguin, Alexandre Charmasson without which this thesis would have been much quicker to write, Justine Lanier for the numerous giggling sessions, David

Gillier for its legendary troubleshooting skills and the awesome beverages, Jacques Kluska for the  food and Fabien Antonioz for feeding the  's but not only (pretty much everything top and bot) !

Et merci la nature !

Chapter I

Introduction

In my thesis, I have developed techniques and made analysis to contribute to the proposition of a space telescope that is able to detect and characterize planetary systems around nearby stars. In the first chapter I will first introduce the field of exoplanetology, i.e. the detection of planets outside the solar system, before presenting the space telescope itself and the technique it uses: astrometry. I will close the chapter by explaining precisely what was my contribution in this context.

Note to the reader: words defined in the glossary appear in a *sans serif italics font* for their first occurrence in the text. Some acronyms are also defined in the glossary, they are signaled by a dotted underline. For electronic versions¹, a tool-tip functionality is available for these acronyms: their full name are displayed when hovering the mouse over them.

1 Context

For thousands of years, humans have gazed in awe at the night sky, pondering about the possibility of life elsewhere in the universe. Since a refractive telescope was pointed to a sky for the first time centuries ago [Galilei, 1610], our knowledge of the heavens has increased dramatically. We have discovered that we live in a galaxy populated with billions of stars like the Sun and that there are billions of galaxies in the observable universe [Johnson., 2013]. For a long time, we could only speculate on the existence of planets around other stars than the Sun (i.e. exoplanets), possibly hosting life like the Earth. We live in exciting times: astronomers have recently become able to detect planets around other stars: the question of habitable worlds around other stars and extra-terrestrial life is more than ever before on the agenda. In this first section I will introduce the field of exoplanet detection and explain why it is relevant to the questions of the formation of planets and of extra-terrestrial life.

¹This manuscript also includes a few animated figures (grouped in appendix A), they are only compatible with **Adobe® Reader®**.

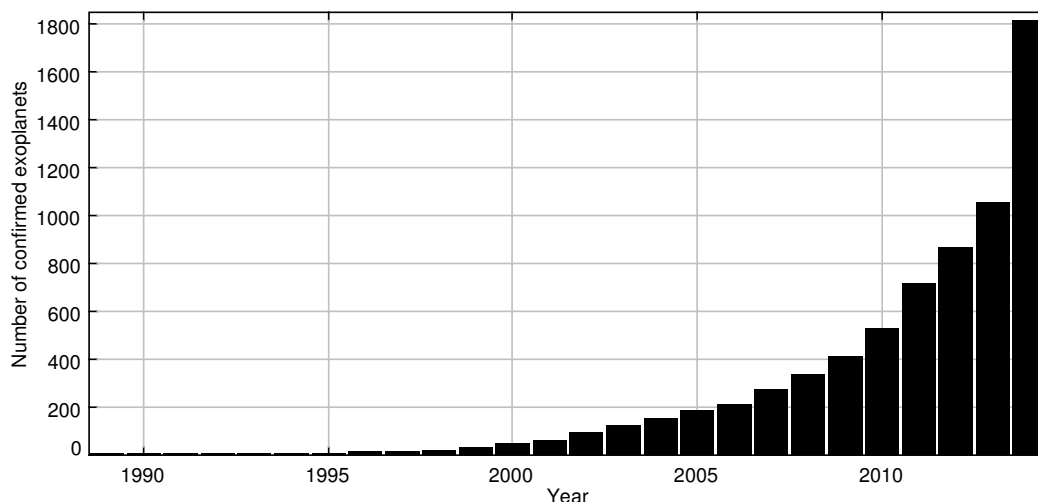


Figure I.1: **Cumulative histogram of the number of confirmed exoplanets, sorted by year of discovery, from 1989 to 2014** (Credit: exoplanet.eu database, updated: 12/07/2014). The histogram starts before 1992 because the database includes a prior discovery [Latham et al., 1989] of an object with a high and uncertain mass, it could be a planet or a very low mass star depending on the orientation of the orbit, see radial velocities in section 1.2.1 for detailed explanations. The high number of new exoplanets in 2014 comes from the Kepler mission [Rowe et al., 2014].

1.1 The beginning of a new field: exoplanetology

1.1.1 The technical challenge

The discovery and confirmation of the very first planets around other stars than the Sun, around a *pulsar* [Wolszczan and Frail, 1992] (*confirmed* only in 1997) and around a *main sequence* star [Mayor and Queloz, 1995] (confirmed in 1995) marked the beginning of a new era in astrophysics. A new field was born and the race for *exoplanets* begun. Since then, the number of known exoplanets has escalated quickly thanks to an ever accelerating rate of discovery, as shown by Fig. I.1. According to the exoplanet.eu database [Schneider et al., 2011], at the end of 2013, the total number of known exoplanets reached the symbolic milestone of one thousand. The increase of the number of detections is due to the diversification of the detection techniques used and the improved sensitivity of each one of them. As the number of detections rose, the statistical biases became well understood and we realized that exoplanets are ubiquitous in our Galaxy: a significant proportion of stars do have planets [Wolfgang and Laughlin, 2011] [Bonfils et al., 2013].

The reason behind this late but quick development is linked to the difficulty of detecting exoplanets, which is a consequence of the great distance between stars and of the large size and luminosity ratio between stars and planets. The average distance between the stars in the Milky Way is of the order of the parsec (pc): the stellar density in the solar neighborhood is $0.15 pc^{-3}$ [Gliese, 1956]. One pc is about 200 000 times the distance between the Earth and the Sun, while the Earth is 10 billion times fainter than the Sun [Guyon et al., 2006], [Woolf and Angel, 1998]. Looking for an Earth around another nearby star is analogous to looking for a firefly next to a light house, observed from hundreds of kilometers away.

Table I.1 gives the planet/star radius, mass and luminosity ratios and angular separations for different kinds of planets around a Sun-like star. The angular separation

Table I.1: Radius, mass, luminosity ratios and angular separations (rad) between an exoplanet and a Sun-like star.

	Radius ratio	Mass ratio	Angular separation	Luminosity ratio
Hot giant	10^{-1}	10^{-3}	5×10^{-8} rad	10^{-6}
Temperate giant			5×10^{-7} rad	10^{-8}
Cold giant			5×10^{-6} rad	10^{-10}
Hot Earth	10^{-2}	3×10^{-6}	same as above	10^{-8}
Temperate Earth				10^{-10}
Cold Earth				10^{-12}

(in radians) is equal to the ratio of the orbital distance over the distance to the star and the Solar System (here we assume that the host star is at 10 pc). The different types of exoplanet considered are: giants (mass and radius of Jupiter) and Earths ($1 M_{\oplus}$, $1 R_{\oplus}$), at different orbital distances. The adjectives hot, temperate and cold correspond respectively to orbital distances of 0.1, 1 and 10 astronomical units (AU). The cold giant is thus a Jupiter at the position of Saturn and the temperate Earth is an analogue of the Earth (an *exo-Earth*). The radius ratio, mass ratio and angular separation are trivial to calculate, the luminosities are scaled from the 10^{-10} value for an Earth, assuming $[1/\text{planet orbital distance}]^2$ and $[\text{planet radius}]^2$ dependencies. The luminosity ratio is given in the visible wavelength and assume that the planet luminosity is dominated by reflection of starlight, so it effectively excludes self-luminous hot Young planets [Oppenheimer and Hinkley, 2009]. This Table is useful as a starting point when comparing different detection methods: it quantifies the technical barrier associated with each case (type of planet/detection method).

Even in the favorable cases the technical challenge of exoplanet detection is daunting, that is why the instruments at our disposal only recently reached the required performances. In order to mitigate the distance, mass and luminosity problems astronomers use various techniques to detect exoplanets in addition to trying to obtain images of them. Several indirect detection methods have been developed, namely: radial velocities, astrometry on the host star, transits and gravitational lenses [Wright and Gaudi, 2013]. The last decade has witnessed a spectacular improvement of all these detection techniques, which resulted in a large number of discoveries and a great diversity of known exoplanets [Udry and Santos, 2007] [Perryman, 2000].

1.1.2 The push towards terrestrial habitable planets

Since about 2005 enough progress has been made to be able to detect terrestrial planets in the so called “habitable zone” (HZ) of their host star: in the exoplanet.eu database there are already a few planets of about $10 M_{\oplus}$ that have been discovered by radial velocities at this date, and their number increase quickly afterwards. This is very well illustrated by the animated version of Fig. I.2. The first super-Earth around a main sequence M star was soon announced [Rivera et al., 2005], and shortly after a super-Earth in habitable zone (also an M star) [Udry et al., 2007]. This is extremely interesting because it brings us closer to finding life outside of the Solar System. Indeed, when looking for exoplanets that could harbor life, we consider two

conditions:

- The planet must be in the HZ , i.e. at the right distance (not too hot nor too cold) from the star so it can have liquid water on the surface. Being in HZ does not ensure the presence of life and being outside the HZ does not exclude the possibility of Earth-like life or any other lifeforms, but planets in HZ are for sure very good candidates for astronomers to look for signs of life in their atmospheres [Rampino and Caldeira, 1994].
- The mass of the planet must be less than $10 M_{\oplus}$. This is the threshold at which a planet is likely to be rocky like Earth with a thin atmosphere. Planets with a rocky core and more massive than $10 M_{\oplus}$ attract a lot of gas during their formation and end up as gas giant with a high pressure and opaque atmosphere, like Neptune for example [Mordasini et al., 2010]. Obviously, such planets are not hospitable for Earth-like life. There is also a minimum mass required: very small planets suffer quick atmospheric loss, because of their low escape velocities [Lammer et al., 2008]. Tectonic activity may also have a critical role in stabilizing the climate by controlling the CO_2 -carbonate cycle [Kump et al., 2000] and small rocky planets tend to lose tectonic activity more quickly. Because of this, it is unlikely that a planet smaller than roughly $0.3 M_{\oplus}$ would be habitable [Raymond et al., 2007]. But this lower mass limit has little practical consequences yet because we seldom detect planets smaller than the Earth.

Figure I.2 is a period-planetary mass diagram of the *confirmed exoplanets*. Keep in mind that the diversity of host stars is not explicit in Fig. I.2. The host stars have not the same *spectral type* (i.e. different masses) and this is another important parameter to consider for a detection. The figure shows the existence of very diverse worlds, from small rocky planets of $0.5 M_{\oplus}$ to giants several times more massive than Jupiter, with orbits from a few hours to thousands of years. Each detection technique has a different sensitivity to the parameters involved, this explains why the planets are grouped by detection techniques into distinct populations on the diagram.

As time goes on, each technique gains in sensitivity and the corresponding population can spread to a larger range of periods and to lower masses. One important thing to notice about mass is that it is almost always technically easier to detect a giant planet than a small one. Small planets are abundant and giants are rare, so the number of detected giant planets is mainly limited by their occurrence rate (and the number of stars we can survey) whereas the number of small planets is limited by our ability to identify their signal in noisy data [Howard et al., 2012]. On the contrary, for the period of the planets, the detection techniques have different regions of optimal sensitivity: they are complementary. Aggregating the results from all of them allow us to have a much more complete view. In the next section we will see how each detection technique works, what are the advantages and drawback of each one of them and what are their preferred regions of the parameter space, relative to the planet periods and the host star mass.

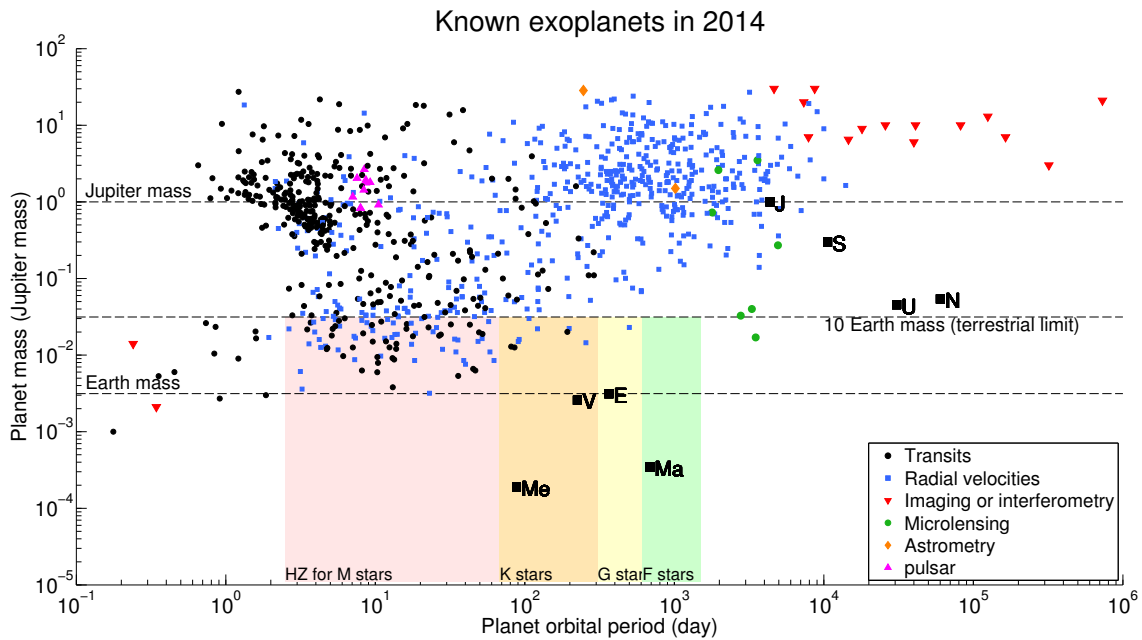


Figure I.2: **Mass-period diagram of the known exoplanets** (Credit: exoplanet.eu database, updated: 02/09/2014). Each point is an exoplanet, its shape and color depends on the detection technique used. The HZ of F, G, K, and M stars are displayed at the bottom. Note that a planet inside one of the zones is not necessarily habitable: the spectral type of its host star has to match accordingly. An animation in the appendix shows the evolution of this diagram from 1992 to 2014. [Go to animation](#)

1.2 Exoplanet detection and characterization techniques

This section quickly presents each one of the exoplanet detection techniques that are in use today. We will see how indirect detection methods use observations of a physical quantity over time to detect changes related to either the orbital dynamics of a couple star/planet (radial velocities, pulsars, astrometry or transits) or galactic dynamics (gravitational lenses). In other words, we can find the planets because they move! On the contrary, with direct imaging, as the same suggest, the photons from the planet itself are detected. For simplicity, the formulas are given for circular orbits: eccentricity $e=0$. In this simple case the equations presented for the radial velocities and astrometry methods are directly derived from the fundamental principles of dynamics and the law of gravitation.

1.2.1 Radial velocities of the host star

Using radial velocities means monitoring the velocity of the host star projected in the direction of the observer. The orbiting motion of a couple of bodies (star and planet) causes the star to have a periodic radial velocity that is characteristic of the planet orbit and mass: the planet and star periods are identical and their radial velocities are proportional. This is illustrated by Fig. I.3. The relative radial speed between the observer and the star causes a shift of the star spectrum, first predicted by [Doppler, 1842]. Although the star speed variations are small compared to the speed of light, this small **Doppler shift** can be detected with a stable instrument thanks to the abundance of spectral absorption lines of stars [Wright and Gaudi,

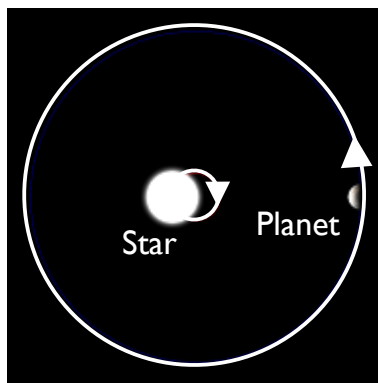


Figure I.3: **Illustration of the star/planet orbital dynamic** (image modified from wikipedia). An observer situated in the plane of the image sees wavelength shifts in the spectrum of the star: as the planet moves on its orbit, the star moves in the opposite direction. [Go to animation](#)

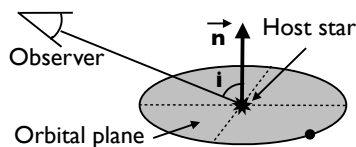


Figure I.4: **Definition of the inclination i** (as used in radial velocities).

2013].

The amplitude of the radial velocity signal is given by Eq. (I.1):

$$A = 0.09 \text{ m.s}^{-1} \times \frac{M_{\text{Planet}}}{M_{\oplus}} \times \left(\frac{M_{\text{Star}}}{M_{\odot}} \right)^{-1} \times \left(\frac{R}{1\text{AU}} \right)^{-\frac{1}{2}} \times \sin i \quad (\text{I.1})$$

Where M_{Planet} is the exoplanet mass, R is the exoplanet semi major axis, M_{Star} is the mass of the observed host star and i is the *inclination* (see Fig. I.4). The constant 0.09 m.s^{-1} correspond to the signal of an exo-Earth around a Sun.

By looking at Eq. (I.1), one can see that radial velocities are best adapted to small mass stars and small period planets (small orbits) seen on an edge-on configuration ($i = 90^\circ$). For face-on configurations ($i = 0^\circ$), no signal is detected. For statistics on a large number of detections, unknown inclinations are not a problem: face-on configurations are less frequent and the statistical bias due to the $\sin i$ term is low. However for a given individual case, it is often not possible to be certain of the planet mass when information on the inclination is not available: only the product $\frac{M_{\text{Planet}}}{M_{\oplus}} \sin(i)$ is known.

1.2.2 Pulsar timing

Pulsars are highly magnetized residual cores of dead stars which are spinning very quickly. They emit regular radio signals as they spin, they are very accurate natural clocks [Matsakis et al., 1997]. The same Doppler effect that occurs in radial velocities is affecting the pulsar signal in the exact same way: the time between the pulses changes with the speed relative to the observer.

1.2.3 Astrometry of the host star

Astrometry measures the motion of the star on the plane of the celestial sphere. Just like for the radial velocities, the presence of a planet causes the star to have an orbit which is characteristic of the planet, called reflex motion or wobble. The star lateral position is measured instead of its radial velocity. This is also illustrated by the Fig. I.3. An observer perpendicular to the orbital plane would see the star wobbling, but this angular motion at real scale is very small. The angular amplitude of the astrometric signal is given by Eq. I.2:

$$A = 3 \mu\text{as} \times \frac{M_{\text{Planet}}}{M_{\oplus}} \times \left(\frac{M_{\text{Star}}}{M_{\odot}} \right)^{-1} \times \frac{a}{1\text{AU}} \times \left(\frac{D}{1\text{pc}} \right)^{-1} \quad (\text{I.2})$$

Where D is the distance between the Sun and the observed star, M_{Planet} is the exoplanet mass, a is the exoplanet semi major axis and M_{Star} is the mass of the observed host star. The constant $3 \mu\text{as}$ (3×10^{-6} arcseconds) corresponds to the signal of an exo-Earth observed from a distance of 1 pc.

Astrometry of the host star is best adapted to intermediate period planets (near HZ) and longer, as long as the period does not exceed the time span of the observations. The astrometric signal is stronger for small stars (all other parameters being equal) but for detection of planets in HZ , the method is more sensitive for massive stars, as the habitable zone is in this case further away from the star, as we will see in the chapter II. At last, astrometry works best with a face-on geometric configurations, but edge-on systems are also detected. Note that it is also possible to do astrometry directly on the planets if they are detected by direct imaging. In this manuscript when we simply refer to **astrometry**, we implicitly mean **astrometry of the host star**. Section 3 will give a much more detailed presentation of astrometry.

1.2.4 Transits

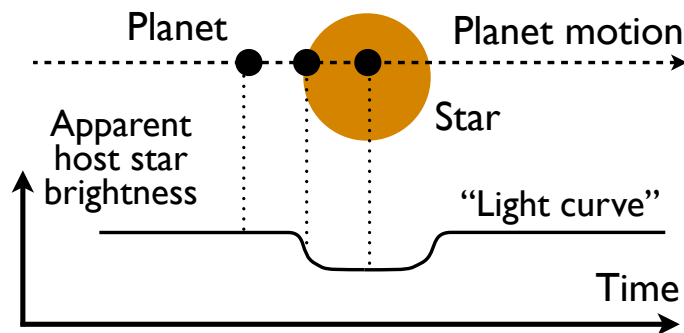


Figure I.5: Schematic of a transit.

The transit method looks at the decrease in apparent brightness of an host star as an exoplanet transits between the star and the observer. This is illustrated by Fig. I.5.

The depth of a transit (the relative decrease in luminosity of the host star) depends on the relative radius of the star and the planet:

$$\rho = \left(\frac{R_{\text{planet}}}{R_{\text{star}}} \right)^2 \quad (\text{I.3})$$

If we refer to Table I.1, we have a straightforward estimation of the depth of the transit of an exo-Earth (around a Sun-like star): 10^{-4} . Furthermore, to see a planet which has a random orientation transiting, the geometric configuration must be such that the planet passes by chance between the observer and the star, the probability (for a circular orbit of semi major axis a) is given by Eq. I.4 [Winn, 2010]:

$$P_{\text{transit}} = \frac{R_{\text{star}} + R_{\text{planet}}}{a} \approx \frac{R_{\text{star}}}{a} \quad (\text{I.4})$$

Where R_{star} is the diameter of the star and a the orbital distance. In most cases the planet is much smaller than the star and the approximation in equation I.4 is valid. The geometric probability of transit decrease with the orbital distance. The number of transits seen in a given time span also decrease with the orbital period. In order to confirm a transit detection one has to see at least 3 transit events: the longest period that can be detected is only $\frac{1}{3}$ of the time span of the observations [Koch et al., 2010]. This makes transits best suitable for short periods (or small orbits). However, exo-Earth detection is possible (transit probability of 0.5%) provided an adequate time span of more than 3 years of observations is available for large number of stars.

It is sometimes possible to obtain the mass of planets or to discover other non transiting planets with transits alone, when planets are in resonance or have very close orbital periods. In this cases they perturb each other and produce Transit timing variations (TTV). The amplitude of the perturbations depends on the masses and periods of the planets. If both planets transits and show visible TTV, both masses can be known, otherwise we mainly have additional information about the non transiting planet [Holman and Murray, 2005].

There is a secondary event, which is frequently found in association with transits: the eclipse, which happens when the planet disappears when passing behind the star. Some systems can have only a transit or an eclipse, if the orbit is not circular. The effect of the eclipse is similar (a relative decrease in luminosity) but it is harder to detect because the planet has a much lower irradiance (W.m^{-2}) than the star.

1.2.5 Gravitational microlensing

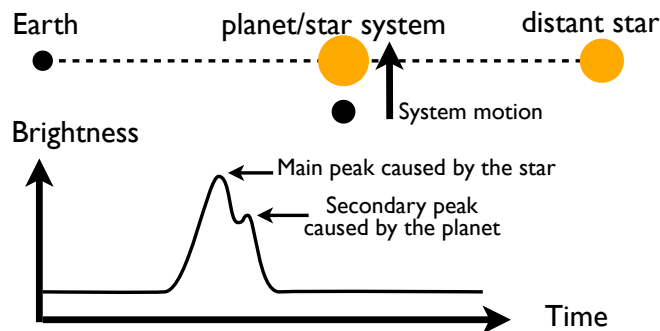
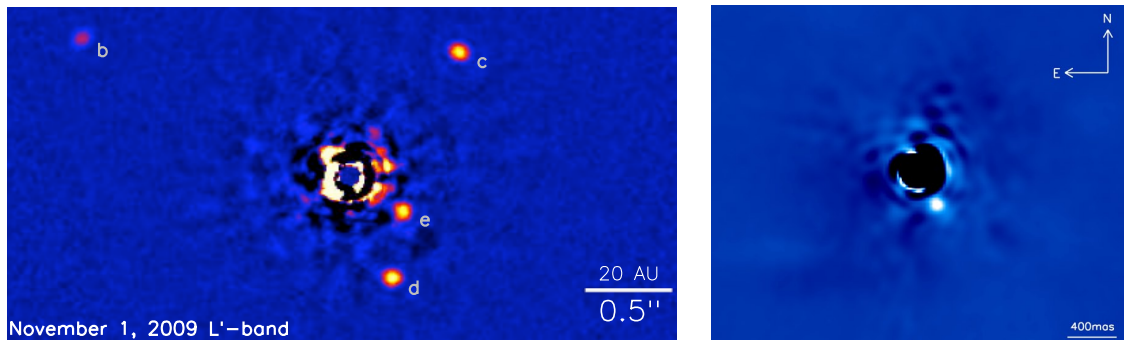


Figure I.6: **Schematic of a gravitational microlensing event.** The magnitude of the secondary peak is greatly exaggerated to be visible.

This method takes advantage of galactic dynamics. When looking towards the center of the Galaxy, there is a non negligible probability to have a temporary near perfect alignment of two stars with the Earth as each object moves within the Galaxy.

When the chance alignment occurs, the star at the back (in the galactic center) is magnified by the one that is closer to the observer, producing a light curve roughly shaped like a bell. If a planet is present around the closer star, it will produce a secondary intensity peak that can be detected (Fig. I.6). Inverting this curve gives information about the planet mass and orbital distance. This method has an optimal sensitivity from 1 to 10 AU from the host star [Gaudi, 2012]. Until now this method has been relatively marginal and has the obvious disadvantage of not being reproducible: chance alignments only occur once. Furthermore, detections are hard to follow-up with other techniques because they occur at great distances (typically thousands of parsecs).

1.2.6 Direct imaging



(a) Four planets around HR 8799, observed with the Keck II [Marois et al., 2010].

(b) A planet orbiting Beta Pictoris, observed with the VLT [Lagrange et al., 2010].

Figure I.7: Both images have been obtained with coronagraphs in L band where the young planets are relatively bright. The complex structures near the center (where the star is) are residuals from the stellar light suppression.

As the name suggests, this method goal is to obtain images of exoplanets around their host star(s). The problem is that current telescopes barely resolve the closest planet systems. The light from the star, which is typically billions of times greater than the one of the planet, is spread over by diffraction into a PSF. The dim signal from the planet is drown into the much brighter PSF and indistinguishable from noise. In order to see the planet, astronomers have thought of several ways to cancel the star light: for example using a coronagraph (Fig. I.7) or interferometric nulling [Oppenheimer and Hinkley, 2009], [Guyon et al., 2006].

The greater the apparent angle between a star and a planet, the easier it is to separate them: direct imaging is best adapted to large periods and close stars. There is a trade-off though, at large periods, the planets are less luminous. However there is a notable exception: very young planets are hot because they have not had the time to cool down after their formation. In this case they emit a lot of infrared radiation and the contrast with the star in the infrared is more favorable [Oppenheimer and Hinkley, 2009].

Table I.2: Qualitative comparison between the different types of information on the planet(s) provided by the different detection methods. A “✓” indicates generally a good constraint, a “(✓)” indicates a degeneracy, a higher degree of uncertainty or a highly model dependent result, a void indicate no information. For applicable cases where partial or degenerate information is available, the explicit form of the information obtained is indicated. For example for transits, the period (and inclination) are well known. In some particular cases, useful constraints on other parameters can also be obtained.

	Radius	Mass	Orbit	Transmission spectrum	Reflection spectrum
Radial velocities		$m \sin(i)$	(✓) - i unknown		
Astrometry		✓	✓		
Transits/Eclipse	✓		(✓) - accurate period and i	✓	(✓)
Microlensing		✓	projected semi major axis		
Direct imaging	(✓)		✓		✓

1.2.7 Summary of detection methods and exoplanet characterization

Exoplanet detection is only the first step, exoplanet characterization is the logical next step. Each detection method only gives partial information about the planets. When a particularly interesting planet is detected, astronomers try to combine several method to **confirm** and **characterize** the planet. When this is possible, very interesting science cases can be explored, at the frontier between several domains. A very interesting aspect of the characterization is the spectrum of the planet atmosphere and/or planet surface, which can be obtained either by phase/eclipse/transit spectroscopy or direct imaging. Table I.2 summarize which information can be provided by which method.

Table I.2 highlight the interesting synergies. For example between transits and radial velocities: a joint detection by both methods removes the inclination ambiguity ($i \approx 90^\circ$) and result in a known mass and radius. This gives away the planet density and allows modeling of the planet composition and internal structure. This also works if the mass is obtained with astrometry. Another important synergy is between radial velocities/astrometry and direct imaging. The later is very precious and expensive telescope time (especially if done from space) and is best used on already known targets. Radial velocities or astrometry can advantageously be used to establish a list of target stars/exoplanets and the observation schedule for which the planets are ideally placed into their orbits for characterization. However this synergy with direct imaging can only be done for very close planets (see section 1.3).

1.2.8 Different types of exoplanet spectra

An important point about exoplanet characterization is that spectra can be obtained in several ways (Fig. I.8). For a transiting planet, a transmission spectrum is obtained by subtracting the spectrum during the transit event with the one obtained

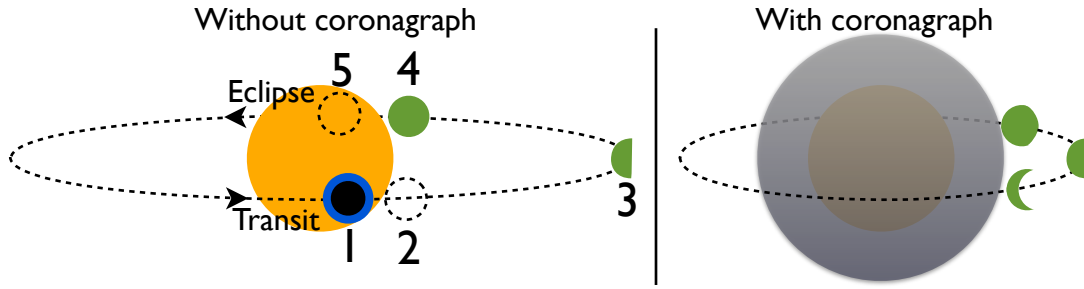


Figure I.8: **Schematic of the different types of spectra of an exoplanet.** The left part is the case without a coronagraph, only the total light from the star plus the planet is seen but one can have a differential spectra of the planet by comparing data from different orbital positions: (1,2) \rightarrow transit atmospheric transmission spectra, (4,5) \rightarrow eclipse reflection spectra, (2,3,4) \rightarrow phase reflection spectra (no transit nor eclipse needed). The right part is the case with a coronagraph: the star light is attenuated and the light/spectrum of the planet is observed directly.

before or after². For a planet close to a edge-on configuration, one can in principle also compute a phase reflection spectrum³. It can be obtained by subtracting spectra at different orbital phases of a planet orbit, because the planet is seen alternatively almost fully illuminated (day side) and almost entirely dark (night side), the planet does not have to transit and no coronagraph is needed in this case. However, if several planets are presents, their phase signals are blended together. If there is an eclipse, a better reflection spectra can be obtained. In any case, a big inconvenient with transmission spectra and phase/eclipse reflection spectra is the photon noise from the star, given that the signal to noise ratio (SNR) for a given wavelength channel λ is:

$$\text{SNR} = N_{\text{signal}}^{\gamma,\lambda} / \sqrt{N_{\text{total}}^{\gamma,\lambda}} \quad (\text{I.5})$$

Where $N_{\text{signal}}^{\gamma,\lambda}$ and $N_{\text{total}}^{\gamma,\lambda}$ are the number of photons respectively from the spectral feature to detect and from the star. While feasible in principle, obtaining useful eclipse/phase reflection spectra often results in an unrealistic integration times for small planets, because the signal/star photon ratio is very low and the photon star noise only goes down as the square root of the time⁴, transmission is only slightly easier. In this regard, direct imaging has a huge advantage: because the photon flux from the star is suppressed or strongly attenuated, the SNR of a reflection spectrum for a given target and given telescope diameter is larger than with differential spectra obtained with transits, eclipses or phase curves.

²The transmission spectrum is the star light passing through the planet atmosphere. This spectrum carries information about the exoplanet atmospheric composition.

³The reflexion spectrum is the star light reflected by the planet surface. This spectrum carries information about the exoplanet atmospheric composition and its surface reflectivity as a function of wavelength

⁴Using the JWST, the upcoming world best space based observatory, detection of spectral features of super-Earth around small stars (lowest hanging fruits in the terrestrial mass regime) would use 2% of the 5 year mission [Belu et al., 2011]

1.3 Understanding planetary formation and searching for life outside of the Solar System

The direct consequence of the improvement of exoplanet detection techniques is to fill the mass/period parameter space. This is very important as it will help astronomers answer the two following fundamental questions: how do planets form? is there life outside of the Solar System? But how exactly are exoplanet detections related those two questions?

1.3.1 Planetary formation

In order to develop accurate planetary formation models, astrophysicists need data to constrain the models results. In particular, the discovery of the first “hot Jupiter” (a giant gaseous planet on a very small orbit) has made the field evolve very rapidly: new models to explain inward planetary migration of gas giants were developed. Before, as only the Solar System planet were known, hot gas giants were only hypothetical. We are now filling the mass/period parameter space so well that we can start to look at the effect of the star mass as well. The data is now sufficient to reconstruct unbiased distributions of exoplanets for many parameters (planet mass, planet period, star mass) and additional detections are helping to increase the accuracy and the span of the distributions. These statistical results are key to refine our understanding of planetary formation [Udry and Santos, 2007].

1.3.2 Life outside the Solar System

Even though small planets (in mass and in size) are the hardest to detect, in some aspects they are also the most interesting. We now arrive at a point where several methods are becoming sensitive enough to detect terrestrial mass planets (i.e. less than $10 M_{\oplus}$) at periods that places them in HZ , where we have a chance to find liquid water at the planetary surface. These terrestrial planets in HZ , which I will simply call habitable planets by abuse of terminology⁵, are the places most conducive to the emergence of life known to date (other than the Earth) [Rampino and Caldeira, 1994]. They are places where we can hope to find complex life-forms outside the Solar System. The first step is to detect the closest of these habitable planets, to know where they are in our solar neighbourhood. Then, the next step is to try to get a spectra of their surface and atmosphere in order to confirm habitability and infer the presence of biological activity if it exists. In order for this second step to be possible by direct imaging using present or near future technology, the planets must be very close, on the order of 10 pc or less [Cockell et al., 2009] [Belu et al., 2011]. In this regard, μ as astrometry offers a unique opportunity to find the closest planet systems including the habitable ones: the reasons behind this are developed in section 2.4.

⁵Being terrestrial and in HZ does not ensure habitability, knowledge of atmospheric density and composition is required to confirm habitability. Strictly speaking, they should be called “potentially habitable”.

2 Space borne missions and ground based instruments for exoplanet science

In this part I present the landscape of recent/planned space missions and of recent/planned ground instruments, in the exoplanet field. I compare the role of the most successful exoplanet detection techniques and explore their potential for the future of exoplanetology and the search for life. The technical challenge of habitable exoplanet detection is so difficult that so far a large part of the related activities are space missions, with the notable exceptions of radial velocities and coronagraphs on very large telescopes.

2.1 Transits

Observations of transits from the ground is very difficult because atmospheric effects have so far limited the accuracy of the photometric curves to a few parts per one thousandth: with this accuracy it is only possible to detect giant planets for Sun-like stars. Numerous new ground surveys, like for example, M_{Earth} [Berta et al., 2011], ExTra⁶, MASCARA (the Multi-site All-Sky CAmERA) [Snellen et al., 2012], NGTS (Next-Generation Transit Survey) [Wheatley et al., 2013] are trying to improve the calibration methods with reference stars in order to increase the photometric accuracy and generally focus on low mass stars where the transit depth is larger. Some of them should be sensitive to terrestrial planets around M stars. On the other hand, space transits missions already have had great success: two have been completed and several others are in preparation. CNES (Centre National d'Etudes Spatiales), in collaboration with ESA (European Space Agency) launched in December 2006 a small sized space telescope (\varnothing 0.27m) called COROT (CONvection ROTation et Transits Planetaires) [Auvergne et al., 2009] that observed transits during for 5 years. In March 2009, NASA (National Aeronautics and Space Administration) launched a much bigger telescope (\varnothing 1.4m): the Kepler⁷ spacecraft which has monitored a fixed field of 150,000 stars continuously over 5 years [Koch et al., 2010]. Both missions were very successful, although the number of detections is much higher for Kepler thanks to its very large size and wide field of view. It has found thousands of *exoplanet candidates*, more than 4200 according to the NASA exoplanet archive⁸ [Akeson et al., 2013].

Kepler has a very interesting characteristic: it was designed to detect transits of planets with radius down to $0.5 R_{\oplus}$, which are terrestrial (the limit between gas giant and terrestrial is around $2 R_{\oplus}$). Although transits are less likely to occur for planets of large periods, the number of stars observed is large enough to yield a significant number of terrestrial and habitable planets. After correction for the incompleteness of the transit detection and the transit probability biases, it has been estimated that $22 \pm 8\%$ of Sun-like stars harbor Earth-size planets orbiting in their habitable zones [Petigura et al., 2013].

⁶Xavier Bonfils, Priv. comm. A presentation is available on the ESO (European Southern Observatory) website: <http://www.eso.org/sci/meetings/2014/exoelt2014/presentations/Bonfils.pdf>

⁷Kepler is not an acronym. The spacecraft was named after the scientist Johannes Kepler (1571-1630), best known for his laws of planetary motion.

⁸updated: 25/06/2014, <http://exoplanetarchive.ipac.caltech.edu/http://exoplanetarchive.ipac.caltech.edu/>

The limitation of these missions arises from the very nature of the transits. In order to detect lots of planets with a practical instrument design, a constant field has been monitored for long periods, thus making the search space a cone containing only a small fraction of the sky. Consequently the target stars are thousands of parsecs away. The habitable exoplanets detected by Kepler and COROT are unlikely to be directly observable for a long time: as explained in section 1.3 the reasonable distance limit for spectroscopy of habitable exoplanet is about 10 pc.

Other mission concepts are trying to address this issue by looking at transits on the whole sky. In this case, we may have some chance of finding some close enough habitable planets: it depends on η_{Earth} , on how far we are willing to probe and on luck. But with a transit probability of 0.5%, we will miss most of the closest exo-Earths. CHEOPS (CHaracterising ExOPlanets Satellite) [Broeg et al., 2013], TESS (Transiting Exoplanet Survey Satellite) [Ricker et al., 2010] and PLATO (Planetary Transits and Oscillations of stars) [Rauer et al., 2013] are missions in preparation that will look for transits around close and bright stars. EChO (Exoplanet Characterisation Observatory) [Tinetti et al., 2012] and JWST (James-Webb Space Telescope) [Clampin, 2008] are respectively proposed and planned missions to carry out transit spectroscopy: the idea is to compare spectra before and during the transits and eclipses to obtain transmission and reflection spectra.

2.2 Radial velocities

Radial velocity on the host star gives information on the orbit and mass of the planet, with one remaining ambiguity though, the angle of the plane of the orbit relative to the observer. This information can sometimes be obtained by other methods if a good habitable exoplanet candidate is found. The spectral signature of the planet is also present in the data even if the final signal is strongly dominated by the signal of the star. It is thus in principle possible to distinguish the two signals when the signal to noise ratio is good enough. However, because of the contrast problem, it is unlikely that the spectrum of an habitable planet will be directly observed (i.e. without canceling of the light of the star first).

A major advantage of radial velocities is that they are possible from the ground, so they are relatively cheap. They are a lot of RV spectrographs in service today, and a significant fraction of them are accurate enough to look for exoplanets. The most notable ones in service today are HARPS (High Accuracy Radial Velocity Planet Searcher) operating at La Silla Observatory and NIRSPEC [McLean et al., 1998] on the Keck II telescope. The precision of the instruments is about 1m/s. Next generation spectrographs will reach a precision of 0.1m/s, but at this point the dominant source of noise will be the star themselves and not the instruments [Mayor et al., 2003]. ESPRESSO (Echelle SPectrograph for Rocky Exoplanet- and Stable Spectroscopic Observations) [Pepe et al., 2014] is an instrument that will be installed on the VLT (Very Large Telescope).

Radial velocities are already capable of detecting habitable super-Earths around M type stars. With future spectrographs, more habitable planets will be detected likely ranging from $1M_{\oplus}$ or less around very low mass stars to *super Earths* around Sun-like stars. But it is unclear whether radial velocities will succeed to go down to exo-Earths around Sun-like stars (0.1 m/s). It depends on the extent to which astronomers are able to filter the stellar noise out of the data [Dumusque, 2010].

2.3 Imaging, coronagraphy and nulling interferometry

The most critical criterion for direct imaging is the distance: the angular separation decrease proportionally with increasing distance and the luminosity decrease as the square of the distance. The distance is even more critical for exo-Earth which are faint and close to their stars. A reasonable limit for the direct observation of an exo-Earth with current technology is 10 pc. Although there is no such observation yet, we already have images of some young giant planets at large periods (see Fig. 1.2, the mass-period diagram, on the upper right). These detections were made with coronagraphs on large ground telescopes, like NaCo (Nasmyth Adaptive Optics System (NAOS) Near-Infrared Imager and Spectrograph (CONICA)) [Lenzen et al., 2003]. Currently there are a lot of instrumental developments for coronagraphy worldwide: recent or near-future ground instruments include for example SPHERE (Spectro Polarimetric High contrast Exoplanet REsearch) for the VLT [Beuzit et al., 2008], GPI (Gemini Planet Imager) [Macintosh et al., 2008] and HiCIAO (High-Contrast Coronagraphic Imager for Adaptive Optics) for the Subaru telescope [Hodapp et al., 2008]. In a slightly more distance future, we expect a next generation of giant telescopes and instruments, such as EPICS for the E-ELT (European Extremely Large Telescope) [Kasper et al., 2010]. The later could have the capability to detect terrestrial planets (less than $10M_{\oplus}$). In space, the HST (Hubble Space Telescope) has detected some planets [Currie et al., 2012] and its successor, the JWST will greatly improve the detection limits, especially for small mass stars [Boccaletti et al., 2005]. SPICA (Space Infrared Telescope for Cosmology and Astrophysics) [Swinyard et al., 2009] and WFIRST (Wide Field Infrared Survey Telescope) [Spergel et al., 2013] are large missions planned by respectively JAXA (Japan Aerospace Exploration Agency) and NASA which will observe in the far infrared/near infrared and will be equipped with coronagraphs.

The goal behind imaging is also to enable the next step, which is spectroscopy of the planet photons, in order to infer their atmosphere composition and/or their surface spectral properties. This is really difficult because it spreads the already weak planet signal into several spectral channels, which result in a very low SNR (Signal to noise ratio⁹). A number of ambitious cutting edge space missions for imaging/spectroscopy of exo-Earth have been under study recently, like Darwin, a nulling interferometer¹⁰ [Cockell et al., 2009], or TPF (Terrestrial Planet Finder), an interferometer/coronagraph [Beichman et al., 1999]. Sadly, these plans are suspended, mainly because of the technical difficulties and the consequently large budgets associated.

2.4 The case for μ as astrometry

Having presented an overview of the state of the art in exoplanet detection, I will now highlight the rationale behind an μ as astrometric mission and its associated science case. Doing so require us to adopt both the instrument and science perspectives, to see the limitation and opportunities. In the subsequent sections, we will see how the case mostly resides in our current inability to find exo-Earths in the Solar neighborhood and to measure their mass. A word of caution is useful here: this is

⁹The SNR gives information about the amplitude of a signal, relative to the noise level.

¹⁰a nulling interferometer combines light from several telescopes and make the beams interfere to destroy the light of the star, by placing it on a dark fringe, where the optical path delay between the telescopes is half a wavelength.

written in mid 2014 and the field is evolving so rapidly that some arguments may become invalid in a not so distant future!

2.4.1 Current limitations of radial velocities

We have already approached the limitations of radial velocities in section 2.2. Next generation instruments will reach a precision of 0.1 m/s, which is precisely the level required for an exo-Earth. However, below 1 m/s, the stellar noise is much larger than the instruments' for most stars. The case of Alpha Centauri Bb is emblematic to the challenge posed by stellar noise. Alpha Cen Bb is a planet with a signal amplitude of 0.51 m/s, recently discovered with the HARPS spectrograph [Dumusque et al., 2012]. It is the closest Sun-like star from the Sun, it is very quiet and it has had the lion's share of the HARPS program observation time with a total of 459 observations over three years. For Sun-like stars, it hardly gets better than this! In spite of this, in order to make the detection possible, multiple signals with amplitudes larger than 0.5 m/s have been removed by various signal processing techniques. The signals have been attributed to other phenomena, such as stellar spots, rotation and jitter. But this very complex processing has raised some doubts and the planet existence is somewhat contested [Hatzes, 2013]. At this level of precision, the slightest error in processing can result in a false apparent signal.

Radial velocities work much better for small mass stars, where the signal in m/s is larger for two reasons: first the signal scales directly with $\frac{M_{\text{planet}}}{M_{\text{star}}}$, and secondly the HZ is closer to the star (short periods/small semi major axis planets give off larger RV signals). Around M stars, the detection is so much easier that RVs have already detected terrestrial planets in the habitable zone. But for solar type stars, we simply do not know if radial velocities will be able to separate the planet from the stellar noise, down to $1M_{\oplus}$ in HZ .

2.4.2 Current limitations of transits

Transits look very promising in the near future. With PLATO, TESS, the JSWT and EChO, we will soon discover many more transiting planets closer than what Kepler has already found and we will have better quality transiting and eclipse spectra, down to a few Earth masses [Tinetti et al., 2012] [Deming et al., 2009]. However the major limitation in the case of very close stars is the geometric transit probability. There are only about 400 Sun-like stars (F, G and K spectral types) closer than 20 pc. Assuming a frequency of habitable planets of about 10 to 20% (result from Kepler) and with a transit probability of 0.5% for an earth analog, there may be no nearby transiting exo-Earth (around a Sun-like star) to detect at all. This will not prevent PLATO and TESS to successfully survey bright stars over all the sky, to look for close-by transiting stars. But these missions will work with many more targets to overcome the transit probability and mostly look at targets further out than 20 pc.

In the case of M stars, transit become much more advantageous. The terrestrial planets are not only more easily detectable thanks to a larger $\frac{R_{\text{planet}}}{R_{\text{star}}}$ ratio, but also the geometric transit probability of a planet in HZ is about 2 to 5%. And on top of that, M stars are much more numerous than higher mass stars. The MEarth catalog, which is mostly complete up to 20 pc, indicates a cumulative count of about 600 M

stars at that distance [Dittmann et al., 2014]. The frequency of habitable planets around M stars is estimated at about 40% [Bonfils et al., 2013]: this means that several of them transit around nearby M dwarfs. The goal of many ground surveys is precisely these very interesting nearby low mass stars.

But not being able to suppress the star light is a problem because of the planet/star contrast: the information obtained by differential spectroscopy is strongly impaired by the photon noise from the star. Direct imaging with a coronagraph can tackle this problem, as we have explained in section 1.2.7. Such a gain will be a determinant factor when looking for biomarkers. That brings us to the next part: direct imaging.

2.4.3 Current limitations of direct imaging

Direct imaging has the capability of both finding our closest neighbors and doing spectroscopy to characterize their atmospheres and surface properties. So why not simply directly detect the planets, skipping radial velocities or astrometry altogether?

The first issue is that we currently know very few suitable target stars for direct imaging of habitable planets. While young and long period planets have already been imaged, habitable planets are much harder. For the latter, angular separation and contrast requirements restrict us close stars: a reasonable distance limit to consider is 10 pc [Guyon et al., 2006]. Any large mission or survey aiming at a spectroscopic characterization must first find where the planets are by spending some time exploring almost blindly, relying mostly on the stellar parameters for prior target selection. If a survey mission can be launched as a medium sized mission (that is what NEAT aims to be) and the coronagraph needs to be a large mission, it makes a lot of sense to have a pre-established list of targets to optimize the design and the utilization of the most costly instrument.

The second issue is that a detection by direct imaging alone gives a very poor constraint on the planet mass. The radius can be estimated by a model, but the result depends on the assumed planet albedo. Mass limits can be estimated from the radius, using more models and/or mass-radius scatter diagrams of exoplanets for which both quantities have been measured. But in the end all we have are approximative mass limits that are highly model dependent.

2.4.4 Summary

Significant progress in the ability to filter stellar noise down to 0.1 m/s on long timescales (year or more) with radial velocities would seriously undermine the motivation for an μ as astrometric mission, but this does not seem very likely to happen in the short term. For the case of close stars, the effort behind neat can be seen as a workaround the stellar noise problem: the astrophysical noise problem is traded for another one, which is instrumental. Transits constitute a valuable parallel avenue of exploration, which has its own merits but cannot correctly address our very close Sun-like neighbors: when looking nearby, we find ourselves cornered in the same part of the parameter space than radial velocities: M stars.

An astrometric solution also has the additional merit of increasing the diversity of exoplanet detection techniques, which brings advantages via the complementarities of

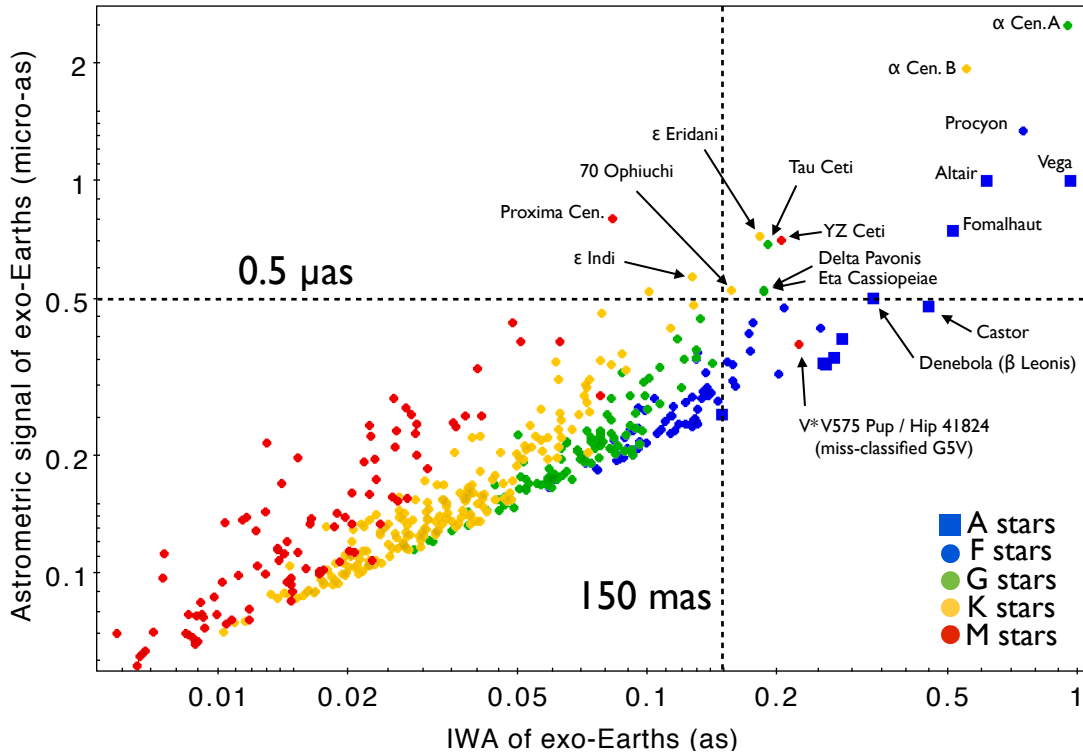


Figure I.9: Astrometric signal of exo-Earth in HZ vs. IWA for nearest F, G and K stars.

methods, for example concerning the orbital periods and the inclination of the systems. Thorough observations of nearby stars by astrometry (at μas accuracy), radial velocities and direct imaging combined would yield very detailed knowledge of close planetary systems. This second aspect would help toward a better comprehension of planetary formation.

Concerning a space coronagraph mission, a precursor astrometric mission would pave the way by making it less risky, easier to prepare and enhancing its scientific yield, because target locations and characteristics would be known beforehand. Above all, it would provide a reliable measure of the planetary masses.

Figure I.9 show the astrometric signal of exo-Earths in HZ versus the inner working angle (IWA) for the nearest A, F, G K and M stars (at less than 20 pc). With an astrometric accuracy of $0.5 \mu\text{as}$ and an IWA smaller than 150 mas, one can combine astrometry and direct imaging for 12 of the easiest targets.

3 Astrometry, exoplanets and NEAT

3.1 Historical presentation of Astrometry

Astrometry is the oldest of all astronomical sciences. It consists in the study of positions and motions of the celestial objects. The first astrometric observation only needs the naked eye as an instrument: some of the brightest objects are moving across the sky relative to the fixed sphere of stars and this is in fact the origin

of the word “planets” (from Greek “asteres **planetai**” i.e. **wandering** stars). The Babylonians are the first civilization known to have left written evidence of extensive studies of the path of the celestial bodies and star catalogs. By inferring from these basic observations and using some mathematics, the Babylonians produced remarkably accurate ephemerides [Aaboe, 1974]. They predicted in particular solar eclipses, daytime durations or the variations of the number of days between two new moons.

Astrometry then continued in the West with the Greeks: Eudoxus (370 BC), Timocharis of Alexandria and Aristillus (300 BC) and then Hipparchus (135 BC) created other star catalogs [Aaboe, 2001]. Hipparchus made his measurements using an astrolabe and obtained the positions of at least 850 stars with an accuracy of about 20 *arcmin* [Lankford, 1997]. He discovered the precession of the equinoxes by comparing his catalog to Timocharis’ and Aristillus’. After that there was very little improvement until the late 16th century. Finally, in 1586, the Danish astronomer Tycho Brahe achieved measurements with 30” accuracy using a quadrant [Kovalevsky and Seidelmann, 2001]. Although the final precision of the catalog is 2’ instead of 30” because the atmosphere refraction causes systematic errors which were not taken into account correctly, this was a huge step forward. At this point, the precision of the instrument (not considering the atmospheric systematics) is limited by the resolution of the eye.

The first practical refracting telescopes were build in 1608, then followed the reflective telescopes in 1668, by Isaac Newton. Observation with telescopes allowed sub arcsecond astrometry, leading to the discovery of the aberration of light [Bradley, 1727] and the nutation of the Earth’s axis [Bradley, 1753], and to the measurement of the first parallax [Bessel, 1838]. Although different setups were used for astrometry, the most common way to measure the parallaxes and separations between double stars was a telescope equipped with a filar micrometer. The latter is a reticle that has two fine parallel wires or threads that can be moved by the observer using a micrometer screw. By placing one wire over one object of interest and moving the other to a second object, the distance between the two objects at the focal plane can be measured with the micrometer portion of the instrument. Note that the objects must be close enough to be in the field of view and that the measure is differential (it needs two objects). The differential accuracy obtained depends on the telescope diameter but can reach a few dozen of miliarcseconds.

The invention of photographic plates allowed to capture and archive images of the sky. The great advantages of the photographic plates were not so much in terms of accuracy, but because much dimmer objects could be observed (with long exposure times) and a large volume of data can be processed and archived. Photographic plates/films were experimented with as early as 1790 by Thomas Wedgwood [Hirsch, 1999] and people quickly realized their potential for astronomy. However, they became widely used only about 100 years later, when their sensitivity and their usage was practical for astronomy. Finally, in the 1980s, CCDs (Charged-Coupled Device¹¹) replaced photographic plates and reduced errors to 1 mas. Automatic control of the instruments coupled with CCDs allowed the creation of the modern catalogs with even larger numbers of stars.

¹¹CCDs are microelectronic devices that are sensitive to light. They operate by shifting charges between each sensitive element, called pixel. They are widely used in digital cameras.

3.2 The recent developments

The digital revolution has given us all the key technologies to enable space missions and ground surveys: automated data acquisition, instrument control, data transfer to Earth, data processing pipelines, data distribution and archiving. For astrometry, this has culminated into the *Hipparcos* (High Precision PARallax COLlecting Satellite¹²) [van Leeuwen, 1997] and *Gaia* (Global Astrometric Interferometer for Astrophysics¹³) [Lindgren et al., 2008] space missions. *Hipparcos* has yielded the parallaxes of 100,000 close stars with an accuracy of 1 mas, which will very soon be superseded by *Gaia* with the parallaxes of 1,000,000,000 stars with an accuracy up to 7 μ as. The success of *Hipparcos* and the exquisite accuracy expected from *Gaia* are largely due to the fact that being in space, these missions are not impeded by atmospheric turbulence.

However access to space is quite recent and still very expensive, atmospheric turbulence has not prevented astronomers from trying accurate astrometry from the ground and persevering despite severe hiccups. The last two centuries are plagued with a history of exoplanet detections by astrometry on the host star [Boss, 2009], such as the infamous planets around 61 Cygni and Lalande 21185 which have never been confirmed. The recurrent reason of these false positives is an underestimation of systematic errors. More recently, astrometry with large ground-base telescopes (2-8 m class) has been more successful. It was initially thought that the precision was limited to about 1 mas, due to the atmospheric image motion which comes from the expression $\sigma = \theta/D^{2/3}$, where D is the telescope diameter and θ the angular separation between the stars [Lindgren, 1980]. It was later found that by using a grid composed of many reference stars, the expression (asymptotically) becomes $\sigma = \theta^{11/6}/D^{3/2}$ [Lazorenko, 2002]. This opens the possibility of narrow angle relative astrometry better than 100 μ as over a field of view of 1', which is a significant improvement over *Hipparcos* and sufficient to detect giant exoplanets around nearby stars [Sahlmann et al., 2013a].

Ground instruments have reached accuracies up to 50 μ as with FORS2 for example [Lazorenko et al., 2009] and we have now some solid astrometric evidence of exoplanets [Sahlmann et al., 2013c]. Another powerful technique that was been developed for astrometry is interferometry on dual stars, with instruments like PTI (Palomar testbed interferometer) [Colavita et al., 1999] and PRIMA (Phase Referenced Imaging and Microarcsecond Astrometry) [van Belle et al., 2008]. Interferometry on dual stars can accurately measure separations, up to a few dozen of μ as (its work better for small separations, under 1"). The progress made from the time of *Hipparcos* until now is summed up in Fig. I.10. In the next section I will talk specifically in more details about exoplanet detection by astrometry on the host star.

¹²*Hipparcos* was a scientific mission of ESA (1989-1993). It was the first space mission devoted to precision astrometry, it measured the parallaxes of 100,000 close and bright stars with an accuracy of 1mas. The name of the mission is an obvious reference to the ancient Greek astronomer Hipparchus.

¹³*Gaia* is a scientific mission of ESA launched in december 2013, for a planned duration of 5 years. It is expected to measure the position of 1 billion objects with an accuracy going from 7 micro arcseconds (for magnitude V=10) to hundreds of micro arcseconds (V=20). *Gaia* works by direct imaging: although it was first planned as an interferometer, this design was abandoned but the name was kept.

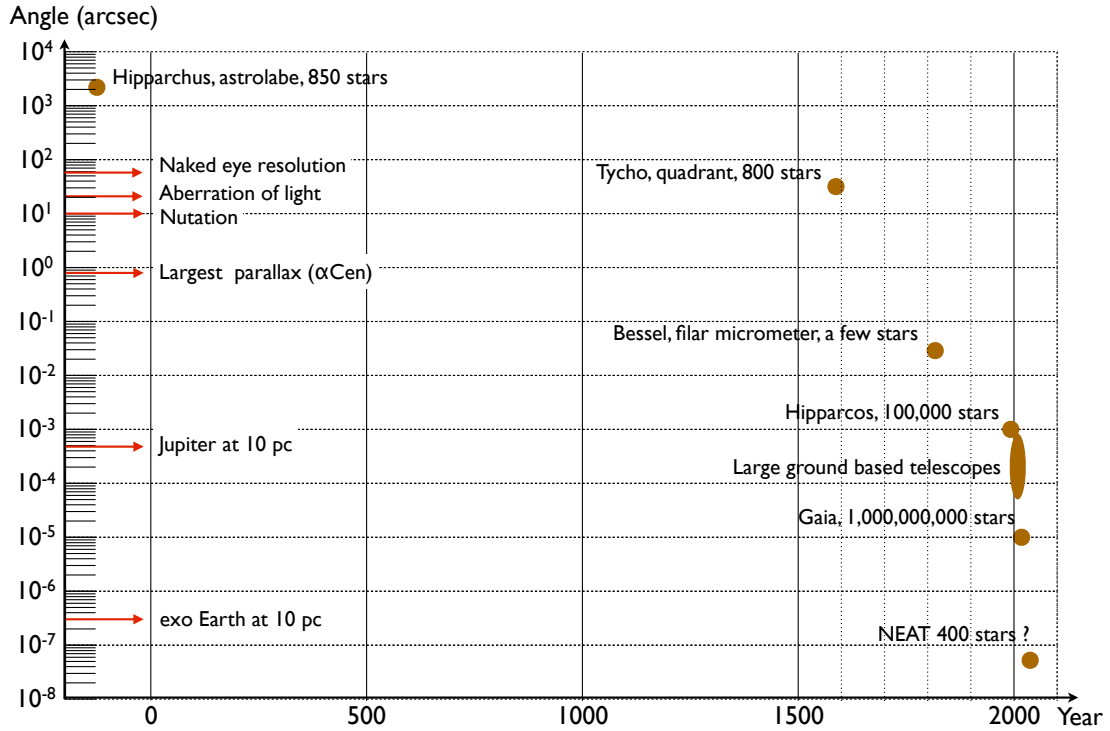


Figure I.10: **2000 years of astrometry: from Hipparchus to Hipparcos.** This plot shows the progress of astrometric measurements versus time. Each dot represent the accuracy obtained after a new breakthrough. On the left the labels indicate the angular amplitude of several phenomena.

3.3 Exoplanet detection using astrometry

3.3.1 Astrometric signal

This concept was briefly presented in section 1.2.3, more details will be given here. I recall the principle: the presence of a planet causes the star to have an orbit which is characteristic of the planet. For a circular orbit, the amplitude of the astrometric signal is:

$$A = 3\mu\text{as} \times \frac{M_{\text{Planet}}}{M_{\oplus}} \times \left(\frac{M_{\text{Star}}}{M_{\odot}}\right)^{-1} \times \frac{a}{1\text{AU}} \times \left(\frac{D}{1\text{pc}}\right)^{-1}$$

Given the very small angular signal generated by planets compared to our current technical capabilities, and the $1/D$ signal amplitude scaling, astrometry is limited to close stars [Malbet et al., 2010]. The signal of an exo-Earth at 10 pc is obvious to derive from this equation: $0.3 \mu\text{as}$. This is a really tiny angle, it is the apparent angle of 0.5 mm on the Moon (seen from the Earth). Yet this is the accuracy that must be reached if one is to detect an exo-Earth in the solar neighborhood: this will become obvious when making the NEAT catalog of target stars (chapter II), from the Hipparcos catalog [Perryman and ESA, 1997]. A minimal distance of 10 pc is highly desirable to have a reasonable number of target stars and detected planets regarding the two scientific goals we have already mentioned (understanding planetary formation and searching for life outside of the Solar System). The first goal requires enough detections for meaningful statistics. For the second one, the idea is to detect at least a few habitable planets, dozens if possible.

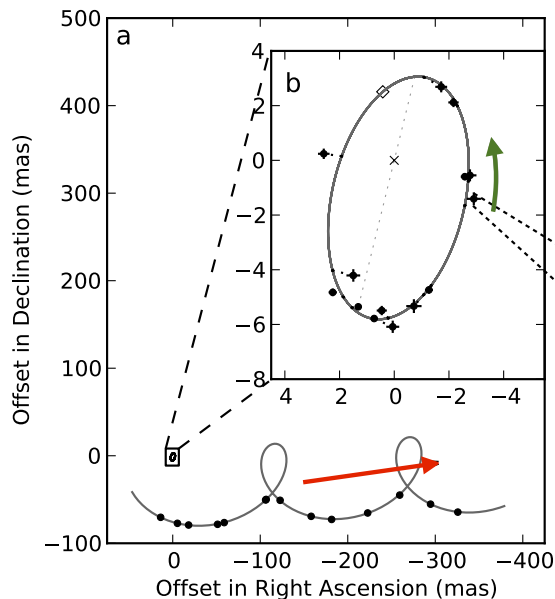


Figure I.11: **Example of accurate multi-epoch astrometric observation.** At first sight, the star motion fits well with a model that includes the proper motion (indicated by the red arrow) and the parallax. The residuals (of parallax and proper motion) are shown blown up in the upper right rectangle, where we see the astrometric signature of a dwarf star companion. The orbital motion is indicated by the green arrow. Figure from [Sahlmann et al., 2013b].

3.3.2 Different types of astrometry

There are two different types of astrometry: absolute and relative. The first kind has been carried out by Hipparcos and will be continued by Gaia. The spacecraft, being advantageously placed in space, have continuous access to the sky over large angles and work in scanning mode. They spin continuously and compare the position of stars in two field of view separated by a large angle (106° for Gaia). This kind of data can be processed to find an absolute (global) astrometric solution for all stars. On the opposite, relative astrometry only needs a limited field of view, this is the kind of astrometry that is being done with ground telescopes, for example with PRIMA or FORS2 [Lazorenko et al., 2009]. In this case, the position of a target star is compared against the position of other reference stars in the field. These are usually more distant, weaker and more numerous, they provide a practical way to construct a constant frame of reference for measuring the target star position. The advantage of this approach is that systematic noise (for example due to the atmosphere) often affects the reference and the target in almost the same way: this makes possible to reach an accuracy (for the target) that competes with global space astrometry, for a few pointed targets of particular interest. In the end, both kinds can in principle be used to detect exoplanets, the determinant factor being the final accuracy of the measurements.

3.3.3 Examples of astrometric observations

Whether global or differential, multi-epoch astrometric observations of a star enable us to see its motion projected on the celestial sphere. An example of multi-epoch differential astrometric observations is presented in Fig. I.11 in relative equatorial

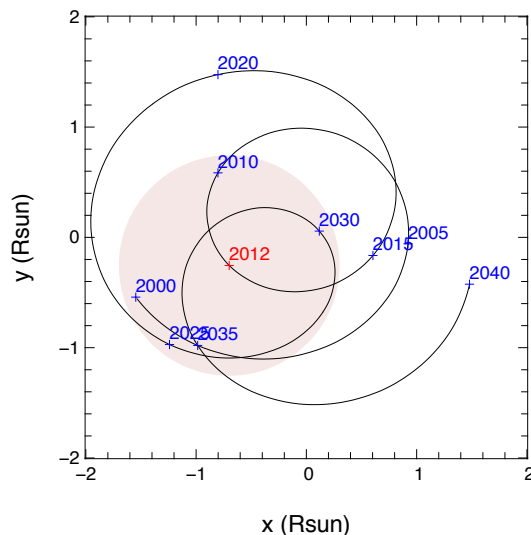


Figure I.12: **Orbit of the Sun between 2000 and 2040.** The astrometric signal (in distance units) generated is the sum of the images of the orbits of each planet scaled down by a factor $M_{\text{planet}}/M_{\text{star}}$. The final motion is dominated by Jupiter and Saturn and its amplitude is on the order of magnitude of the Sun diameter. For the Earth, the signal is about 2000 times smaller.

coordinates. The nutation, precession and aberration of light disappear thanks to difference with references stars. The trajectory looks like a cycloid: the observed motion is in first approximation a combination of the proper motion (uniform constant speed move) and the parallax (sinusoidal back and forth motion with a period of one year). Hypothetical planetary signals would be much smaller and would not be directly visible on the figure.

If the astrometric accuracy is good enough and several planets are present around a star, the residuals from a proper motion, parallax and eventual stellar companions fit (like in Fig. I.11) would show even smaller wobbles that look like Fig. I.12.

3.3.4 Retrieving the planet orbits

In order to find the planets in the sum of astrometric signals, one can use a Fourier analysis to detect each planet, one at a time. Each planet has an orbit which is identical to the orbit with a different period: it is not possible for two planets to have identical or close periods, or else the planetary system would be unstable because close encounters would occur between the planets [Davies et al., 2013]. So by fitting the perturbation associated with each period until only noise is left, one can in principle fit all of the system planets with statically significant signal (i.e. above the detection threshold) one by one. Of course, another condition is that the number of measurements must be greater than the number of parameters, or the inversion problem is degenerate. Figure I.13 shows the parameters necessary to characterize an orbit. In total 7 parameters are needed to uniquely specify a star orbital motion caused by one planet: the planet mass plus the six Kepler orbital elements [Bate et al., 1971]. So the number of parameters needed to characterize N_{planets} from a multi-epochs astrometric observation of a single star is: $N_{\text{param}} = 5 + 7N_{\text{planets}}$. The first 5 base parameters are: position (right ascension/declination), proper motion (right ascension/declination) and parallax. If star companions are present, the orbital motion adds 7 parameters per companion.

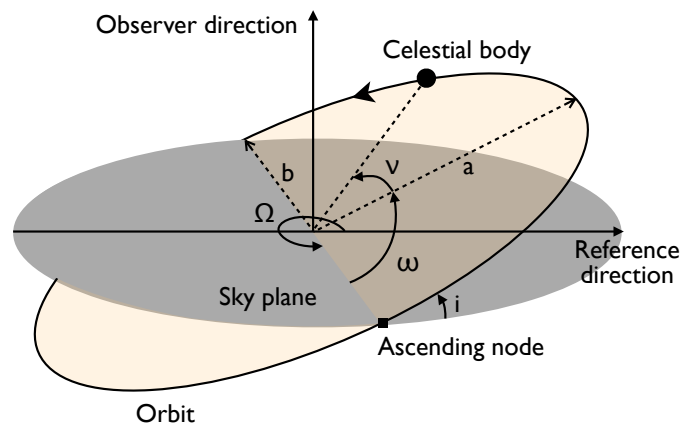


Figure I.13: **Illustration of the Kepler orbital parameters.** The parameters are: semimajor axis a , eccentricity $e = \sqrt{1 - \left(\frac{b}{a}\right)^2}$, inclination i , longitude of the ascending node Ω , argument of periapsis ω and true anomaly ν .

A complete fit with real data, from proper motion and parallax to terrestrial planets orbits is quite tricky to do properly. In order to demonstrate the feasibility of the whole process and to check for degeneracies, a double blind test was conducted in 2009 by NASA [Traub et al., 2009]. A set multi epoch astrometric and radial velocity data for single stars was generated by a first team, then other teams analyzed the signals to try to detect the planets and characterize their orbits and masses, of course without knowing the planets simulated by the first team. The conclusions of the test are:

- The presence of giant planets does not prevent the detection of the smaller ones.
- There is sharp change at $\text{SNR}^{14} = 6$, where the completeness of detection is around 50%, and is close to 100% for $\text{SNR} > 10$. These were theoretical predictions and are well confirmed by the experiment.
- The parameters can be retrieved from the data with reasonable errors (less than 10% for the most important parameters like mass and period, with a $\text{SNR} > 10$).
- The degeneracy between the parameters is in general low, except in some particular configurations, for example near edge-on inclinations can be confused with high eccentricity.
- As orbital periods start to exceed the astrometric data time span, the detection threshold raises and the problem becomes degenerate (for the outer planets). In this case, partial orbits can still be fitted and this does not affect the detection of short period planets. Some loose parameters with large error bars or only upper/lower bounds are obtained for the large period planets.
- Radial velocities measurements are an important complement to astrometric ones.

Another blind test has been started in February 2014 in Europe by the NEAT consortium (managed by Guillem Anglada). In this study we have added some refinements, we only give the relative positions of the reference stars and the target star. This allows simulating noise on the references (this was neglected in the previous double

¹⁴The SNR is defined here as the ratio between the astrometric signal as given by Eq. I.2 and the differential astrometric accuracy noise between two epochs.

blind test): even if they are further away, reference stars can have companions or giant planets that will be detectable and will introduce errors on the target.

The double blind phase of the test ended the 08/10/2012, the teams have officially handed their results on the blind data set (priv. comm.). From a first analysis of the results, we can already draw the following conclusions:

- The presence of noise around the reference stars did not change significantly the results compared to the previous double blind test, detection thresholds are close to theoretical predictions ($\text{SNR} \approx 6$).
- Very noisy reference stars (usually with giant planets around them) can be easily spotted and dealt with, at least by removing them from the astrometric solution.

3.3.5 Noise of astrophysical nature

At last, in order for the detection to be possible, the astrophysical astrometric noise must be smaller than the astrometric signal (or can be calibrated out). Indeed, stars are active objects and present several features on their surface that have different brightness and change in time. All of these dynamical features rotate with the star, in particular dark spots, when going from one side to the other, introduce an astrometric jitter by moving the effective barycenter of light. Several studies have tried to quantify these effects and found that even for an exo-Earth around a Sun analog, the astrometric jitter is smaller than the signal except for very active stars [Makarov et al., 2010], at least 5 times more active than the Sun [Lagrange et al., 2011].

3.3.6 Summary

To summarize, all the following conditions must be fulfilled in order to enable the detection of an exoplanet by astrometry on the host star:

- SNR of 6.
- Number of observations greater than $N_{\text{param}} = 5 + 7N_{\text{planets}}$ to avoid degeneracy
- Time span longer than the planet period
- Astrophysical astrometric noise smaller than the astrometric signal (true for exo-Earths around most main sequence stars)

3.3.7 The near future: giant planets with Gaia

Gaia, which has been launched in december 2013 and should complete its nominal mission within 5 years, will find thousands of giant exoplanets by astrometry [Lindgren et al., 2008]. The reason why Hipparcos did not find any planets unlike Gaia is because its accuracy is just above the critical threshold (Fig. I.10: Hipparcos is slightly above “Jupiter at 10 pc”). On the opposite, Gaia has the capability to detect giant exoplanets around stars up to a few hundreds of parsecs (several hundred thousand stars). Even though giant planets are fairly rare, by the sheer number of stars surveyed, Gaia will have a huge impact on our knowledge of exoplanets.

3.3.8 Next generation astrometric instrument concepts

Unfortunately Gaia accuracy will fall short of detecting exo-Earth around our closest neighbors. Gaia was conceived to look at very faint stars and saturation of its detectors will prevent to reach the photon limit for stars below magnitude 6. For bright stars, the noise floor is expected to be at best $7 \mu\text{as}$ [Lindgren et al., 2008].

Here are a few interesting space-borne mission concepts that have been studied or proposed to succeed to Gaia:

Corono-astrometry This concept combines coronagraphic imaging with astrometric measurements [Guyon et al., 2012]. Both measurements are done simultaneously with a single telescope: the central part of the field enters a coronagraph, while the outer part is imaged by a wide field camera. The large outer field give access to reference stars. The primary mirror is marked with small dots arranged in a regular grid that creates diffraction spikes. The spikes can be used to calibrate of the FoV distortion and measure the position of the central star.

SIM (Space Interferometry Mission) SIM is an optical interferometer capable of μas accuracy that was developed at the JPL [Goullioud, 2010]. The interferometer configuration is of the Michelson type: the beams from two telescopes (50 cm in diameter separated by a distance of 6.5 m) is recombined to create interference fringes.

NEAT (Nearby Earth Astrometric Telescope) NEAT was proposed in 2010 at the ESA call for M class missions [Malbet et al., 2012]. It is an astrometric optical imager in a very simple optical configuration: only one (primary) mirror and a detector at the focal plane. The mirror and the detector are 40 m apart and on-board two spacecraft flying in formation. This design with only one optical surface allows for a minimal distortion of the FoV, advantageous for μas astrometry.

STEP (Search for Terrestrial Extrasolar Planets) STEP¹⁵ is a mission of CAS (Chinese Academy of Science) / NSSC (National Space Science Center) selected as part of the advanced research project in the Chinese Strategic Pioneer Program (SPP) on Space Science. STEP is a pointed astrometric mission similar to NEAT but it uses a compact configuration with several mirrors [Chen, 2014]. The telescope has to be equipped with metrology systems for the CCD and the mirrors to enable μas astrometry.

Despite the interest of the exoplanet community, none of the 3 first projects is actually scheduled to fly in the near future. The SIM-Lite was canceled by NASA after the the Astro2010 Decadal Report, despite a successful technology demonstration. The corono-astrometry is still at an early phase of numerical simulation / lab demonstration [Guyon et al., 2013], and NEAT was proposed to ESA in 2010 in the framework of the call for M3 missions in the Cosmic Vision plan [Malbet et al., 2012], but it was not selected to fly. At last, if STEP is approved to enter phase B

¹⁵STEP is a mission of CAS (Chinese Academy of Science) / NSSC (National Space Science Center) selected as part of the advanced research project in the Chinese Strategic Pioneer Program (SPP) on Space Science. STEP is a pointed astrometric mission similar to NEAT but it uses a compact configuration with several mirrors. If approved to enter phase B around 2015, STEP should be planned for launch in 2020.

around 2015, it should be planned for launch in 2020.

4 My contribution in the context of NEAT

The research is organized into two main axis: the first one is fairly general and relative to the assessment and the optimization of a NEAT-like mission from the science perspective. A very important aspect of this is the creation of a catalog of potential targets stars and the discussion of how one should select the final targets and allocate the observation time between them. The second one is the demonstration of the feasibility of the detection of nearby Earth-like exoplanets by astrometry, based on the design of the NEAT mission: the NEAT lab demonstration.

4.1 NEAT mission: science case and optimization

An important aspect of the mission, which is closely related to the science case, is the selection of the target stars. Given that the NEAT mission has not been selected yet, it would be an overkill to establish a complete/final list of targets. However, it is quite useful to start with an approximative one, which can be constructed easily from the readily available Hipparcos catalog. Such a list can be used to estimate the detection threshold for each star and the total science yield as a function of the total observing time available and its allocation between the targets. Using this list as a tool, we will discuss the trade-offs between the two scientific objectives of NEAT. This will be second part of the chapter II (after the presentation of the NEAT instrument). Part of this work has been used as a contribution to the μ -NEAT proposal in 2012 (an adaptation of NEAT as a S class mission) and for the NEAT double blind test.

A delicate question that has been glossed over is section 3.3 (Exoplanet detection using astrometry) is: what should be the number of epochs (i.e. instrument visits) per target? We have seen that too few visits can result in an under-constrained problem if they are too many planets around a given target star ($5 + 7N_{\text{planets}}$ parameters per star are needed). On the other hand, one can not simply decide to use a arbitrarily large margin for the number of visits because a real instrument will lose precious photon collecting time whenever it has to change target (or “slew”). Additionally, for the NEAT instrument in the formation flying configuration, fuel has to be used every time the target is changed. More visits per target means that the total number of reconfigurations has to increase which results in either:

- a longer slewing time (to decrease fuel use per reconfiguration): the effective time spent staring at the stars and hence the number of collected photons is smaller, so the telescope is less efficient
- or more fuel is used: the telescope is more massive/more expensive

As the number of planets is not known prior to the observations, one has to use a assume a value (plus an eventual margin) estimated from established results from other detection methods. The last part of the chapter II will explain how to find the optimal number of visits.

4.2 NEAT lab demo

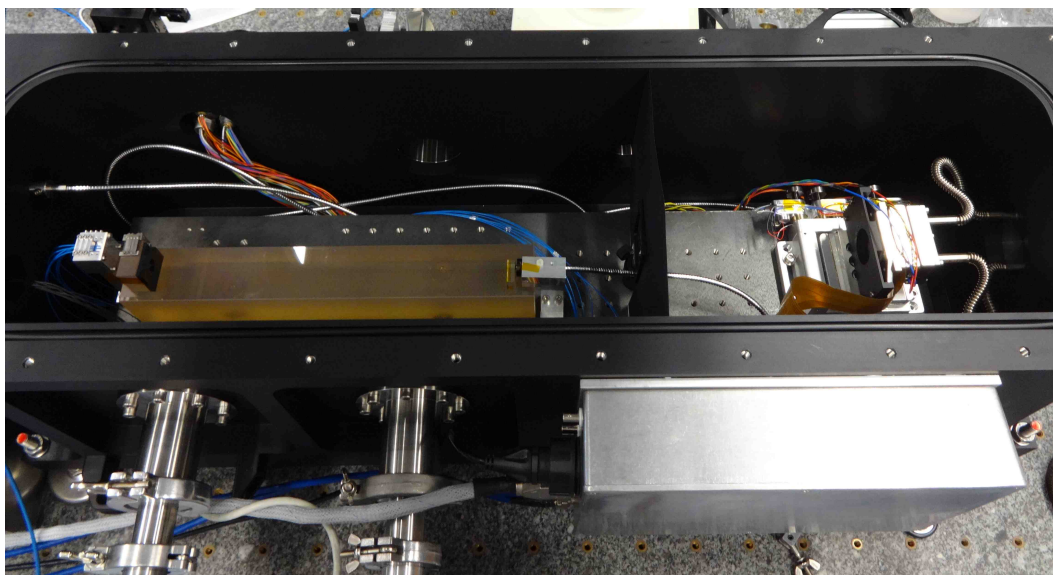


Figure I.14: **Picture of the NEAT demo experiment in its vacuum chamber.** The testbed imitates the configuration of the NEAT mission and has two main sub-systems. The first one produces the pseudo stars: a blackbody light source is fed into a large core fiber and lights-up a pinhole mask in the object plane, which is imaged by a mirror on the CCD. The second sub-system is the metrology, it projects young fringes on the CCD. The fringes are created by two single mode fibers facing the CCD and fixed on the mirror.

The rationale behind a sub- μ as astrometric survey of nearby stars has been described in section 2.4. We will see in chapter II that the 0.3μ as accuracy required to detect an exo-Earth up to 10 pc, given the chosen configuration (diameter of 1 meter, focal distance of 40 meters, pixel size of 10 microns), corresponds to a need to control focal plane calibration errors to roughly 5μ pixels. Although this number can slightly vary depending on the number of measurements per target star and the error budget allocation choice, for the proof of principle we will stick to the baseline specification which is 5μ pixels at Nyquist sampling. Given that the NEAT mission feasibility is dependent on this calibration method, which is a first of its kind, it has to be demonstrated in the lab, prior to being applied in space. This is the reason why CNES (Centre National d'Etudes Spatiales¹⁶) has financed the NEAT demo experiment (Fig. I.14), which has been assembled and operated at IPAG (Institut de Planetologie et d'Astrophysique de Grenoble).

This experiment is the core of this thesis and is the object of chapters III, IV and V. Chapter III presents the testbed and its specifications, the tree product and the test results (critical individual components and sub-systems), chapter IV explains how the data is analyzed and chapter V gives the final experiment results. A positive conclusion from this experiment is critical to reinforce the credibility of future NEAT/ μ -NEAT proposals.

¹⁶CNES is the French Space Agency. Established in 1961 and headquartered in Paris, its current annual budget is about 1.9 billion euros (2012).

Chapter II

NEAT mission

This chapter is linked to two critical aspects of the thesis. The first one is awareness of the broad context and scientific issues that lie behind the mission concept. As the field is evolving very quickly, it is necessary to understand the implication of new discoveries and to stay open minded. It is possible for a given mission concept to become less interesting or even obsolete within a few years, or on the contrary more interesting, as new missions are selected and discoveries unfold.

The second aspect is the participation to the calls for space missions. Writing proposals is a time consuming and delicate exercise that relies on the availability of high quality technical content, in order to advocate for a specific mission concept. Putting in this chapter my work related to the NEAT mission concept and its scientific case is a good way to organize and archive content for later use. The initial proposal of NEAT in 2010 (ESA call for M3) occurred before my PhD, but I have participated into a μ -NEAT proposal in 2012 (ESA call for S class missions) and the next opportunity is the upcoming ESA call for M4 missions with a deadline for proposals mid January 2015. The consortium of the former NEAT mission will make a new proposal for a mission called Theia. The content of this chapter will provide very useful material to contribute for this new proposal.

1 Presentation of NEAT

The design of the NEAT mission is way out of the scope of this document. A CNES phase 0 study which objective was to study the trade-offs between different missions designs was in preparation, but it was unfortunately canceled after the selection of PLATO, which changed the priorities for the CNES. Figure II.1 illustrates 3 different possible configurations: the first one is the formation flying as presented in the NEAT proposal, the second one is a study by NASA called EXAM, with a 0.6 m primary mirror and a 20 m deployable boom, the third one is more standard, it is a compact three mirror configuration (called KOSCH). The mission that was proposed to ESA in 2010 was based on the formation flying configuration [Malbet et al., 2012], it is the only one that has been studied extensively by the NEAT consortium to this date. In the subsequent discussions, formation flying will be considered as the default option.

The mission objective is to find most of the exoplanets in our Solar neighbourhood

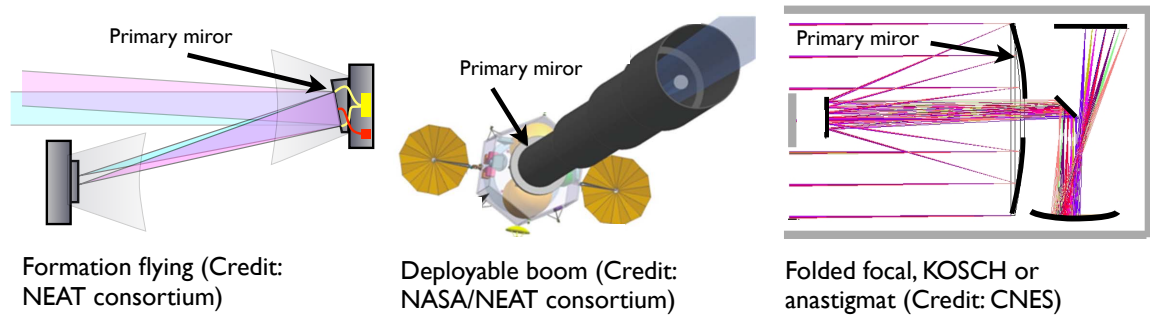


Figure II.1: Illustration of 3 possible configurations for NEAT.

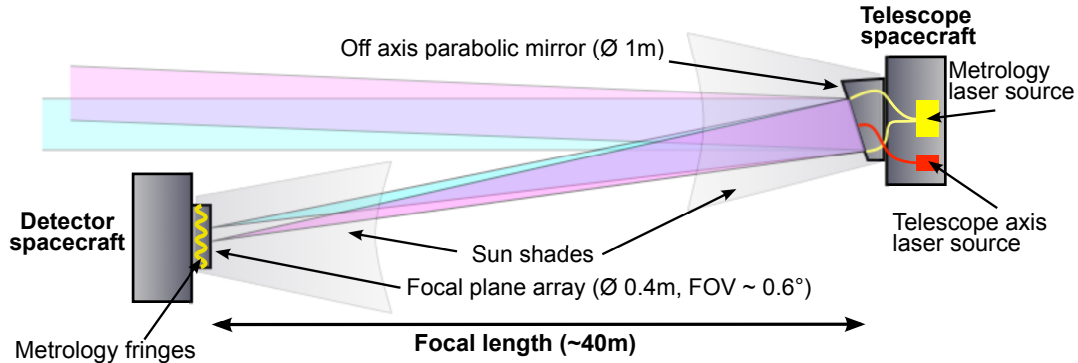


Figure II.2: **Schematic of the NEAT formation flying spacecraft.** NEAT is composed of a mirror spacecraft and a detector spacecraft. A metrology system located on the mirror projects dynamic Young fringes on the detector. The fringes allow a very precise calibration of the CCD. The optical configuration is an off-axis parabola so there is no obscuration of the field of view. At last, Sun shades prevent direct or reflected Sun light from reaching the CCD. All three aspects (metrology, no obscuration and Sun shades) are critical to enable micro arcsecond accuracy.

using differential astrometry (on the host star) to complete the measurements obtained by other techniques. Astrometry can lower the threshold of detection and characterization down to the level of $1 M_{\oplus}$ in the habitable zone of each system, enabling the astronomers to explore in a systematic manner all solar-type stars (FGK spectral type) up to 20 pc from the Sun. In the formation flying configuration, one satellite carries the primary (and only) mirror and another satellite carries the focal plane (Fig. II.2). A calibration system is used to characterize the focal plane with a laser metrology.

1.1 Principle of the pointed differential astrometric measure

With NEAT, unlike Gaia and Hipparcos, measures of star positions are made differentially with a set of background reference stars that are located in the field of view of 0.6° of the instrument of each target star. As there are a few hundreds of targets located randomly in all sky direction, there is almost no overlap and the telescope has to point each target, one after another.

To be able to point any star while flying in formation, the mirror spacecraft is loaded with enough fuel to navigate around the detector and position itself in the right

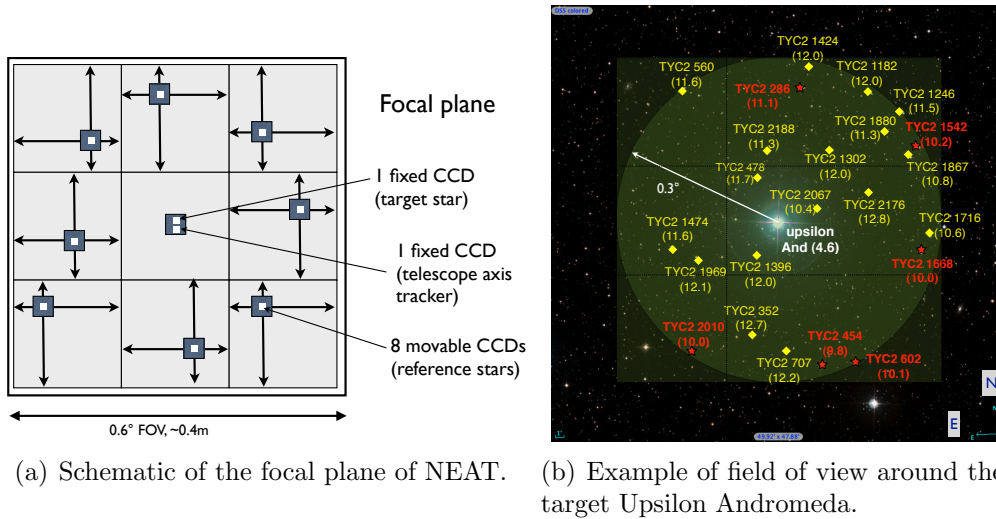


Figure II.3: **Explanation of the focal plane operation.** After the two spacecraft have repositioned correctly, the mirror is oriented to place the target star on the dedicated central fixed CCD. The best 8 reference stars compatible with the configuration are selected and each mobile CCD moves to its assigned reference star.

configuration every time the target is changed. When the satellites are in position, 8 mobile platforms position themselves on the location of reference stars, as described in Fig. II.3. When in position, data is acquired for a few hours (mostly depending on the target priority ranking and the brightness of the reference stars). During this time, the altitude and the relative positions of each spacecraft are stabilized. The finest corrections are done with tip-tilt actuators on the primary mirror, in order to freeze the centroids positions on the same pixels during data acquisition. The complete sequence of events is shown in Table II.4. The stability requirement for the centroids relative to the pixels depends on the accuracy obtained after the focal plane calibration and the data processing. The NEAT lab demonstration, which is the core of this thesis, will explore this aspect (chapters IV and V).

1.2 Single epoch astrometric accuracy of NEAT

The baseline specification for NEAT sets the detection limit at $0.3 \mu\text{as}$ at the end of the mission, corresponding to an exo-Earth at 10 pc, with an SNR of 6. This translates into a final multi epoch accuracy of

$$\sigma_f = \frac{0.3 \mu\text{as}}{6} = 0.05 \mu\text{as} \quad (\text{II.1})$$

We have seen that the minimal number of single epoch measurements required is $N_{\text{param}} = 5 + 7N_{\text{planets}}$. From here we assume an average of 3 planets detected per star¹ which yields $N_{\text{param}} = 26$. We then conservatively assume an effective

¹The recent exoplanet detection with HARPS and Kepler have allowed us to estimate the distribution of exoplanet for a broad range of masses and periods [Wolfgang and Laughlin, 2011] [Alibert et al., 2013b]. Given the detection limits of NEAT, we estimate that it will detect in average less than 3 planets per star.

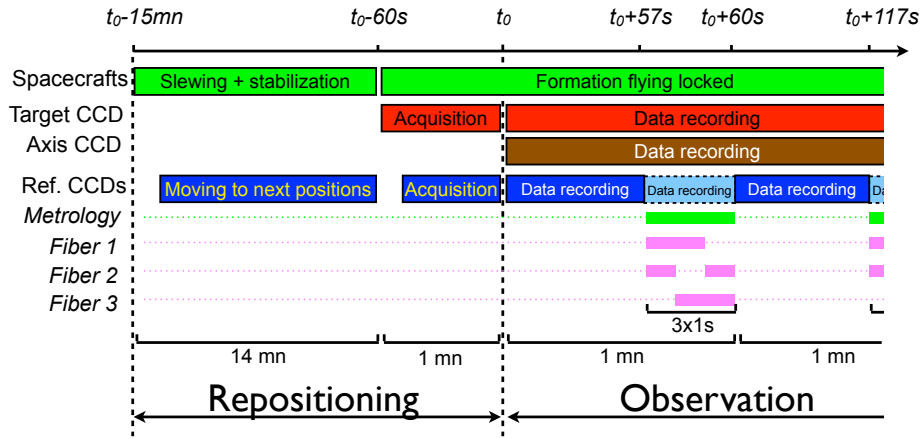


Figure II.4: **Sequence of NEAT operations for a single epoch measurement.** The sequence starts with slewing the spacecraft from the previous target to the new one. Then, the actual observation is composed of repeated 1 minute blocks alternating data recording and metrology. Source: 2010 NEAT proposal.

number of measurements of more than twice the number of parameters², for example $N_{\text{meas}} = 62$. This leaves a number of independent data points $N_{\text{indep}} = 36$. Assuming white noises only, the relation between the multi epoch accuracy, the single epoch accuracy σ_0 and the number of free measurements N_{indep} is:

$$\sigma_f = \frac{\sigma_0}{\sqrt{N_{\text{indep}}}} \Rightarrow \sigma_0 \approx 0.3\mu\text{as} \quad (\text{II.2})$$

Assuming a nominal $10\ \mu\text{m}$ pixel pixel size (necessary for Nyquist sampling of the PSF), and a focal of $f = 40\ \text{m}$, an angle of $\theta = 0.3\ \mu\text{as}$ corresponds on the CCD to displacement of 6 millionth of a pixel (or $6\ \mu\text{pixels}$), using $\delta_{\text{CCD}} = \theta f$. This means that all errors combined must not exceed $6\ \mu\text{pixels}$ for each epoch, including the residual error after CCD metrology calibration. The actual exact requirements are more complicated to calculate as errors of different sources can be allocated in different ways and the number of epochs can be increased. More visits per target has advantageous effects on systematic errors but not on photon noise. Another strategy can be to break each single epoch measurement into several individuals measurements in order to average systematic errors. An astrometric error budget by [Goullioud, 2010] showed that the main requirement can be reached with a CCD calibration error of $5\ \mu\text{pixels}$. The next paragraph explains how each major error source is controlled to the required level.

1.3 How NEAT reaches μas accuracy?

Using relative astrometry from space works in our favor by eliminating/minimizing a lot of systematic errors that would otherwise prevent micro-arcsecond accuracy, like for example, atmospheric refraction and aberration of light. But there are a lot of critical sources of error that remain. They are listed below with explanations of how the current concept deals with them.

²Determination of the optimal number of visits (one visit provides 2 measurements) is a complex issue because a lot of parameters are impacted (see section 2). In short: more visits reduce systematic errors but increase the number of reconfigurations, which decrease effective observation time and increase fuel/mass requirements.

1.3.1 Control of photon noise error

This error is due to the finite number of photons constituting the centroids (target and reference stars). This is a fundamental limitation and represents an ideal error limit for both the centroid estimation method and the instrument as a whole. A fundamental relation in our experiment is the precision reached for a given number of detected photo-electrons. Even if we knew the exact position of every photon detected during the integration (as if the pixels were all perfect and infinitely small and the detector had an infinite size), the best estimator of the centroid location would be the average location of all N_{ph} photo-electrons, and would have a standard deviation of $\frac{\sigma_{\text{PSF}}}{\sqrt{N_{\text{ph}}}}$ (by direct application of the Central Limit Theorem). In this relation σ_{PSF} is the standard deviation for one photon, i.e. it is the first moment of the PSF intensity distribution. This has important consequences in the design of the telescope. From this fundamental relation, we know how many photo-electrons we have to collect in order to reach a specified precision (with a margin left for systematic errors). From the number of targets and the mission duration, we also know that we have to integrate in about one hour. Together, the two constraints tell us what should be the diameter of the mirror, as it happens: about 1 meter.

1.3.2 Control of beam walk errors

When an optical system forms images of two distant points (coming from different angles), systematic errors caused by the shape of the optical surfaces can arise (Fig. II.5) [Shao et al., 2011]. For NEAT the issue is addressed by having only one optical surface and no obscuration, this ensures that the most of the systematic error is common to the whole field of view. This imposes a large distance between the mirror and the focal plane because of the minimum pixel size and the Nyquist sampling condition (see section 1.3.3), and the need to control optical aberrations. Although most systematic errors are common to the whole field of view, variable aberrations can induce differential systematic errors: there are additional stability requirements that increases with optical aberrations. The 2010 NEAT proposal went for a focal of 40 m (accommodated by formation flying), resulting in pixel size of 10 microns. About the stability requirements, studies in the context of the proposal have determined that a wavefront stability of $\lambda/6000$ and a stability of 1 cm of the focus were sufficient to keep differential errors below 5×10^{-6} pixels. However a new analysis done by Jean-Michel Le Duigou (CNES) found lower tolerances (a few mm for the focus, $\lambda/60000$), but still technically feasible (priv. comm., doc. referenced in appendix C).

The formation flying has important consequences on the mission: the number of re-pointings is limited by the quantity of fuel aboard the spacecraft. Other options are to use a deployable boom or to use a more standard optical configuration, like a TMA (Three-mirror Anastigmatic) or Korsh configuration. This latter case is interesting because it eliminates the need for formation flying or deployable booms, which are both delicate points when considering space missions. Only one compact spacecraft is needed but the systematic optical distortion errors have to be calibrated to $0.3 \mu\text{as}$. This is non trivial and has not been demonstrated to date.

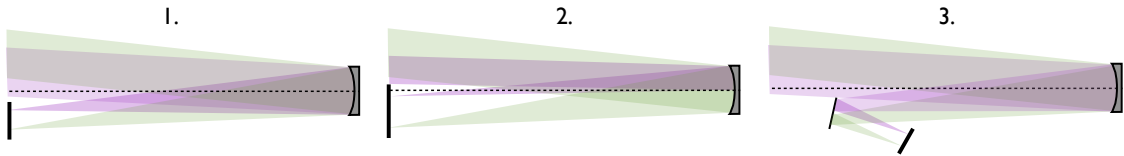


Figure II.5: **Illustration of the “beam walk” problem (term coined by Mike Shao).** Configuration 1 is NEAT-like, there is no obscuration. Configuration 2 has some obscuration on part of the field: the purple beam footprint is only half of the mirror and is affected by different systematic errors than the green one. Configuration 3 has two mirrors: the beams have not the same footprint on the secondary mirror, they are also affected by different systematic errors. A TMA configuration with a central obscuration by the secondary would suffer from the issues of configurations 2 and 3.

A Chinese mission called STEP (Search for Terrestrial Extrasolar Planets³) [Chen, 2014] uses the configuration with several mirrors. A possibility to calibrate the beam walk errors is to use globular clusters⁴: moving and/or rotating the cluster in the field of view gives the information needed to fit the optical distortion field. Additionally, more metrology systems have to be used to monitor changes of the optical surfaces. So there is a trade-off between a configuration with a single optical surface (which has to accommodate a long focal), and a TMA or Korsch (which has to use more calibrations).

In this thesis we work on the basis of the default NEAT configuration (formation flying). We assume that the beam walk problem can be solved by an appropriate spacecraft design and concentrate our efforts on the characterization of errors caused by the detector. However the beam walk issue is a major point to consider for any kind of μas astrometric mission: the formation flying configuration brings a lot of inconveniences. Demonstrating μas calibration of a TMA or Korsch configuration is highly desirable.

1.3.3 Pixelation errors and focal plane calibration

The CCD introduce errors related to the pixels, which are of several types. First, each pixel integrate the signal over a surface, and if the centroid is not at least Nyquist sampled (more than 2 pixels per $\lambda f/D$), it will introduce sampling errors. Moreover, inter pixel variations also introduce some errors, even when the centroids are properly sampled: pixels have different dark currents, sensitivities, they are not regularly spaced and the quantum efficiency (QE) profile within each pixel is not uniform. While the dark current and the sensitivity variations are usually calibrated with darks and flat fields, at our level or precision we have to take into account all the parameters. This is the role of the interferometric metrology system located on mirror spacecraft, with has fibers positioned on the mirror edge and pointed towards

³STEP is a mission of CAS (Chinese Academy of Science) / NSSC (National Space Science Center) selected as part of the advanced research project in the Chinese Strategic Pioneer Program (SPP) on Space Science. STEP is a pointed astrometric mission similar to NEAT but it uses a compact configuration with several mirrors. If approved to enter phase B around 2015, STEP should be planned for launch in 2020.

⁴A globular cluster is a compact group of up to one million stars

the detector

Two fibers are turned-on at a time to project Young fringes on the detector and a differential phase modulation between the fibers is used to make the fringes dynamically sweep the focal plane. The basic principle is the following: each pixel sees a sinusoidal signal whose characteristics (amplitude, offset, frequency and phase) give information about the pixel sensitivity and location. Another important aspect of the metrology is related to the mobile CCDs: by knowing the relative location of each pixel, one is able to measure the position of each reference star CCD with a very high accuracy, by averaging individual pixel positions. This is critical to the mission, as these positions must be known to a few micropixels. The metrology fringes act like a ruler. The fringe pattern produced by the metrology is at the first order proportional to:

$$I(x, y) \propto 2I_0^2 \left[1 + \cos \left(\phi_0 + \Delta\phi(t) + \frac{2\pi(xB_x + yB_y)}{\lambda L} \right) \right] \quad (\text{II.3})$$

Where I_0 is the intensity for one fiber, ϕ_0 is the origin phase, $\Delta\phi(t)$ is the phase modulation applied between the two fibers and B_x and B_y are the (x,y) coordinates of the baseline between the fibers.

The signal seen by each pixel is the convolution of the PRF (Pixel Response function⁵) and the fringe pattern along the modulation direction, which is perpendicular to the fringes. If the modulation is regular ($\Delta\phi(t) = 2\pi ft$), the pixel signals are pure sinusoids.

The phase difference between the measurement and the phase expected from the spatial fit gives the pixel offset. More elaborate models using several bases can obtain more information and probe the PRF, inside the pixel. Simulations have been done, they showed that μ pixel can be reached, provided that the PRF are well characterized [Zhai et al., 2011]. This was only a short introduction about the theoretical principle of the calibration. The NEAT lab demo is an experiment to demonstrate this calibration technique, it is the core of this thesis. The algorithms used to analyze the data are presented in chapter IV.

1.4 Error budget

An detailed error budget, accounting instrument systematic error has been developed in the framework of the NEAT proposal of 2010 by Renaud Goullioud (priv. comm.). The document is listed in appendix C. Figure II.6 is the high level summary of the error budget.

⁵A PRF is a function representing a pixel sensitivity to light (or quantum efficiency) in the CCD plane.

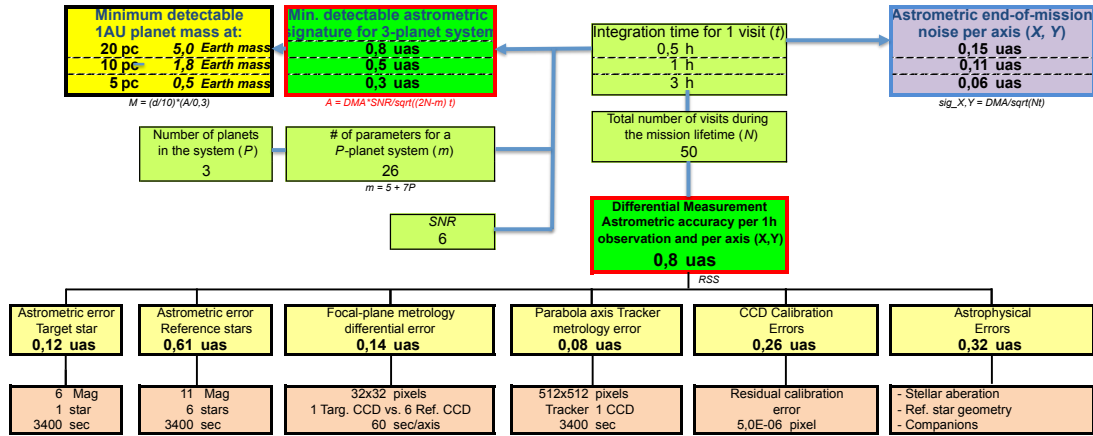


Figure II.6: **High level NEAT error budget.** The goal of the NEAT lab-demo is to demonstrate the number inside the “Residual calibration error” box. Figure from [Malbet et al., 2012].

2 Optimization of the number of visits per target

This work improves upon a previous memo by Fabien Malbet and Alain Léger (priv. comm.). The first memo showed how to compute the optimal number of visits by taking into account the number of free astrometric parameters, the (average) number of planets expected around each target star and the characteristics of the NEAT instrument. One key parameter is the time required for slewing between targets. In the previous memo this parameter was fixed at a constant value of 15 minutes. In reality, for a formation flying configuration, the slew time depends on the total number of slews (target changes) needed.

Compared to the previous analysis, I have introduced the following improvements:

- I consider both cases: constant slew time (deployable boom or compact configuration) and variable slew time (formation flying configuration).
- For the case of formation flying, the variable slew time is introduced in a way that fixes the total quantity of fuel used during the mission.
- I have made a spreadsheet for easier numerical application (document referenced in appendix C).

2.1 Description of the model

In the paragraph 1.2 we have seen that to detect a planet that induces an astrometric signal A (given by Eq. I.2), one need to reach a multi-epoch accuracy of $\sigma_f = A / SNR$ with an SNR of 6. With a detection threshold corresponding to an exo-Earth at 10 pc and using a reasonable assumption of about 60 visits per target, we have seen that the single epoch accuracy σ_0 needed is about $0.3 \mu as$.

I will look more closely at the impact of the number of visits on the multi-epoch accuracy. The method is applicable for any of the three telescope designs presented previously: the value of the penalty associated with a target switch (or reconfiguration) changes, but the principle stay the same. I will apply the method with

different numerical constants depending on which configuration we consider.

First I list the notations and equations that will be useful for this discussion. When applicable I also give the values used for numerical application:

- The number of parameters needed to fit p planets around a given target star: $m = 5 + 7p$. We have seen previously that this value is not well known because it depends on the number of detectable planets per star. For NEAT we assume $p = 3 \Rightarrow m = 26$.
- The number of visits per target: N_{vis} . This is the number we want to optimize. We know that it will be more than 26 (number of free parameters) and less than a few hundreds (too much time spent switching between targets).
- The time effectively spent observing a target during a visit (i.e. collecting the “science” photons): T .
- The number of measurements per visit: α . In our case this number is on debate. Some people think that since we have 2D measurements $N_{\text{meas}} = 2N_{\text{vis}}$ whereas others think that the x and y measurements are not strictly independent yielding to $N_{\text{meas}} = N_{\text{vis}}$. The NEAT double blind test should provide useful insight. Here we will use $N_{\text{meas}} = \alpha N_{\text{vis}}$ with $\alpha = 2$ for numerical implementation.
- The number of independent measurements: $N_{\text{indep}} = \alpha N_{\text{vis}} - m$. This is simply the number of measurements minus the number of free astrometric parameters (m).
- The number of NEAT targets in the main science program: $N_{\text{targets}} = 200$.
- The number of slews (i.e. a telescope reconfiguration, to change target): $N_{\text{slews}} = N_{\text{vis}} N_{\text{targets}}$.
- The duration of a slew: h . This number can be a constant or depend of the number of visits per target (for formation flying).
- The total time spent on a target (observation + slews): $T^* = N_{\text{vis}}(T + h)$

Let us determine h as a function of the number of visits (formation flying case). For NEAT the reconfiguration time is typically 15 to 30 minutes, but the exact duration will depend on the number of visits. Each reconfiguration uses fuel, which is a significant part of the satellite total mass and therefore cost! As for this exercise we want to change only N_{vis} and keep all other things equal, a fixed amount of available fuel also means a fixed amount of **delta-v** (noted ΔV_{tot})⁶. If each reconfiguration has to use in average $\Delta V_{\text{tot}}/N_{\text{vis}}$, then more of them will make each one longer, but by how much?

To answer this question I will consider a very simple model: I neglect any fine propulsion adjustment and I simply consider that the reconfiguration consist of two impulses (one to start moving the spacecraft, one to stop at the new configuration).

⁶In astrodynamics the delta-v (literally “change in velocity”) is a measure of the amount of work that is needed to change from one trajectory to another by making an orbital maneuver, in units of speed. Delta-v is produced by the use of propellant by reaction engines to produce a thrust that accelerates the spacecraft.

In this case, the average time required to change target is:

$$\bar{h} = \frac{N_{\text{slews}}}{G_1} = \frac{N_{\text{vis}} N_{\text{targets}}}{G_1} = \frac{N_{\text{vis}}}{G_2} \quad (\text{II.4})$$

where $G_{1,2}$ are constants related to ΔV_{tot} . They can be estimated from the nominal parameters used in the 2011 NEAT proposal. For example, for 20000 slews of 15 min yield: $G_1 = 1333 \text{ min}^{-1}$ and $G_2 = G_1/N_{\text{targets}} = 6.67 \text{ min}^{-1}$.

Note that in our case (formation flying), the slew time also depends on the focal length and on the angular separation between the targets. There is a case to be made for optimization of average slew time by going faster (using more fuel) when the targets are further apart. But we can apply all the principles we have discussed above to the sum (or average) speed of “optimized” slews: if we use twice as much ΔV holding the slew time distribution constant, the total slew time is halved. The relations we have defined above are valid for any slew time distribution.

Now I write the equations between number of visits, the duration of visits, the number of parameters and the multi/single epoch accuracies:

$$\sigma_f = \frac{\sigma_0}{\sqrt{N_{\text{indep}}}} \quad (\text{II.5})$$

$$= \frac{\sigma_0}{\sqrt{\alpha N_{\text{vis}} - m}} \quad (\text{II.6})$$

$$= \frac{\sigma_{T_0}}{\sqrt{T/T_0} \sqrt{\alpha N_{\text{vis}} - m}} \quad (\text{II.7})$$

Here σ_{T_0} is the precision that NEAT can reach in one single observation which last T_0 . From a previous NEAT error budget [Goullioud, 2010] we know that typically $\sigma_{T_0} = 0.8 \mu\text{as}$ for $T_0 = 1 \text{ h}$. This is indeed mandatory if NEAT is to reach its advertised scientific goals. In Eq. II.7, we have implicitly defined $\sigma_0 = \frac{\sigma_{T_0}}{\sqrt{T/T_0}}$.

There is a critical hidden assumption in this last relation: it is that systematic errors, for example due to the instrument and calibration residuals, can also be averaged as the square root of the time spend on a target within a single epoch.

Now that I have defined all the relations I need, I will search for the minimum of T^* as a function of T . This is equivalent to optimize N_{vis} because these two related quantities are the only variables in the expression of T^* (provided that h is also expressed as a function of T). In the end we will obtain the number of visits that optimizes the total time spent on a target, for a given multi epoch accuracy and fixed quantity of propellant fuel.

First let us express N_{vis} as a function of T using Eq. II.7:

$$N_{\text{vis}} = \frac{1}{\alpha} \times \left[\frac{T_0}{T} \left(\frac{\sigma_{T_0}}{\sigma_f} \right)^2 + m \right] = \frac{1}{\alpha} \times \left[\frac{B}{T} + m \right] \quad (\text{II.8})$$

I have introduced the constant $B = T_0 \left(\frac{\sigma_{T_0}}{\sigma_f} \right)^2$ (for the sake of simplicity). I now replace N_{vis} in the definition of T^* .

$$T^* = \frac{1}{\alpha} \times \left[\frac{B}{T} + m \right] (T + h) \quad (\text{II.9})$$

Now consider two cases for h :

Case 1: h is a constant, this is valid for deployable boom and folded focal configurations

$$\frac{dT^*}{dT} = -\frac{1}{\alpha} \left[\frac{B}{T^2} \right] [T + h] + \frac{1}{\alpha} \left[\frac{B}{T} + m \right] \quad (\text{II.10})$$

$$\frac{dT^*}{dT} = 0 \Leftrightarrow \frac{B(T + h)}{T^2} = \frac{B}{T} + m \quad (\text{II.11})$$

$$\Rightarrow T_{\text{opt}} = \sqrt{\frac{Bh}{m}} \quad (\text{II.12})$$

Case 2: $h = N_{\text{targets}}/G_2$, this is valid for the formation flying configuration

$$T^* = \left[\frac{B}{T} + m \right] \left[T + \frac{1}{\alpha G_2} \left(\frac{B}{T} + m \right) \right] \quad (\text{II.13})$$

$$= B + \frac{B^2}{\alpha G_2 T^2} + \frac{2mB}{\alpha G_2 T} + mT + \frac{m^2}{\alpha G_2} \quad (\text{II.14})$$

$$\frac{dT^*}{dT} = \frac{1}{\alpha} \left[\frac{-2B^2}{\alpha G_2 T^3} + m + \frac{-2mB}{\alpha G_2 T^2} \right] \quad (\text{II.15})$$

$$\frac{dT^*}{dT} = 0 \Leftrightarrow \alpha m G_2 T^3 - 2mBT - 2B^2 = 0 \quad (\text{II.16})$$

The root of this 3rd degree polynomial exists and is unique because there is no quadratic term. An analytical formula of the solution exists but we will spare ourselves its expression which is rather cumbersome. The table II.1 sums up the numerical results for different values of h , calculated by an excel spreadsheet (`Nvisits_optimal.xls`). We consider 4 different scenarios:

1. Compact configuration (folded focal, one spacecraft: quick reconfiguration, $h=3$ min)
2. A deployable boom (assumes $h=15$ min for a reconfiguration, to account for boom inertia)
3. Formation flying, large delta-v (uses an average value of $h=15$ min from the NEAT proposal of 2010)
4. Formation flying, low delta-v (assumes half the delta-V than the NEAT 2010 proposal: average value of $h=30$ min)

2.2 Numerical results

Table II.1 shows the optimal visits duration and numbers of visits for different slew times durations and types (constant / variable).

Table II.1: Slew time versus optimal visit duration and number of visits.

Scenario	h	T	N_{vis}
1	3 min (constant)	0.702 h	195
2	15 min (constant)	1.57 h	95
3	15 min average ($= \frac{N_{\text{vis}}}{G_2}$)	1.96 h	78
4	30 min average ($= \frac{N_{\text{vis}}}{G_2}$)	2.51 h	64

2.3 Discussion

The goal was to investigate wherever the optimal number of visit is far from the reasonable assumption of about 60 visits, and to see if different constraints on h change the optimum significantly. When using the simplest approach for NEAT (scenario 2, $h=15$ min and is not adjusted for the number of visits), we find $N_{\text{vis}} = 95$. This was the approach used by the initial memo from Fabien Malbet and Alain Léger. The result reflects the trade-off between wanting to split the photons into as many epochs as possible (to make $\alpha N_{\text{vis}} \gg m$) and losing effective photon collecting time for every additional visit. Of course, we see that when the slew penalty is much smaller (scenario 1), optimal N_{vis} increases to 195.

The critical difference between scenario 2 and 3 is taking into account the fact that with formation flying, if there are less visits, more gas can be used per slew, so slews are shorter, so more time is available for photon collecting. This is an additional incentive to have less visits, and as expected, this results in a lower optimal number of visits: 78 versus 95. Scenario 4 is a test to see how the N_{vis} optimum is sensible to ΔV_{tot} . The result of 64 visits indicates that the mission can accommodate a tighter constraint on fuel without losing too much photon collecting time (6400 hours of slewing instead of 3900, for a total of 22000 hours).

On the other hand, the optimum is very sensitive to σ_f . For scenario 3, changing σ_f from $0.05 \mu\text{as}$ to $0.025 \mu\text{as}$ changes the optimal number of visits to 119, this is almost a linear increase. This means that there is also a case for choosing an optimal number of visits which is different for each target. Remember that $0.05 \mu\text{as}$ is the σ_f needed for an exo-Earth at 10 pc... NEAT will not observe only Suns at 10 pc!

But having different numbers of visits per target has to be considered together with yet another very important kind of optimization: the order in which the stars are targeted to minimize the total angular separation. And to top it all, there are also the issues of having good (regular?) time samplings and the solar exclusion angle. All these problems have to be solved together, with the additional constraint that it would be highly desirable to adapt the number of visits at the end of the mission in function of the number of planets already detected. If we find a very interesting system, no doubt we will want to come back more often before the mission is over. Obviously the whole problem is not trivial to solve and one would have to think of some simplifications and/or using numerical simulations to obtain a workable solution.

One interesting idea with formation flying could be to dedicate a ΔV reserve (a few %) to an end of mission “slow mode”. At the end or after the nominal five year mission, the spacecraft would only observe the few most promising targets (most likely a dozen), the ones which have habitable planets and are high priority targets

for direct detection/spectroscopic characterization, or stars for which there are potential (habitable) planets with signals slightly below the detection threshold (high false alarm probability). This would be an attempt to confirm near-detections and improve the knowledge about the orbital parameters of interesting detections. There is an additional interesting benefit to have a long temporal baseline by prolonging the mission: the knowledge of the true anomaly of habitable planets at the date of their direct detection would be greatly improved. With so few targets, the spacecraft could accommodate very slow slews and use very little fuel, it would spend a long time on each star and obtain exquisite accuracy per epoch. The approach is very low risk: if prolonging the mission in this way is not thought to be worth it after all, the ΔV reserve can simply be burned (quickly) in the continuity of the nominal mission.

To conclude the section, I will make some remarks about how to improve the model. In our flexible h scenarios, we have considered to have a strict $1/N_{\text{vis}}$ dependency. A more accurate model would include a fixed overtime to account for the fine propulsion adjustment needed to enter the static formation flying configuration and the metrology calibration that must take place before data can be acquired.

3 Construction of the catalog of NEAT targets and references

3.1 The NEAT catalogs

This part will explain how the NEAT catalogs are constructed. Of course we are not talking here of a complete and definitive catalog of targets for an actual NEAT mission, but only an approximative catalog which is a tool to:

- obtain statistical information about the target and references
- test time allocation strategies by comparing their yields

The list of target stars of an actual mission would have several differences:

- The Hipparcos catalog is not complete for K and M stars up to 20 pc. A list based on the Gaia survey, which should be available before 2017, would be preferable.
- The main science program is specifically aimed at main sequence stars, so nearby stars would likely be checked against spectral miss-classification and any star found outside of the main sequence removed from the list.
- Close multiple stars should have a special treatment. It may be possible to use their relative orbits as a kind of reference resulting in an exquisite accuracy. On the other hand, overlap of their PSFs will make data reduction more complex. The final accuracy depends on the separation between them, the instrument design and the processing. We have not explored this delicate issue significantly yet. Depending on whether a given binary turns out to be more or less suitable for exoplanet detection, one might want to spend more or less time than for single stars on them. To be accurate, one should also take into account that both can be observed at the same time.

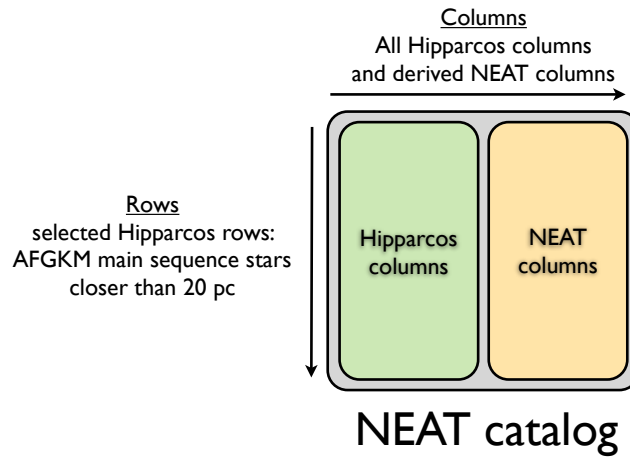


Figure II.7: **Schematic view of the NEAT catalog of target stars.** The NEAT targets are selected within the Hipparcos catalog. The part called NEAT columns are computed values from the Hipparcos original columns, they are useful in relation to the 3 main functions of the catalog mentioned above.

- Very close stars that are not on the main sequence are also interesting science targets but in practice they will be covered by secondary science programs on a case by case basis. We only consider the main science program here.

The important fact is that the Hipparcos catalog is already fairly good (for completeness and spectral classification), so these changes would only affect a few percent of the targets. To simplify the issue with multiple stars, when computing mass detection thresholds in habitable zones, we will consider each star as if it were single and we include the companion(s) in the list of references.

Before going into details, I will clarify some terms that will be used in this part: the “NEAT catalog of targets” will consist of all the main sequence stars of spectral types A, F, G, K and M located at a distance of less than 20 pc from the Sun (Fig. II.7), of the Hipparcos catalog. This makes up for a total of 455 target stars. This catalog also include several new columns called “NEAT columns” which are values computed from the Hipparcos data using known physical relations. What I call the final list of targets is relative to the time allocation exercise (and not an actual mission): it is a subset of the NEAT catalog of targets, relative to a given allocation strategy. As the observation time available of the NEAT mission is not infinite, almost any allocation scheme benefits by discarding some of the most difficult targets, thus freeing more time for the easiest ones.

The rational for selecting stars from A to M spectral types is the following. For stars more massive than A, the orbital period at the inner edge of the habitable zone becomes larger than the mission duration (5 years) and the star become very short lived (less than a few hundred million years). They are not suitable targets for detecting planets in HZ. Moreover, there is no B star at less than 20 pc. M stars are harder for astrometry in HZ (see section 4.2) and better suited for radial velocities. However, because they are so numerous, there is a bunch of really close ones that are very interesting targets. Although Hipparcos is very incomplete for M stars, the early and very close ones are bright enough to figure in it.

The NEAT catalog of references is constructed from the catalog of targets, by finding out which stars are in the field of view of NEAT (0.6°) when it is pointed to a target.

This is done by crossmatching⁷ the NEAT catalog of targets with a subset of the Tycho catalog which contain all stars suitable as references. The process I used to create both catalogs using Topcat⁸ is explained in details in a memo untitled “Creation and exploitation of the NEAT catalog” where I describe the operations step by step, in the form of a tutorial. Here I will briefly explain how the critical NEAT columns are calculated, then I will focus on the results. For more details I invite the reader to refer to the memo which can be found in the appendix F.

3.2 Creation of the NEAT columns

For our purposes, the needed columns are (for each star): distance, *bolometric luminosity*, mass and the distances of the inner and outer edges of the HZ. The main point of this is to determine the amplitude of the astrometric signals of planets (of a given mass) located at the inner and outer edge of the HZ. The distance is directly obtained from the Hipparcos parallax. The bolometric luminosity (L) is derived from the V and B band magnitudes and relations with the effective temperature [Flower, 1996]. The mass (M) is estimated using the following general relation: $L \propto M^{3.5}$. The locations of the HZ edges are given for two types of limits: the maximum greenhouse/runaway greenhouse limits (pessimistic), and the early Mars and recent Venus limits (more optimistic) based on [Kasting et al., 1993].

We now have all the information to calculate the amplitude of the astrometric signal of an hypothetical exo-Earth in a circular orbit at any one of the four HZ edges defined earlier. We can simply scale it from the one of the Earth/Sun couple, via the following equation:

$$A = 3\mu\text{as} \times \frac{M_{\text{Planet}}}{M_{\oplus}} \times \left(\frac{M_{\text{Star}}}{M_{\odot}}\right)^{-1} \times \frac{R}{1\text{AU}} \times \left(\frac{D}{1\text{pc}}\right)^{-1}$$

The astrometric signals of an exo-Earth at this four orbital distances is the information that we store in the columns, the signal for any planetary mass is trivial to obtain from there: it scales proportionally with $M_{\text{planet}}/M_{\oplus}$.

4 Statistical analysis of the NEAT catalogs

4.1 Availability of reference stars

From the catalog of the reference stars, we can determine **the distribution of the size of the groups of reference stars** and the distribution of the **equivalent magnitudes**. A “group” consists of the reference stars associated with one NEAT target. The equivalent magnitude is the magnitude of a star which flux would be equal to the sum of the flux of the references. In the error budget associated with the NEAT proposal, we have assumed 6 reference stars of magnitude 11 per target

⁷A “crossmatch” between two catalogs of astronomical sources is a process usually used to identify which objects are in both catalogs by comparing their positions on the sky, with a specified tolerance. Here I make a slightly diverted usage of the crossmatch to find which objects are in a given field of view, by using a tolerance equal to the radius of the FoV.

⁸TOPCAT is an interactive graphical viewer and editor for tabular data, specialized for astronomical data, developed by Mark Taylor.

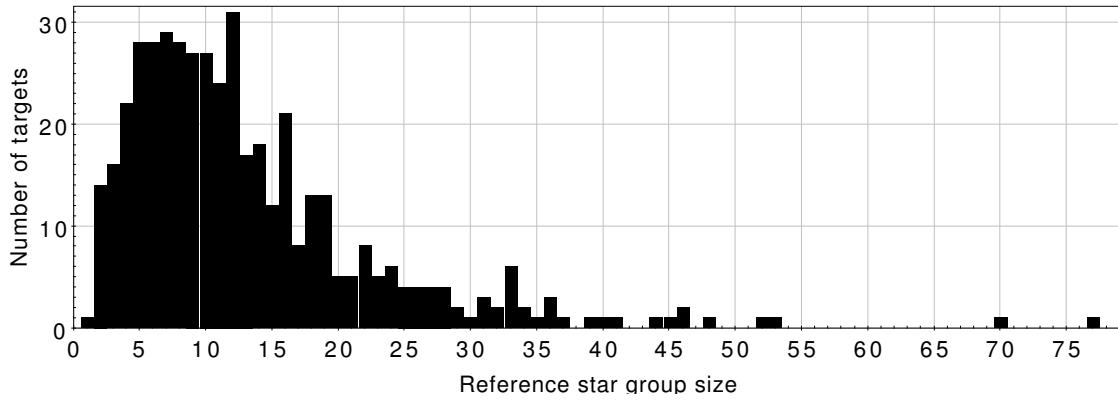


Figure II.8: **Distribution of the number of reference stars per NEAT target star.**

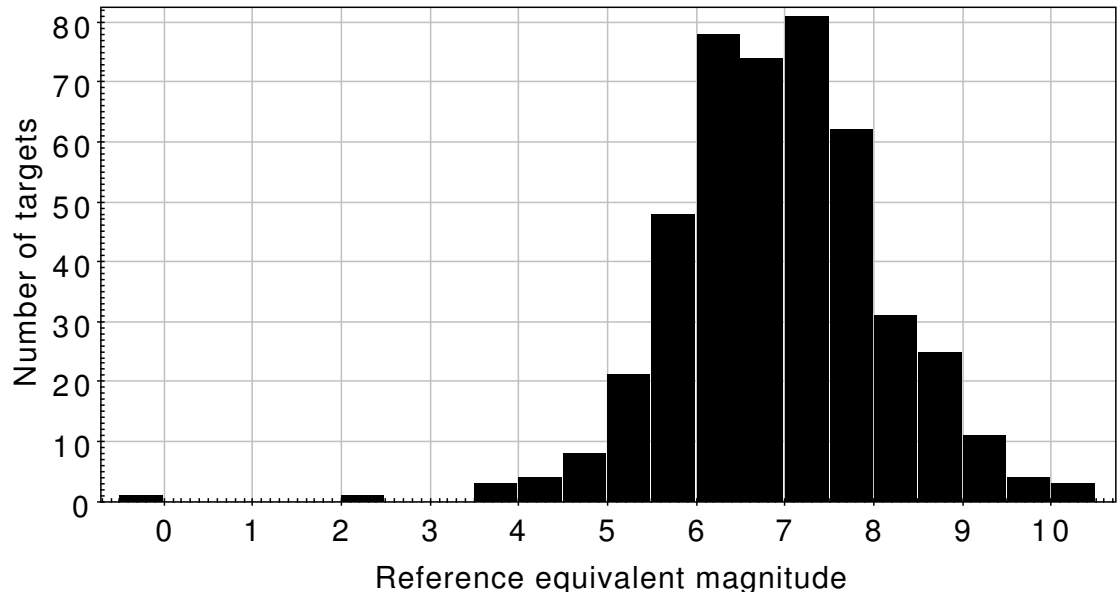


Figure II.9: **Distribution of the equivalent magnitudes of groups of reference stars (one group per target).**

(equivalent magnitude of 9.05). The histograms will tell us what is the proportion of stars for which the assumptions are invalid. Figure II.8 gives the distribution of the size of the groups and Fig. II.9 gives the distribution of equivalent magnitudes.

Overall there are few stars that do not meet the assumptions made for the NEAT error budget: for these stars, the accuracy will be degraded. For the worst cases, the accuracy will be very poor and they will most likely not make it into the list of final targets which will prioritize the easiest ones. Less than 4 reference stars (30 targets out of 455) can become really problematic, a reference equivalent magnitude above 10 as well (3 targets out of 455). These stars must be dealt with on a case by case basis: are they really interesting targets and worth extra observation time?

4.2 Astrometric signal in HZ versus stellar mass

Overall, the astrometric signal (A) in HZ increases with the host stellar mass (M). This is the result of several competing effects:

1. The star luminosity increase with the mass: $L \propto M^{3.8}$
2. The orbital distance of the HZ increase with the luminosity: $R(\text{HZ}) \propto L^{0.5}$
3. The albedo of the planet is higher for bluer light (it moves the HZ slightly closer to the star)
4. The ratio $\frac{M_{\text{planet}}}{M_{\text{star}}}$ is smaller

The net effect of 1 and 2 is an increase of the astrometric signal ($A \propto M^{1.9}$). This is somewhat attenuated by 3 (but it is a weak effect). We can take the albedo into account by defining an effective luminosity $L_{\text{eff}} \approx L^{-\alpha}$ and we obtain for 1, 2 and 3: $A \propto M^{1.9-\alpha/2}$. The effect of 4 is to subtract 1 to the total power. So we finally obtain: $A \propto M^{0.9-\alpha/2}$. This relation is approximative, as we have used several approximated power laws: the $L = f(M)$ relationship breaks down for M stars (the limit is around $0.43 M_{\odot}$) and the albedo effect is in our case modeled by a piecewise linear function. In reality the exact albedo effect will be non linear and specific to each planet.

Figure II.10 shows the astrometric signal in HZ versus the stellar mass. In order to separate the effects of the distance and the stellar mass, Fig. II.11 shows the astrometric signal in HZ (μas) multiplied by the distance to the Sun (pc) versus the stellar mass. This is equivalent to moving all the targets at a distance of 1 pc from the Sun.

Figure II.11 confirms that the spectral effect is weak and that the astrometric signal in HZ increase with stellar mass, roughly as $M^{0.63}$ ($\Rightarrow \alpha = 0.54$)⁹. This result is important, it tells us that astrometry is complementary with radial velocities when searching for planets in the habitable zone. Indeed, for radial velocities, exoplanet detection in HZ becomes harder when the stellar mass increases. There is an important caveat that must be noted here: the increase in astrometric signal with stellar mass goes with a period increase. The temporal baseline must be larger than the period to fully take advantage of the increased signal amplitude. For stars later than A, the orbital period at the inner edge of the HZ becomes larger than 5 years (the nominal duration of the NEAT mission).

4.3 Crossmatch with already known exoplanets

In order to know which of the NEAT targets already have known exoplanets around them, I crossmatch the NEAT catalog of targets with the subset for exoplanets located at less than 20 pc from the Sun. The exoplanets are taken from the exoplanet.eu database (1821 exoplanets). The results of the crossmatch are given in Table II.2 and Fig. II.12. Table II.2 tells several interesting facts:

- Among the 1821 exoplanets candidates, only 126 are located at less than 20 pc.
- The fraction of main sequence stars that have known exoplanets is not significantly higher than the fraction for all stars. We have not put a particularly strong emphasis on main sequence stars in past surveys.
- The known systems have in average 1.7 planet(s): we have mostly found isolated exoplanets because of detection biases.
- We expect on average several planets per star, around almost every star: many more exoplanets are yet to be discovered in our solar neighborhood.

⁹Extrapolating from the following data points: (M=0.42, A=2.0) and (M=2.0, A=6.0).

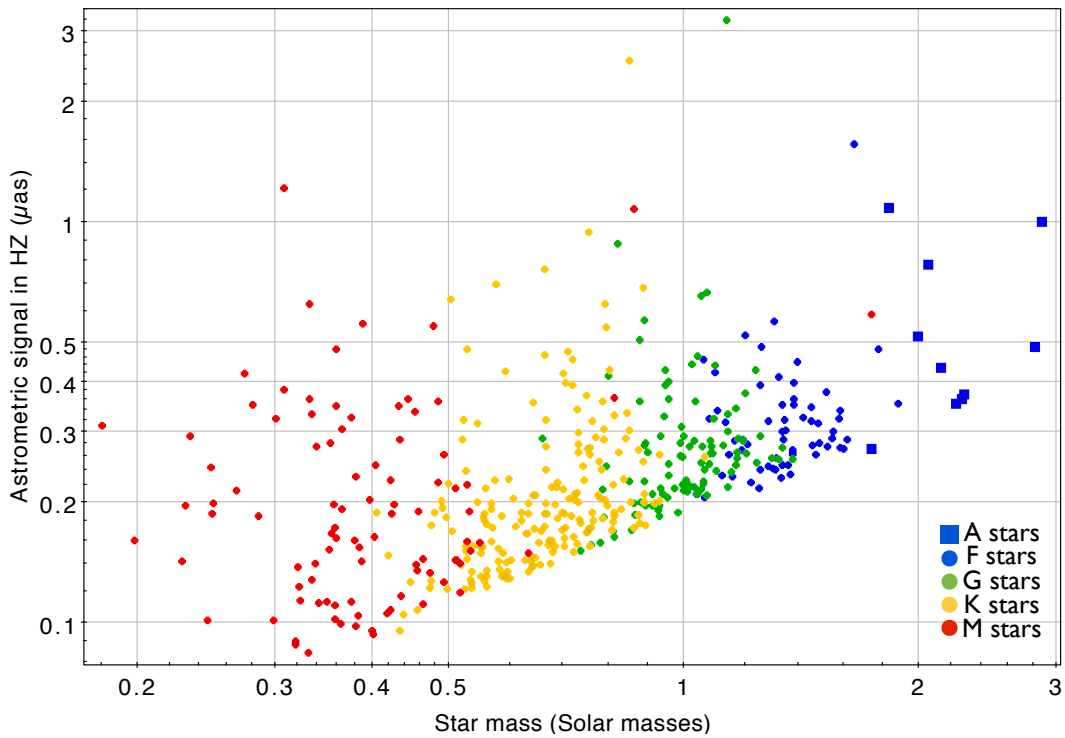


Figure II.10: **Astrometric signal in HZ versus star mass for the NEAT targets, by spectral type.** The different areas corresponding to spectral type from M to A are easily distinguishable. The bottom line is for stars close to 20 pc, the vertical dispersion is caused by the distance. Low hanging fruits (and their spectral types) are easy to spot on this plot. The two stars at the very top (G and K) are the Alpha Centauri system. A few blatant spectral miss classifications (for example 2 M stars with $M > 0.8M_{\odot}$) are visible on the plot.

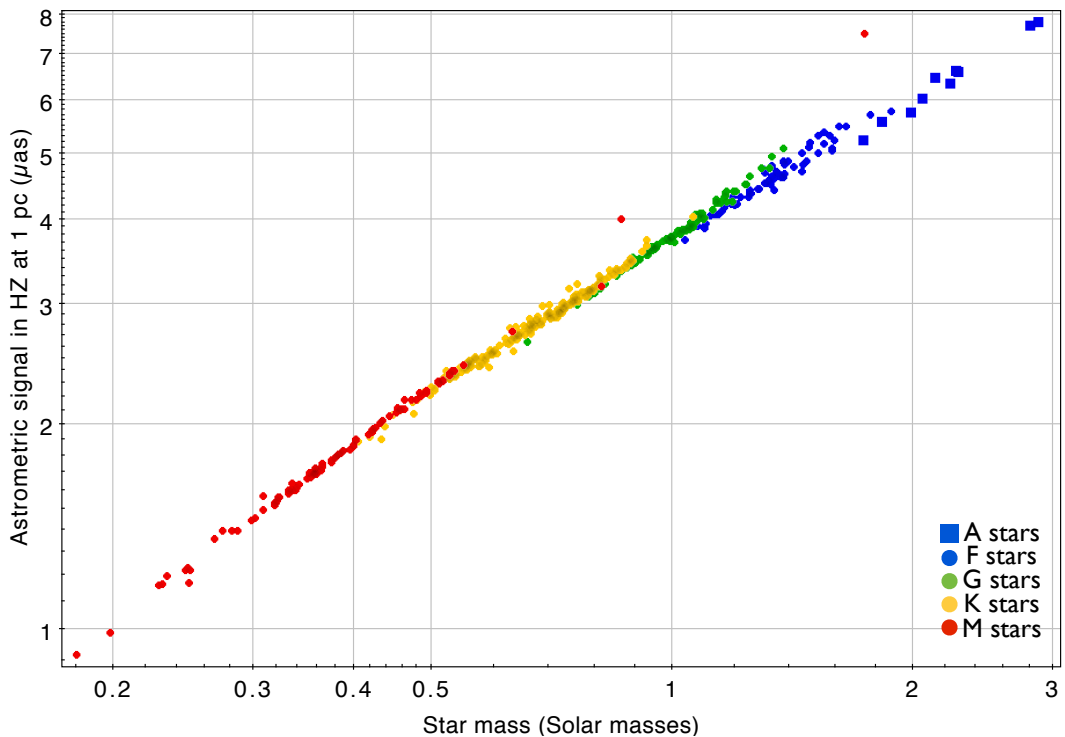


Figure II.11: **Astrometric signal in HZ times distance versus star mass for the NEAT targets, by spectral type.** Multiplying by the distance has normalized the astrometric signal to the signal seen at a distance of 1 pc.

Table II.2: **Number of stars with known exoplanets (updated 02/09/2014).** Two different star subsets are compared: the first one is all Hipparcos stars closer than 20 pc (934 stars) and the second one is the NEAT catalog of targets (455 stars). The “Exoplanet count” tells how many exoplanets have been successfully associated with a Hipparcos host star, the “Star count” tells how many Hipparcos stars host at least one known exoplanet. There is a small fraction of exoplanets for which no host star is found, they are most likely around M stars that are too faint for Hipparcos.

Hipparcos subset	Exoplanet count	Exoplanet count (%)	Star count	Star count (%)
All stars < 20 pc	113/126	90%	64/934	6.9%
Main sequence AFGKM stars < 20 pc	74/126	59%	39/455	8.6%

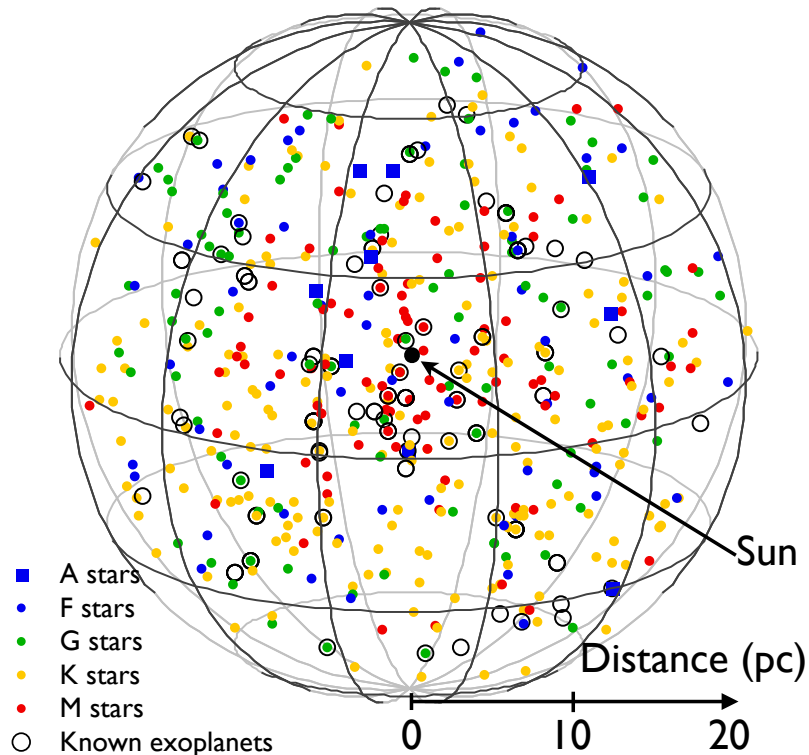


Figure II.12: **3D representation of the catalog of the NEAT catalog of targets, by spectral type (updated 02/09/2014).** The stars are crossmatched with the list of known exoplanets, the ones with at least one known exoplanet in orbit are circled. There are 10 A, 62 F, 97 G, 192 K and 94 M stars.

5 Allocation strategies and science yields

In the NEAT catalog, we have constructed estimations of the astrometric signal of planets in HZ (A_{HZ}), instrumental accuracy as a function of time ($\sigma_{\text{target/h}}$) and the observation time needed to detect an Earth in HZ around a given target (TexoEarth). The accuracy is given in units of $\mu\text{as}\cdot\text{h}^{-0.5}$. This is because it increases as the square root of the number of photons, which is proportional to time. The accuracy also takes into account the brightness of the target stars and the reference stars. For most targets the photon noise of the reference stars is the limiting factor, but sometimes the opposite can be true. This is important to take all these factors into account to have a reliable estimation of the observation time needed to detect astrometric signatures around each star and to rank them properly by increasing difficulty. The detailed reasoning to define the columns is explained in the neat catalog memo.

The fundamental approximation that enables this analysis is that we forget the complex considerations about how to optimize the number of visits, their duration and the number of slews required. We retain only the total time of effective observation per target (excluding slew time from this total). The approximation is valid because the number of epochs per target, number of data points per epoch or integration time per data point all increase the accuracy roughly as a power 0.5 when the number of independent measurements is larger than the number of free parameters.

The planetary systems are based on a list of 344 synthesized planetary systems kindly provided by Yann Alibert, they were originally generated for the NEAT double blind test (for non-blind test runs). The planet systems are randomly assigned to target stars. For detailed informations about the population synthesis model, refer to [Alibert et al., 2013a]. The fundamental assumptions of the planet synthesis model are:

- Maximum of 10 planets per system
- Star mass of $1M_{\odot}$
- Alpha disk model (1+1D model, azimuthal symmetry, $\alpha = 2 \times 10^{-3}$)
- Migration model based on [Mordasini et al., 2011] and [Dittkrist et al., 2014]
- Disk properties (mass and lifetime) should be similar to observations

The analysis consists in distributing the total effective observation time among the targets: once we have done that, the relations and models mentioned above are used to derive the planet yield (any planet with a SNR > 6 is considered to be detected). Based on the content of the NEAT proposal of 2010, the total observing time is 22000 hours. Six time allocation scenarios have been tested. Figure II.13 shows the time distribution corresponding to each scenario. This analysis is carried out with a matlab script (`observational_strategy_yield.m`).

The 6 bar plots highlight the trade-offs between the allocation schemes. The difference between **1**, **2** and **3** is that we increasingly concentrate more time on easy targets. **1** yields more giant planets than **2**, but slightly less terrestrial ones. However when we reduce the number of targets too much (**3**), we obtain less giant but also less terrestrial planets. In this case we have already spent a fair amount of time on the easy targets in **2**, so the additional observation time around these do not compensate for the planet loss of the “medium” targets (ranked 100 to 200).

The idea behind schemes **4**, **5** and **6** is to see whether having an unequal distribution time can yield better results. We test several possibilities:

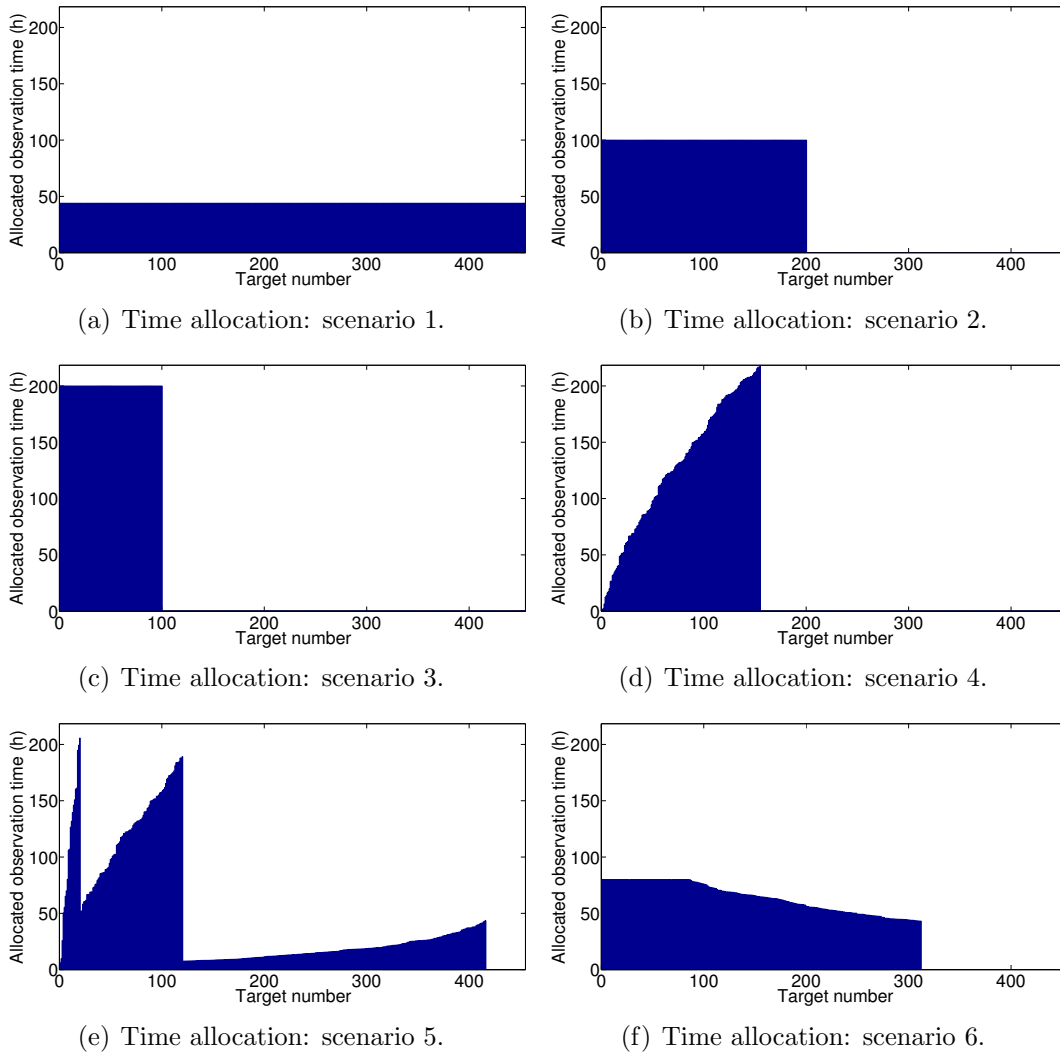


Figure II.13: Time distribution per target for 6 different time allocation schemes.

- In **4**, I choose to spend more time on hard targets, by having for each star an observation time that allows the detection of an Earth at the inner edge of the habitable zone. The advantage is that we avoid using more time than necessary on easy targets. But this also causes the allocation time to increase very quickly (see Fig. II.13(d)) and I run out of time around the target number 160. The overall result is not very good compared to **5**.
- In **5** the approach is similar, but I mitigate the problems encountered in **4** by having several mass detection thresholds. When the allocated time has become too large, the threshold is changed to a higher mass value. The final yield difference with **4** is sensible. However if we look at the distribution of allocated time, the jumps when we change threshold feel unnatural: we are using a lot of time for targets just before the peak and not enough for targets just after, which are only slightly harder. This approach (**5**) was the one used in the NEAT proposal.
- In **6**, the idea is to mainly spend more time on easy targets, but with some caps to avoid wasting too much time. The first time cap is flat, the second one is equal to the time needed to detect a $0.5 M_{\oplus}$ planet in HZ. In practice the second cap make almost no difference (very few targets concerned), so I

ignore it and only apply the first one. For harder targets, the time spent is proportional to $\frac{1}{T_{exoEarth}^\alpha}$. Around harder targets, we reduce the time spent: we only hope to detect massive super-Earth and giant planets.

In the end the simulation indicates that **6** finds the most terrestrial exoplanets. It seems to be a good compromise for splitting time between easy and hard targets, because a significant fraction of the giant planets are detected (55%), not very far from the maximum obtained with **1** (75%).

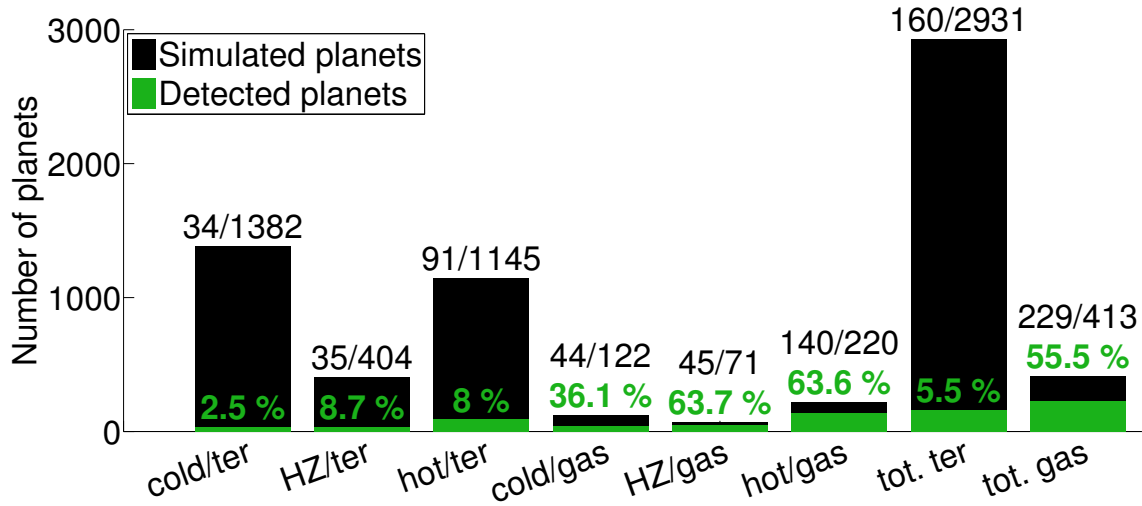


Figure II.14: Exoplanet yields for allocation scheme number 6.

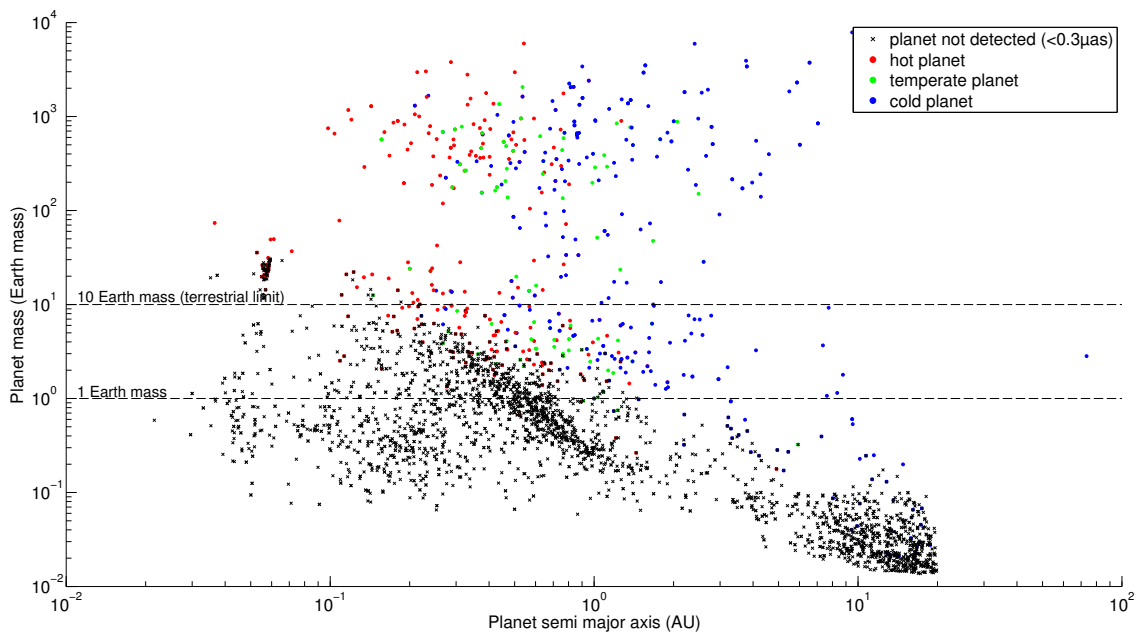


Figure II.15: Mass period diagram of the NEAT mission simulated exoplanet yield.

6 Conclusion

I have shown that with an accuracy on the order of $0.7 \mu\text{as}\cdot\text{h}^{-0.5}$, and with a mission duration of 5 years, NEAT is capable of finding dozens of nearby habitable planets, the closest of which would be the best targets for direct imaging and spectroscopic characterization. I have presented a process from which one can:

- Create catalogs of target and reference stars for a pointed astrometric mission aiming at detecting nearby exo-Earths
- Acquire various statistics about the reference stars and in particular check if the hypothesis made in the NEAT error budget are correct
- Estimate the science yield of the mission, as a function of mission and telescope parameters, the distribution of the observation time between the targets

Because the process is documented at each step, parts of the process can be modified and easily adapted to work with the rest of it. A new input catalog can be used (for example from Gaia), the error budget can be updated and the planet population synthesis model can be improved or swapped for an empirical one based on observations only. Some parameters require only minimal work to update the final result: the time allocation scheme and mission duration can be changed in the final script before execution. The NEAT catalog of target and references and all the associated tools will be very valuable to provide content for the incoming Theia proposal.

Chapter III

NEAT lab demo: concept, specifications, design and test results

1 Foreword

Before going into details, I will have a word about the management of the NEAT lab demonstration. From the start, a project-like approach was taken, to be able to go through the specification, design, procurement, assembling, test and operation phase of the testbed within the 3 years limited by my working contract with CNES: this time framework is rather short for an academic research project with such an ambitious and unprecedented goal. To minimize costs and delays and maximize flexibility, we have chosen to take advantage of the local resources (mainly mechanical, optical and IT manpower and expertise) by locally designing and manufacturing as much components as we could. Having a small and modular experiment was very important for us.

One of the main difficulties in organizing the project was dealing with the limited and somewhat unpredictable availability of the people. The NEAT lab demo being a small project, we would typically require people to work in average for 10 to 20% of their time for us, but we had occasionally the need for stronger commitments to solve specific problems. Of course the availability and need for specific manpower would not always coincide. The initial standard planning approach using a Gantt-like tool quickly revealed to be impractical. The solution that was adopted was to use a low level of planning but to increase communication, follow up and feedback. During the design, commissioning, assembling and testing phases we had weekly meetings and we used a “snapshot spreadsheet” to visualize the current state of the project. It proved to be a very convenient tool, it was very easy to update and allowed us to quickly identify priorities by giving us a good overview about the state of the project. The spreadsheet is more relevant to the design and test phases and will be presented in the appropriate place (section 5: design overview).

Many people from IPAG, IAS (Institut d’Astrophysique Spatiale) and CEA (Commissariat à l’Énergie Atomique et aux Énergies Alternatives) have brought their expertise and made the NEAT testbed a reality. Here is the list of people arranged by domains, to help identify who worked on what: Pierre Kern, François

Hénault, Alain Léger (optics, error budget), Eric Stadler, Noel Ventura (Mechanics), Guillermo Martin, Alain Delboulbé (Metrology) , Olivier Preis (lab environment), Christophe Cara, Modeste Donati, Christophe Doumayrou, Philippe Feautrier (CCD and readout electronics) and Sylvain Lafrasse (IT).

To conclude this section, I have to mention the VESTA experiment (Validation Experiment for Solar-system STaring Astrometry¹), which team was composed of Mike Shao, Bijan Nemati, Chengxing Zhai and Inseob Hahn. In summer 2012, I spent two months at JPL working on a high accuracy astrometric testbed: VESTA. This visit and the interaction with the team was very beneficial to me, I was able to acquire invaluable experience on the design, the operation and the data analysis of the astrometric testbed. As a result we were able to anticipate a lot of issues when designing our own experiment in Grenoble. A lot of specifications of our own experiment are based on the experience gained at the JPL.

2 High level specifications and concept

The primary goal of the NEAT lab demonstration is to show that centroiding can be done at the required accuracy, 5×10^{-6} pixel, with the help of a calibration system and provided that some eventual conditions (that are to be discovered) are met. Obtaining such a performance would validate the fact that systematic errors caused by the pixels can indeed be controlled down to 5×10^{-6} pixels and are not a show stopper for the detection of nearby exo-Earths with NEAT as it was proposed at the 2010 ESA call for M class missions.

Additionally, even if this ultimate goal of 5×10^{-6} pixel accuracy is not reached, the lab demonstration has other important goals that would be very beneficial to subsequent NEAT proposals and more broadly astrometric and transit missions. The most important aspect is the quantitative understanding of all the systematic error sources that must be corrected for to improve the accuracy, from pixels to micro pixels. Another critical aspect is the impact of the observational strategy on the final accuracy: one can chose to move the CCD to a lot of different places to average pixel errors, or to come back to precisely the same positions every time to subtract the systematic errors. In fact it might be possible to come up with a way of obtaining astrometric measurements with a precision greater than $0.3 \mu\text{as}$ even if the pixel calibration does not reach the accuracy of 5×10^{-6} pixel.

In order to explore all the aspects mentioned above in the most sensible manner, the NEAT lab demo mimics the configuration of the NEAT instrument very closely: the concept shown in Fig. III.1 is the starting point from which we derive at first the specifications and then the complete design of the testbed.

¹VESTA is a high accuracy astrometry testbed that was operated at the JPL, it was very similar to and preceded the NEAT lab demonstration.

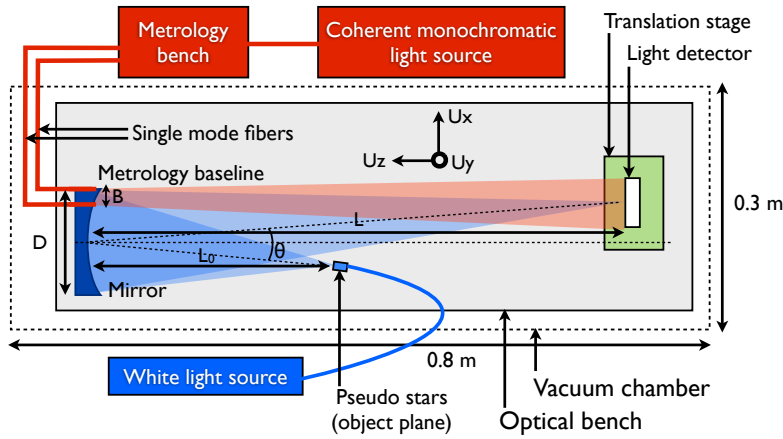


Figure III.1: **Concept for the NEAT lab demo (top view, not to scale).** The elements associated with the metrology, the pseudo stars and the mechanical supports are respectively in red, blue and grey/green. The (X,Y,Z) axis indicated on the figure will be used consistently throughout the document to indicate directions.

The concept includes numerous key elements that are grouped into 4 sub-systems:

Metrology It produces Young fringes on the detector, they are used for calibration, just like in the case of the spacecraft. We use single mode fibers (SMF), their tips are seen as punctual sources by the detector.

Pseudo stars On the NEAT instrument, an off axis parabola focuses the target and reference stars (which are punctual objects optically located at infinity) on the detector. Here we have to use a slightly different configuration where the stars are produced artificially, hence the name of “pseudo stars”. The device that produces them has to be located inside the available space, which is a cuboid of dimensions $0.3 \times 0.3 \times 0.8$ m. Just like for the NEAT instrument, using only one optical surface and having no obscuration in the field of view is critical. The optical configuration is thus with a “real object at a finite distance”. The specification of this system has to be such that the pseudo stars on the detector have no significant difference than ones that would be produced by real stars.

Light detector It will be a CCD or a CMOS.

Mechanical supports and environment control This broad category regroup all mechanical supports and environment control system, in particular it includes the vacuum chamber, which has crucial functionalities. Generally speaking, it reproduces the mechanical and thermal stability of space, at least partially. It is very important to have very little or no pressure inside the chamber to decrease the effect of atmospheric turbulence. Additionally, it allows the detector to work at a lower temperature, which would be impossible at atmospheric pressure because of water condensation or ice deposition. This is needed to control the level of dark current as most detectors do not work optimally at ambient temperature.

The maximum dimensions of the optical bench ($0.3 \times 0.3 \times 0.8$ m) originated at first from the size of a vacuum chamber at IAS, in which the experiment was to be installed. The precise dimensions later became irrelevant because we decided to assemble and operate the testbed directly at IPAG, but we continued with the same

Table III.1: Notations.

Parameter	Notation
distance mirror to CCD	L
distance mirror to pseudo star objects	L_0
min/max wavelength of pseudo stars	$\lambda_{\min}/\lambda_{\max}$
diameter of the entrance pupil	D
mirror focal length	f
separation between pseudo stars objects	s
pseudo stars pinhole diameter	d
off axis angle (pseudo stars)	θ
metrology source wavelength	λ_m
metrology baseline	B
pixel size	e
detector frame format ($N \times N$ pixels)	N

numbers. From an optical point of view, the scale can be chosen arbitrarily as we will see in the pseudo stars specifications (pixel size and Nyquist sampling condition). But as it turns out, working at this scale was a very good trade-off: the optical and mechanical elements are readily available and large enough to be easily manipulated by hand, yet they are small enough to keep costs under control. In the end we have an affordable and flexible system.

Another critical aspect is the mobility of the detector. In order to rigorously determine the accuracy of the calibration, we have to be able to induce a common translation motion of several pixels on all the pseudo stars. With a smaller displacement (or no displacement at all), one would greatly underestimate the residual noise after calibration because the biases caused by the pixels would be strongly correlated. On the other hand, for other kinds of analysis, it is interesting to come back to precisely the same positions, so the translation stage should also be accurate, to a fraction of a pixel (10% or better). Understanding why we do all these different types of analysis and what kind of information will bring each one is quite subtle and cannot be detailed here (see section 2.4: analysis of pseudo star data). To conclude this part I recall that what we want to characterize in this experiment is the error caused by the pixels and not those caused by the optics. For our purposes this second part of the problem is assumed to be solved by either formation flying, a deployable boom or an advanced calibration of the optics. Table III.1 summarize the notations for the critical dimensions and parameters that will be used consistently throughout this document.

3 Specifications

In this section we list the specifications for each sub-system of the testbed, which have been obtained by a wide variety of methods. Some are straightforward consequences of the concept or high level specifications. Whenever possible and practical we have performed calculations to obtain precise quantitative specifications. But lacking this, we have at times relied on the experience gained at the JPL with the VESTA experiment, used guesstimates and/or helped our decisions based on the content of the NEAT proposal of 2010. At last, these specifications are not exhaus-

tive: there are a lot of uncertain areas. In particular, the validity of the error budgets depends on the data analysis methods used. Moreover, our understanding of error propagations has evolved while we have explored the data. We will see in section 1.3 (data analysis of pseudo stars) that we had to deal with quite nasty surprises when looking at the real data.

3.1 Mechanical supports and environment

Mechanical supports:

- The optical bench inside the vacuum chamber (plus all the components installed on it) fits into a cuboid of dimensions $0.3 \times 0.3 \times 0.8$ m.
- The relative positions of the pseudo stars objects and the mirror are constrained by a zerodur bench with a coefficient of thermal expansion lower than 1×10^{-7} .
- The relative position of the pseudo stars (image) and the detector is stable on the X,Y and Z axis to $0.01e$ (to avoid blurring effects)
- The light detector is installed on a translation stage, allowing motor controlled translation in the X and Y direction, with a resolution smaller than $0.1e$. Accurate translation ($< 0.1\text{mm}$) in the Z direction is also possible, at least manually, to adjust the focal point. The resolution on the Z axis is sufficient to have a defocus effect smaller than 1% of the PSF width. Coarse tip-tilt (rotations on X and Y axis) is possible, at least manually.

Vacuum chamber:

- The chamber withstands vacuum ($P < 1\text{mbar}$).
- The sealing quality allows a critical pressure threshold P_{crit} to be reached and maintained without pumping for at least a few hours. The critical pressure threshold P_{crit} is such that it allows the detector to safely operate at a temperature T_{CCD} , corresponding to a dark current $< d_{\text{crit}}$ (see detector specifications). The correspondence between P_{crit} and T_{CCD} is given by the P-T phase diagram of water (this is necessary to avoid the formation of ice or dew on the detector).

Environment:

- Sufficient precautions are taken to provide a dust free environment for the unprotected detector, during data acquisition or modification of the configuration inside the vacuum chamber.
- The temperature of the detector is stable to at least 0.1°C over one hour.

3.2 Detector/pixel specifications

We have to use an off-the-shelve CMOS or CCD in order to limit costs. The model has to accommodate the following constraints:

- Read noise of less than 10 electrons.
- High product “frame rate \times effective well size”, because we want to be able to run the experiment in a “reasonable time” (at most 1 hour, ideally a few minutes). The number of pseudo star and metrology photons needed for 5×10^{-6}

accuracy and corresponding integration times are not trivial to derive: these values are determined by photometric budgets (see sections 4.2.1 and 4.2.2).

- Dark current $< d_{\text{crit}}$ at near or sub 0°C temperature: the residual noise from dark subtraction is less than 10 electrons.
- The detector is free of any optical surface, the matrix of pixels is exposed to air or vacuum to avoid beam walk errors.
- The number of pixels allows at least 5 centroids to be placed on the CCD, while the separation between the star images is enough to ensure that the contamination between the stars in the fitting window is smaller than 10 electrons per frame.

3.3 Pseudo stars specifications

- There is only one optical surface between the pseudo star objects and their images, no obscuration anywhere in the field of view.
- The pseudo stars are diffraction limited.
- The size of the pupil is adapted to the pixel size to have Nyquist sampling of the PSF. This constraint is deliberately placed on the pupil size because it is easy to adapt whereas the pixel size is determined by the choice of the detector model (off-the-shelf).
- Pseudo stars can be remotely turned on/off (altogether).
- The flux at the center of the star images is enough to fill $2/3$ of the quantum well, at the maximum framerate.

3.4 Metrology specifications

- There is no optical surface nor obscuration between the fibers tips (punctual sources) and the detector.
- The metrology can be remotely turned on/off.
- A total of at least 3 different fringe spacings are available in the vertical and the horizontal directions.
- The user can turn on any combination of one or two fibers.
- The metrology wavelength is less than 700 nm, to avoid fringing on the detector.
- The fringe spacings range from 2 pixels (Nyquist sampling) to about 10 pixels.
- The flux on a bright fringe is enough to fill $2/3$ of the quantum well, at the maximum framerate.
- The fringe visibility is more than 0.5 for all baselines and fairly stable (RSD less than 10%).
- The phase modulation amplitude between any two lanes is greater than 2π .
- Stray light is controlled to an intensity level that does not perturb centroid measurements by more than 5×10^{-6} pixel.

4 Critical design constraints

4.1 Nyquist sampling of pseudo stars and pupil size

In order to comply rigorously with the Nyquist sampling requirement, one has to use the shortest wavelength of the pseudo star light spectrum. Using a “midband” average wavelength as reference could result in under-sampling of part of the signal and aliasing. The choice of this minimum wavelength λ_{\min} is somewhat arbitrary as the detector spectral response curve does not necessarily have a steep cut-off profile. We will use a conservative estimate of the minimum wavelength by requiring that the quantum efficiency for $\lambda < \lambda_{\min}$ is less than 10% of the peak efficiency. We keep the option to add a filter to the white source later if aliasing proves to be an issue. This also means that the detector coating for the NEAT demo and NEAT mission should have a spectral profile with a steep cut-off.

In the NEAT-demo optical configuration the size of the diffraction spot is related to the pupil size which is the mirror diameter, and the distance between the mirror and the detector rather than the focal length (see appendix H for a quick justification). Thus the Nyquist sampling condition is:

$$2e \leq \frac{L\lambda_{\min}}{D} \quad (\text{III.1})$$

4.2 Photometric relations

The goal of the next two sections is to determine the pseudo star and metrology integration times needed to reach the targeted accuracy and what are the conditions for which each light source (metrology and pseudo stars) have sufficient fluxes to efficiently fill the pixels quantum wells. Keep in mind that we are looking for orders of magnitudes here, not parts per million. We will use a lot of approximations to get simpler expressions.

Table III.2 lists the notations introduced for these photometric budgets. A visual summary of the photometric relations and where they physically apply in the experiment is shown in Fig. III.2. We have initially considered two possibilities for the pseudo stars: either a pinhole mask combined with a MMF or a bundle of SMF. For the sake of clarity and simplicity, I the summary I only show the relations for the MMF case which was the one to be implemented. After the summary, I present in details how I:

- get from the photometric result per say (the photo-electron flux for the brightest pixels, noted $F_{\max/\text{pix}}$) to the final integration time, by defining a source optimality factor (this part is common for metrology and pseudo stars).
- determine the number of photons needed for the metrology and the pseudo stars (N_{e-}).
- obtain each relation, following the light path step by step from the sources to the detector, for the pseudo stars (section 4.2.1) and the metrology (section 4.2.2).

The numerical applications with the parameters used in the design are shown in spreadsheets (see section 6.1), here we only derive the analytical expressions. The

Table III.2: Notations used in photon budgets. Dimensionless units are noted with a “-”.

Parameter	Notation	Unit
Common notations		
Source optimality factor	η	-
Effective quantum well size	w	-
Total integration time	T_{tot}	s
Total number of frames	N_{frames}	-
Integration time between two frames	T_i	s
Source limited integration time	T_i^γ	s
Minimum integration time allowed by the detector	T_{min}	s
Mean quantum efficiency	ρ_{pix}	-
Maximum photon flux per pixel	$F_{max/pix}^\gamma$	s-1
Maximum e- flux per pixel	$F_{max/pix}^{e-}$	s-1
Pseudo stars		
Minimum number of photo-electrons per star	N_{e-}^*	-
Effective wavelength	λ_{eff}	m
Black body temperature	T_s	K
Spectral irradiance (Plank law)	$B(\lambda, T_s)$	W.m-2.sr-1.m-1
Min/max wavelength for flux integration	$\lambda_{min}/\lambda_{max}$	m
Radiance inside a MMF	L_{fibre}	W.m-2.sr-1
Irradiance on the mirror	E_{mirror}	W.m-2
Power (one star)	P_{im}	W
Photon flux (one star)	F_{im}^γ	s-1
Ratio: brightest pixel flux/total star flux	R_{flux}	-
Metrology		
Minimum number of photo-electrons per pixel	N_{e-}^P	-
Power at the metrology fiber tips	P_{tip}	W
Numerical aperture of the metrology fibers	θ	Radians
Pixel flux for one metrology fiber	P_{pix}	W
Pixel photon flux at the detector for one fiber	F_{pix}^{e-}	s-1
Fringe visibility	V	-

number of photo-electrons needed is an order of magnitude estimation, based on first principles, which assumes that the location noise σ_r caused by photon noise contributes 50% in the Root Sum Square (RSS) of the total location noise, the rest being caused by systematics.

□ Integration time

The final estimated integration time is a function of the number of photo-electrons needed, the detector characteristics (size of quantum well and frame rate) and the optimality factor η of each source. The source optimality factor is a measure of how well the sources are adapted to a given setup, i.e. the design parameters of the testbed and choice of detector. $\eta < 1$ indicates that the experiment would be quicker with a higher photon flux, $\eta > 1$ indicates that the detector is limiting the speed at which we can absorb photons and $\eta = 1$ signifies that the flux is perfectly matched

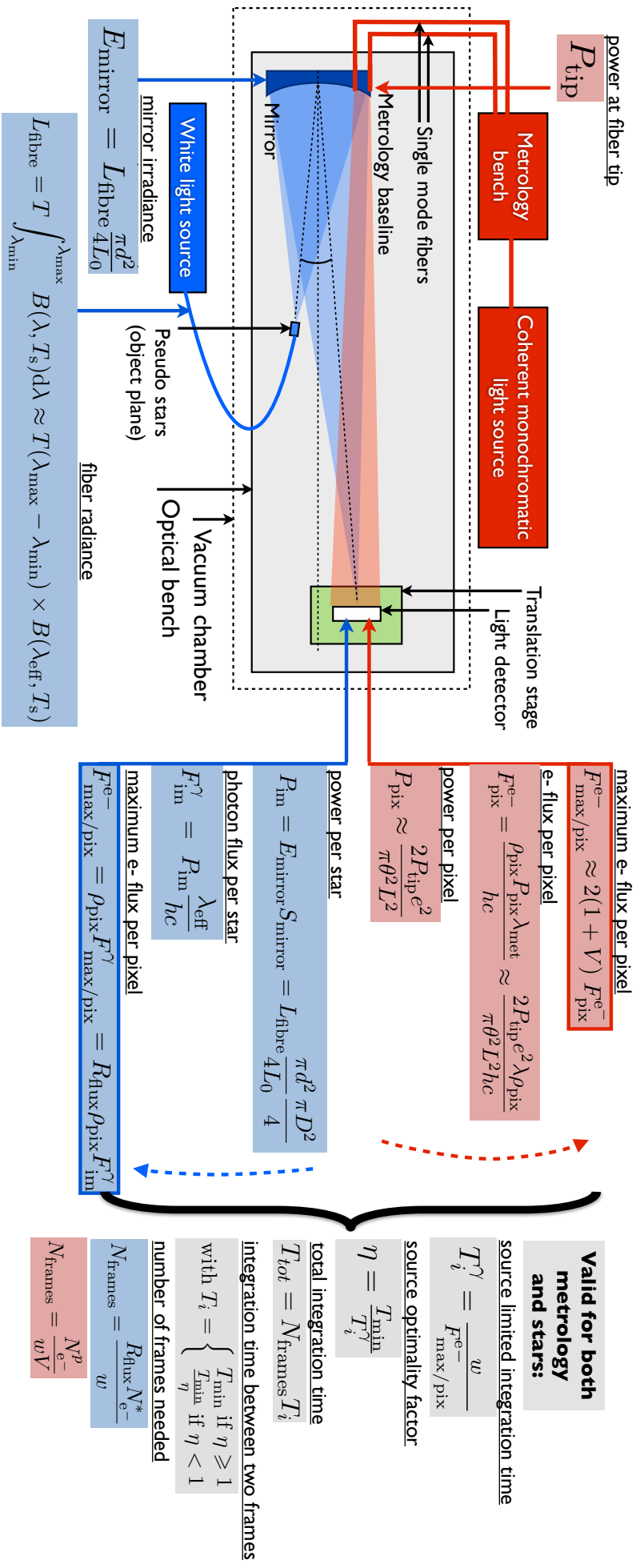


Figure III.2: **Photometric budget summary.** The elements associated with the metrology, the pseudo stars are respectively in red and blue. Relations in gray are valid for both. The relations that give the photometric results per say (photo-electron flux for the brightest pixels, $F_{\text{max/pix}}^{e-}$) are framed in red/blue.

with the detector characteristics. By definition, $\eta = 1$ is when the pixels that receive the most flux are filled at 2/3 of the detector quantum well size at the maximum frame rate. This proportion is a safety factor to avoid being too close to saturation and risking non-linear response. We note w this effective electron capacity, equal to 2/3 of the detector full quantum well.

The time needed to reach the targeted accuracy is:

$$T_{tot} = N_{\text{frames}} T_i, \text{ with } T_i = \begin{cases} T_{\min} & \text{if } \eta \geq 1 \\ \frac{T_{\min}}{\eta} & \text{if } \eta < 1 \end{cases} \quad (\text{III.2})$$

where N_{frames} is the total number of frames and T_i the integration time between two frames. The value of N_{frames} is linked to the number of photo-electrons needed per pixel or per centroid for respectively the metrology and the pseudo stars. We have also introduced the variable T_{\min} : it is the minimum read time for one frame (inverse of the maximum frame rate of the detector), it is fixed by the model of the detector and the design of the readout electronics. We consider that if the light source is the limiting factor, the integration time T_i is expanded by a factor $1/\eta$ (slower frame rate) so that the 2/3 filling factor still stands. If $\eta > 1$ the total time is not shorter because in this case we must attenuate the flux of the source to avoid having more than w electrons per pixel per frame.

In practice we first calculate T_i^γ , the source/photon limited integration time. Then we have $\eta = \frac{T_{\min}}{T_i^\gamma}$ and we can deduce the final T_i .

4.2.1 Pseudo star photometric relations

□ Number of photo-electrons

For the centroids, the photon location noise is $\sigma_r^* = 3.5 \times 10^{-6}$ (50% RSS of 5×10^{-6}). We note the minimum number of photo-electrons for each pseudo star $N_{e^-}^*$, it verifies: $\sigma_r^* = \frac{\sigma_{\text{PSF}}}{\sqrt{N_{e^-}^*}}$. Here σ_{PSF} is expressed in units of pixels. If we approximate the Airy profile with a Gaussian of standard deviation $\sigma = 0.42\lambda L/D^2$, we obtain: $\sigma_{\text{PSF}} = 0.84$ pixel (because of the Nyquist sampling condition) which yields $N_{e^-}^* = 5.7 \times 10^{10}$.

We now consider two cases: the pseudo star objects are either SMF tips or a pinhole mask back-lighted by a very large core MMF fiber.

□ SMF case: photon flux on the image plane

The power coupled from a black body source to a SMF is approximated by:

$$P_{\text{fibre}} = T\lambda_{\text{eff}}^2 \times \int_{\lambda_{\min}}^{\lambda_{\max}} B(\lambda, T_s) d\lambda \approx T\lambda_{\text{eff}}^2 \times (\lambda_{\max} - \lambda_{\min}) \times B(\lambda_{\text{eff}}, T_s) \quad (\text{III.3})$$

In this relation T is an optical coefficient transmission, T_s is the black body temperature, B is the plank law and λ_{eff} is defined as: $\frac{\lambda_{\max} + \lambda_{\min}}{2}$.

²This value of 0.42 is obtained by least square fit of a Gaussian on the central lobe of the Airy disk.

The power arriving on the detector in one spot is the output of one SMF, multiplied by the mirror coupling coefficient, i.e. the fraction of the light collected by the mirror, in the Gaussian beam case: $P_{\text{im}} = P_{\text{fibre}} \times \rho_{\text{mirror,Gaussian}}$. The conversion to a photon flux in the focal plane is done via the following relation: $F_{\text{im}}^\gamma = P_{\text{im}} \frac{\lambda_{\text{eff}}}{hc}$.

□ SMF case: Mirror coupling coefficient (Gaussian beam)

The pseudo stellar sources are fiber tips and emit Gaussian beams that reflect on the mirror and are sent on the image plane. The mirror collects only a small fraction of the light because the NA of the fibre is larger than the apparent angle of the pupil (seen from the object point). As a result only the central part of the beam is collected. The losses due to the mirror surface reflectivity which are typically a few percent are neglected.

According to the Gaussian beam model, the intensity of the light at the point (r, z) is

$$I(r, z) = I_0 \left(\frac{w_0}{w(z)} \right)^2 \exp \left(\frac{-2r^2}{w^2(z)} \right) \quad (\text{III.4})$$

r is the distance to optical axis and z is the distance between the source and the projection on the optical axis.

In the expression above, we have $w(z) = w_0 \sqrt{1 + \left(\frac{z}{z_R} \right)^2}$. As we are in the far field regime, we can simplify this expression: $w(z) = w_0 \times \frac{z}{z_R} \approx \frac{\lambda}{\pi w_0} z = \theta z$. We have introduced theta, the numerical aperture of the fiber.

To calculate the coefficient ρ_{mirror} , we have to integrate the intensity over the pupil:

$$\begin{aligned} P_{\text{transmitted}} &= \int_{\phi=0}^{\phi=2\pi} \int_{r=0}^{r=R=D/2} I_0 \left(\frac{w_0}{w(z)} \right)^2 \exp \left(\frac{-2r^2}{w^2(z)} \right) r dr d\phi \\ &= \frac{\pi}{2} \times I_0 \times w_0^2 \left[1 - \exp \left(\frac{-2R^2}{w^2(z)} \right) \right] \\ &= P_0 \left[1 - \exp \left(\frac{-2R^2}{w^2(z)} \right) \right] \end{aligned} \quad (\text{III.5})$$

P_0 , which is the total power of the beam, appears in this expression. Thus we have:

$$\rho_{\text{mirror,Gaussian}} = \frac{P_{\text{transmitted}}}{P_0} = 1 - \exp \left(-\frac{1}{2} \left(\frac{D}{\theta L_0} \right)^2 \right) \quad (\text{III.6})$$

where L_0 is the distance between the sources and the mirror.

□ MMF case: photon flux on the image plane

The radiance (W.m⁻².sr⁻¹) inside the MMF is conserved, it is the same as the black body source that was injected.

$$L_{\text{fibre}} = T \int_{\lambda_{\text{min}}}^{\lambda_{\text{max}}} B(\lambda, T_s) d\lambda \approx T(\lambda_{\text{max}} - \lambda_{\text{min}}) \times B(\lambda_{\text{eff}}, T_s) \quad (\text{III.7})$$

The radiance of each pinhole is also the same as the fiber radiance because the holes are close to the fiber extremity, compared to the fiber diameter: the fiber tip is seen as an infinite plane. We assume that the pinholes diameters are large enough so we can neglect diffraction (we will see later in the design that it is the case). The irradiance (W.m^{-2}) of one pinhole on the mirror depends on its solid angle, seen from the mirror, is: $E_{\text{mirror}} = L_{\text{fibre}} \frac{\pi d^2}{4L_0}$. The power per pinhole collected by the mirror, which is also the power in one pseudo star image is:

$$P_{\text{im}} = E_{\text{mirror}} S_{\text{mirror}} = L_{\text{fibre}} \frac{\pi d^2}{4L_0} \frac{\pi D^2}{4} \quad (\text{III.8})$$

This last result can also be obtained by directly using the definition of the optical etendue:

$P_{\text{im}} = L_{\text{fibre}} G$. The conversion to a photon flux in the CCD plane is done via the following relation:

$$F_{\text{im}}^\gamma = P_{\text{im}} \frac{\lambda_{\text{eff}}}{hc} \quad (\text{III.9})$$

□ Maximum photon flux per pixel

The intensity at the center of an airy disk peaks at $I_0 = \frac{P_0 \pi D^2}{4\lambda^2 L^2}$, with P_0 the total power transmitted through the pupil, D the diameter of the pupil, L the distance pupil to image plane. We chose D to be at Nyquist sampling: $D = \frac{\lambda L}{2e}$. The flux on the central pixel is upper-bounded by:

$$I_0 \times e^2 = P_0 \times \frac{\pi(\lambda L)^2}{4\lambda^2 L^2 4e^2} \times e^2 = \frac{\pi}{16} P_0 = R_{\text{flux}} P_0 \approx 0.20 P_0 \quad (\text{only at Nyquist sampling}) \quad (\text{III.10})$$

Thus, the maximum flux of photon per pixel is: $F_{\text{max/pix}}^\gamma = R_{\text{flux}} F_{\text{im}}^\gamma$. The coefficient R_{flux} is the ratio of the flux on the central pixel versus the total flux of the centroid. The value of 0.20 is valid for a monochromatic source. In the polychromatic case, as the Nyquist sampling is for $\lambda = \lambda_{\text{min}}$, for larger wavelengths the centroid will be oversampled, i.e. spread on more pixels. As a consequence, the polychromatic R_{flux} coefficient will be slightly lower.

□ Source limited integration time:

$$T_i^\gamma = \frac{w}{F_{\text{max/pix}}^{\text{e-}}} \quad \text{with} \quad F_{\text{max/pix}}^{\text{e-}} = \rho_{\text{pix}} F_{\text{max/pix}}^\gamma = R_{\text{flux}} \rho_{\text{pix}} F_{\text{im}}^\gamma.$$

I have introduced ρ_{pix} , as the mean quantum efficiency of the detector's pixels between λ_{min} and λ_{max} .

Finally, the expression of T_i^γ is:

$$T_i^\gamma = \frac{w}{\rho_{\text{pix}} F_{\text{im}}^\gamma R_{\text{flux}}} \quad (\text{III.11})$$

□ Number of frames:

The cumulated number of photo-electrons collected per star is:

$$N_{e^-}^* = T_i N_{\text{frames}} F_{\text{im}}^\gamma \times \rho_{\text{pix}} = \frac{w N_{\text{frames}}}{R_{\text{flux}}} \Rightarrow N_{\text{frames}} = \frac{R_{\text{flux}} N_{e^-}^*}{w} \quad (\text{III.12})$$

At last, the total time is easily calculated from the values of T_i (source limited), T_{min} and N_{frames} . The η factor tells which speed regimes applies (source of detector limited).

4.2.2 Metrology photometric relations

□ Number of photo-electrons

For the metrology, the maximum photon location noise on each pixel is $\sigma_r^p = 2.1 \times 10^{-5}$ (50% RSS of $3 \times 10^{-5} = 0.17 \times 5 \times 10^{-6}$). The factor 0.17 from numerical simulations, this is an empirical coefficient between the centroid location error and the pixel location error, caused by spatial averaging over several pixels, see section 2.4. We note the minimum number of photo-electrons for each pixel $N_{e^-}^p$, it verifies: $\sigma_r^p = \frac{\sigma_{\text{pixel}}}{\sqrt{N_{e^-}^p}}$. Here σ_{pixel} is expressed in units of pixels. Assuming no cross talk between pixels, σ_{pixel} cannot be greater than $1/\sqrt{12}$ (we consider a uniform PRF as the worst case). This yields $N_{e^-}^p = 1.9 \times 10^8$.

□ Integrated metrology fiber output

Unlike the pseudo stars, the metrology system is almost entirely made of integrated components. The light travels in free space for the last step only, from the fiber tips to the detector. To calculate the transmission from the coherent monochromatic source to the fiber tips, we do not use any radiometric calculation, we simply compute the product of the transmission of each one of the metrology component, from the source to the fiber tips. The transmission are generally specified by the hardware manufacturer, if this is not the case we use typical values. The power in the fiber right after the source is either given by the manufacturer, or we estimate at 30% of the power in free space if we have to inject the beam into a SMF with a lens (typical value). The power output at each fiber tip is noted P_{tip} .

□ Maximum photon flux per pixel

The Gaussian profile emitted by one fiber, at $r=0$ (axis aligned with the propagation direction and centered on the fiber) is given by: $I(r=0, z) = \left(\frac{w_0}{w(z)}\right)^2 I_0$ where w_0 is the beam waist at the origin, $w(z)$ is the beam waist at the longitudinal position of coordinate z and I_0 is the intensity at the beam origin. In the far field approximation, we have $w(z) = \theta z$ where θ is the numerical aperture of the fibre. As we also have $I_0 = \frac{2P_{\text{tip}}}{\pi w_0^2}$, we can rewrite I as:

$$I(r=0, z) = \frac{2P_{\text{tip}}}{\pi w_0^2} \times \frac{w_0^2}{\theta^2 z^2} = \frac{2P_{\text{tip}}}{\pi \theta^2 z^2} \quad (\text{III.13})$$

The power incident, flux of on one pixel at the center of the beam is:

$$P_{\text{pix}} \approx \frac{2P_{\text{tip}}e^2}{\pi\theta^2L^2} \quad (\text{III.14})$$

We can safely assume a uniform illumination of the pixel (we will see in the design that the fiber beam is much larger than even the chip itself). The corresponding photo electron flux is:

$$F_{\text{pix}}^{e^-} = \frac{\rho_{\text{pix}}P_{\text{pix}}\lambda_{\text{met}}}{hc} \approx \frac{2P_{\text{tip}}e^2\lambda\rho_{\text{pix}}}{\pi\theta^2L^2hc} \quad (\text{III.15})$$

They are two fibers creating an interference pattern proportional to:

$$2I'_0(1 + V \cos(\phi)) \quad (\text{III.16})$$

where V is the visibility and $I'_0 = T_i \times F_{\text{pix}}^{e^-}$ is the number of electrons per frame generated by one fibre (at the focal plane). The number of photo-electrons collected per frame by a pixel located in a bright fringe is:

$$F_{\text{max/pix}}^{e^-} \approx 2(1 + V) F_{\text{pix}}^{e^-} \quad (\text{III.17})$$

□ **Source limited integration time:**

$$T_i^\gamma = \frac{w}{F_{\text{max/pix}}^{e^-}} \quad (\text{III.18})$$

□ **Number of frames:**

Only the “AC” component of the signal can be used to determine pixel offsets, the “DC” component only add noise. For the number of frames we only take into account the “useful” photo-electrons:

$$N_{\text{frames}} = \frac{N_{e^-}^p}{wV} \quad (\text{III.19})$$

5 Design

In this part I will review the technical solutions we have chosen. Some remarks that have already been made about the methods used to derive the specifications are also relevant to the design phase. While for some specifications we were able to derive analytical relations and identify precise constraints on the design (see previous section), for others we lacked knowledge that could only be obtained with advanced numerical simulations or experiments with real data. Because of this, some specifications are closer to a wish list than actual rigorous requirements, in particular those concerning the mechanical and thermal stability and the environment. Rigorously enforcing these targets into the design would have required thermal and mechanical simulations, most likely by finite element methods, for which we lacked manpower. In practice we have used a mix of best effort and trial and error approaches concerning these aspects of the experiment. For the most critical specifications, we have

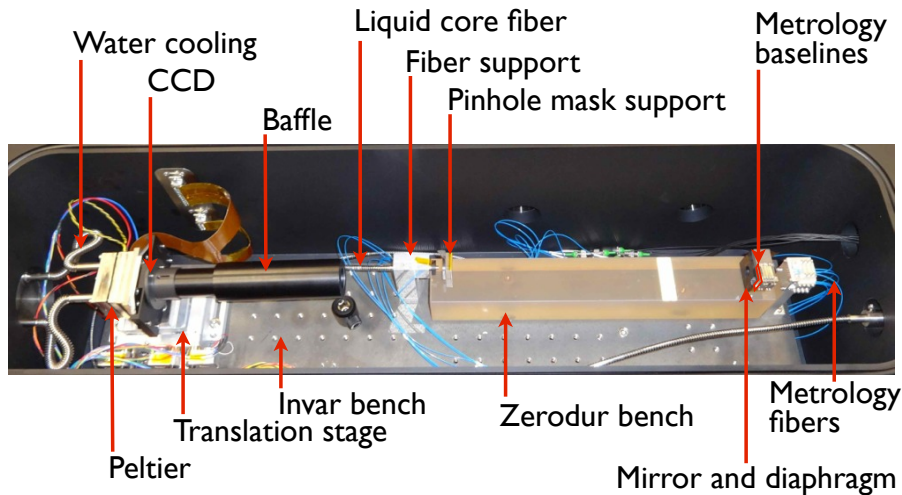


Figure III.3: Optical bench inside the vacuum chamber.

done extensive measurements to check the performances of particular components or sub-parts of the whole experiment (section 6).

The trial an error method has been particularly essential in investigating stray light issues. We based our initial design mainly on my experience at the JPL, but the conditions for the NEAT-demo were substantially different than for VESTA (much smaller vacuum chamber). The initial results were not satisfactory and we have then tested 4 different baffles. An initial memo was written but it is now completely outdated (as we have since learned a lot by experimentation) and at the date of completion of this manuscript, we are still actively investigating the issue and we have no definitive conclusions about how to control the stray light down to the required level. In this chapter we present the version 4 of the baffle which has been in use for most of the data that is presented in chapter IV.

5.1 Overview

Now let me give an overview of the design through some schematics: Fig. III.3 is a labeled picture of the interior of the vacuum chamber. Figure III.4 is the product tree of the testbed components. The high level categories are organized by functionality.

Our tool of choice to monitor our progress during the design, assembling and test phases of the experiment was the so-called “snapshot spreadsheet”, shown by Fig. III.5. One can see that at the time of this snapshot (07/05/2013) most of the components had been designed and procured, we were mostly checking their normal operation and we had also begun the tests.

5.2 Sub-systems

I will now present the most important sub-systems, by functional groups or one at a time. I will mostly describe them from a functional and qualitative point of view.

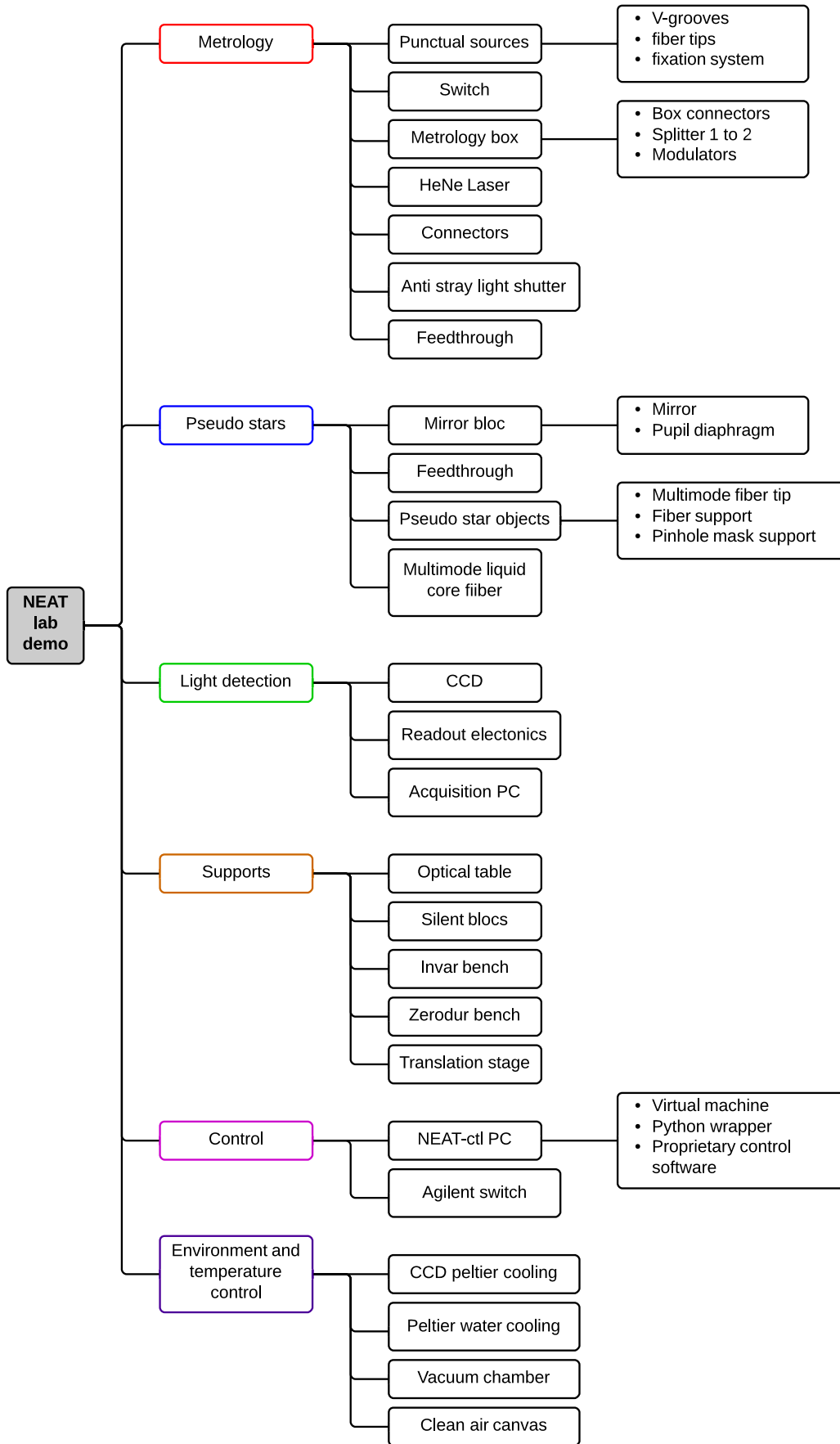


Figure III.4: Product tree by functionality.

components/systems	Quantity	design/ choice?	ordered/ in prod.?	delivered ?	operational?	critical for phase 1? (air)	critical for phase 2? (vacuum)	urgent?	tests done?	compliant?	test time (days)	priority
Metrology		83%	75%	75%	58%			-	24%	0	6,5	{1}
HeNe Laser	1	1	1	1	1	y	y		100%	1	3	1
phase modulator	2	1	1	1	1	y	y		50%	0	2	2
single mode fiber	enough	1	1	1	1	y	y					
connector	enough	1	1	1	1	y	y		0%	0	0,5	3
splitter	1	1	1	1	1	y	y		0%	0	0,5	4
anti stray light shutter	1	0	0	0	0				0%	0	0	5
anti stray light shutter controler	1	0	0	0	0							
fibre shutters	4	1	1	1	0				17%	0		
V-grooves	6	1	1	1	0	y	y	y	0%	0	0,5	6
interface air vacuum	1	1	1	1	1		y					
support fibres metrology	1	1	0	0	0	y	y	y				
GBF	1	1	1	1	1	y	y					
Pseudo stellar sources		88%	88%	88%	75%			-	32%	0	-	{2}
white light source	1	1	1	1	1	y	y		33%	0	1	1
mirror	1	1	1	1	1	y	y		0%	0	0,75	2
white-light source shutter		0	0	0	0							
filter	1	1	1	1	1	y	y					
pinhole mask	2	1	1	1	1	y	y		100%	1	0,5	3
liquide core fiber	2	1	1	1	1	y	y		25%	0	-	4
pupil diaphragm	1	1	1	1	1	y	y		0%	0	-	5
liquid Fibers support	1	1	1	1	0	y	y	y				
interface air vacuum	1	1	1	1	1		y					
CCD and acquisition		100%	100%	100%	67%							
CCD	2	1	1	1	1	y	y		0%	0	-	1
PC-CEA + software	1	1	1	1	0	y	y					
CCD electronics	1	1	1	1	1	y	y		0%	0	-	2
Bench / Mechanical parts		100%	93%	93%	57%			-	0%	0	-	{3}
CCD shutter	1	1	1	1	0		y					
CCD shutter controler	1	1	1	1	0		y					
zerodur bench	1	1	1	1	1	y	y		0%	0	-	3
invar bench	1	1	1	1	1	y	y		0%	0	-	4
translation stage	1	1	1	1	0	y	y		0%	0	-	5
translation stage controler	1	1	1	1	0							
affle CCD	1	1	0	0	0				0%	0	-	6
silent blocks	3	1	1	1	1	y	y		0%	0	-	-
vacuum chamber	1	1	1	1	1	y	y		0%	0	-	-
nitrogen trap	1	1	1	1	1		y		0%	0	-	-
vacuum pump	1	1	1	1	0		y		0%	0	-	-
acquisition central	1	1	1	1	1							
oscilloscope	1	1	1	1	1							
PC control / data processing	1	1	1	1	1							
Temperature control		60%	60%	60%	0%			-	0%	0	-	
peltier	1	1	1	1	0		y		0%	0	-	
peltier controler	1	1	1	1	0		y					
water colling	1	1	1	1	0		y		0%	0	-	
temperature controler box	1	0	0	0	0							
Phase modulators box	1	0	0	0	0				0%	0	-	
Sensors		1	1	0	0			-	0%	0	-	
Accelerometer 1 (coarse)	1	1	1	0	0				0%	0	-	
Accelerometer 2 (Alain Léger)	1	1	1	1	1				0%	0	-	
Temperature sensors	6	1	1	1	0				0%	0	-	
Vacuum sensor	1	1	1	1	0				0%	0	-	

Figure III.5: **Snapshot spreadsheet.** The view correspond to the state of the project as of 07/05/2013. From left to right, the 4 central columns with binary values respectively mean: we know exactly which component we need, i.e. we have a complete trap design or we have chosen a model if the component is bought off-the-shelf (*design/choice*), we are waiting for delivery or local manufacture (*ordered/in prod*), the component is available in the lab (*delivered*), the component is not broken and is suitable for integration (*operational*). The test phase is different than the *operational* check step: we characterize critical properties of the components, sometimes checking them for conformity with manufacturer specifications, for example the stability in intensity and wavelength of the light sources. Some components on the spreadsheet have become outdated as the design has changed.

5.2.1 Light detector and readout electronics

The detector is a crucial part of our experiment. Our final choice was the “CCD39-01” from e2v³. The readout electronics and software have been developed and tested by the CEA. The CCD 39-01 is a back illuminated visible CCD, with a frame size of 80 by 80 pixels. The physical pixel size is 24 μm (making for a total sensitive area of 1,92 by 1,92 mm). To enable high frame rate operation (up to 1000 Hz), the chip has 4 amplifiers, i.e. the imaging area is split into 4 square areas which we call quadrants, of 40 by 40 pixels. Each quadrant has a separate readout channel (different wires and electronics components). This has important implications for the data analysis.

There is a lot more I could say about the CCD, but I am not going to give more details here. Several documents contain relevant information on many aspects: the readout electronics are extensively documented in the “NEATRO” document provided by the CEA (see appendix C). Practical information on how to operate the CCD and how the CCD raw data is converted into fits files is found in the NEAT user manual (appendix E). At last, the section 6.6 summarizes the result of the standard characterization of the CCD (photon transfer curve, linearity, dark current and readout noise).

5.2.2 Metrology

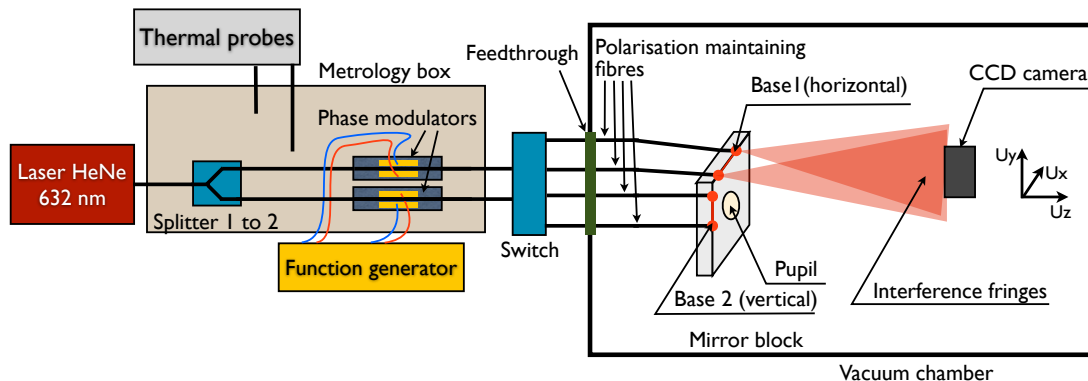


Figure III.6: **Schematic of the metrology.** The axis are indicated on the figure: Z is aligned with the optical axis, X and Y are aligned with the horizontal and vertical directions within the focal plane.

The metrology is made of integrated components from the laser to the bases (see Fig. III.6). The source for the metrology is a HeNe laser. Its light is split into two fibers, which are fed into two lithium niobate phase modulators to apply a periodic phase shift between the lanes. This configuration ensures that the phase modulation is applied between the two point sources constituting each base. A switch can be used to select any combination of one or zero fibers on the mirror and most combinations of two fibers. During the metrology calibration phase, two vertically and horizontally aligned fibers are selected successively to project respectively horizontal

³e2v is a private British company specialized in semiconductors, radio-frequency applications and medical and spatial imaging.

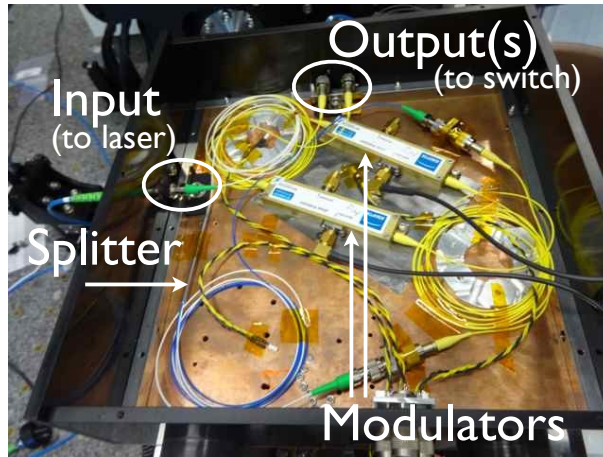


Figure III.7: Picture of the metrology box.

and vertical dynamic Young fringes. We use a linearly polarized laser and polarization maintaining fiber all the way from the laser to the fiber tips. The fiber splitter and the modulators are packed into a box (see Fig. III.7).

With the kind of switch we use, we can not address any combination of two fibers. The set of final available baselines is determined by how we connect the fibers between the switch output and the mirror. The switch presents itself as a single casing with 2 inputs and 8 outputs, but it consists of two 1x4 switches in parallel inside. This configuration is the result of a tender: we have chosen not to stage several switches to maximize throughput and keep the cost and complexity low. There was no truly 2x8 switch commercially available (with all the required specifications) and in our price range, this is the reason we use this particular configuration. As a result, only 16 (4×4) baselines are accessible, over a total of 28 (number of 2-combinations among the 8 fiber tips). Appendix 7 explains how we have optimized the configuration and includes a spreadsheet showing the current one (i.e. the connections at every interface and the final baselines, with their corresponding switch commands). Of course the file can also be edited to assess alternative configurations.

5.2.3 Pseudo stars

The pseudo stellar sources system function is to project 5 stars onto the CCD. The 4 outer stars represent reference stars, the central star is the target. This star configuration allows us to perform a precise differential measurement: XY position offset and scale changes can be measured between the stars. In order to use a reasonable approximation of the spectrum of a real star, we use a black body source. The schematic of the system is presented by Fig. III.8. A picture showing all elements of the pseudo stellar sources before integration is shown by Fig. III.9. Figure III.10 shows the spatial layout of the pinholes.

We used a magnification factor of 2 and an off axis angle of 2 degrees. This configuration allows the installation of the pseudo stellar sources and the detector without any beam obstruction with some margins to accommodate the supports. Additionally, with an aperture as small as 5 mm, a spherical surface is sufficient to obtain optical aberrations that produce a spot diagram smaller than the diffraction pattern in the whole field of view.

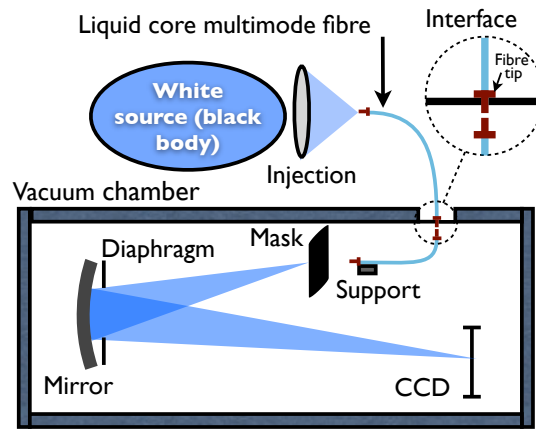


Figure III.8: Schematic of the pseudo stars sources.

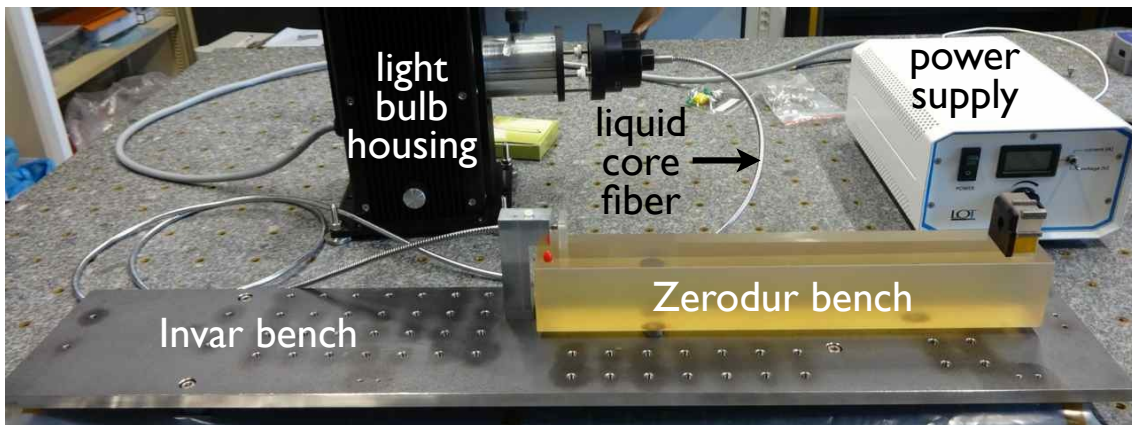


Figure III.9: **Pseudo stars before integration in the vacuum chamber.** The lower metal bench is made of invar (low dilatation material). The translucent yellowish glass block is the zerodur bench and has an ultra-low dilatation coefficient lower than 10^{-7}K^{-1} . On the left side of the zerodur bench: the pinhole mask that is back lighted by the liquid core fiber. On the right side: the mirror block with the diaphragm (in black). One can also see invar rails on the top of the mirror block, their function is to hold the metrology fibres in the V-grooves located between them.

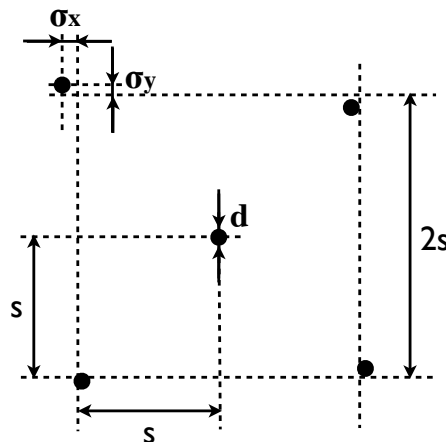


Figure III.10: **Layout of the pinholes on the mask.** The holes are arranged like the dots for the number 5 on a dice, with 4 outer stars forming a square and one (representing the target) in the center. We have introduced small offsets, noted as $\sigma_{x/y}$ on the figure, to prevent the stars from falling into the same fractional positions relative to the pixels.

5.2.4 Flat field

Note the absence of specifications for this system. We had initially planned to derive the flat field using single metrology fibers. However, stray light is much harder to control in coherent light than in incoherent light. If we note I_0 the direct intensity from the light source and I_1 the stray light intensity after (multiple) reflection(s), the perturbation in coherent light is $\propto \sqrt{\frac{I_1}{I_0}}$ instead of directly proportional to $\frac{I_1}{I_0}$ (see appendix I). We have only added this system in the latter stages of the experiment (after the first light). The design of the system and choice of the components was derived mostly on an experimental basis.

This system is very simple, it consists of a high power broadband white light LED (400 to 700 nm) connected to a multimode fiber which tip is taped on the mirror block and oriented toward the CCD. The light source is located outside the vacuum chamber, a custom made feed-through enables operation in vacuum. For experimental tests and reliability (by redundancy), we have two fibers with respectively 200 μm and 365 μm diameter cores.

The main reason for having a multimode fiber is the luminous flux needed to operate the CCD in a photon noise limited regime and to accumulate photons at a recent rate, resulting in a total integration time similar to the other systems (a few minutes). We did not find suitable commercially available light sources within our price range that could deliver enough light to the CCD: with a SMF, a superluminescent type of source is required. There are possible issues when using a MMF rather than a SMF because of speckles produced by the fiber which we try to evaluate experimentally.

5.2.5 Mechanical supports and lab environment

Figure III.11 is a picture of the lab where you can see the vacuum chamber on the optical table, inside the canvas. We use a standard optical table with pneumatic suspension. The picture illustrates the design approach pretty well: we have stacked four stages of vibration damping in order to stabilize the core of the experiment: in addition to the table suspension, the vacuum chamber is installed on damping supports, the invar bench inside the chamber is installed on silent blocks (another kind of damping support) and there is a last stage of damping between the invar and the Zerodur bench.

The canvas is equipped with a casing at the top (Fig. III.11) that provides filtered and clean air in close proximity of the detector (vacuum chamber, metrology and optical table). This is important to avoid dust contamination on the detector as all protections have to be removed during normal operation. This setup is very convenient because it allows us to open the chamber at anytime and make modifications to the configuration inside without worrying about dust contamination. Operations involving the CCD can be done in immediate proximity (on the optical table), without having to use a clean room. We still have to be somewhat careful about dust outside the canvas: it can still be brought inside by direct contact. We use lab coats, shoe covers and mob caps inside the lab. The air conditioning system (located under the roof, not visible in the picture) also filters the air and works slightly overpressure to avoid air leaks from the outside.

The temperature is stabilized at several stages: first for the whole lab with the air

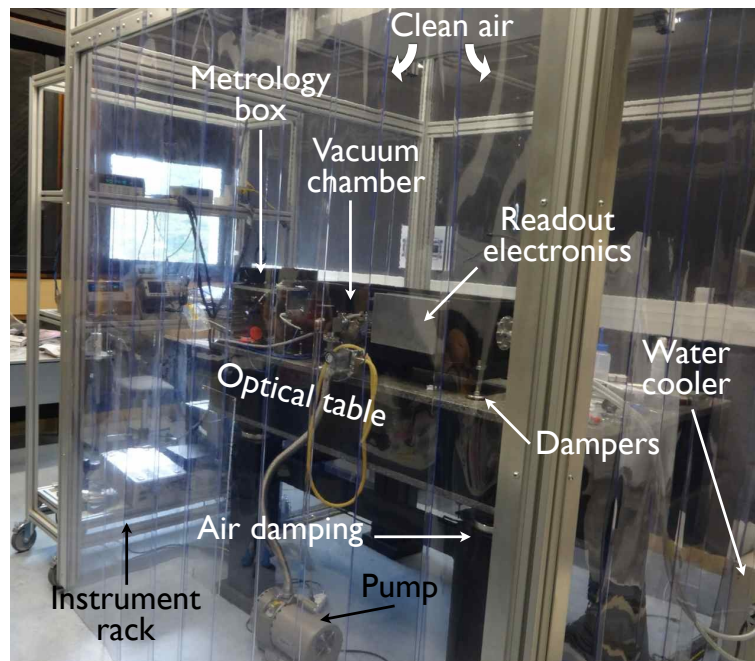


Figure III.11: Picture of the environment around the vacuum chamber.

conditioning system, the stability is about 1°K . Inside the vacuum chamber, the stability is improved by the insulation of the canvas and the mass of the chamber. Thermal stability for the CCD has to be active because it heats during operation. We use a two stage cooling system: the CCD is cooled by a Peltier, which is cooled by water circulation. All the elements producing heat have been moved away from the CCD as far as possible: the readout electronics are just outside the vacuum chamber, their distance is limited by the length of electronic cables to the chip. Because we read at high speed we need short cables. The other heat producing instruments (power supplies, controllers, PCs...) are placed outside of the canvas, on the instrument rack.

Figure III.7 shows the interior of the metrology box. It contains a splitter and the modulators and also has damping supports (vibration cause phase jitter). Another aspect is the thermal insulation, the idea here was to provide a homogeneous thermal environment to avoid differential thermal effect between the two metrology lanes. But because the switch and the fibers connected to it are not insulated, the noise reduction is not effective. However if phase thermal drifts proves to be a problem we have the option to insulate everything between the box and the vacuum chamber. The box is outside the vacuum chamber to minimize thermal perturbations on the detector and because vacuum compatible components are generally harder to find, for starters because of heat dissipation.

At last, a word about the vacuum: we only use a primary pump, because we only need a medium vacuum (a fraction of milibar). On the other hand, we want to stop the pumping during data acquisition, so we need good vacuum sealing and have to be careful with every vacuum interface. We seal with either standard components (interfaces with rubber joints and screws) or glue for some custom made interfaces for the SMF (metrology) and MMF (pseudo stars, flat fields). A control of all the interfaces with a helium leak detector showed that there is no significant leak.

5.3 Baffles

We have used 4 baffle versions so far:

- v1: initial design, aluminum tube with 4 circular vanes.** The initial design (v1) was generating 4 visible bright spots (several % above the flat field level, a few pixel width) in white and laser light. The cause was attributed beyond any doubt to reflections on the baffle edges. Each circular edge each vane corresponded to one spot, and their positions were linked to the baffle orientation.
- v2: a baffle made of paper sheets.** This was an attempt to have a better quality baffling by replacing the bright aluminum edges by black paper. In this version they were only two vanes, one in the middle of the vacuum chamber and one close to the detector. A paper sheet has a thickness of typically 100 μm , about the same as the baffle edges. The bright spots were not visible anymore but analysis of data quality indicated almost no difference with the paper baffle and no baffle at all, whereas the first version of the baffle was already improving the signal.
- v3: same as v1, with improved bevels for the vanes edges.** Version 3 is modified from the first one, bevel precision was improved and the width of the vanes edges was measured under microscope to be about 50 μm instead of the previous 100 μm . However this improvement was the best we could do with our local mechanical equipment and still not sufficient. The baffle was also suffering from a very tight field of view. Narrow angular tolerances and unreliable translation stage tip tilt resulted in a constant need to check the baffle orientation.
- v4: plastic tube, razor blades, modular design.** Version 4 is build from a larger tube. The new design addresses the issues with the previous versions. The optical apertures are made with razor blades, which provide a very fine optical edge ($<1\mu\text{m}$). The design is modular, to allow quick modifications if required: each new vane consist of a holder piece, on which the razor blades are attached. Vanes can be positioned anywhere inside the baffle and be inserted/removed for modification. For better performance, most interior surfaces are covered with a light absorbing material (“metal velvet” acktar[®]).

Figures III.12, III.13 and III.14 are pictures of the different baffles inside the vacuum chamber. Figure III.15 is the optical schematic for the baffle v4. It shows how the baffle was designed with respect to avoid critical reflections. Figure III.16 shows the FoVs of baffles v1/v3 and v4 on the mirror block.

5.4 Parameters and components summary

The values we have chosen for the design parameters previously introduced in section 2 as notations are presented by Table III.3. The components that have been bought off-the-shelf and their references are presented in a table in appendix D. For the components that have been the object of a tender, we refer the reader to the list of reference documents (appendix C).

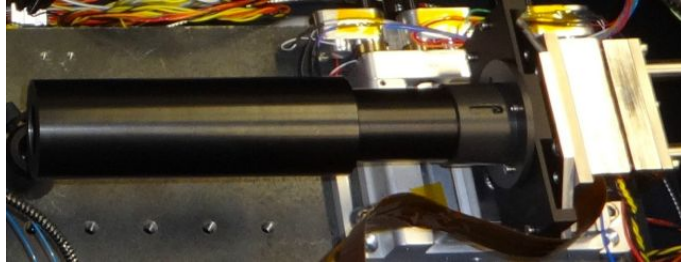


Figure III.12: **Baffle v1/3.**

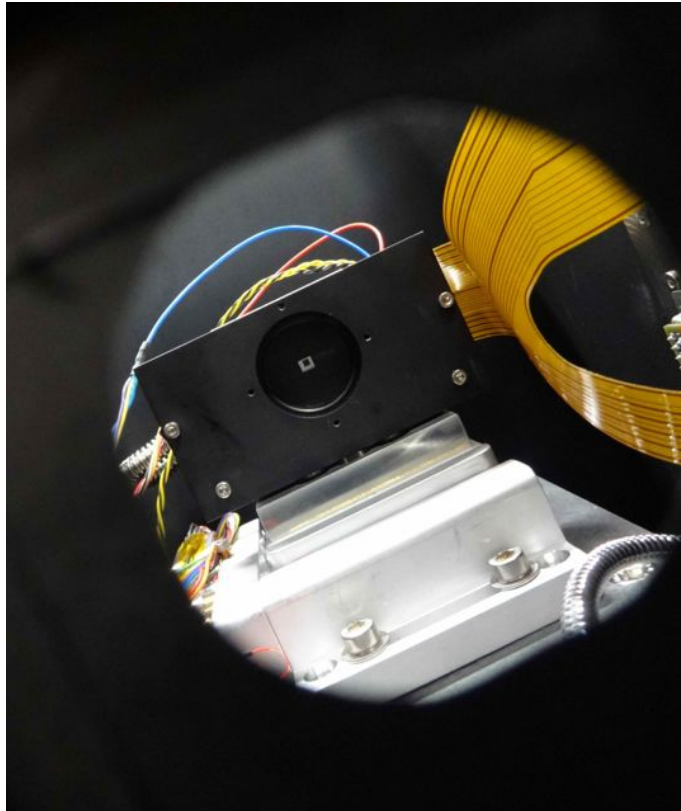


Figure III.13: **Baffle v2.** The picture is taken in front of the chip, just behind the outer vane inside the vacuum chamber. The small square inside the bright area is the sensitive area of the chip. The black square around the bright area next to the chip is the inner vane.

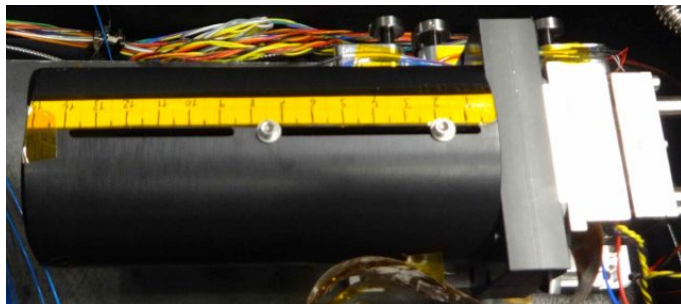


Figure III.14: **Baffle v4.**

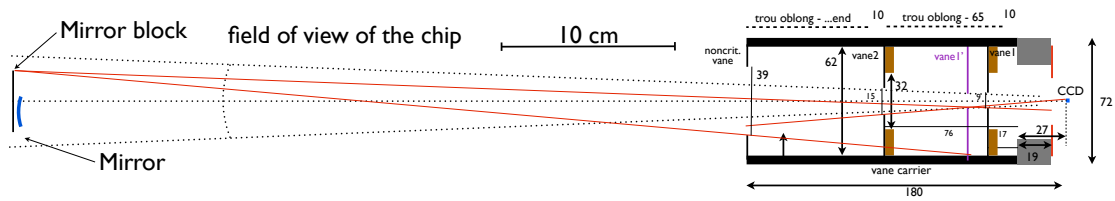


Figure III.15: **Optical schematic for the baffle v4.** No ray can reach the detector after only one reflection, except for on the vane edges, which are very thin (razor blades edges).

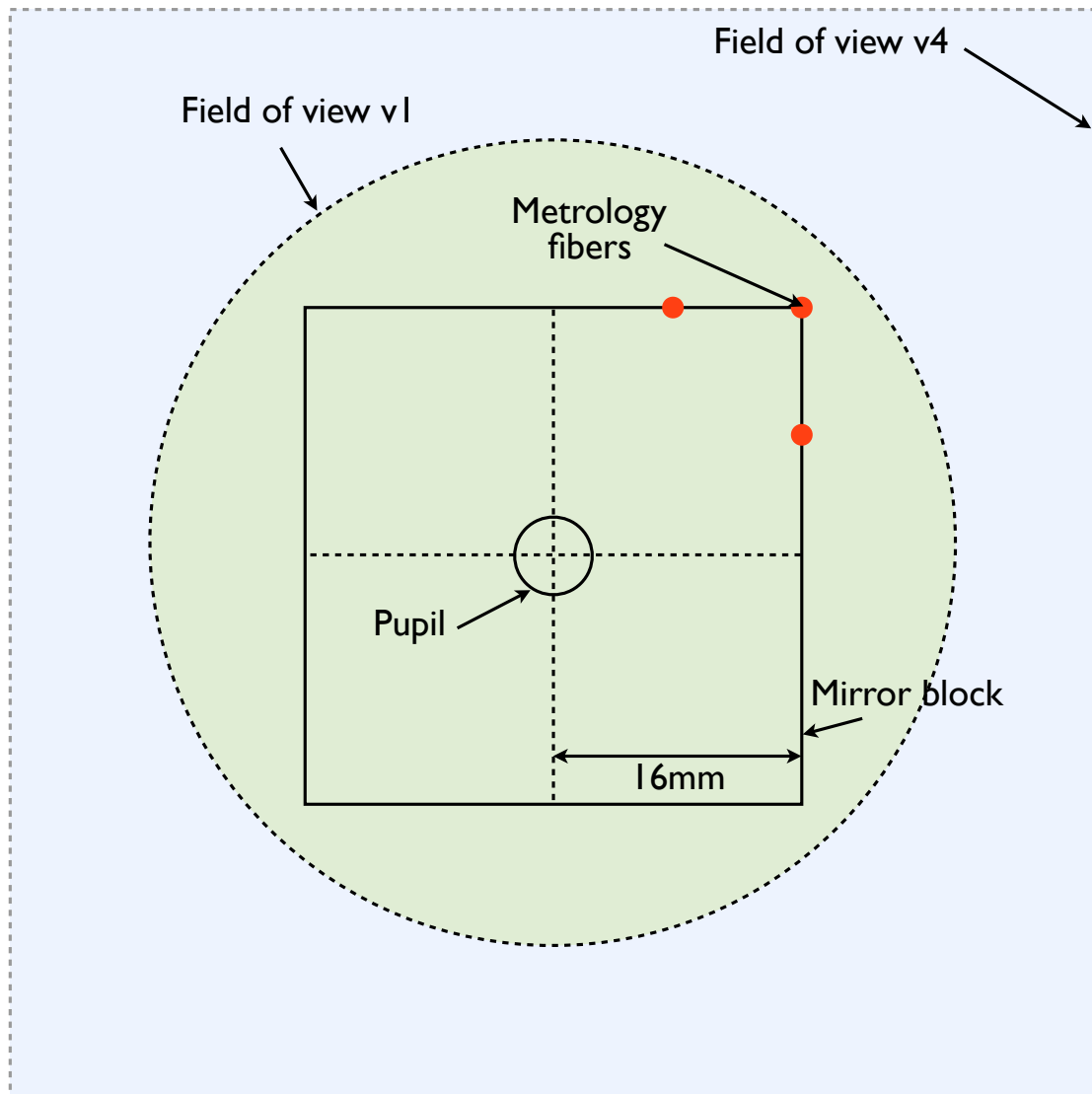


Figure III.16: **Fields of view of baffle v1/v3 and v4.**

Table III.3: Design parameters.

Parameter	Notation	Value
distance mirror to CCD	L	600 mm
distance mirror to pseudo star objects	L_0	300 mm
min/max wavelength of pseudo stars	$\lambda_{\min}/\lambda_{\max}$	400 nm/800 nm
diameter of the entrance pupil	D	5 ± 1 mm
mirror focal length	f	200 ± 5 mm
separation between pseudo stars objects	s	240 μm
pseudo stars pinhole diameter	d	15 μm
off axis angle (pseudo stars)	θ	2°
metrology source wavelength	λ_m	633 nm
metrology baseline	B	from 1 to 6 mm
pixel size	e	24 μm
size of the detector matrix	N	80x80 pixels
effective quantum well size	w	200,000 e^-

6 Compliance and tests

In this part we go back to the specifications and check whether they are respected or not. The goal is not to be exhaustive: some items are trivial. For example, the vacuum chamber wasn't crushed when we pumped for the first time (obviously). These items are left implicitly verified and at best they appear verified in the final compliance table. On the opposite, all the critical specifications are looked at in detail in the following sections.

6.1 Photometric budgets

In this section I will present the photometric budget spreadsheet for the pseudo stars (Fig. III.18) and the metrology (Fig. III.17). The spreadsheet primary goal was of course to help us during the design phase, however it is only presented here because now that the experiment is working, we can compare the theoretical values with the radiometric and photon flux measurements, which are shown in the *Measured* columns. We will see how well the design complies with the specifications both “in theory” and “in practice”, so we can also detect eventual errors and/or questionable approximations made during the photometric assessment: this is very valuable feedback.

6.2 Diffraction limited PSF

During the design process, we controlled the amplitude of the geometric aberrations relative to the size of the PSF for several configurations, using ray tracing simulations. As expected, we have observed that the aberrations increase with pupil size and off-axis angle. More importantly, we have also observed that aberrations are very small with a simple spherical mirror close to a “2f-2f” configuration, when object and image are at the same distance from the mirror ($L = L_0$). In our setup, we can not use this exact setup because of mechanical obstruction issues: the pseudo star objects would collide with the translation stage. In the end, we have used $L = 600$ mm, $L_0 = 300$ mm, $f = 200$ mm and $\theta = 2^\circ$ which is optically not very different

Constants	Notation	Values	Units	Measured
speed of light in vacuum	C	3,00E+08	m/s	
Plank constant	h	6,63E-34	J.s	
Parameters				
Laser power output	Plaser	6,30E-03	W	7,00E-03
Number of FC connectors	Nfc	5	-	
FC connector losses	Lfc	-0,10	db	
Number of 1->2 splitters	Ns	1	-	
1->2 splitters losses	Ls	-3,70	db	
Modulator losses	Lmod	-6,00	db	
Switch losses	Lswitch	-2,00	db	
PM fibres NA	θ	0,0830	-	
visibility	V	0,6000	-	
distance fibres to CCD	L	0,6	m	
effective well size	w	200000	-	
pixel size	e	2,40E-05	m	
CCD mean quantum efficiency	ρ_{pix}	8,00E-01	-	
metrology wavelength	λ_m	6,32E-07	m	
Detector minimum read time	Tmin	1,00E-03	s	
Number of metrology photons needed / pixel	Np_e	1,90E+08	-	
Intermediate quantities				
Transmission of integrated metrology	T	-1,22E+01	db	
Metrology power output (one fiber)	Ptip	3,80E-04	W	
Metrology mean power / pixel (one fiber, beam center)	Ppix	5,61E-11	W	
Photo electron max flux / pixel (one fiber, beam center)	Fe_pix	1,43E+08	s-1	
Fringe photon flux / pixel (max)	Fe_max_pix	4,57E+08	s-1	
Number of metrology frames needed	Nf	1,58E+03	-	
Final quantities				
Integration time (source limited)	Ty_i	4,38E-04	s	
Source optimality coefficient	η	2,28	-	0.4
Integration time	Ti	1,00E-03	-	
Total integration time	Ttot	1,58E+00	-	

Figure III.17: Metrology photon budget.

Constants and parameters	Notation	Values	Units	Measured
Physical constants				
speed of light in vacuum	C	3,00E+08	m/s	
Plank constant	h	6,63E-34	J.s	
Boltzman constant	kb	1,38E-23	m ² .kg.s ⁻² .K ⁻¹	
Parameters				
effective wavelength	λ_{eff}	6,00E-07	m	
wavelength width	$\Delta\lambda$	4,00E-07	m	
entrance pupil diameter	D	5,00E-03	m	
distance pseudo stellar sources to CCD	L0	3,00E-01	m	
distance mirror to CCD	L	6,00E-01	m	
optics + fibres transmission	T	7,00E-01	-	
CCD quantum efficiency	ρ_{pix}	8,00E-01	-	
effective quantum well size	w	2,00E+05	-	
minimum read time	Tmin	1,00E-03	s	
ratio central pixel flux/centroid flux	Rflux	2,00E-01	-	
Number of photon-electrons needed	Ne-	5,70E+10	-	
Parameters (SMF)				
SMF NA	NA	0,13	-	
White source temperature	Ts	3,00E+03	K	
Black body emissivity	ϵ	1,00E+00	-	
Parameters (MMF)				
pinhole diameter	d	1,50E-05	m	
Intermediate quantities				
Number of frames needed	Nf	5,70E+04	-	
Black body spectral irradiance	Slbb	5,13E+11	W.m ⁻³ .sr ⁻¹	
Black body irradiance	lbb	2,05E+05	W.m ⁻² .sr ⁻¹	
Intermediate quantities (SMF)				
SMF power (one fibre)	Psmf	5,17E-08	W	2,00E-07
ρ_{mirror}	ρ_{SMF}	8,18E-03	-	
flux on CCD (one spot)	P _{im_smf}	4,24E-10	W	
photon flux on CCD (one spot)	F _{y_im_smf}	1,28E+09	s ⁻¹	
photo-electron flux on CCD (one spot)	Fe _{-im_smf}	1,02E+09	s ⁻¹	
Intermediate quantities (MMF)				
Fiber irradiance	L _{fiber}	1,44E+05	W.m ⁻² .sr ⁻¹	
pinhole power (one pinhole)	Phole	2,54E-05	W	
Irradiance on mirror	E _{mirror}	8,47E-05	W.m ⁻²	
flux on CCD (one spot)	P _{im_mmf}	1,66E-09	W	3,30E-09
photon flux on CCD (one spot)	F _{y_im_mmf}	5,02E+09	s ⁻¹	
photo-electron flux on CCD (one spot)	Fe _{-im_mmf}	4,01E+09	s ⁻¹	
Final quantities (SMF)				
Integration time (source limited)	T _{y_i_smf}	9,78E-04	s	
Source optimality coefficient	η	1,02	-	
Integration time	Ti	1,00E-03	s	
Total integration time	Ttot	5,70E+01	s	
Final quantities (MMF)				
White source exposure time	T _{y_i_mmf}	2,49E-04	s	
Source optimality coefficient	η	4,01	-	0.8
Integration time	Ti	1,00E-03	s	
Total integration time	Ttot	5,70E+01	s	

Figure III.18: Pseudo stars photon budget.

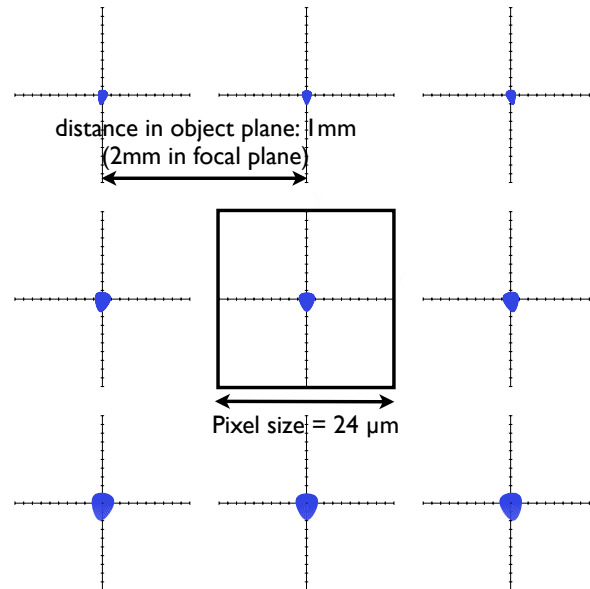


Figure III.19: **Spot diagrams for the final optical set-up.** The size of the geometrical aberrations are about 10% of the pixel size, much smaller than the size of the PSF which has a diameter about 5 pixels. The spot diagrams are spaced by $240\ \mu\text{m}$ in the object plane.

than “2f-2f” and result in magnification of the source object by a factor two. Figure III.19 shows a spot diagram calculated by ray tracing for the selected configuration: it validates the fact that we are indeed diffraction limited.

The size of the pinhole is contained by the fact that they must be seen as quasi-punctual sources, i.e. their geometric image has to be smaller than the diffraction. The diameter of the geometric image is given by $d \frac{L}{L-f} = 30\ \mu\text{m}$. With the current parameters, this value is barely larger than the pixel size and smaller than the central airy spot.

To have a defocus of less than 1%, assuming a PSF central lobe of about 5 pixels, the position on the Z axis must be accurate to $0.01 \times \frac{5eL}{D} = 0.14\ \text{mm}$ (the requirement is much easier than for the X and Y axis). The translation stage has an excellent resolution (about 0.001 pixel or 24 nm) on all axis, of course the condition is respected.

The last important aspect to verify is relative to the chromaticity. We have specified a pixel size corresponding to Nyquist sampling for a wavelength of 400 nm, here we will look at the real PSF and fit its width. We expect to find a spot size larger than for a theoretical Airy spot (@400 nm), as the real PSF consists of wavelengths up to about 800 nm. In fact, as the black body emission curve increases up to 800 nm, we should be dominated by red light and see a width close to twice Nyquist sampling, but not greater.

6.3 Safe operation of the CCD: temperature and critical pressure

Under a certain range of pressure/temperature/relative humidity (P/T/RH), dew or ice can form on the CCD. In order to operate safely, one must avoid this at all times.

The exact conditions at which dew or ice will form on the CCD in the P/T/RH parameter space are complex to determine, that is why we make simplifications. First, we only consider a limited number of modes of operation obtained by choosing a combination of P/T parameters values: we can work in air ($P=1$ bar) or vacuum ($P < P_{\text{crit}}$) and at ambient ($\sim 25^\circ\text{C}$), cool (17°C) or cold (-10°C) temperature.

The table III.4 gives the possible modes of operation among all 6 possibilities defined above.

Table III.4: **Table of possible P/T operation modes for the CCD**

	$T = 25^\circ\text{C}$	$T = 17^\circ\text{C}$	$T = -10^\circ\text{C}$
$P=1$ bar	✓	✓	×
$P < P_{\text{crit}}$	✓	✓	✓

In practice, we will retain 4 modes:

1. In air, ambient temperature. Although far from ideal, it is possible to operate in air with no cooling at all. Operating the CCD will heat it slightly, to around 25°C . In this mode, the equilibrium temperature of the CCD will be high and unstable, dark current and read noise may be high and variable. This is useful if one wants to have images very quickly.
2. In air, cool temperature ($T_{\text{CCD}} = 17^\circ\text{C}$)
3. In vacuum, cool temperature ($T_{\text{CCD}} = 17^\circ\text{C}$)
4. In vacuum, cold temperature ($T_{\text{CCD}} = -10^\circ\text{C}$). This setup is expected to give the best performances: the CCD is specified for operation at this temperature.

These 4 possible modes allow us to explore both the effect of a large change of T_{CCD} or P on the experiment, and gives us a way to either have the best data quality, or to have data more quickly. We have the choice to go into vacuum or not: this is an important constraint to keep in mind in case one wants to do experiments which involve manual handling inside the vacuum chamber, such as stray light tests. In this case, pumping and pressurization are needed between each different configuration. If one wants to operate at -10°C , vacuum is required and the same thing applies.

Now we have to check the requirement specified for the vacuum chamber and the pump: a pressure threshold P_{crit} can be reached and maintained without pumping for at least a few hours. The critical pressure threshold P_{crit} is such that it allows the detector to safely operate at a temperature T_{CCD} , corresponding to a dark current $< d_{\text{crit}}$ (see detector specifications).

Pumping tests with the vacuum chamber showed that pressures of less than 0.1 mbar can be reached and maintained for about a day. Cooling tests showed that $T_{\text{CCD}} = -10^\circ\text{C}$ can be reached easily and quickly by using a water temperature of 8°C . From the PT phase diagram of water, we know that at -10°C , water only becomes solid for pressures higher than 2 mbars. To have some margins, we have defined the critical pressure $P = 0.5$ mbar. This is the point at which the circuit breaker will automatically shut down the cooling systems. We also define another critical pressure threshold (P_{low}) that needs to be reached before the circuit breaker can be armed, lower than the first threshold to form an hysteresis cycle. We have fixed $P_{\text{low}} = 0.2$ mbar to allow for some pressure increase in all cases.

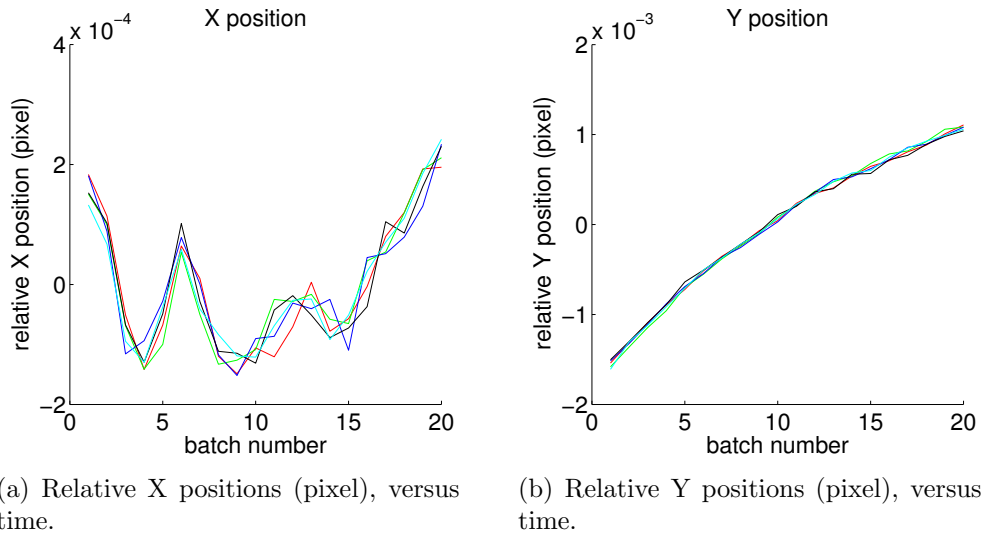


Figure III.20: The position of each centroid is shown relative to its position at $t=0$. The horizontal units are batches of frames, i.e. packets of averaged frames for each position measurement. Batches consists of 4000 frames equivalent to 5 seconds (framerate is 800 Hz), so the total duration of the stability measurement is 100 sec. Horizontal motion (X axis) shows an oscillating pattern, whereas vertical motion is more linear and could be caused by thermal effects.

We have solved the case for safe operation mode n°4 ($T = -10^{\circ}\text{C}$ and $P < 0.5$ mbar). What about the other 3? The PT phase diagram of water also tells us that operation in mode n°3 is even safer. This is also true for any temperature above -10°C , as long as ($P < 0.5$ mbar). For mode number 2, we are at atmospheric pressure, the safe limit is given by the dew point, with depends on the RH. In temperate climates, it is very rare to have dew points above 15°C , so we have conservatively set the limit at 17°C . Of course, operation at (moderately) higher temperatures is also safe.

6.4 Mechanical and thermal stability

The mechanical stability of the testbed was measured by recording the motion of the pseudo stars relative to the CCD versus time. We are interested in timescales of typically one minute, this is the time needed to for photon noise to reach 5×10^{-6} pixel with the pseudo stars. Figures III.20(a) and III.20(b) show the position of each one of the 5 centroids, respectively on the horizontal and vertical directions. The amplitudes are less than 3×10^{-3} pixel PtV, below the 0.01 pixel specified.

The thermal stability was measured in two different sets of conditions: at 17°C in air, or at -10°C in vacuum, while the CCD is recording data (to be in the most realistic conditions). There are several thermal sensors in the chamber, here we use the one closest to the CCD. The probe is fixed on the copper block that makes a thermal mass with the CCD chip (the two are connected with thermal paste). Figure III.21(a) and III.21(b) show the temperature versus time at respectively 17°C and -10°C . The thermal stabilities are respectively 2.5×10^{-3} and 2.6×10^{-3} , both are below the specification (0.1°C).

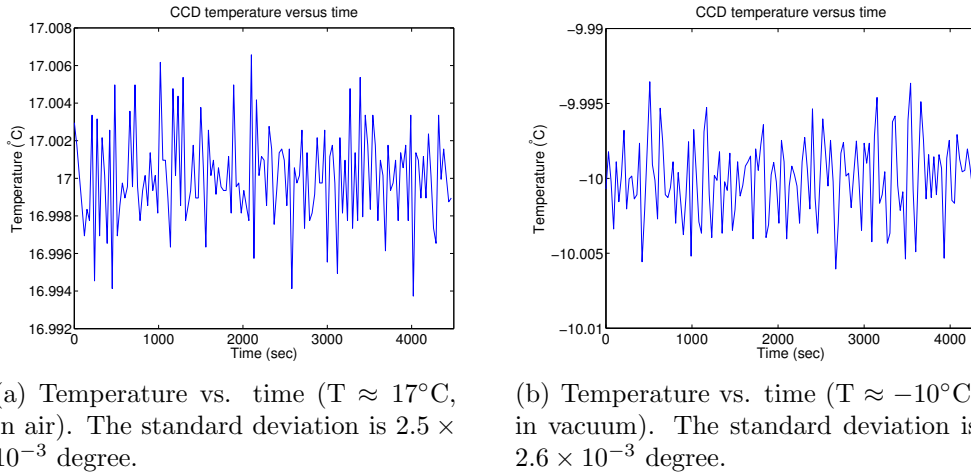


Figure III.21: CCD temperature vs. time in air and in vacuum.

6.5 Individual components tests

In this section we look at tests on individual components only. Table III.5 lists the tests performed and their result. As the detail for each test is quite fastidious, they have been put in the appendix. Links on the right column send to the corresponding test report. The compliance presented here is relative to the constructor specifications and not the ones needed for the neat-demo. There is no easy and unique solution for deriving the complete hardware specification from the needed centroiding accuracy. The relations between the two will also depend on the experimental methods and data processing used. In practice, we have often chosen the components specifications using rules of thumb, by estimating the effect of uncalibrated noise on the pixels values or locations.

So what exactly is the purpose of these tests? In the end, experimenting with the hardware gave us valuable practical experience and knowledge about the noise inherent to each component. This will also help us to build the error budget of the experiment. Moreover, some tests have been necessary at an early stage to validate some technical solutions, like for example our custom made vacuum feed-through. In such cases, detecting potential failures early was important to avoid large delays.

6.6 CCD calibration results

This set of preliminary calibrations took place with an integrating sphere in a different lab than the one hosting the neat-demo, it was required to check the performances of the CCD at an early stage. These results are very important to the success of the experiment. Depending on the outcome, we may have to include specific corrections when analyzing the data. For these calibrations, we had to leave the glass protection window in front of the chip because it was not in a dust free environment. The CCD was enclosed in an aluminum box, facing a round aperture (in the box) through which we inserted the baffle of the integrating sphere. There was no active cooling system and we worked at ambient temperature (about 25°C).

With the setup I have described, I have performed the following calibrations: photon transfer curve, linearity, flat field, dark current and readout noise. For the first

Table III.5: List of tests of individual components.

Component tested	Test name / Test ID	Compl.	Specification / Result	Link to Table
Laser HeNe 1.5mW	Intensity stability / 1	Yes	$1 \times 10^{-3} / 9.5 \times 10^{-5}$	TABLE
Laser HeNe 1.5mW	Polarization linearity / 2	Yes	1000:1 / 5400:1	TABLE
Laser HeNe 1.5mW	Polarisation angular stability / 3	NS	NS / $[0.038; 0.24]^\circ$	TABLE
Laser HeNe 1.5mW	Stabilization time / 4	No	30 min / 60-70 min	TABLE
Laser HeNe 1.5mW	Wavelength stability / 5	No	$2 \times 10^{-9} / 1.5 \times 10^{-8}$	TABLE
Liquid core fiber	Plug interface leakage / 6	Yes	Air tight / Air tight	TABLE
Liquid core fiber	Degassing / 7	Yes	Air tight / Air tight	TABLE
Integrated-optical phase modulators	Attenuation / 8	Yes	6 db / 5.94 db	TABLE
Halogen light sources	White light source stability / 9	NS	NS / 8%	TABLE

two calibrations I used a conventional dark subtraction (subtraction of an averaged dark to each frame), prior to the processing. Some results are just indicative and cannot be directly applied for the neat-demo data analysis, in particular flat fields (because of the window), dark current and read noise (because of the temperature). Fortunately, they can be repeated in the neat-demo lab inside the vacuum chamber if necessary, albeit the flat will have to be without the integrating sphere.

Dark current and readout noise have been tested again inside the vacuum chamber at lower temperatures and are presented in this section as well. Numerous other flat fields have been measured inside the chamber, but they are much more closely related to the data analysis and are presented in the chapter V.

□ Notations

To briefly explain the principle of each calibration, I will use the following notations:

- Signal (in counts) on the CCD: $S = kN_0 + S_{\text{offset}}$
- Temporal variance of the signal: $\sigma_S^2 = k^2 s_0^2 + k^2 s_r^2$

with:

- k : gain (ADU/e-)
- N_0 : number of photo-electrons generated
- S_{offset} : electronic offset (in ADU)
- s_r : readout noise (in e-)
- s_0 : photo-electron shot noise (in e-)

Additionally, I note the exposure time for one frame: T_{exp} (i.e. the inverse of the frame rate). The colors on the plots (green, blue, red, black) correspond to one quadrant each.

6.6.1 Photon transfer curve (integrating sphere)

□ Theory

The photon transfer curve is a plot of the temporal variance of the pixels versus the dark-subtracted signal, for different flat fields with different exposure times or different exposure intensities.

As we have $s_0^2 = N_0 = \frac{S - S_{\text{offset}}}{k}$, we can write:

$$\sigma_S^2 = k^2 s_r^2 + k^2 (S - S_{\text{offset}})$$

So plotting σ_S^2 versus $S - S_{\text{offset}}$ will allow us to recover:

- k^2 : the slope of the linear fit
- $k^2 s_r^2$: the value for $N_0 = 0$

Strictly speaking, one cannot really obtain $S - S_{\text{offset}}$, because the dark current realization is different in the dark data than in the flat field data. These relations are only valid when the residual noise from dark subtraction (i.e. dark noise) is negligible compared to the photon noise. In practice we have 4 photon transfer curves, one for each quadrant of the CCD, because the electronics are different for each one. We define for each quadrant a 10×10 pixel window in which we do the calibration for every pixel and average the results afterwards. Spatial averaging in this manner increases the precision of the calibration. The great advantage of this method is that it does not require knowledge of the absolute exposure luminance or exposure time.

If we use different exposure intensities (with a constant frame rate), the point at which the linear fit crosses the vertical axis is not only the readout noise, but the sum of the dark and readout noises. In this case the extrapolated value correspond to a null intensity but not to a null exposure time. Whether we vary the frame rate or the intensity, the measure of the readout noise is intrinsically unreliable, because it is extrapolated from data which is dominated by photon noise. To properly measure dark and readout noise we use other sets of experiments, where we do not expose the detector to light.

□ Method and results

We have taken two sets of measurements (Fig. III.22 and Fig. III.23). The lines are linear least square fits (one fit per quadrant).

Set 1 (11/06/2013): this first curve was performed by changing the luminance (the integrating sphere is equipped with a shutter that can be open between 0 and 100%). The frequency was low enough (100 Hz) so that the A/D converter could reach close to 65000 counts with the shutter fully open. The gain is close to 10 for all quadrants (fit between 0 and 27000 counts). The noise reaches its maximum value for 27000 counts. This is because we are reaching saturation (the size of the quantum wells is about 30000 counts). We notice 2 outliers in green around a “signal - dark” of 5000 counts.

Set 2 (14/06/2013): this second curve was performed in the same way, but this time the frequency was increased to 200 Hz. The goal was to obtain the maximum

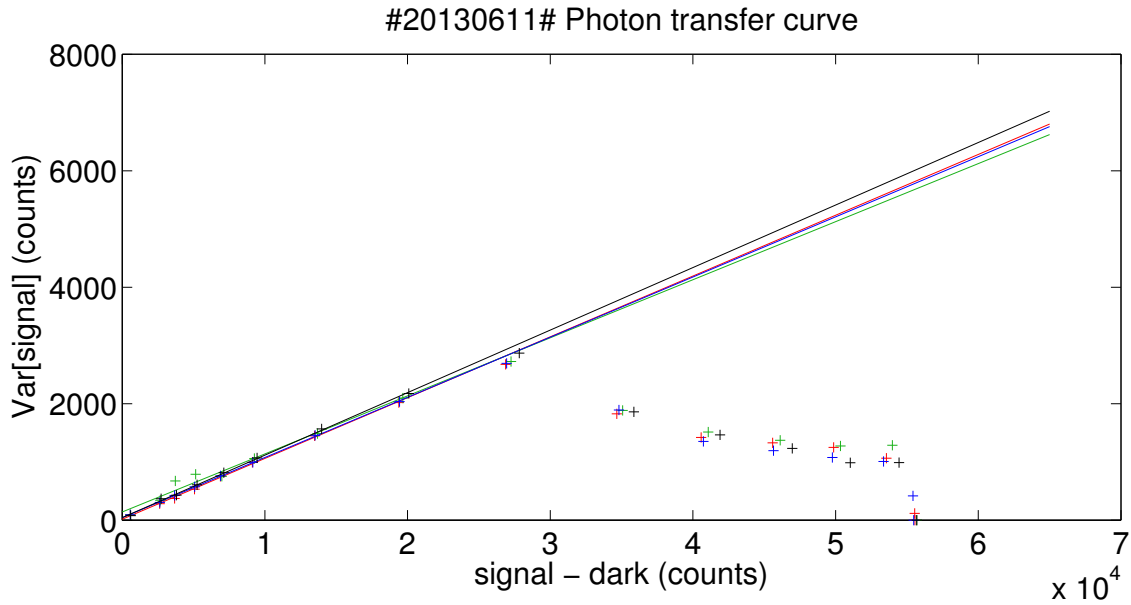


Figure III.22: **Photon transfer curve: σ_S^2 vs. $S - S_{\text{offset}}$ (Set 1: 11/06/2013).** The Framerate is 100 Hz.

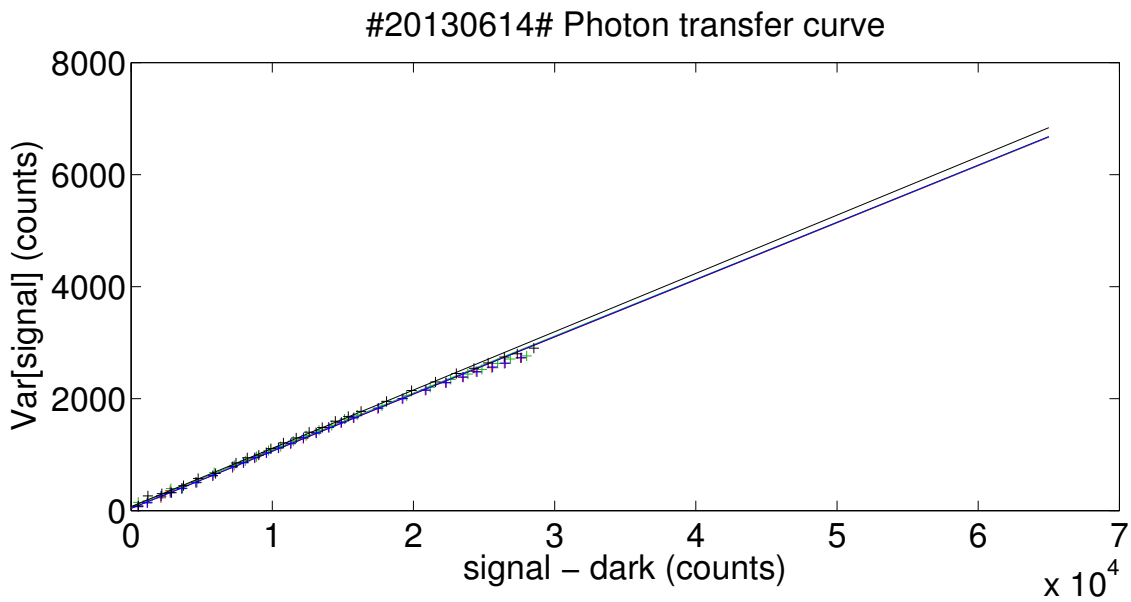


Figure III.23: **Photon transfer curve: σ_S^2 vs. $S - S_{\text{offset}}$ (Set 2: 14/06/2013).** The Framerate is 200 Hz.

number of data points between 0 and 30000 counts (saturation level), to obtain a better fit.

For the second set, the fit was done between 0 and 24000 counts because for higher values there is visible deviation from linearity. The values found for k , for quadrant 1 to 4 are respectively: 0.10142, 0.10099, 0.10146, 0.10344. All values are close to 0.1 ADU/pixel. If we express the gain in units of e-/ADU, we obtain a value of about 10. In the subsequent discussions we will use a factor of 10 to convert from ADU to e-.

The values for a null illumination are respectively: 45, 71, 44, 76. This yield noise values (noted s) of:

$$7\text{ADU} < ks < 9\text{ADU}$$

$$\Rightarrow 70e^- < s < 90e^-$$

These values of noise are the sum of the read noise and the dark current noise (at 200 Hz).

6.6.2 Linearity (integrating sphere)

□ Theory

To test the linearity we plot $S - S_{\text{offset}}$ versus the exposure time. We keep the luminance constant and we change the framerate (thus changing also the exposure time). The clock of the CCD is very accurate and we know the exposure time with a precision of a few nanoseconds.

$S = kN_0 + S_{\text{offset}} = kT_{\text{exp}}F + S_{\text{offset}}$, where F is the flux of photons/sec/pixel.

We are not interested in knowing F but in looking at the deviation of the points from a perfect line ($S - S_{\text{offset}}$ vs. T_{exp}). We however need to have a very stable flux: we need it more stable than the non-linearity we aim to measure. After plotting the fit, we plot the fit residuals and then the relative residuals. The maximum of these last residuals gives the difference to perfect linearity.

□ Method and results

First we have checked the RSD of the flux emitted by the lamp used during the calibration. A tool was available to export recorded flux data, we have determined that on the timescale of 1 minute needed for the calibration, the flux RSD was smaller than 10^{-4} . For the linearity test itself, the position of the shutter was set to have about 27000 counts (close to saturation) for the largest exposure time used (5 ms). We have used frames rates ranging from 200 Hz to 977 Hz.

Figure III.24 is a plot of the dark subtracted signal versus the exposure time. Figure III.25 is a plot of (absolute) residuals of Fig. III.24 in counts. Figure III.26 is a plot of (relative) residuals of Fig. III.24 in counts.

The maximum is at 0.2% (for an exposure time of 3.3 ms). All the values are also above -0.1%. In conclusion for this test, no quadrant deviate of more than 0.2% from the linear response, when averaging a zone of 10 by 10 pixels.

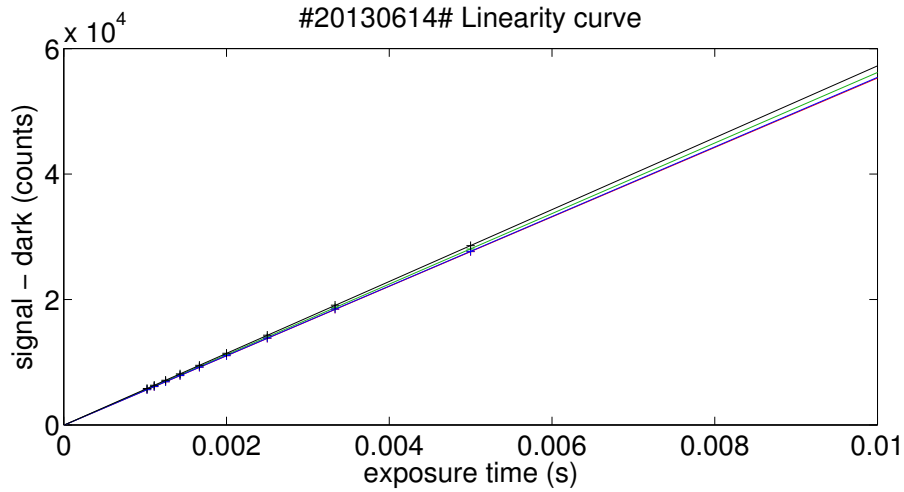


Figure III.24: Linearity curve: $S - S_{\text{offset}}$ vs. T_{exp} .

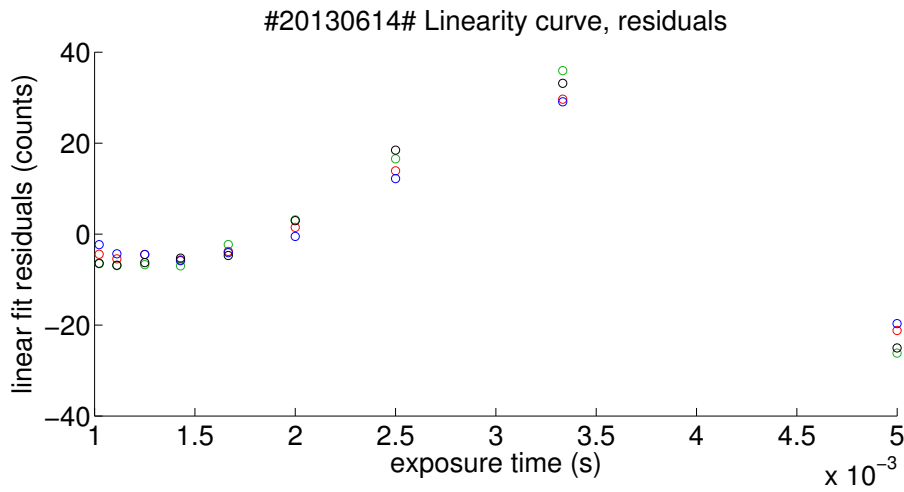


Figure III.25: Linearity test: absolute residuals (counts).

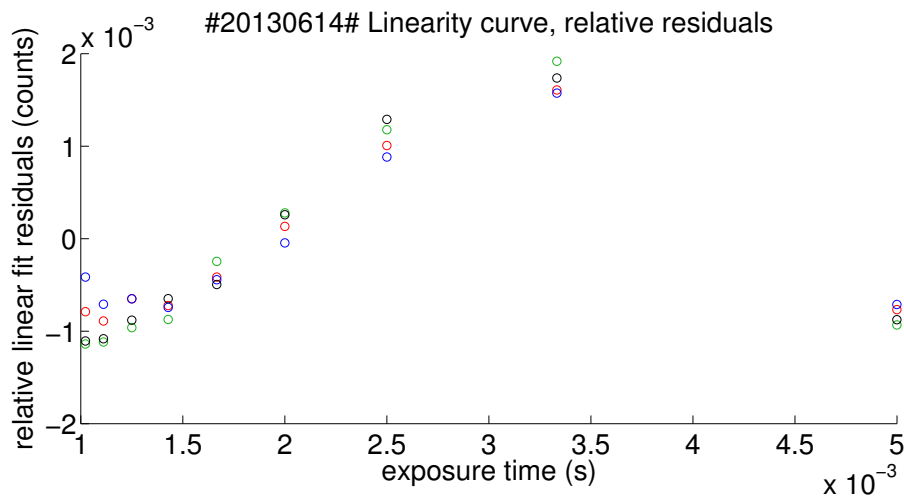
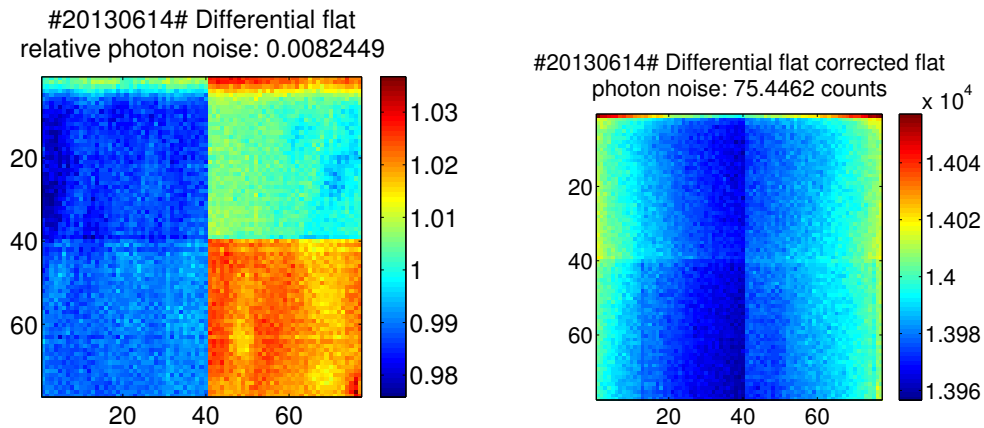


Figure III.26: Linearity test: relative residuals (counts).

6.6.3 Flat field (integrating sphere)



(a) **Differential flat field.** The photon noise indicated in the figure title is a theoretical value calculated from the averages of each dark-subtracted flat used in the process. It corresponds roughly to the granularity (within quadrants) we see in the image.

(b) **Differential flat corrected flat field.** The photon noise is a theoretical value. It corresponds roughly to the small scale granularity of the image.

Figure III.27: Flat fields.

Here we test the pixel response non uniformity (PRNU), by temporally averaging the pixel counts. Figure III.27(a) is a differential flat: it is the difference between a flat with high flux (near saturation) and a flat with low flux (near dark). We use this differential method to have the most linear response possible. The variations are caused by differences in sensitivity between the pixels and photon noise, but we integrate for a time long enough to ensure that the latter is smaller than the sensitivity differences.

There are very clear variations between each quadrant, with systematic biases near the edges (more sensitive pixels) and smaller biases forming spots inside the quadrants. However the interpretation is ambiguous: the variations can also be caused by the protection window. Figure III.27(b) is a flat with a medium flux divided by the previous flat. The result has a very smooth profile, the residual inhomogeneities seen here are caused by photon shot noise and variations of non linearity between the pixels.

There are no significant changes in non linearity between the pixels in the center of the chip. This shows that the linearity results are valid over all the central area. There seem to be a small gradient between the middle and the edges, of the same order than the non linearity of individual pixels: 0.3% (from 1.398 to 1.402×10^4 counts). Given the small magnitude of the effect, it is hard to tell if this is a real change in non linearity or it has a different cause. Overall, the linearity can be considered to be very good. Very close to the edges we see larger biases, in particular the top and bottom rows, but they can be easily cropped without losing much space.

6.6.4 Dark current and readout noise

□ Theory

In absence of light, the residual signal (in counts) on the CCD is caused by thermal electrons, plus the offset: $S = kF_{\text{dark}}T_{\text{exp}} + S_{\text{offset}}$, where F_{dark} is the rate of thermally generated electrons (so called dark current), expressed in e-/pixel/s. Without photons, the temporal variance of the signal is: $\sigma_S^2 = k^2s_r^2 + k^2F_{\text{dark}}t$.

To obtain the dark current we plot S as a function of T_{exp} . The slope of the fit gives F_{dark} . To obtain the readout noise we plot σ_S^2 as a function of T_{exp} . The readout noise is at the intersection of the linear fit with the vertical axis.

□ Method and results

Both measurements are obtained from the same set of measurements, which are dark fields at a range of different frame rates. The dark current and the readout noise can be very sensitive to temperature, so we should not take the results obtained with the integrating sphere setup at face value. These first results (set 1: 14/06/2013) are obtained at ambient temperature, plus a few degrees because the CCD heats up during operation to around 25°C. The cooling is only passive, through air and the aluminum box enclosure. The two other sets (set 2: 30/09/2014 and set 3: 02/10/2014) have been obtained inside the vacuum chamber with active cooling at respective temperatures of 17°C and -10°C (stable to 2.5 mK). For each data set, I show the plots from which I derive the dark current and readout noise estimations.

In all sets the data was obtained by using different frame rates ranging from 50 Hz to 977 Hz with the lamp of the integrating sphere or any other light source shut-off (our setups prevent any visible light from arriving to the detector when the lamps are off). For the dark current estimation (Fig. III.28 III.29 and III.30), pixel count values are averaged temporally and spatially over a 10×10 pixel zone at the center of each quadrant. For the readout noise (Fig. III.31, III.32 and III.33), we use the same data and compute the temporal standard deviation (for each exposure time). The noise values are also averaged spatially over zones of 10×10 pixels. On the plots the readout noises are given (for each quadrant) by the intersection of the fit and the vertical axis (null exposure time).

In the CCD39 product sheet, the dark currents are specified for $V_{\text{ss}}=9\text{V}$ (in our experiment we use $V_{\text{ss}}=8\text{V}$ ⁴). At 25,17 and -10°C, their respective values are specified at 70000, 40000 and 3000 e-/pixel/s. According to the plots, the dark current is about 90000 e-/pixel/s at 25°C, 30000 e-/pixel/s at 17°C and negligible at -10°C (the value is too small to be measured). From the data, we confirm that:

- At 25°C / 200 Hz, the dark variance is about 450 e- or 45 counts, which is too small to affect the precision of the photon transfer calibration (Y values range from 0 to 3000 counts).
- At 17°C, the dark noise for the lower frame rate we use (100 Hz), is $\approx \sqrt{300} \approx 17\text{e-}$, smaller than the measured read noise (50 e- or more).

The measured readout noise is typically about 5 counts / 50 e-, significantly higher than the initial specification (1 count / 10 e-). Generally speaking, a readout noise of 50 e- should not have any tangible consequence for our experiment: for a flux as low as 10000 e-/frame, the photon noise will be 100 e-, already larger than the

⁴ V_{ss} is one of the critical CCD control voltages, defined by the readout electronics design.

readout noise. For all kinds of measurement (flat, metrology, pseudo stars) we have been able to fill a significant fraction of the quantum wells, typically 1/3 (i.e. 100000 e-) or more.

On the other hand we have observed something that is potentially problematic: the CCD exhibits some worrying instabilities with respect to its readout noise. Sometimes the readout noise within one quadrant increases to a much higher level, which can be as high as 30 counts. Figure III.33 illustrates this: one of the quadrants has a noise of about 20 counts (at all frequencies), whereas all the others are at about 5. The data was taken for a CCD temperature of -10°C (in vacuum), after 8 hours of continuous acquisition to allow for the temperature of the electronic equipment to be very stable. On Fig. III.32, the readout noise levels are high for some couples of quadrants / framerates.

The CCD control interface come with a handy “quick look” utility, which display two images in real time, one is the number of counts and the other one shows the noise calculated over 25 frames. The instabilities have thus been observed in real time, and of course the level of noise derived in the calibration presented above is compatible with the quick look indicator (so we have no reason not to trust it!). From what we have seen during the experiments, we can say the following about the instabilities:

- They appears quite frequently, they make up for typically 50% of the time the CCD is operating
- They appears/disappears slowly, ramping up/down for several minutes
- Once stabilized, the readout noise can also stay constant for hours
- Rebooting the CCD and its electronics most often does not change the readout noise levels.
- The readout noise level in the anomalous quadrant often stabilizes somewhere between 10 and 20 counts, but it can be as high as 30 counts.
- It does not always affect the same quadrant.
- It has been observed on all chips (we have several science qualified copies of the CCD chip, the chip in the chamber has been swapped several times).

Unfortunately we have been unable to pin down a convincing cause for the instabilities. A level of noise of 30 counts is much more consequent: it is comparable to the photon noise for a high flux: about 1/3 of the full quantum well. One can speculate about the nature of this additional noise: if it is not white Gaussian noise, it could compromise the experiment success. We will remain alert of this aspect when analyzing the data.

6.7 Compliance table

I will conclude this chapter by some remarks about the non compliance/compliance of some parameters and their potential impact on the experiment.

Dust free environment Dust control worked quite well overall, we however had one instance were some dust was deposited unto the CCD. Large dust particles became visible on the CCD (they induced large effective QE drops, of several

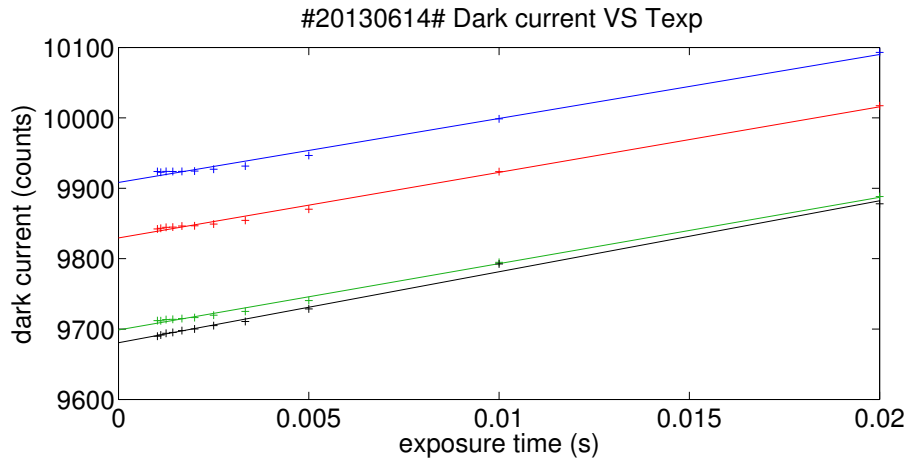


Figure III.28: **Dark current vs. exposure time (set 1: 14/06/2013, $T \approx 25^\circ\text{C}$).** The slope is the dark current per pixel.

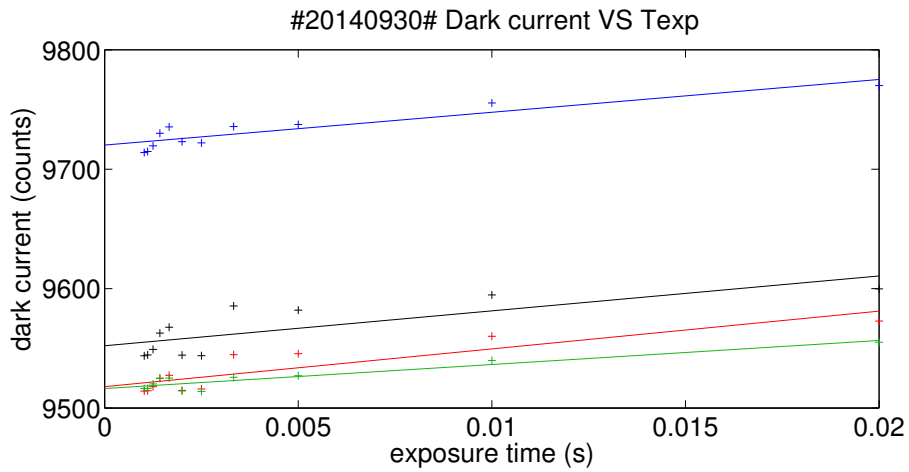


Figure III.29: **Dark current vs. exposure time (set 2: 30/09/2014, $T = 17^\circ\text{C}$).** The slope is the dark current per pixel.

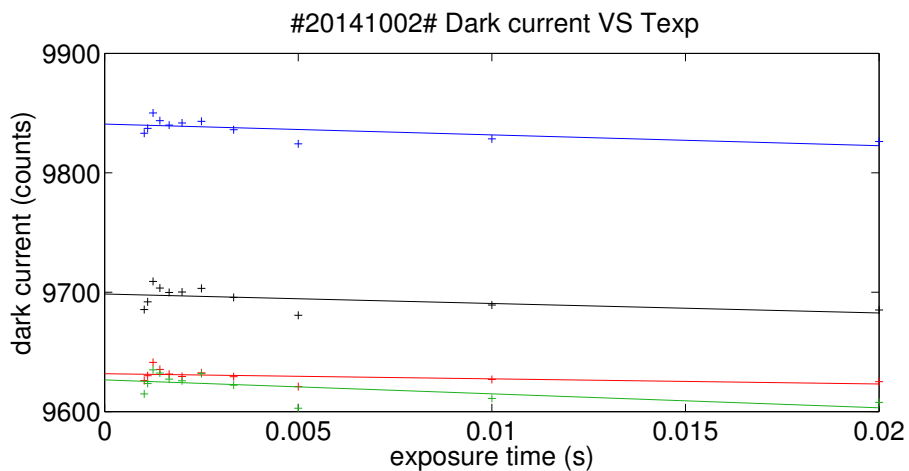


Figure III.30: **Dark current vs. exposure time (set 3: 02/10/2014, $T = -10^\circ\text{C}$).** The slope is the dark current per pixel.

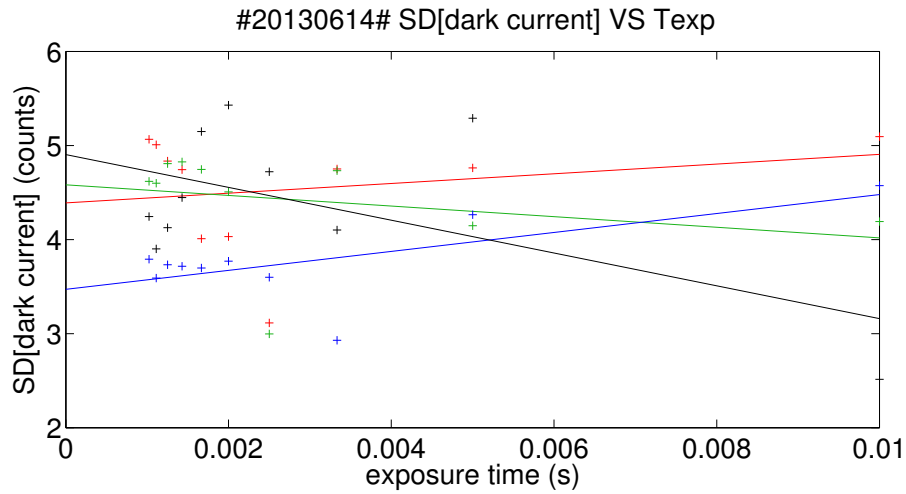


Figure III.31: **Dark current standard deviation vs. exposure time (set 1: 14/06/2013, $T \approx 25^\circ\text{C}$)**. The intersection with the vertical axis is the read noise.

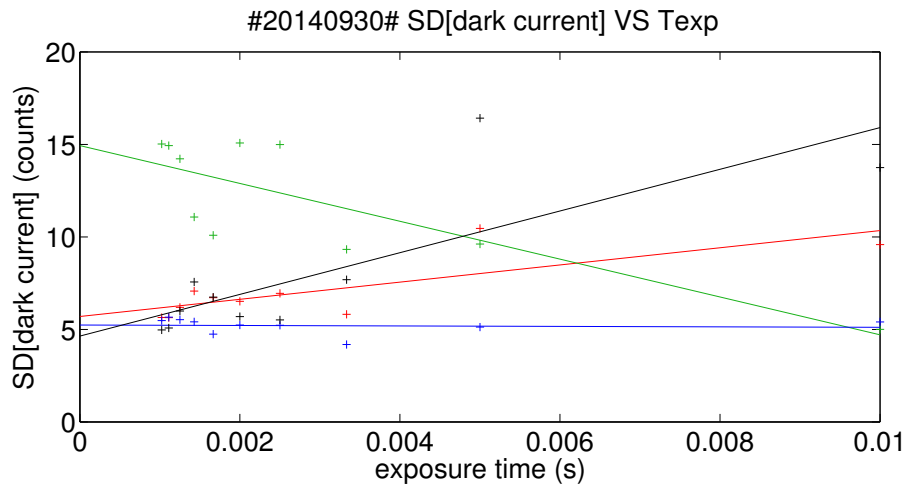


Figure III.32: **Dark current standard deviation vs. exposure time (set 2: 30/09/2014, $T = 17^\circ\text{C}$)**. The intersection with the vertical axis is the read noise.

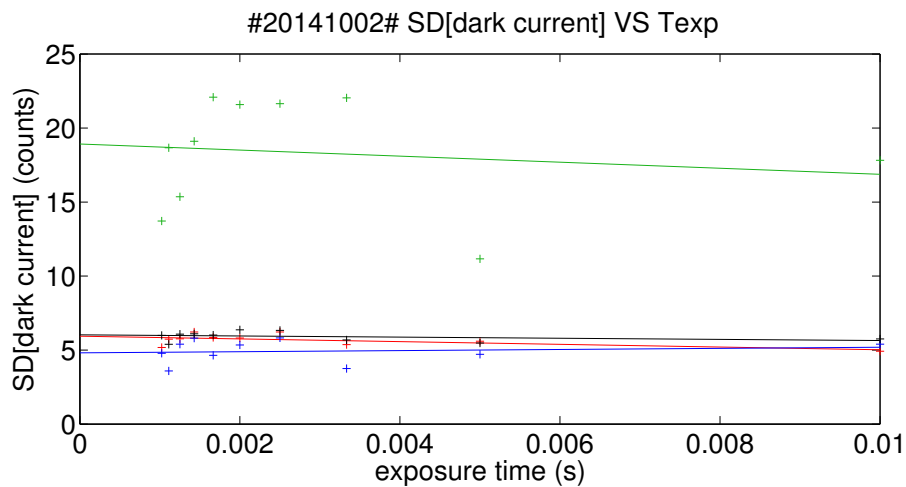


Figure III.33: **Dark current standard deviation vs. exposure time (set 3: 02/10/2014, $T = -10^\circ\text{C}$)**. The intersection with the vertical axis is the read noise.

Table III.6: Notations.

#	Criterion	Specification	Measured/Design	Comp.?
Detector and environment				
1	Stability of pseudo star images	$1 \times 10^{-2}e$	$3 \times 10^{-3}e$	Yes
2	Translation stage resolution X/Y	$0.1e$	$1 \times 10^{-3}e$	Yes
3	Translation stage resolution Z	1.4×10^{-4} m	2.4×10^{-8} m	Yes
4	X/Y rotation	Manual coarse rotation	Motorized rotation	Yes
5	Critical pressure	$P < 0.5$ mbar for several hours	-	Yes
6	Dust free environment	Best effort	-	-
7	Detector temperature stability	0.1 K over 1 h	$2.6 \times 10^{-3}K$ over 1 h	Yes
8	Read noise	10 e-	40 to 300 e-	No
9	Pseudo stars and metrology integration times	less than a few minutes	see phot. budgets (6.1)	Yes
10	Dark noise	10 e- @ T_{crit}	20 e- @ $17^\circ C$ 5 e- @ $-10^\circ C$	Yes
Pseudo stars				
11	Geometric aberrations	Diffraction limited	see section 6.2	Yes
12	Spatial sampling	Nyquist sampling	see section 4.1	Yes
Metrology				
13	Number of baselines for each direction	3+ metrology baselines	4 metrology baselines	Yes
14	Fringe visibility	$V > 0.5$	$V \gtrsim 0.5$	Yes
15	Phase modulation	$> 2\pi$	$> 6\pi$	Yes

% over one or a few pixels). We were able to remove most of them by blowing nitrogen unto the CCD, but a few small particles stayed on the chip, producing QE drops of about 1%. The CCD was not removed from the vacuum chamber during this incident and we were doing the usual kinds of modifications inside the chamber (baffle changes, stray light tests). Dust could have been brought by contact inside the chamber, but we do not know the exact cause, i.e. how it got unto the CCD.

Readout noise Readout issues have been extensively described in section 6.6.4. I will only give a brief summary here. The readout noise was specified at 10 e-, but the measurements showed a “baseline” level of about 40-50 e-. However this later readout noise level is still small compared to the photon noise in the conditions of our experiment. The instability of the readout noise level is much more concerning, it can ramp up to about 300 e-. If this noise is not strictly white and Gaussian this could have a serious impact on the experiment.

Dark noise The dark noise level is only slightly higher than the specification, even at $17^\circ C$ (20 e- for 10 e-). In any case it is smaller than the readout noise and it should not have any impact on the experiment, even when we are in air and we cannot go at low temperatures.

Integration time The photo-electron fluxes measured by the detector are lower by more than a factor 2 than the values predicted by the photometric assessment, for both the metrology and the pseudo stars. However the integration time

does not become problematic at all (still a few minutes), because they were margins for the sources (the predicted values were detector-limited). The measured values are still fairly close to the detector limit.

Chapter IV

NEAT lab demo: data analysis methods and simulations

1 Introduction

1.1 Error models

In this chapter I present the methods we have used to analyze different types of data (stars, metrology and flats) and quantify the accuracy of the centroid measurements. In addition to the data reduction process itself which yields pixel and star positions from raw images, our set of tools also included an analytic error model by François Henault and numeric models that I developed myself.

The analytic error model resulted in a spreadsheet with which we can understand error propagation quantitatively and determine some specifications on the stability or calibration accuracy needed on some error sources like pixel QE, offsets or laser intensity. Numerical models have been used for debugging, checking the data processing for artifacts and characterizing errors that are hard to assess analytically. To enable all this, numerical models are merged with the standard data analysis using a “Y” architecture (see Fig. IV.1).

For actual data, additional processing steps are required (preprocessing): a dark subtraction and a possible flat calibration (the later is optional). This distinct treatment is necessary because the synthetic data model is quite simple. Photo-electron counts are directly converted from a photon count estimation by an homogeneous scaling factor. It does not simulate all the potentially complex behaviors of the CCD and its electronics. But the core of the processing (the most complex part) i.e. the fringe fit and derivation of pixel position for metrology data and the PSF re-sampling for pseudo star data, is common to synthetic and actual data. This is critical because it allows:

- A reliable debugging of this complex part. When synthetic data is injected, the exact solution is known and is used to determine true errors (computed solutions minus the exact ones). Under ideal conditions (no noise), the true error should be close to zero, within the numerical precision. Every time a significant modification is made to the core, one can quickly re-check the processing by switching between ideal and actual data.

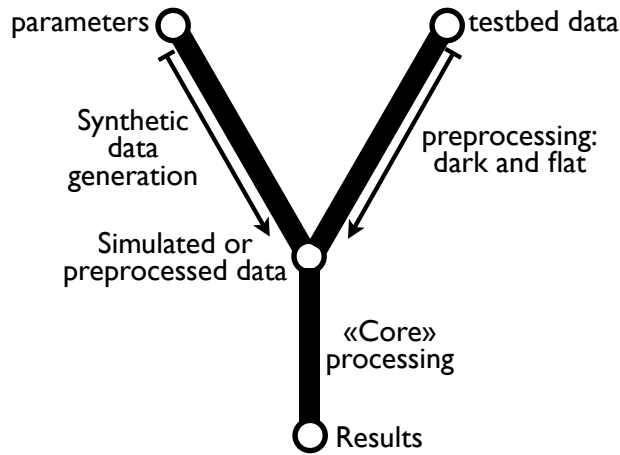


Figure IV.1: **Data and model flow diagram.** The pseudo star and metrology data analysis scripts both follow this architecture. An option setting parameter can be used to switch between synthetic and actual data.

- Characterization of artifacts introduced by the processing. True errors can still be determined when any kind of perturbation(s) (random noises or systematics) are added to the synthetic data. One can determine the conditions under which the resulting accuracy is compatible with the experiment objective.
- Confirmation and extension of the analytical model. With the same kind of process (true error analysis), applied in Monte Carlo simulations, one can test each noise source separately, possibly for different noise amplitudes, and find empirical relations between the noise sources and the final accuracy. The consistency between the analytical and numerical models can be checked and more complex noise sources can also be characterized.

1.2 Units and rules of thumb

Before going into the subject, a word about the units we will use to express the performances of the testbed: we mainly express distances and standard deviations SD in units of pixels, sometimes implicitly to simplify the notation. We will also use relative standard deviations (RSD), so beware of confusing the two !

I will present a lot of maps of pixel properties (QEs, offsets, read noise etc, over an area of 80 by 80 pixels). For some maps the spatial standard deviation is calculated as part of the analysis pipeline and indicated in the title, but most often this is not the case. There is however a useful rule of thumb that can be used to estimate the SD for white Gaussian noise: the peak to valley (PtV) variation, which is given by the max/min values of the color scale legend, is equal to about 6 to 7 times the SD (it is defined by extreme values and thus varies randomly by about 20%). When looking at the difference between two maps, the effective SD is increased by a factor $\sqrt{2}$, the difference, to a factor 8.5 to 10. In the case of the comparison between two flat fields, for example to estimate photon noise, the rule of thumb is very easy to apply: the noise is about 0.1 times the PtV given by the color scale.

In section 3.2, we derive coefficients between the amplitude some types of noise and the error on the centroid, which are also rules of thumb. Combining both rules gives

an estimation of the contribution of a given random noise or even a particular kind of systematic to the centroiding error.

2 Data analysis: methods

2.1 Overview

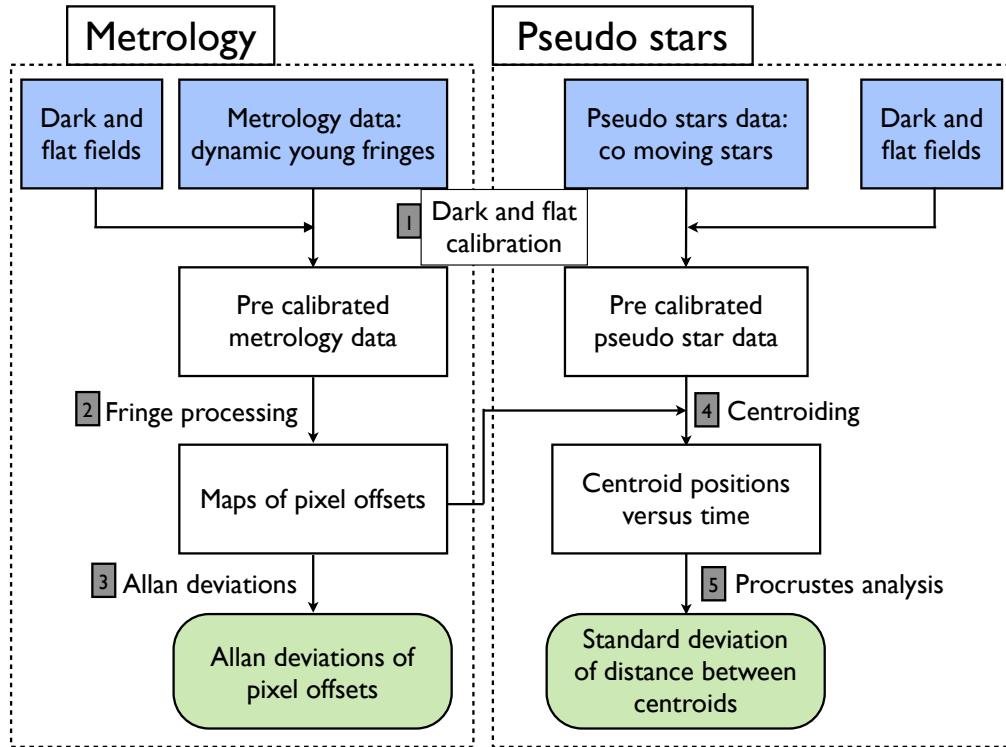


Figure IV.2: **Overview of data reduction process for the NEAT testbed.** Steps 1 to 5 of the process are described in the next sections.

The next sections focus on the data analysis methods for the dark and flat fields, metrology data and the pseudo star data. Figure IV.2 is a diagram summarizing the different types of calibrations involved, it shows how the metrology and pseudo star signal processing are linked together.

2.2 Dark and flat fields

The first step of the data reduction is the standard dark subtraction (of a temporally averaged dark frame) and flat division. For both pseudo star and metrology data, dark subtraction is systematic, while the flat field division is optional. The application to the data is straightforward: the reduced data cube is simply: $I' = (I - I_{\text{dark}})/I_{\text{flat}}$. The delicate part here is obtaining a high quality flat field in the first place. The vacuum chamber doesn't allow for an integrating sphere, it would block the light from pseudo stars and the metrology: we have to use fibers located on the mirror block. It can be a metrology fiber or a different used only for the flat. The method consist in turning-on only one metrology fiber (or the flat fiber), which will produce a fairly flat intensity pattern on the CCD. The intensity

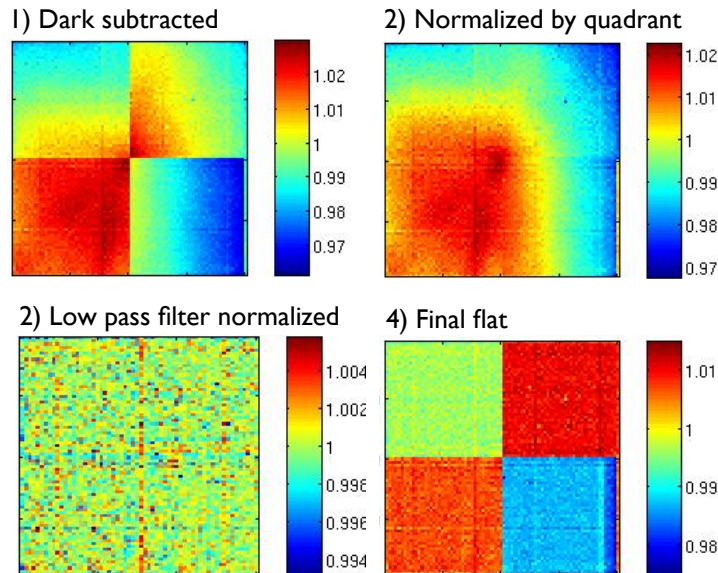


Figure IV.3: **Flat field processing.** (1) Image after dark subtraction, temporal normalization, temporal averaging and spatial normalization. (2) The relative gain between the quadrants have been compensated, assuming continuity of the intensity between the quadrants. (3) The image had been divided by its low pass filter component to obtain. (4) The quadrant relative gains are added back into the data, this is the “final flat” that will can be used for the centroids or the metrology. The images used here have a very poor quality (good for illustration purposes), of course we use better ones to derive the actual flat field.

profile produced is a Gaussian beam whose waist of about 10 cm is much larger than the CCD field (2 mm). So what is seen by the detector is an intensity gradient with an eventual slight curvature, which has to be “detrended”. The method used to obtain the flat field is illustrated by Fig. IV.3.

The first step of the flat field processing consist of:

- Dark subtraction
- Temporal normalization: each frame is scaled to have an average flux equal to the average intensity level of the first frame
- Calculation of theoretical photon noise and measured photon noise
- Temporal averaging to obtain a mean frame
- Spatial normalization: the mean frame is normalized, the average pixel value is set to 1

An important point is that we expect the flat to be much better with incoherent light, unlike the metrology fringes. Coherent light produces relative intensity variations $\propto \sqrt{I_1/I_0}$ instead of $\propto I_1/I_0$ because of interferences (I_0 is the intensity of the fiber, I_1 is the intensity of a parasite reflection). The interference pattern can be quite complex and have spatial features unresolved by the pixels if the angular separation is too large, so it can not be properly detrended. This is the case for example for reflections on the edges of the stop apertures of the baffle.

Table IV.1: Table of metrology variables for data analysis.

Notation	Name	Absorbed noises
$B(t)$	Average intensity	Laser flux, offset fluctuations
$A(t)$	Amplitude	Laser flux and polar. fluctuations
$K_x(t)$	Metrology wavevector (x proj.)	Laser freq. fluctuation, thermal expansion
$K_y(t)$	Metrology wavevector (y proj.)	Laser freq. fluctuation, thermal expansion
$\phi(t)$	Differential phase	phase jitter (thermal and mechanical)
$\iota(i, j)$	Pixel relative intensity	Pixel QE variations
$\alpha(i, j)$	Pixel relative amplitude	Pixel QE variations, visibility vs. space
$\delta_x(i, j)$	Pixel offsets (x proj.)	-
$\delta_y(i, j)$	Pixel offsets (y proj.)	-

2.3 Metrology

2.3.1 Global solution

The interference pattern created at the CCD with a monochromatic source and for given metrology baseline B of coordinates (B_x, B_y) is:

$$I(x, y, t) \propto 2I_0 \left[1 + V \cos \left(\phi_0 + \Delta\phi(t) + \frac{2\pi(xB_x + yB_y)}{\lambda_{\text{met}}L} \right) \right] \quad (\text{IV.1})$$

Where I_0 is the average intensity at the focal plane for one fiber, L is the distance between the fibers and the CCD, ϕ_0 is a static phase difference, $\Delta\phi(t)$ is the modulation applied between the lines, λ_{met} the wavelength of the laser source. Although the exact shape of the fringes is hyperbolic, at the first order the fringes are straight and aligned with the direction perpendicular to the metrology baseline. If we also assume that the point sources are of equal intensity and that the intensity created at the focal plane is uniform we have a fringe visibility of $V = 1$. In reality, the visibility is affected by the intensity and polarization mismatch between the point sources. Each fiber project a Gaussian beam whose intensity is spatially dependent and the beams are not co-centered.

Because all pixels see different visibilities and different average intensities, the solution for the cube of metrology data is searched under the following form:

$$I(i, j, t) = B(t)\iota(i, j) + A(t)\alpha(i, j) \sin [iK_x(t) + jK_y(t) + \phi(t) + \delta_x(i, j)K_x(t) + \delta_y(i, j)K_y(t)] \quad (\text{IV.2})$$

Where i, j are integer pixel position indexes and δ_x and δ_y are pixel offsets, i.e. the difference between the pixel true locations and an ideal regularly spaced grid. Here we have decoupled time and spatial variations. Also, I have implicitly transformed t into a discrete index representing a frame number. I will keep using this notation for consistency and because it naturally carries the connotation of a dimension associated with time. The meaning of all remaining variables is explained in table IV.1. The table also mention which kind of noise are absorbed by the variables.

Because there are degeneracies between the variables, we force the mean values of ι and α to 1, the mean pixel offset to zero and the offset gradient to zero. This is

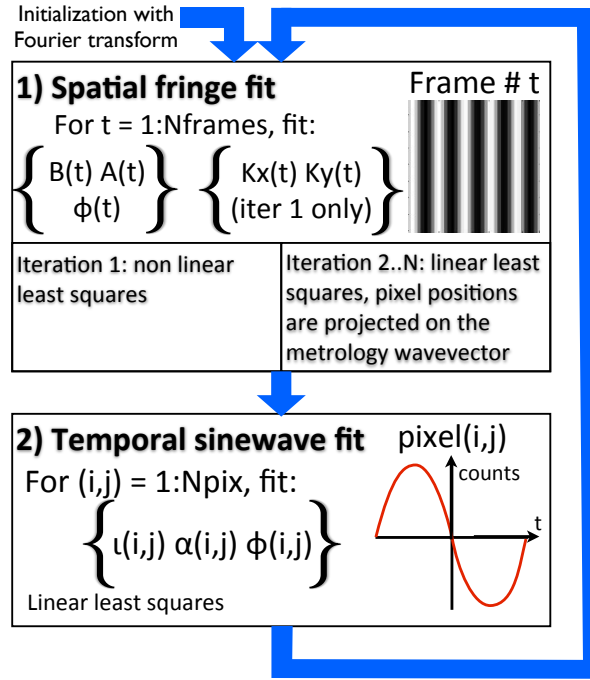


Figure IV.4: **Iterative process used to fit the metrology fringes (step 1 in Fig. IV.2).** The difference between the measured phase of a pixel ($\phi(i, j)$) and the phase expected (global fringe phase) is the phase offset caused by the pixel offset projected in the direction of the wavevector.

equivalent to adding we add the following constraints:

$$\left\{ \begin{array}{l} \sum_{i=1}^n \sum_{j=1}^m \iota(i, j) = nm \\ \sum_{i=1}^n \sum_{j=1}^m \alpha(i, j) = nm \\ \sum_{i=1}^n \sum_{j=1}^m \delta_x(i, j) = 0 \\ \sum_{i=1}^n \sum_{j=1}^m \delta_y(i, j) = 0 \\ \sum_{i=1}^n \sum_{j=1}^m i\delta_y(i, j) = 0 \\ \sum_{i=1}^n \sum_{j=1}^m j\delta_x(i, j) = 0 \end{array} \right. \quad (\text{IV.3})$$

2.3.2 Minimization strategy

A set of metrology data cube has a size of about $80 \times 80 \times \text{Number of frames}$, a large cube can contain as many as 200000 frames. The problem is non linear as the fringe spacing is a free parameter. The total number of fitted parameters ($80 \times 80 + 5 \times \text{Number of frames}$) is not practical for a straightforward least square minimization of the whole cube, that is why we use an iterative process. First a spatial fit is done on each frame to constrain the time dependent variables and then a temporal fit is done on each pixel to constrain the space (or pixel) dependent variables (see Fig. IV.4). This order is highly preferable as the global phase is very noisy and can easily be fitted by the spatial fit, but not by the temporal fit.

The spatial fit is a non linear least square minimization for the first iteration, it uses a Levenberg-Marquardt optimization procedure. The fit is initialized with parameters obtained from a Fourier transform on the first frame. From one frame to the next all parameters can be reused for initialization. The temporal sinewave fit is always a linear one. The method for the temporal fit is very similar to the standard

linearization technique used on a sinewave whose period is known. The difference is that we instead know the phase of the 2D carrier sinewave (not including pixel offsets) at each pixel and for each frame. After normalization to average frame intensity and average frame amplitude, the signal is a pure sinewave with a constant offset whose phase carries information on the pixel location projected along the modulation direction:

$$I(i, j, t) = \iota(i, j) + \alpha(i, j) \sin[\phi(t) + \phi(i, j)] = a_{i,j} \sin(\phi(t)) + b_{i,j} \cos(\phi(t)) + c_{i,j} \quad (\text{IV.4})$$

□ Linear temporal fit

A least square minimization of the sum:

$$S_{i,j} = \sum_{t=0}^{N-1} [I(i, j, t) - a_{i,j} \sin(\phi(t)) - b_{i,j} \cos(\phi(t)) - c_{i,j}]^2 \quad (\text{IV.5})$$

yields the values for a , b and c from which $\alpha(i, j)$, $\phi(i, j)$ and $\iota(i, j)$ are derived for each pixel: this is the temporal fit. We obtain pixel phases:

$$\phi(i, j) = iK_x(t) + jK_y(t) + \delta_x(i, j)K_x(t) + \delta_y(i, j)K_y(t) \quad (\text{IV.6})$$

Also knowing the metrology wavevector (see Fig. IV.5), we derive the projected phase offsets: $\delta_x(i, j)K_x + \delta_y(i, j)K_y$ (for this final step K is assumed constant), from which we have the spatial offset. The detail for the linearization of the fit is explained below.

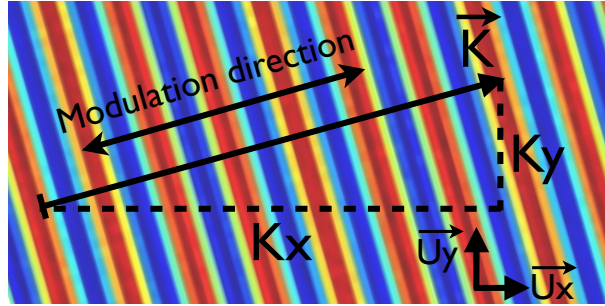


Figure IV.5: **Definition of the wave vector.** For a given metrology orientation, the wave vector is defined as: $\vec{K} = (K_x(t), K_y(t))$ for a plane wave of the form: $I(x, y, t) \propto \sin(xK_x(t) + yK_y(t) + \phi(t))$. The wave vector is by definition perpendicular to the fringes and aligned with the modulation direction, i.e. the apparent motion of the fringes when the phase changes. The default distance unit is the pixel, so the magnitude of the vectors is $|\vec{K}| = 2\pi/\lambda$, with lambda in pixel units.

We want to fit a pure sinewave, and just like in the usual case when the frequency is known, the fit can be linearized. Instead we know the phase of the carrier wave for each point in time (i.e. frame), but the principle is the same. As long as we know the true phase, the fit works even if sampling points are not evenly spaced in time or if the phase has jitter. The first step is to rewrite the sinewave and decompose it into cos and sin components, which has already been done in Eq. (IV.4). We have introduced three coefficients $(a, b, c) \in \mathbb{R}^3$. The equality is obtained when a, b, c verify:

$$\begin{cases} a = \alpha \cos \phi_{i,j} \\ b = \alpha \sin \phi_{i,j} \\ c = \iota \end{cases} \quad (\text{IV.7})$$

For simplicity we have dropped most of the i, j indexes and have rewritten the phases $\phi(i, j) = \phi_{i,j}$ and $\phi(t) = \phi_t$. The system above is equivalent to:

$$\begin{cases} \alpha = \sqrt{a^2 + b^2} \\ \phi_{i,j} = \arctan2(b, a) \\ \iota = c \end{cases} \quad (\text{IV.8})$$

We fit the constants (a,b,c) by minimizing S , the sum of the quadratic errors between the model and the data points: $S = \sum_{t=0}^{N-1} ((I_t) - (a \sin(\phi_t) + b \cos(\phi_t) + c))^2$. The minimum verifies:

$$\begin{cases} \frac{\partial S}{\partial c} = 0 \\ \frac{\partial S}{\partial a} = 0 \\ \frac{\partial S}{\partial b} = 0 \end{cases} \Leftrightarrow \begin{cases} \sum_{t=0}^{N-1} I_n - a \sin(\phi_t) - b \cos(\phi_t) - c = 0 \\ \sum_{t=0}^{N-1} \sin(\phi_t)(I_n - a \sin(\phi_t) - b \cos(\phi_t) - c) = 0 \\ \sum_{t=0}^{N-1} \cos(\phi_t)(I_n - a \sin(\phi_t) - b \cos(\phi_t) - c) = 0 \end{cases} \quad (\text{IV.9})$$

$$\Leftrightarrow \begin{bmatrix} 1 & \sum_{t=0}^{t-1} \sin(\phi_t) & \sum_{i=0}^{t-1} \cos(\phi_t) \\ \sum_{t=0}^{t-1} \sin(\phi_t) & \sum_{i=0}^{t-1} \sin^2(\phi_t) & \sum_{i=0}^{t-1} \cos(\phi_t) \sin(\phi_t) \\ \sum_{t=0}^{t-1} \cos(\phi_t) & \sum_{i=0}^{t-1} \cos(\phi_t) \sin(\phi_t) & \sum_{i=0}^{t-1} \cos^2(\phi_t) \end{bmatrix} \times \begin{bmatrix} c \\ a \\ b \end{bmatrix} = \begin{bmatrix} \sum_{t=0}^{n-1} I_n \\ \sum_{t=0}^{n-1} I_n \sin(\phi_t) \\ \sum_{t=0}^{n-1} I_n \cos(\phi_t) \end{bmatrix} \quad (\text{IV.10})$$

□ Deprojection of pixel offsets

At this point, it is very important to understand that everything we have described about the metrology reduction process applies to a single set of data with a quasi constant $K = (K_x(t), K_y(t)) \approx (K_x, K_y)$ metrology wavevector. The values of δ_x and δ_y are internal to the iteration process are not the true pixel offsets, the vector $\delta_x \vec{U}_x + \delta_y \vec{U}_y$ is equal to the true pixel offset **projected** unto the metrology wavevector: $\delta_r \vec{K}$. To solve the degeneracy, we repeat the iterative analysis presented above on two sets of metrology fringes (with noncolinear wavectors): two map of projected pixel offsets are obtained. The wavelength vectors of each data set are not strictly perpendicular but fairly close in practice. From this two maps, true x and y offsets (i.e. coordinates in a standard orthonormal basis) are derived by solving for each pixel the intersection between the projected offset coordinates $(\delta_{r,1} \delta_{r,2})$. Figure IV.6 illustrates this “deprojection” problem, the solution is found by straightforward application of Euclidean geometry in the detector plane.

We want to transform a set of two non-aligned projected offsets into X,Y offset coordinates. Let (α_1, α_2) be the coefficients such that $\vec{OP}_1 = \alpha_1 \vec{OM}_1$ and $\vec{OP}_2 = \alpha_2 \vec{OM}_2$: they are the offsets measured by the metrology. So we know the wave vectors \vec{K}_1, \vec{K}_2 and the projections α_1, α_2 and we have to find the Cartesian coordinates of the point $I = (x, y)$ which by construction lies at the intersection of lines (D_1) and (D_2) in figIV.6. One can not use a simple base change: it would yield the coordinates of the point $F = \vec{OP}_1 + \vec{OP}_2$ which has a different location than I if the metrology

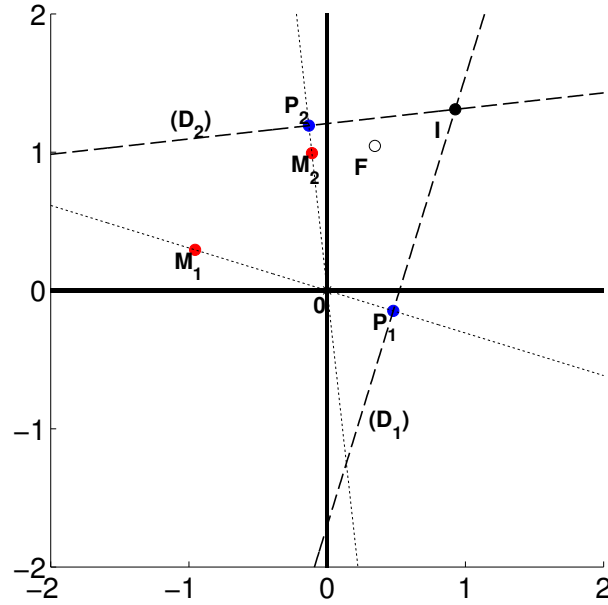


Figure IV.6: **Illustration of the deprojection problem.** $\overrightarrow{OM_1}$ and $\overrightarrow{OM_2}$ are the wave vectors normalized to a length of one pixel. The points P_1 and P_2 are the measured offsets, i.e. the projections of the true pixel offset (point I), unto the lines generated by the wave vectors. The axis units are in pixels. Simply summing the projected offsets gives a wrong answer (point F).

baselines are not orthogonal.

Let the coordinates of the normalized wave vectors be $k_{x,1}, k_{y,1}, k_{x,2}, k_{y,2}$, for respectively metrology cube 1 (first baseline/orientation) and cube 2 (second baseline/orientation). The direction vectors of lines (D_1) and (D_2) are noted $c_{x/y,1/2}$ and have trivial relations with the wave vectors coordinates:

$$\begin{cases} c_{x,1} = k_{y,1} \\ c_{y,1} = -k_{x,1} \\ c_{x,2} = k_{y,2} \\ c_{y,2} = -k_{x,2} \end{cases} \quad (\text{IV.11})$$

The lines (D_1) and (D_2) are passing through respectively $P_1 = (d_{x,1}, d_{y,1})$ and $P_2 = (d_{x,2}, d_{y,2})$, of coordinates:

$$\begin{cases} d_{x,1} = k_{x,1}\alpha_1 \\ d_{y,1} = k_{y,1}\alpha_1 \\ d_{x,2} = k_{x,2}\alpha_2 \\ d_{y,2} = k_{y,2}\alpha_2 \end{cases} \quad (\text{IV.12})$$

The parametric equation of line (D_1) , passing through P_1 , of direction vector $(c_{x,1}, c_{y,1})$, is:

$$\begin{cases} x = c_{x,1}t + d_{x,1} \\ y = c_{y,1}t + d_{y,1} \end{cases} \quad (\text{IV.13})$$

t is removed from the system above:

$$\begin{cases} c_{y,1}x = c_{y,1}c_{x,1}t + c_{y,1}d_{x,1} \\ c_{x,1}y = c_{x,1}c_{y,1}t + c_{x,1}d_{y,1} \end{cases} \Rightarrow c_{y,1}x - c_{x,1}y = c_{y,1}d_{x,1} - c_{x,1}d_{y,1} \quad (\text{IV.14})$$

The second line has the same equation, but with index 2. The coordinates of the point P is at the lines intersection and thus verifies the system:

$$\begin{cases} c_{y,1}x - c_{x,1}y = c_{y,1}d_{x,1} - c_{x,1}d_{y,1} \\ c_{y,2}x - c_{x,2}y = c_{y,2}d_{x,2} - c_{x,2}d_{y,2} \end{cases} \quad (\text{IV.15})$$

By multiplying Eq. (1) by $c_{x,2}$ and Eq. (2) by $c_{x,1}$, we find x :

$$\Rightarrow x(c_{x,2}c_{y,1} - c_{x,1}c_{y,2}) = c_{y,1}c_{x,2}d_{x,1} - c_{y,2}c_{x,1}d_{x,2} \quad (\text{IV.16})$$

$$\Rightarrow x = \frac{c_{x,2}c_{x,1}d_{y,2} + c_{y,1}c_{x,2}d_{x,1} - c_{y,2}c_{x,1}d_{x,2} - c_{x,2}c_{x,1}d_{y,1}}{c_{x,2}c_{y,1} - c_{x,1}c_{y,2}} \quad (\text{IV.17})$$

The solution for y is analog (indexes 1 and 2 are switched). The final solution is:

$$x = \frac{c_{x,2}c_{x,1}d_{y,2} + c_{y,1}c_{x,2}d_{x,1} - c_{y,2}c_{x,1}d_{x,2} - c_{x,2}c_{x,1}d_{y,1}}{c_{x,2}c_{y,1} - c_{x,1}c_{y,2}} \quad (\text{IV.18})$$

$$y = \frac{c_{x,1}c_{x,2}d_{y,1} + c_{y,2}c_{x,1}d_{x,2} - c_{y,1}c_{x,2}d_{x,1} - c_{x,1}c_{x,2}d_{y,2}}{c_{x,1}c_{y,2} - c_{x,2}c_{y,1}} \quad (\text{IV.19})$$

2.3.3 Allan deviations

The second important result given by the metrology, besides the pixel offsets, is the Allan deviation. The latter can be calculated directly on the normalized projected pixel offsets. Our interest here is to estimate the accuracy of the pixel positions we have obtained. This estimation is almost insensitive to the basis in which the coordinates are expressed, as long as the vectors of the basis are close to orthonormal. Figure IV.7 shows how the Allan deviations are calculated.

The starting point is the dark subtracted frames and the final solution of the spatial fits from the previous iterative process. Using these as starting values, the temporal pixel fits are performed on small parts of the data called batches, instead of the whole data cube. The number of frames in each batch is calculated so that the temporal signal seen by each pixel covers at least one sinewave period: this is needed to have a well constrained fit. One obtains a map of the pixel offset for each batch, this was the first step.

For the second step, the Allan deviations per say are applied on the cube of pixel offsets. The principle is to form groups of pixel offsets maps (in fact group of batches), to calculate the average within each group and then the standard deviation between the groups. The final standard deviation depends on how many batches each group has.

Each group corresponds to one point on the Allan deviation plot, so the second step is repeated for different group sizes. The maximum group size is when the standard deviation is calculated on only two groups. The point of doing all this is to simulate doing several experiment and looking how the accuracy changes with the experiment duration. By splitting the data into several subsets, only one experiment is needed.

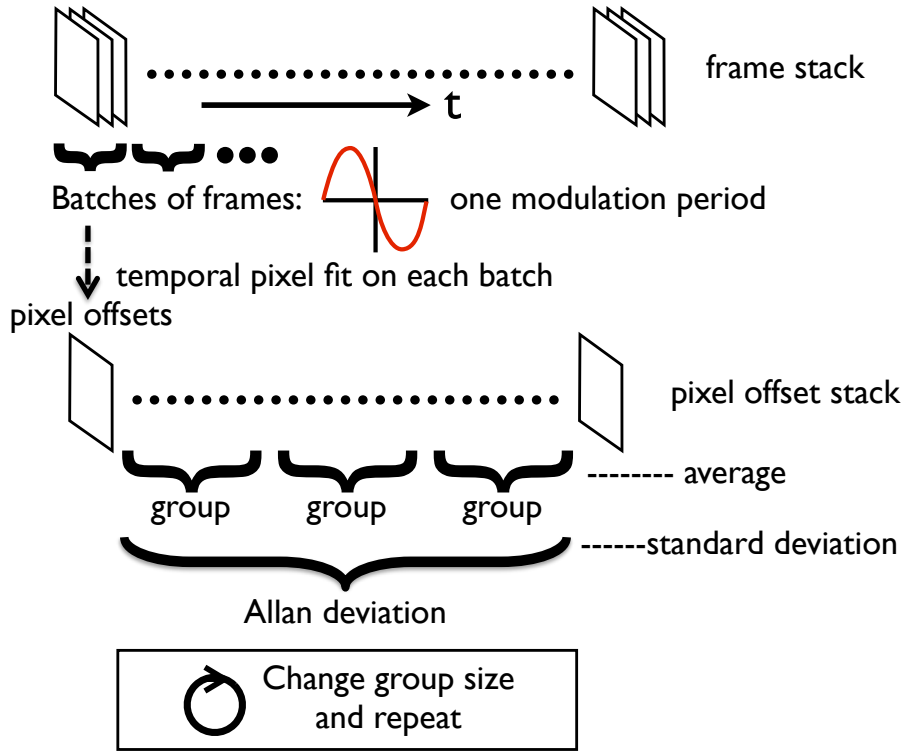


Figure IV.7: Diagram of the process used to calculate the Allan deviations (step 2 in Fig. IV.2).

□ Relation between the photon noise and the standard deviation on measured pixel offsets

Consider a sine wave seen by a punctual pixel: $f(r) = A \sin(2\pi r/\lambda) = A \sin(Kr)$. The derivative is $\frac{df}{dr} = Ak \cos(Kr)$, the value of $\frac{df(0)}{dr} = AK$ is thus the gradient of the sinewave seen by a pixel at position 0. This position is optimal for the measurement: it is where the photon count is most sensitive to the pixel offset, and inversely where the offset is least sensitive to photon noise. For an individual frame and an optimally located pixel, the error on the projected pixel offset $E(\Delta r)$ as a function of the photon noise $E(N_{\text{frame}}^-)$ is: $E(\Delta r) = \frac{E(N_{\text{frame}}^-)}{AK}$

In reality a sinewave is fitted on a batch of frames covering a period, but we consider that the error on the pixel position is mostly constrained by the frame near the optimal points, so in the end the photon noise decrease as $\propto \sqrt{N_{\text{frames}}/2}$ to take into account that they are frames for which the gradient is near 0. The final result is:

$$E(\Delta r) = \frac{E(N_{\text{frame}}^-) \sqrt{N_{\text{frames}}/2}}{AK} \quad (\text{IV.20})$$

2.4 Pseudo stars

We have worked with with two different centroiding methods. The first one is a simple Gaussian fit with 7 parameters (background level, intensity, position X, position Y, width X, width Y, angle). The second one is a Fourier-resampling technique. The principle is to measure the displacement between two images by

resampling with phase ramp in the Fourier domain. We use the following property of the Fourier transform (noted \mathcal{F}):

$$\mathcal{F}[\text{PSF}(x - x_0, y - y_0)] = \exp[-i2\pi(x_0x + y_0y)]\mathcal{F}[\text{PSF}(x, y)] \quad (\text{IV.21})$$

In practice, I use Eq. (IV.22) as a way to translate the second PSF at the location of the first one. The vector (x_0, y_0) for which the residual image between the first PSF and the resampled second PSF is minimal (in the least square sense) is the displacement. Thus the vector (x_0, y_0) is found by minimization of the expression:

$$\sum_{x,y} \left[\mathcal{F}[\text{PSF1}(x, y)] - \exp[-i2\pi(x_0x + y_0y)]\mathcal{F}[\text{PSF2}(x, y)] \right]^2 \quad (\text{IV.22})$$

When done on Nyquist sampled data, it is equivalent to a perfect interpolation. Another advantage of this method is that we are essentially using the data itself to reconstruct the PSF and we do not need a model of the PSF in the first place, thus avoiding potential errors caused by a model/data PSF mismatch. But this method has a drawback: it only gives relative motion. In order to know the distance from one centroid to another, we have to use an autocorrelation between two distinct centroids. However, because we have an optical configuration with only one optical surface and no obscuration of the field of view, the PSF is expected to be nearly invariant. The errors of this process should be mainly caused by the pixels, which can be calibrated by the metrology.

To take the pixel offsets into account, a intermediate step is added. Before calculating the offset with Eq. (IV.22), we correct the PSFs by finding its theoretical shape for null offsets $P_0(i, j)$. Eq. (IV.22) is then applied between the $P_0(i, j)$ corresponding to each PSF. This is done by using the CCD model, generated from the pixel offsets. A least square minimization is done on the product between:

- An oversampled version of P_0 obtained by zero padding in the Fourier domain
- The part of the CCD model (concatenation of PRFs) corresponding to the active fitting window

More precisely, the residuals are the difference between the data and the product we have defined above. To efficiently evaluate the residuals, in a manner practical for iterative optimization, the function returns a residual array with the same sampling than the original PSF, by summing the product array over each pixel.

The last step is the SD analysis of the centroid positions, with or without Procrustes analysis. At this point we have a measure of the coordinates of each centroid versus the time, for one or more positions on the CCD. We perform several types of analysis. For the first type (lets call it quasistatic), we monitor the centroids locations versus time at a fixed position: we do not use the motors of the translation stage. We can then calculate the SD of the distances between the outer centroids and the central one. This measure is sensible to some environmental factors such as mechanical stability, air turbulence etc... but if the centroid positions are stable enough, the pixel errors are nearly constant and therefore do not affect the measures significantly. The centroids motion are caused by mechanical vibrations and are typically less than one 1% of a pixel. A complete Procrustes analysis is actually not needed to obtain this particular result, only the translation is compensated.

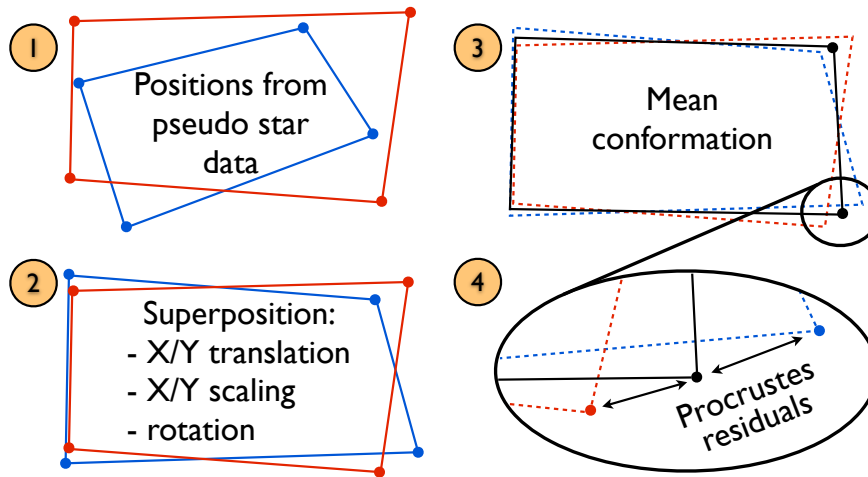


Figure IV.8: **Diagram of the Procrustes analysis.**

For the second type of analysis (lets call it dynamic), we move the centroids at different positions on the CCD with the translation stage. The amplitude of the motion between each position can be controlled and can range between 1% of a pixel to several pixels. We also calculate the SD of the distances between the outer centroids and the central one. But this is not enough: because the translation stage induces large tip-tilt errors we have to take into account vertical and horizontal scale changes. In order to calibrate the scales, we use the centroid themselves, by doing a Procrustes analysis. The principle is to find the geometric transformation that result in the closest overlap of the measured centroid positions (Procrustes superimposition). The residuals between the overlaps indirectly yields the final accuracy. The number of parameters needed to define the transformation is 5 (translation X and Y, scaling X and Y, rotation), which is less than the number of data points (2 axes \times 5 centroids for each position). This is what makes the analysis possible. Figure IV.8 is illustrates how the Procrustes analysis is done and how the residuals are obtained.

3 Results on simulated data

3.1 Metrology

□ Data generation

The principle is to project an ideal pattern of fringes onto a CCD model, as illustrated by Fig. IV.9. The frames are generated one by one, by shifting the fringes. The result is a simulated metrology data cube of dynamic fringes that carry the information of pixel sensitivities, offsets and widths.

$$\text{PRF}(x, y) = A * \exp \left[\frac{(x - x_0)^n}{2\sigma_x^n} + \frac{(y - y_0)^n}{2\sigma_y^n} \right] \quad (\text{IV.23})$$

□ Results

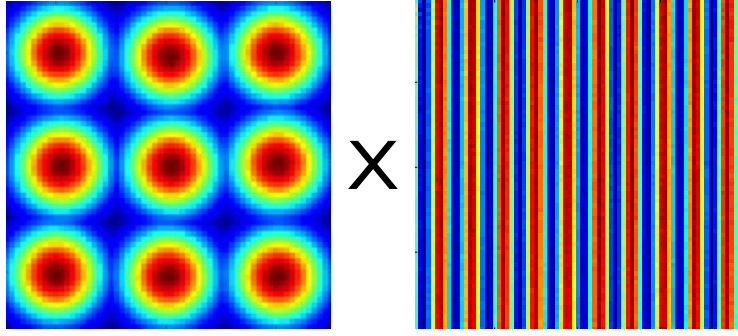


Figure IV.9: **Principle of fringe generation in the metrology model.** First a CCD model consisting of all the PRF concatenated together is generated (image on the left). PRFs consist of a truncated parametric hyper-Gaussian (see Eq. IV.23), whose parameters vary from pixel to pixel. The pixel sensitivity corresponds to the sum of all the elements in the PRF, the pixel offset corresponds to its barycenter and the width is its standard deviation. This model is then multiplied with over sampled model images of the fringes (image on the right). In reality the fringes are much larger than the pixels, typical interfringe distances are from 3 to 8 pixels.

The metrology model is used in two ways. The first one is the comparison between the CCD model and the results from the processing. The most important results here are the pixel sensitivities and offsets and we want to make sure that the processing does not introduce biases greater than 1 micro pixels for the pixel offset and 1 ppm for the pixel sensitivities. This is easy to check because the exact solution is known, so a simple subtraction between the model and the processing output yields the bias.

The second result is the Allan deviation. When working with real data, one does not have access to the exact solution, so other methods have to be used. Our main tool here is the Allan deviation analysis, which gives information about the standard deviation of the pixels offsets as a function of the number of frames used for the fit. For ideal photon noise limited measures, one expect the standard deviation to decrease proportionally to the square of the number of frames. Allan deviations on simulated data are useful because they provide a mean to check that the data analysis method is well behaved: the standard deviation should be in agreement with the theoretical photon noise limit and it should decrease as the square root of the number of frames.

Figure IV.10 shows the Allan deviation obtained after analysis of 200,000 simulated fringes. The goal is to validate the pipeline and the photon error budget. This number of frames corresponds to about 3 minutes of data with our setup. We can acquire data up to 1000 Hz, but in practice we work somewhere between 600 and 800 Hz because of the intensity limit set by the metrology fibers output.

For groups of 200 batches (i.e. 100,000 frames), the accuracy reaches 2×10^{-6} for groups of pixels and 2×10^{-5} for individual pixels. This level of accuracy is entirely satisfactory (see section 3.2 to understand why). The expected deviations from photon noise are indicated by horizontal dashed lines on the plot and they coincide almost perfectly with the measured Allan deviations. The top black line shows what the deviation for groups of one batch should be: as expected, it crosses the left axis of the plot at the same place than the Allan deviation curve (black line). They are actually two lines near the top, almost on top on each other: the dark one is for

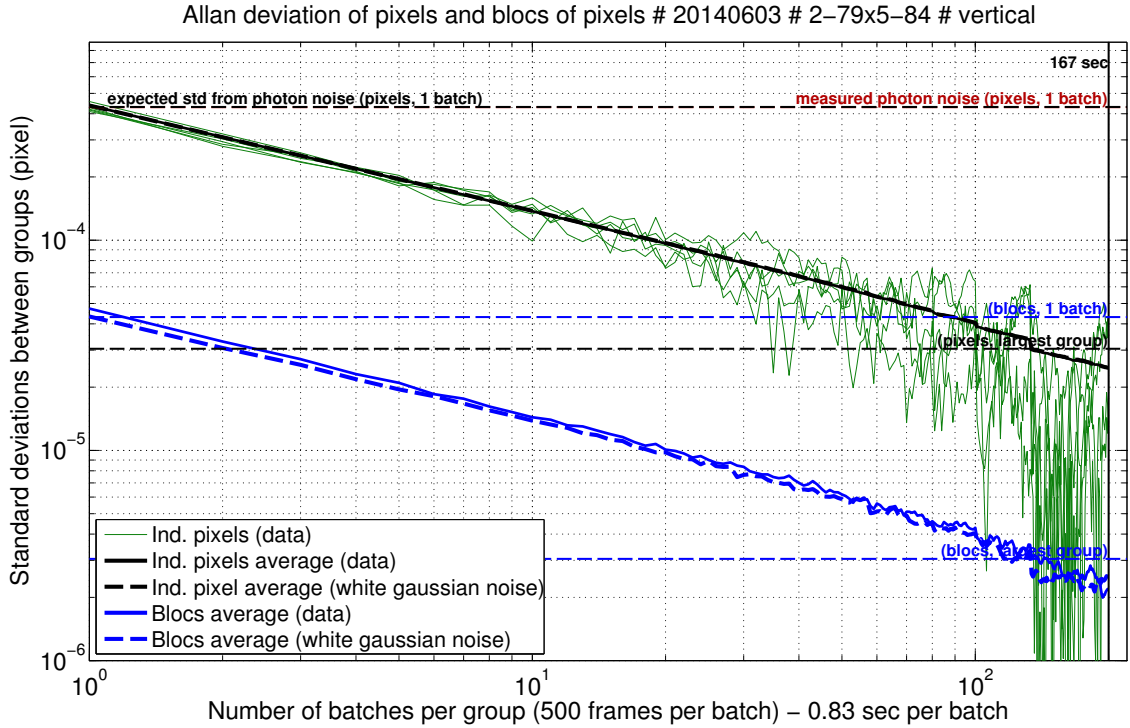


Figure IV.10: **Allan deviations of simulated data.** The amplitude, visibility and photon noise of simulated fringes are adjusted to values typical of real experiment ($B = 10000$ counts, $A = 6000$ counts, 1 count = 10 photons). Additional sources of noise are simulated, such as laser intensity (1×10^{-2} RSD), fringe phase (1×10^{-2} radian SD) and pixel QE (1×10^{-5} RSD). The plot shows deviations for individuals pixels (plain red), their average deviation (plain black) and the average for blocks of 10 by 10 pixels in (plain blue). The dotted black and blue curves are for a cube of white noise whose standard deviation is matched to the data for groups of 1 batch. Averaging Allan deviations over pixels or blocks is important because they tend to be noisy (plain red) when the final deviation is derived from very few groups. Horizontal dotted blue and black lines are various estimations of the photon limit.

theoretical photon noise, the red one is for measured photon noise using the first frame of the data cube. No red noises or read noise was included in the model. In the real experiment the read noise is negligible compared to photon noise.

Figure IV.11 shows maps of the difference between the measured pixel offsets and the true solution (pixel offset simulation input) for different values of pixel QE RSD. This is the ultimate metric to check the accuracy of the result, because biases constant in time are not visible in the Allan deviation. For low pixel QE RSD ($< 1 \times 10^{-5}$), the standard deviation of 2×10^{-5} seen in Fig. IV.11 is coherent with the value given by Allan deviation (i.e. the photon noise floor). However, tests with higher values of pixel QE RSD show residual spatial bias above photon noise floor, while the Allan deviation is unaffected. This is an eventual point to improve, but a good pre-flat calibration of the actual metrology data can in principle take care of this problem.

In conclusion, although a small bias could persist if the metrology data is not properly flat calibrated (ideally to an accuracy of 1×10^{-5}), the Allan deviations are not affected and are a good way to control for the presence of correlated noise. The comparison between simulations and actual data will give us clues about what kind of noises are present in the data.

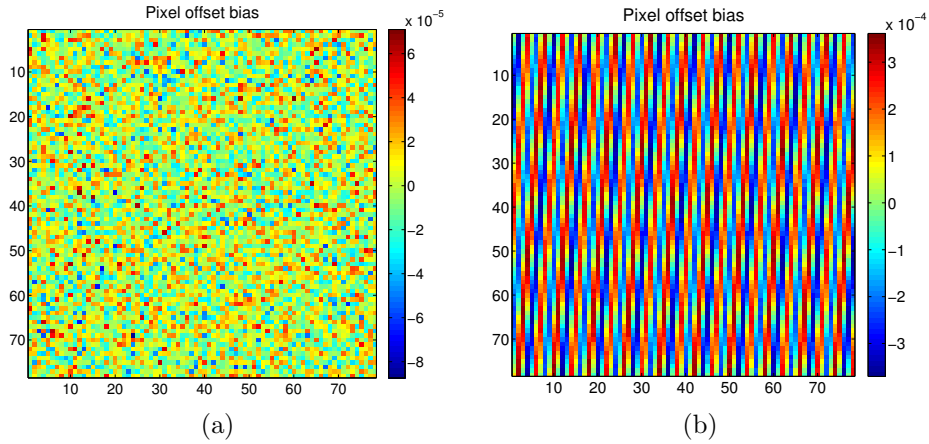


Figure IV.11: **Pixel offsets bias for different pixel QE RSD.** The maps show the difference between the pixel offsets found after reduction and the solution of the simulation, for pixel QE RSD of 1×10^{-5} (a), and 1×10^{-2} (b). The residuals for (a) are in agreement with the photon noise floor, while a systematic bias of a few 1×10^{-4} pixels is visible for (b). Both have same photon noise.

3.2 Pseudo stars

□ Data generation

In the pseudo star model, we approximate PSF with Gaussian functions whose width is roughly equivalent to an Airy spot at the average wavelength for our experiment (about 600 nm). The reason for using a Gaussian instead of a more complex PSF shape, such as a polychromatic sum of Airy function or a PSF derived from the data is simplicity and efficiency. The goal is to estimate the relations between the uncertainties on various parameters (pixel sensitivities, pixel offsets, ghost centroids) and the centroiding accuracy. We want to have at least a rough estimation (within a factor of two or better) of the impact of all the parameters, in order to rank them and connect the accuracy of different types of calibration and the final errors on the centroids. This effectively tells us what error sources will dominate and should be addressed in priority, this is an important step toward a complete error budget. This model also makes use of the CCD model: in order to generate the pixel value, the product between oversampled Gaussian centroids and a simulated CCD is calculated for each pixel.

□ Results

The result from the simulations are used in two different ways. The first goal is to validate the reduction process itself, as capable of reaching 1×10^{-6} pixel in ideal conditions. We have validated the accuracy in ideal conditions for both centroiding techniques (Gaussian and autocorrelation). Of course validation of Gaussian fitting on Gaussian data does not tell much of the performances on real data, it is nothing more than an advanced debugging method. The accuracy of a Gaussian fit on a real centroid is about a few mili-pixels, but it is still very useful. We will actually use Gaussian fits on real time data to monitor the position of the translation stage and reposition the CCD at an accuracy of 1% of the pixel for future tests.

The second goal is to explore what are the impact of different types of noise by

Table IV.2: Results from pseudo stars model. The error on pseudo stars measured locations is always in pixel units.

Error type	Error normalization / definition	Error on centroid
Pixel sensitivity: σ_{QE}	average pixel sensitivity = 1	$0.5 \sigma_{\text{QE}}$
Photon noise: σ_{ph}	relative photon noise calculated for the pixel with the highest value	$0.75 \sigma_{\text{ph}}$
Pixel offset: σ_{offset}	offset expressed in pixel units	$0.15 \sigma_{\text{offset}}$
Pixel read noise: σ_{read}	relative read noise calculated for the pixel with the highest value	$1.1 \sigma_{\text{read}}$
Ghost centroids: σ_{ghost}	ghost intensity relative to the main centroid, ghost located randomly within 2 pixels of the star center	$1.2 \sigma_{\text{ghost}}$

injecting them one at a time into the simulated data, in Monte Carlo simulations. Because we use Gaussian PSFs, in these simulations we can directly compare the input centroid locations with the fit results, thus relying on absolute positions (as opposed to distances) and we can also skip the Procrustes analysis. We have used the model to estimate the relations between the uncertainties on various parameters (pixel sensitivities, pixel offsets, ghost centroids) and the centroiding accuracy, the results are summarized in Table IV.2.

Another useful aspect of these Monte Carlo simulations is the estimation of the proportion of random star position error that is absorbed by the Procrustes supersimposition. Among 10 observables, we allow for a fit with 5 degrees of freedom (2 translation, 2 scaling, 1 rotation), which will inevitably lead us to underestimate the final noise. Simulations have showed that Procrustes supersimposition only decrease the error by about 20%. When we express the final accuracy after the Procrustes supersimposition we correct the estimation for this factor.

We can draw interesting conclusions from these relations. In order to reach an error of 5×10^{-6} on the centroid, one only needs to calibrate the pixels positions to about 3×10^{-5} and the accuracy of the flat field has to be better than 1×10^{-5} . The experience is very sensitive to the presence of a ghost centroid near the real one: its intensity must be lower than 4×10^{-6} times the main centroid intensity.

Chapter V

NEAT lab demo: results and conclusions

During the progression of the experiment, we had a lot of discussion with JPL where a similar experiment (VESTA) was carried out and we exchanged data (both ways). To validate the data processing and to better understand the nature of the errors, we have compared the result of our analysis with theirs on some of their data. The complete analysis of JPL data began only a few weeks ago and is at a preliminary stage. The data has some differences, like having only two centroids instead of 5, some adaptations of the processing are required.

We did not get feedback about the result they have obtained with our data yet. However, we have completed a equivalent analysis of their data set. The final accuracy is not in complete agreement, in particular after the last part of their analysis which consisted in making groups of positions. They have moved the centroids by increments of a fraction of a pixel only: in the final analysis, the 30 positions are arranged into 3 groups of 10 (group are made on the basis of proximity). The result are nevertheless already very interesting, they are presented presented in appendix B. This will avoid confusion with data from our own experiment.

1 Result on actual data

Before presenting the results, I must explain why the analysis may seem incomplete, in particular the metrology. There are major hardware issues that remain to be solved. Nearly all the elements needed to solve the problems have been supplied and the bench is being upgraded so there is no need to try to work around the problems. Here is the list of issues that are being solved:

- One of the CCD quadrants showed an anomalous behavior, with a standard deviation on the pixel offsets up to 10 times higher than the rest of the CCD. The cause of this behavior is uncertain, however the problem disappeared when the chip was swapped with another one. Unfortunately a quadrant of the new chip died very quickly, we had to put the previous chip back without a complete set of data in vacuum to work with. The third (and last) copy of the chip has been transferred from CEA to IPAG and will be installed soon. Until then, to mitigate the issue we have restricted the Allan deviation analysis to parts of

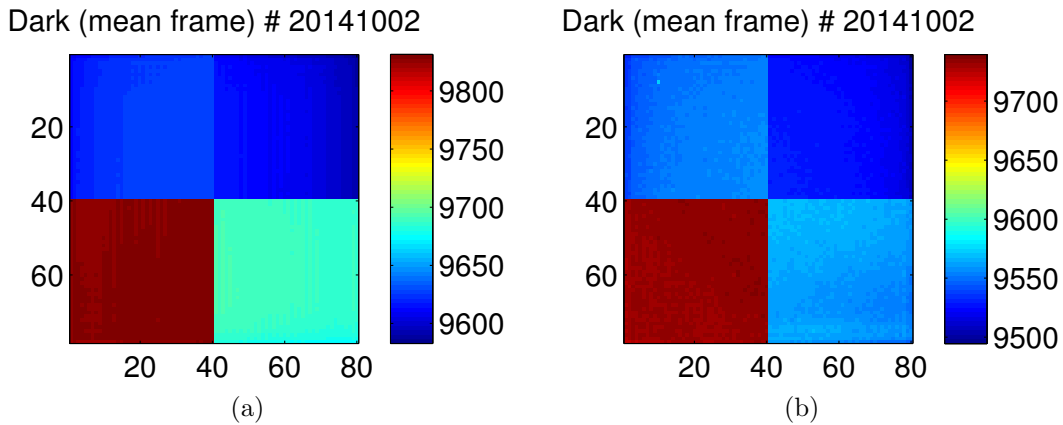


Figure V.1: **Mean dark frames at 100 Hz at 17°C (left) and -10°C (right).** The darks have each 3000 frames, the theoretical SD of the pixel values are 0.1 count (the final error is dominated by the quantification).

the CCD unaffected by the problem. However, when calculating all the pixel offsets (we need the complete map for centroid corrections), there is a concern that errors from the bad quadrant can propagate into other quadrants.

- The metrology fiber tips have been damaged. A new system is being installed. When the data presented here was taken, only two baselines (one vertical, one horizontal) were available. The horizontal baseline is with the new system, the vertical baseline is with the old one. We can look for differences in the quality of the data between the vertical and the horizontal direction with Allan deviations, but we can not compare pixel maps obtained with different sets of baselines.

1.1 Dark and flat fields

1.1.1 Darks

Figure V.1 shows typical dark frames at 17 and -10°C. To illustrate the readout noise instability issue (refer to section 6.6.4 for a detailed description of the issue), Fig. V.2 shows two darks taken in identical conditions. When an instability appears, the high noise is usually restricted to one quadrant and the noise level is fairly variable for different pixels within this quadrant. The stability of the dark over long time scales (a minute) is good in the sense that the SD is not higher than the readout noise. This is equivalent to say that there is no drift.

1.1.2 Flat fields

Our setup for flat fields consists of two multimode fibers of respective diameters of 200 and 360 μm attached to the mirror and pointing in the direction of the detector. The light source is a broadband high power LED (400 to 700 nm), plugged to either one of the fibers (fiber swapping is manual). The duration of the flat fields is adapted to reach roughly the same photon noise with either fiber: it has to be longer with the smaller fiber. In practice we obtain relative photon noises of less than 2×10^{-5} for integration times of 360 and 180 seconds (on respectively 200 and 360 μm fibers).

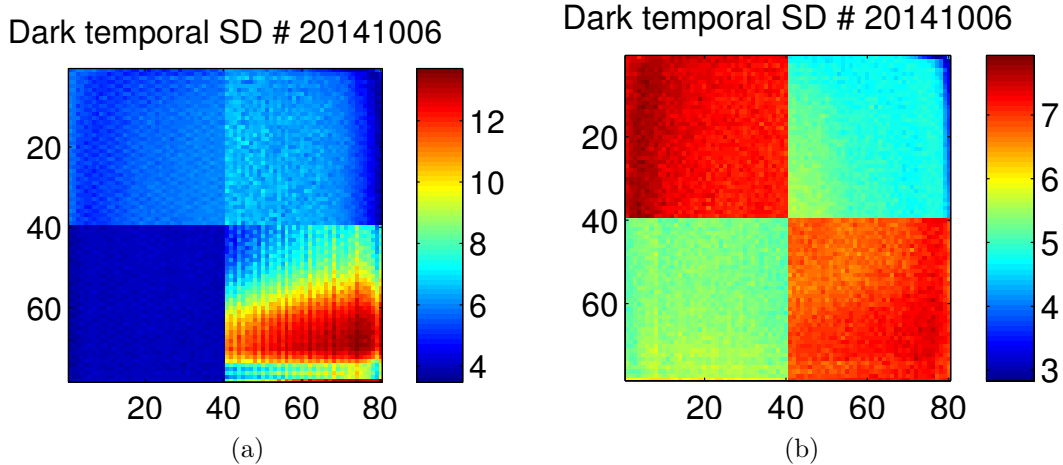


Figure V.2: **Temporal noise in dark data cubes.** The cubes have been taken in identical conditions: -10°C , 100 Hz framerate, 30 seconds of acquisition (about 3000 frames in total).

Simulations have showed that the relative errors on pixel QEs has to be less than 1×10^{-5} to reach the ultimate accuracy goal on the centroids. With a relative photon noise of 2×10^{-5} , we can in principle get very close to the ultimate requirement (in the best case). But we have to also quantify the systematics errors, and we will see that in practice they are a slightly higher than the photon noise. To estimate the quality of the flat field, we use several comparison techniques. First, by comparing two flat fields taken in the exact same conditions (one after the other), we expect to see the photon noise, provided that the setup is stable enough. We can also estimate the photon noise directly from one flat field because we know the acquisition parameters (number of frames, number of photons per frame), so we can check that the two are consistent. Secondly, some systematics can be estimated by using fibers located at different places on the mirror, moving them or by translating the CCD between two flats.

If stray light is generated by the baffle or other elements within the vacuum chamber, moving the CCD or the fibers will change the stray light intensity distribution. When moving the fibers, we are also sensitive to systematics caused by the fiber themselves, their tips and their orientation, such as differences in illumination gradient or speckles. Speckles can indeed appear for multimode fibers, even in white light (they will be strongly attenuated). To investigate the effect of speckles, we can simply move the part of the fiber which is located outside of the vacuum chamber (between the source and the vacuum plug) between two flat fields, or scramble it during the acquisition.

Figure V.3 shows the raw images that were obtained using the 200 μm and 360 μm fibers located on the mirror (step 1). Figure V.4 shows the flat fields at step 2 (after quadrant normalization). Figure V.5 shows the flat fields at step 3 (after low pass filter normalization). Figure V.6 shows the final flat fields taking account the quadrant gains. Figures V.7(a), V.7(b), V.8(a) and V.9(a) shows the difference between 200 μm / 360 μm flats for respectively: raw flat images, after step 2, after step 3 and after step 4. All these flats come from the same data set (30/09/2014) and were taken in the same conditions (100 Hz, 17°C).

The first flat difference on Fig. V.7(a) is affected by various systematics at the

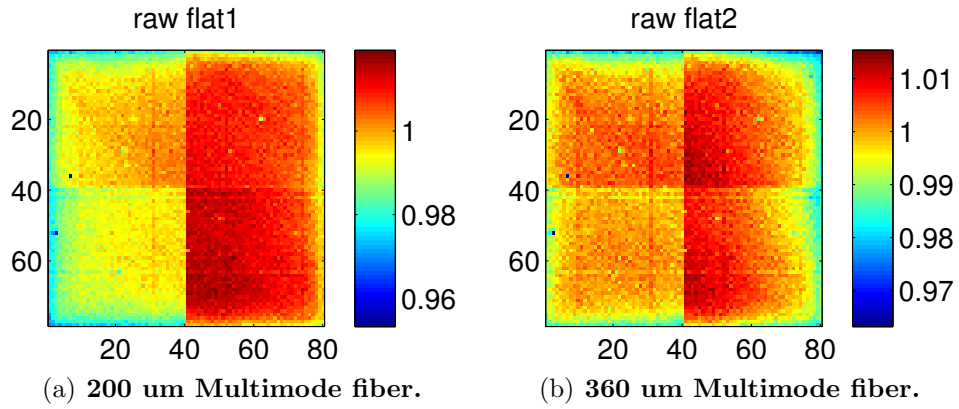


Figure V.3: Raw flat fields.

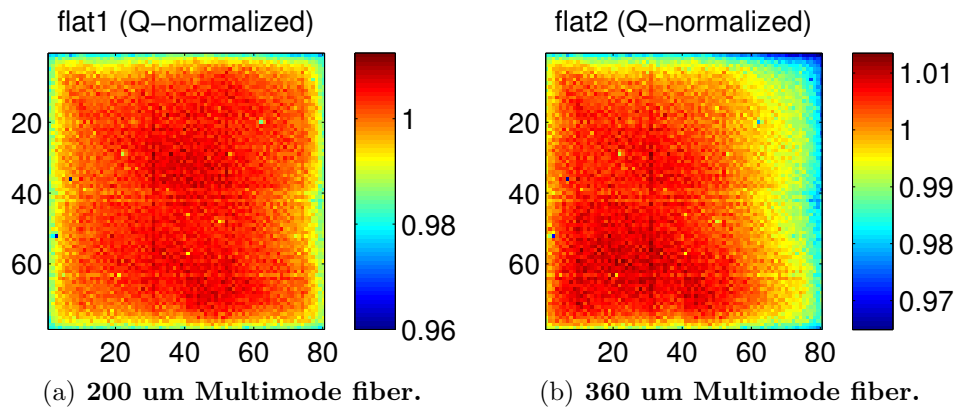


Figure V.4: Quadrant normalized flat fields.

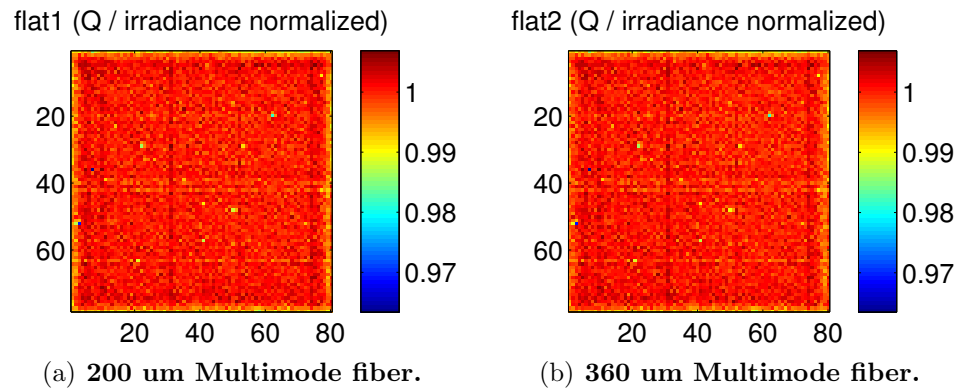


Figure V.5: Quadrant / irradiance normalized flat fields.

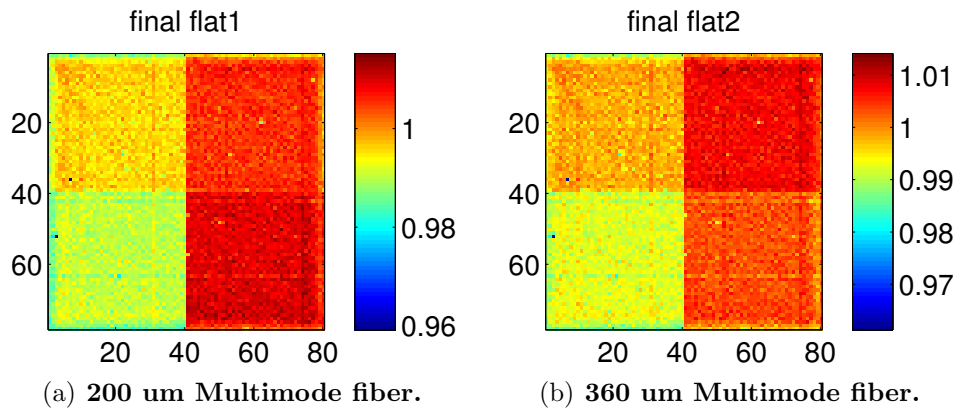


Figure V.6: Final flat fields.

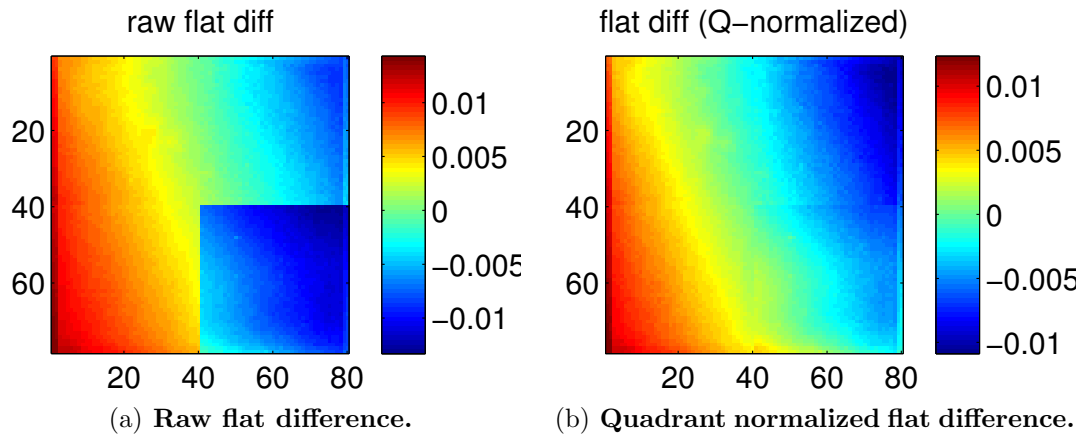


Figure V.7: Raw and quadrant normalized flat fields differences.

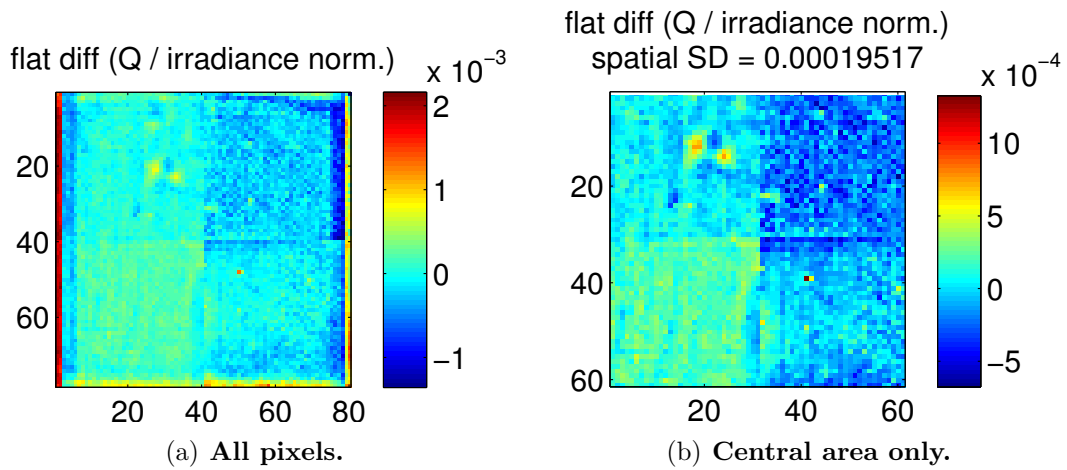


Figure V.8: Quadrant / irradiance normalized flat field difference.

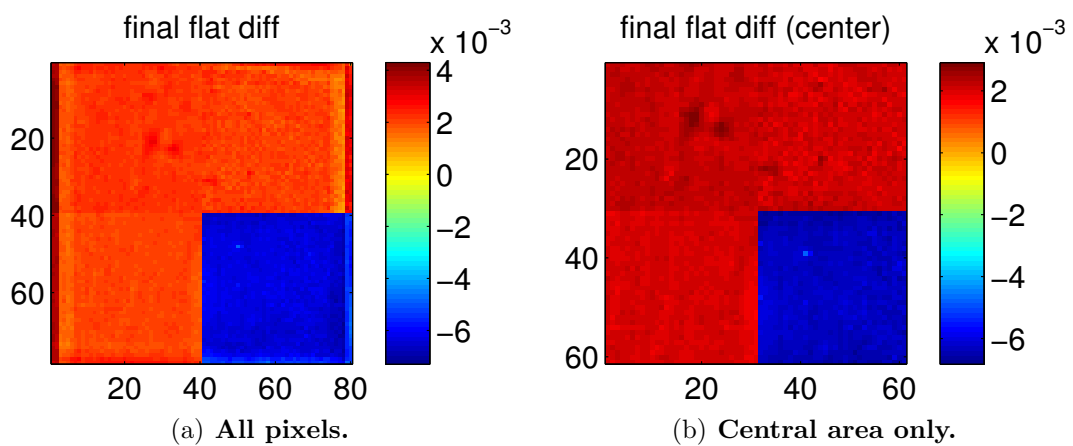


Figure V.9: Final flat field difference.

same time (gradient and the quadrant differences are visible). After correction for quadrant gains (Fig. V.7(b)), the dominant effect becomes the gradient difference between the two fibers. Once the irradiance ($\text{W}\cdot\text{m}^{-2}$) has been normalized, yet more subtle effects are visible. On Fig. V.8 systematic biases are visible at a level of a few parts per thousand. Weird systematics often appear near the edges of the CCD, so we often compare the flats over the central region of the CCD only, by cropping the outer 10 pixels on each side (Fig. V.8(b)). On the latter figure, we ideally want to see only photon noise left. If this is the case, it means what after corrections, the flat field is close to the photon limit, with the caveat that we have not introduced common distortions for both flats during the processing.

The final flat difference (Fig. V.9) is affected by quadrant gains instabilities which are not constant (relative to one another). This can be caused by thermal drifts of the readout electronic components which are located in an aluminum box outside of the vacuum chamber. The box temperature is not regulated. At the interface between quadrants, the relative pixel gains are only stable to about 1%. The consequences of this are the following:

- We will avoid putting centroid too close to quadrants edges. Error propagation indicates that if we do not do this we will introduce errors up to 5×10^{-3} pixel.
- We will still apply the final flat fields to the data. In case the fitting window for the stars slightly overlaps with another quadrant, this will keep the QE error near the fitting window edge to about 1%. This is important because we have to put centroids near quadrant edges to avoid ghosts (see section 1.3).
- When trying to estimate smaller systematics, we always correct for the quadrant gains. In practice we want to correct for both quadrant gains and irradiance, so we can either compare the flat field at step (3) of the processing, or use final flat fields (which are saved into files) and allow for a re-normalization of the quadrants before calculating the difference. We also use the central area only to get rid of the systematics near the CCD edges.

The series of flat fields we have presented in Fig. V.3 to V.9(a) was affected by a lot of systematics. It was chosen mainly because it illustrates very well what kinds of systematics are in the data, and why we need the processing to remove the largest effects (quadrant gains and gradient) to see them. On subsequent tests, we have done more tests and we have clearly identified at least one other source of systematic errors. Figure V.10 shows differences between flat fields obtained with the 360 μm fiber (central area), where the CCD was moved between the flats and with or without shielding the mirror.

When the CCD is moved we see negative/positive ghost pairs, corresponding to the ghost start and end positions. When the CCD is immobile and the mirror is shielded, we only see the positive part. From these tests we conclude that a ghost is produced by the mirror, by the conjugate reflection between the CCD and the pinhole mask. We initially planned for a shutter that would shield the mirror during metrology and flat field data acquisition to avoid this specific stray light reflection but the shutter was never installed because its motor was not functioning properly.

In another set of tests (all done with the same fiber, 360 μm core), we have tried to quantify eventual systematics caused by speckles (Fig. V.11). Scrambling seems to help and bending the fiber seems to have some effects, however the results are not

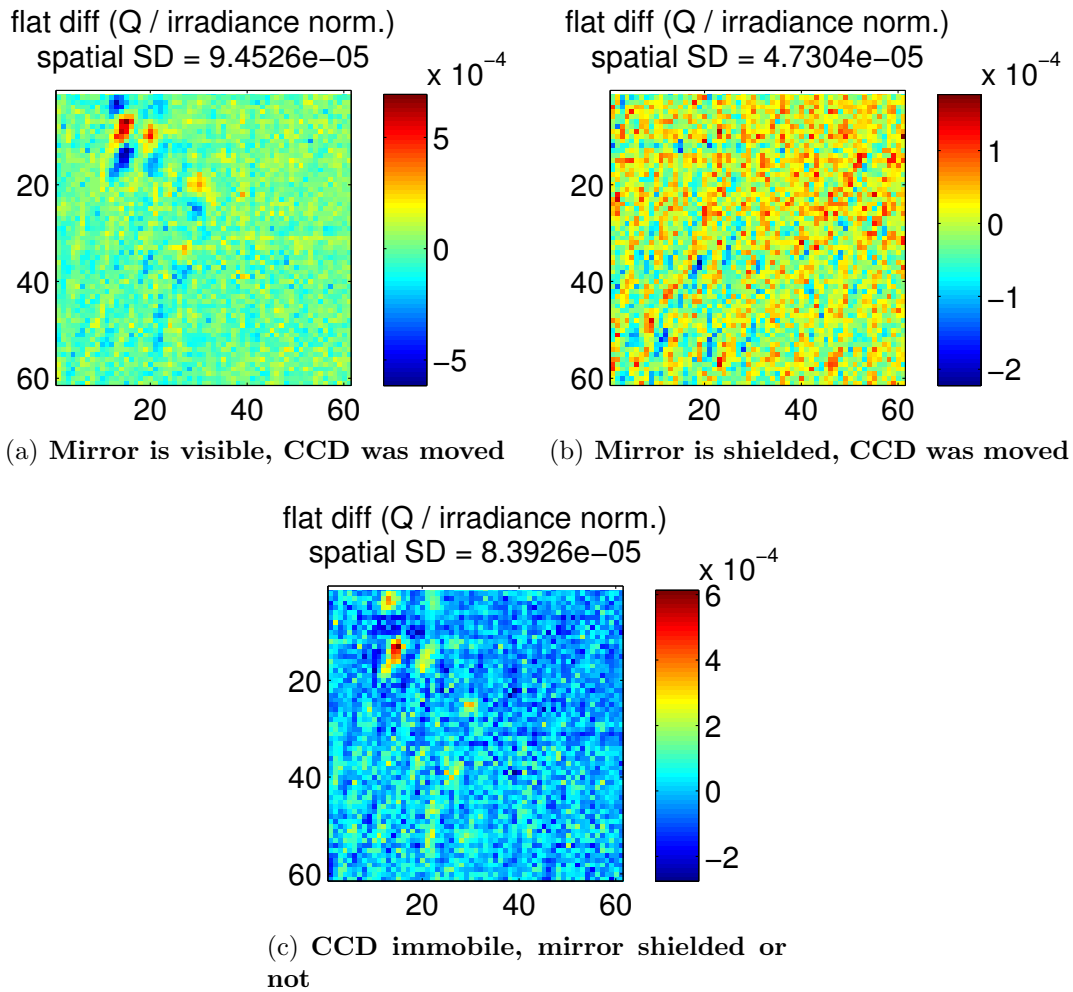


Figure V.10: **Flat field differences.** For differences (a) and (b), the CCD was moved by about 5 pixels between the two flats. (c) shows the difference between a “normal” setup and when the mirror was shielded by a black paper.

very conclusive and further analysis is needed. Figure V.11(b) shows slightly higher SD and PtV variations, but the PtV increase is caused by 4 pixels in a symmetrical layout with respect to the center of the CCD: the cause could be electronic.

Figure V.12 shows the flat field that has been used to process the pseudo star data. The SD of the pixels QE that affects the centroid measurements is given by Fig. V.12(a) as long as the centroids do not come too close to quadrant edges. The pixel QE RSD within quadrants is measured at 2.5×10^{-3} . The 6 factor rule is dangerous to apply here, the dust on the CCD produces outliers (extremely low values).

Stray light from the mirror or other sources could be responsible for the patterns visible on Fig. V.10(b), which is still a factor 3 above photon noise. For the error propagation analysis, we will retain the values of 2.5×10^{-3} for the pixel QE RSD and 5×10^{-5} for the accuracy of their measurement.

1.2 Metrology

Metrology calibrations have been done for a variety of operating conditions: in air (CCD temperature stabilized at 17°C) and in vacuum ($P < 0.5$ mbar, CCD

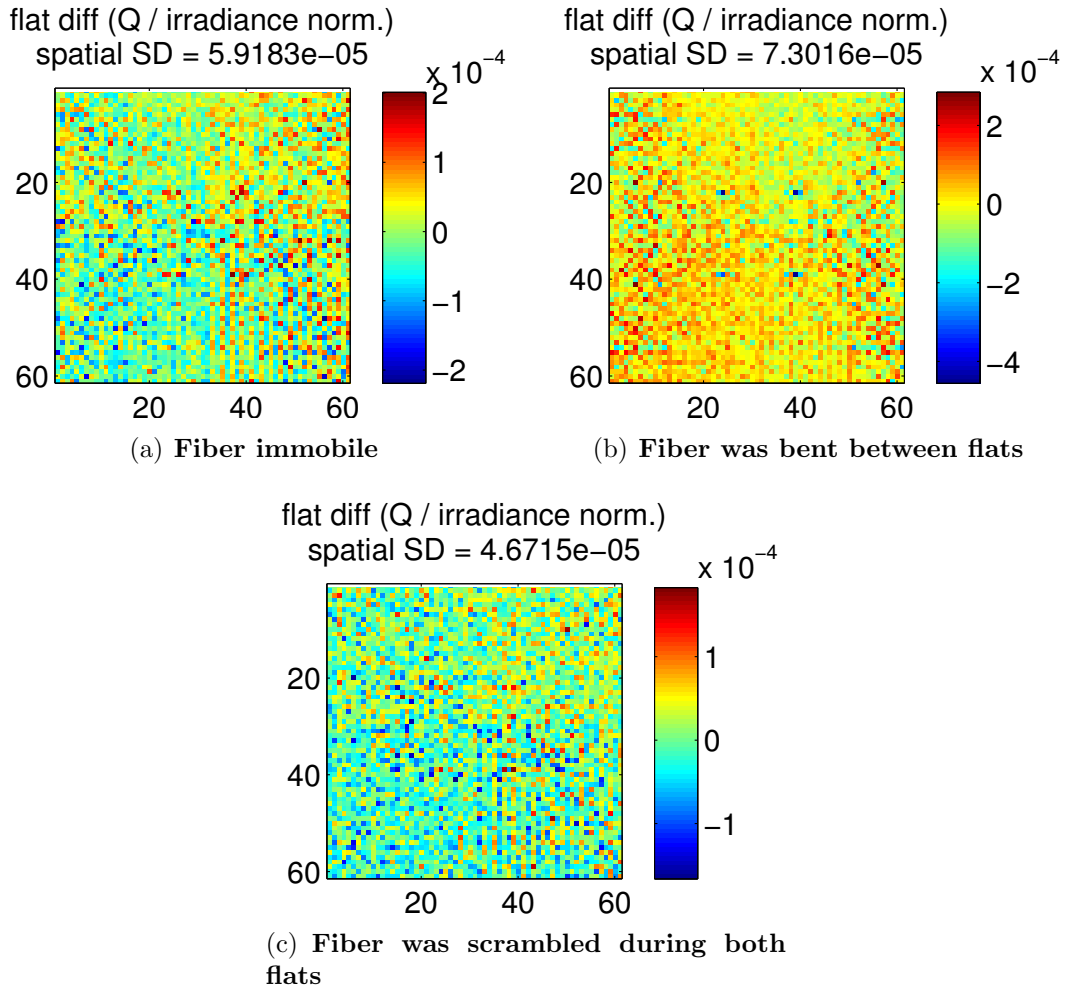


Figure V.11: **Flat field differences.** (a): two flat done successively in identical conditions. (b): the fiber (only the part outside the vacuum chamber was bent between the acquisitions. (c): the fiber was manually and continuously scrambled during both flats.

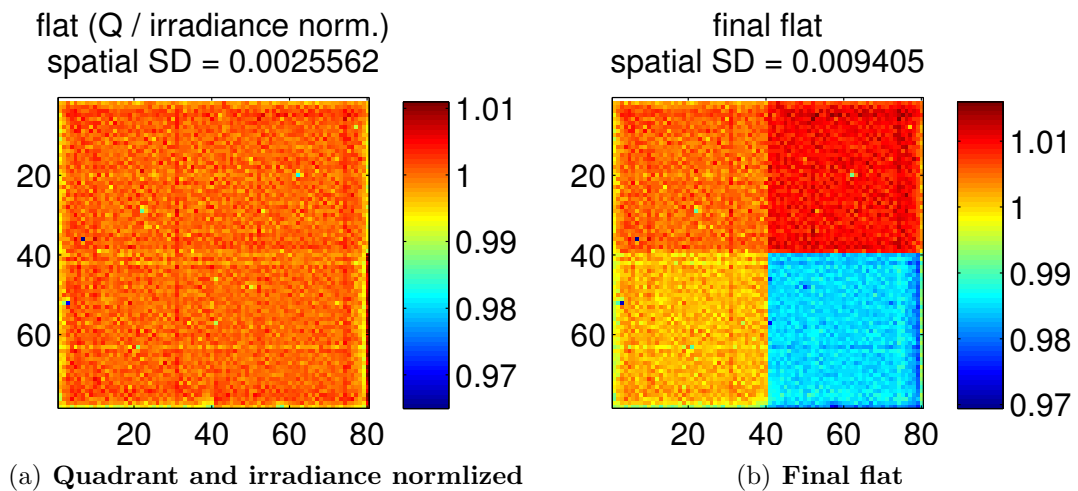


Figure V.12: Flat field used for the pseudo star data processing.

temperature stabilized at -10°C) for different metrology baselines. In air I have used different setups for stray light. For a complete characterization of the pixel offsets in each direction we need two non collinear baselines. It is best to have perpendicular baselines, in practice the baselines are nearly perpendicular, one is roughly vertical and the other roughly horizontal. Note that the terms designating the baselines (vertical/horizontal) corresponds to their physical alignment in the vacuum chamber. As the images of the data cube are displayed with a 90° rotation compared to the physical layout of the pixels, the vertical baseline corresponds to the vertical fringes and vice versa in the horizontal direction.

To avoid having too many plots, instead of showing the full Allan deviation curve, I will sometimes only mention numerical values which correspond to the measured noise for the largest group size (largest integration time). On the plot it corresponds to the end of the (black and blue) curves on the right side.

1.2.1 Allan deviation in air, 17°C , baffle v3, vertical baseline, one quadrant (upper left).

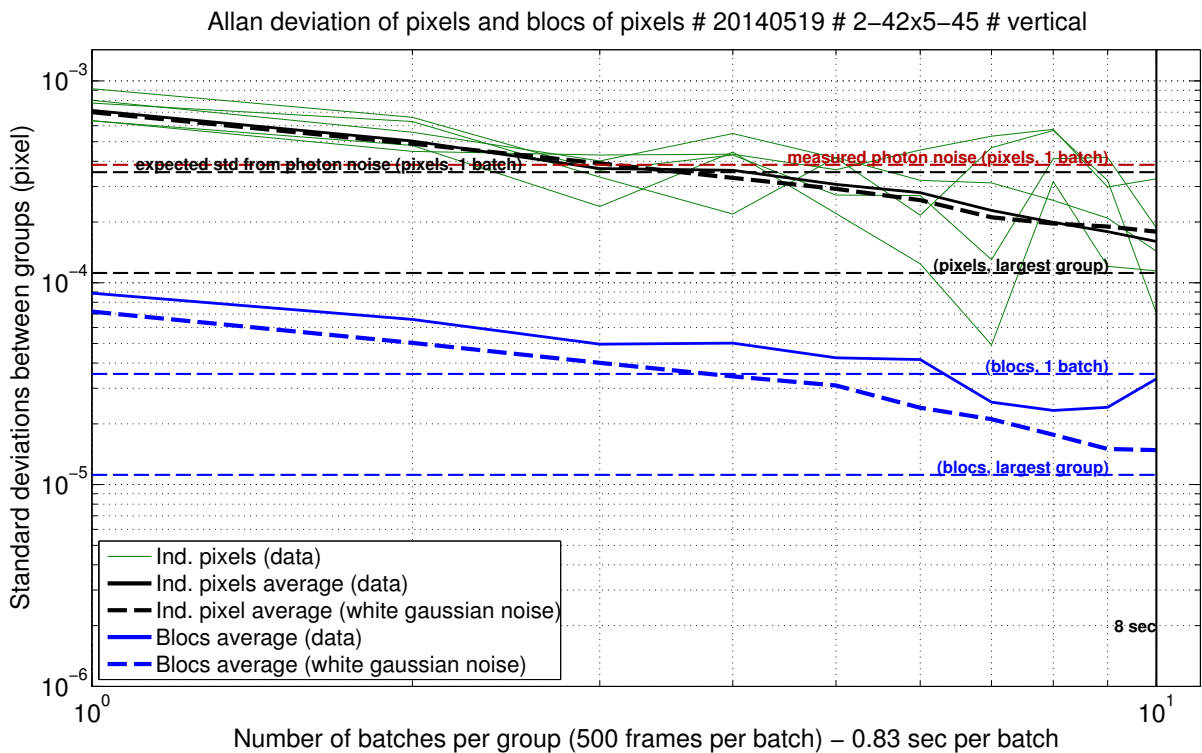


Figure V.13: Allan deviations of pixels and blocks of pixels.

Figure V.13 shows the Allan deviation obtained the 19/05/2014. This result was presented in the SPIE 2014 paper (it was the best measure obtained by then). Only one quadrant was used in this analysis to avoid having pixels from the “bad quadrant” in the data.

They are noticeable differences with the simulated data. Firstly the level of noise is higher than the expected photon noise limit by a factor 2.5. Secondly, the gain of spatial averaging (blocks of pixels) is slightly less the expected factor of 10. Thirdly, tests on larger data sets (up to 50000 frames) show degraded accuracy: the two

symptoms mentioned above worsen (worse spatial averaging, larger gap with theoretical photon noise) and the standard deviation does not fall as quickly. This indicates the presence of spatial and temporal red noise.

For this particular data set, we have also have looked at the impact of stray light on Allan deviations and found interesting results. A test without the baffle (all other things constant) yielded: Allan deviation of 3×10^{-4} for pixels (versus 2×10^{-4}) and 2×10^{-4} only for groups of pixels (with baffle 3×10^{-5}). Tests with a baffle made of paper sheets have shown similar result than with no baffle.

1.2.2 Allan deviation in vacuum, -10°C , baffle v4, vertical baseline, two quadrants (left).

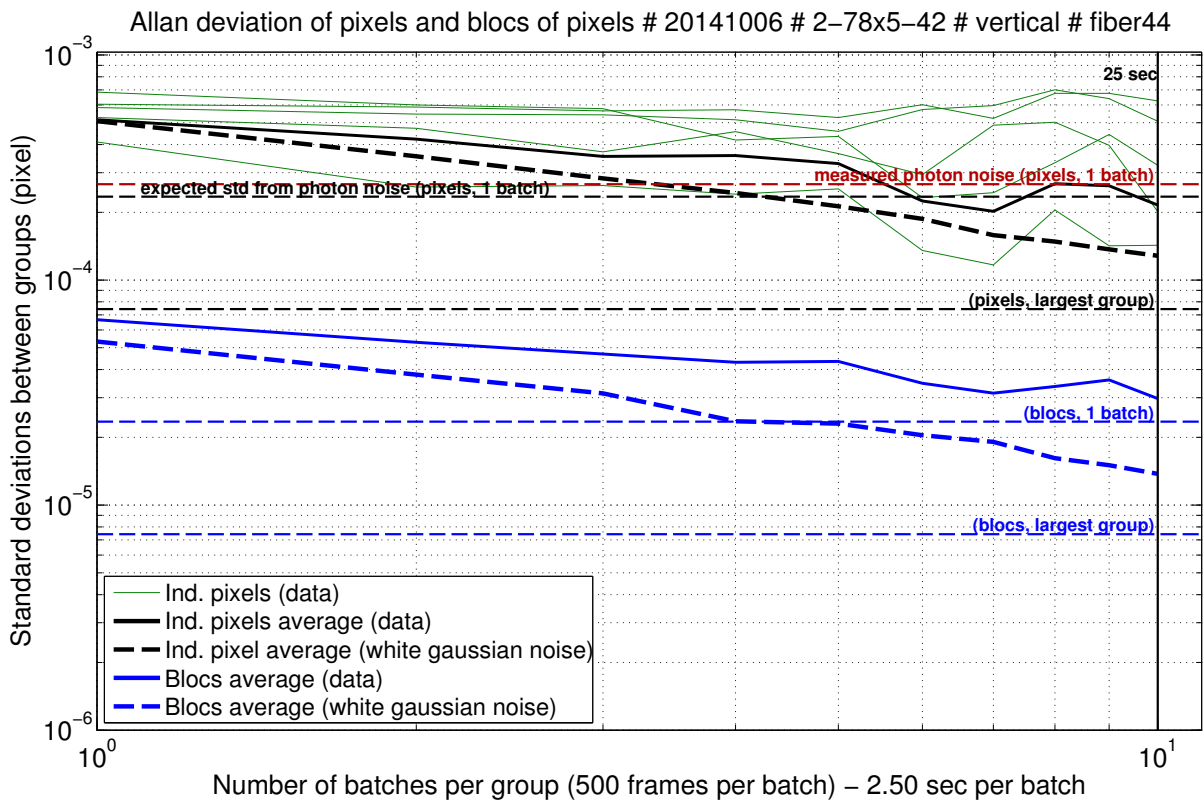


Figure V.14: Allan deviations of pixels and blocks of pixels.

Figure V.14 shows the Allan deviations obtained the 06/10/2014 on a vertical baseline. These results are nearly identical to the previous ones (photon noise higher than expected, accuracy gets worse with more frames).

1.2.3 Allan deviation in vacuum, -10°C , baffle v4, horizontal baseline, two quadrants (left).

Figure V.15 shows the Allan deviations obtained the 06/10/2014 on a horizontal baseline. The fiber holding system is different for these fibers, it was changed because the previous system had damaged fiber tips. With the new system, fibers are glued inside holes in an invar bar and the tips are polished. With the old system, fiber tips were put into Zerodur V-grooves located on the mirror. The new system is much

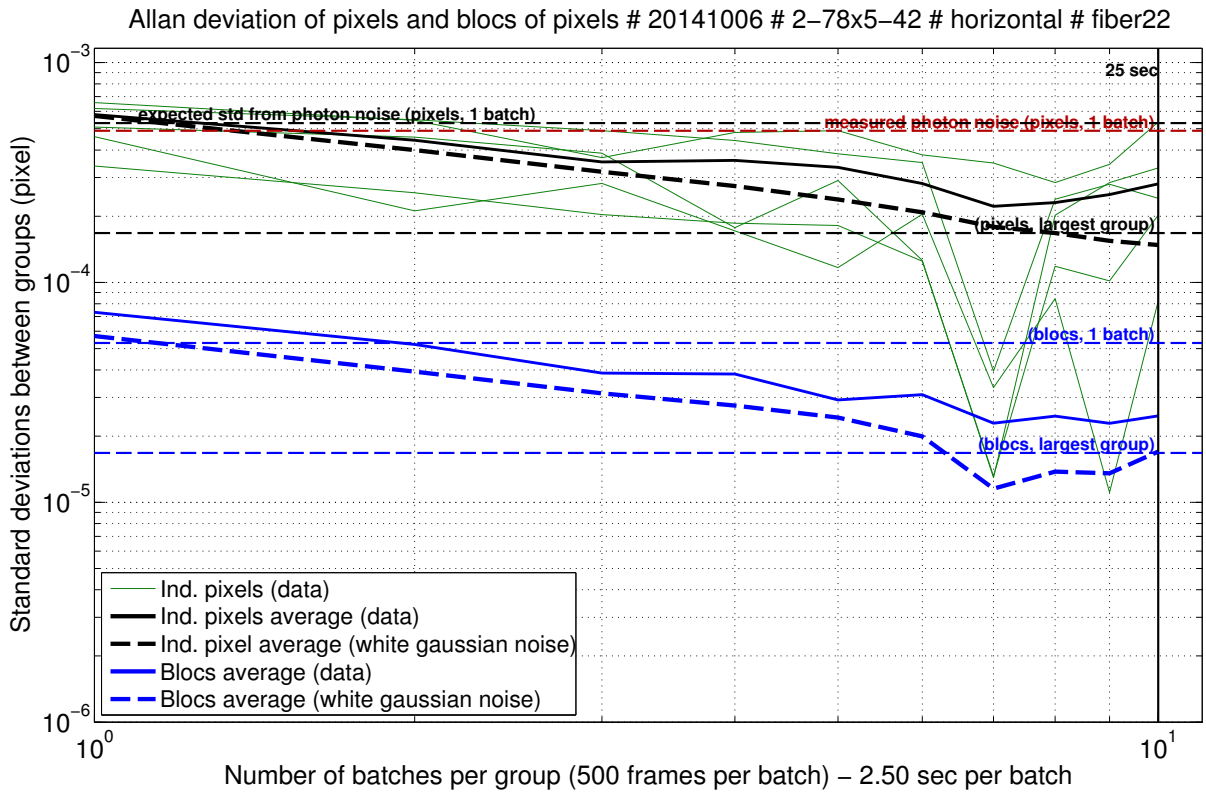


Figure V.15: Allan deviations of pixels and blocks of pixels.

easier to install and the tips are easier to clean. The results do not show significant differences with the vertical fibers.

1.2.4 Pixel offsets, -10°C, baffle v4, all quadrants

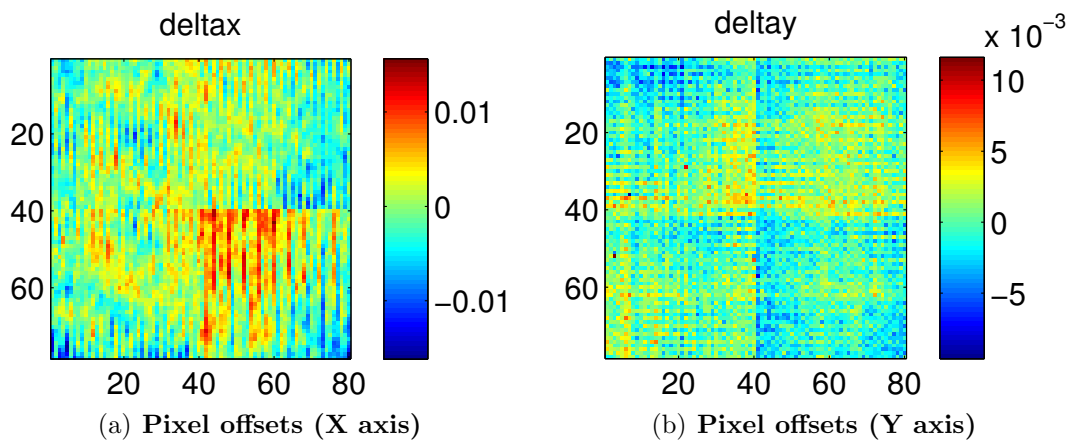


Figure V.16: Measured pixel offsets (with baselines “22” and “44”).

Figure V.16 shows the pixel offsets obtained with the 06/10/2014 data set, corresponding to the Allan deviations of Fig. V.14 and V.15.

To illustrate the stray light issue, Fig. V.17 shows the flat field difference between the normal flat (in white light) and another flat field derived from the metrology (fiber 04). The pixel offsets along the X axis show a pattern with a similar spatial scale than the the flat field difference and could be a result of stray light.

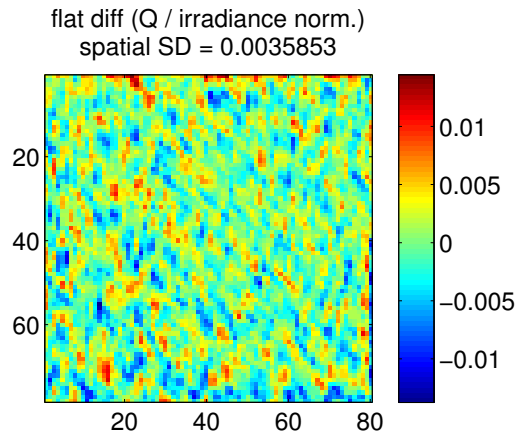


Figure V.17: **Flat difference between coherent and incoherent (white light).** Only one fiber is active to take the flat field in coherent light. The granular structure is thought to be caused by coherent stray light.

1.2.5 Conclusions

Having worse results with longer integration times is not a good sign at all, it suggests that there is a source of red noise in the data, other than the bad quadrants. This means that the real accuracy could be worse than what is indicated by the Allan deviation. We have investigated the effect of stray light: some improvement was seen when going from no baffle to the baffle (v3): the SD gain after spatial averaging was much closer to the expected than the factor 10. However for single pixels there is no improvement, and no improvement at all when improving the baffle (v3 to v4). There may be another factor other than stray light affecting the data.

It was initially planned to compare these result with the same map obtained with other baselines, but no other suitable baselines were available (horizontally or vertically) because of damaged fibers tip and connectors. This test would have allowed a more robust estimation of eventual biases in the pixel offsets measurement.

1.3 Pseudo stars

1.3.1 Ghosting issues

The first major issue that was identified in pseudo star data was the present of electronic ghosts. Figure V.18 shows an image that has been processed to make ghosts visible and overlaid with lines that highlight the ghost symmetries. They are created by a coupling between the quadrants of the CCD. The intensities of the ghost centroids relative to the real stars are at a level from 1 to 3×10^{-3} (depending on the quadrants). The ghosts can induce centroiding errors larger than 1 milipixel, so we must find a way to deal with them as we go to have any chance to have interesting results. We have found techniques to reduce their impact, but that strongly affects what we can do with the experiment. That is why we present the ghosts first.

Assuming that ghosts are faint replicas of the centroids, simulations on synthetic data have shown that ghosts can cause errors up to 1.2 times the relative ghost intensity (in pixel units, when the ghost is close to the centroid maximum). It is thus of vital importance to mitigate the impact of ghosts in order to reach accuracies

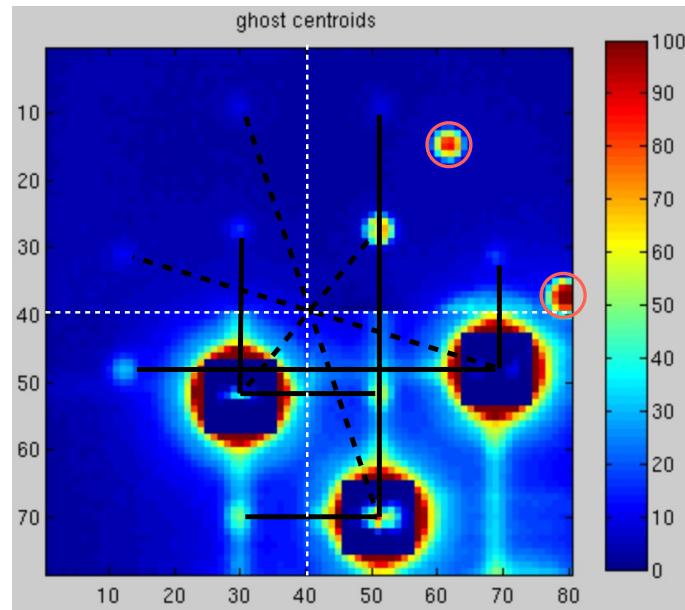


Figure V.18: **Image of the ghost centroids.** There are 3 main stars in the image. It has been processed: the fitting windows (11 by 11 for this test) are replaced by the residuals and the values below 0 and above 100 are truncated. The residuals inside the fitting windows are caused by the centroids motion (this image is extracted from a video). The two brightest ghosts (circled in pink) are defects in the pinhole mask, they are faint but real pseudo stars. They are however co moving the main stars and thus always stays outside of the fitting window. The problematic ghosts are the smaller ones, which are caused by coupling between quadrants during the CCD readout. Their symmetries with respect to the main stars are indicated by black lines (dotted for central symmetry, plain for reflection symmetry). The dotted white line indicates the limits between quadrants. These ghosts can cross the fitting windows when moving the CCD with the translation stage and bias the measurements. Some ghosts are rather faint, they might not be seen on black and white printed paper.

better than a few milipixels. One can think of two kinds of strategies to mitigate the problem: either getting rid of the ghosts or avoiding them (putting them as far away from the centroids as possible). In practice the ghosts have sometimes more complex and extended shapes, as shown by Fig. V.19 and Fig. V.20, which is a data set obtained when trying to calibrate the ghosts. A single centroid was moved to different places in an attempt to calibrate the ghosts: the hope was that the ghosts would be very stable within a quadrant and could easily be subtracted out, but it turned out not to be the case. Another set of data with 16 positions taken at -10°C has shown more stable ghosts, but still not constant within all the quadrant and with some halos. Also the cause of the improvement is not necessarily the temperature but could be linked to the readout noise instabilities instead. During a pseudo star measurement, there is no guaranty that wide ghosts can not appear.

(a) Getting rid of the ghosts

To eliminate the ghosts, we have tried to identify the cause of the problem. After consultation with an expert, we have suspected a resistive type of coupling to be responsible. Our main tentative to solve the issue has consisted in lowering the impedance of the ground wire of the chip. The “flex rigid”, i.e. the flexible cable

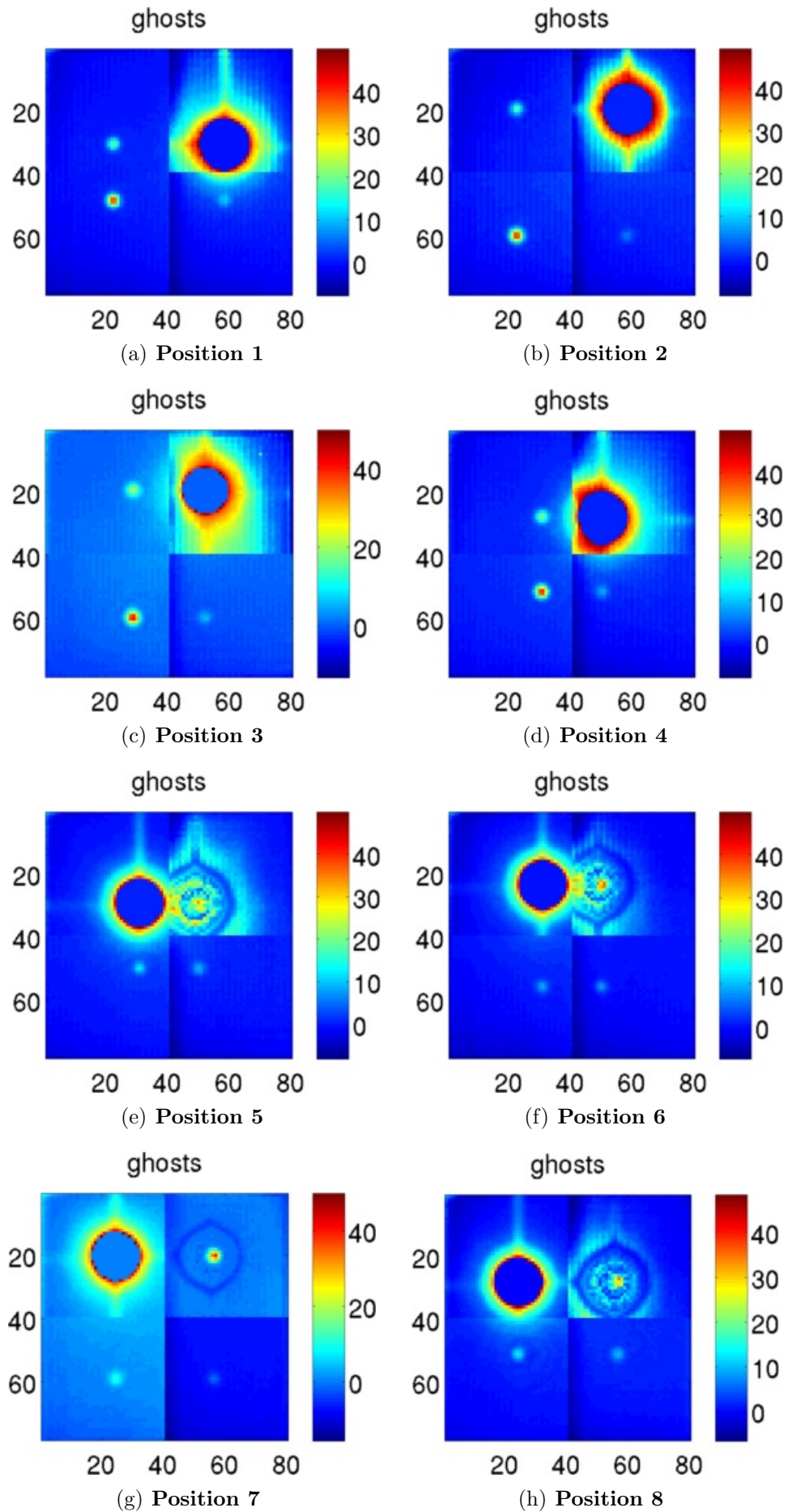


Figure V.19: Ghosts for one centroid at 8 different positions on the CCD (positions 1 to 8).

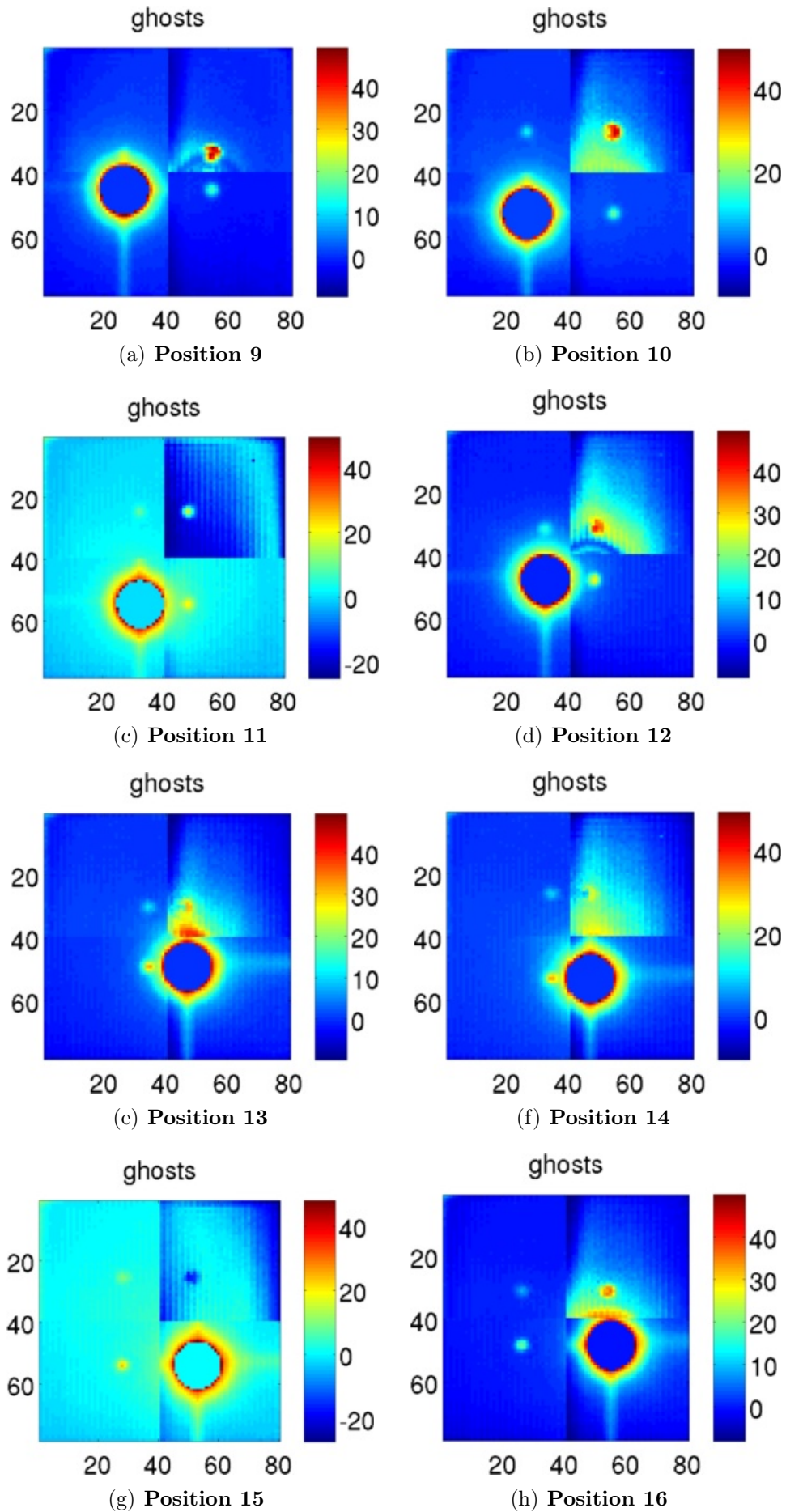


Figure V.20: Ghosts for one centroid at 8 different positions on the CCD (positions 9 to 16).

connecting the chip and the readout electronics (outside the vacuum chamber) was retro-fitted with a large and low-impedance ground connection. More precisely, the new connection was a copper adhesive tape manually welded to the chip mass pins. However the tests indicated no change of the ghosts intensities after the intervention.

Another idea was to tamper with the CCD voltage controls and see if it has any effect on the ghosts. In order to be able to do this in an interactive manner, a new advanced type of quicklook was developed and included in a new version of the labview acquisition/control program. This new utility allow a visualization of the ghosts in real time, by performing a quick processing. The processing consist in an offset for each quadrant that bring their background levels to the same value (using either a median pixel count value, or the maximums in the distributions of counts), and min/max thresholds for pixel counts values. Truncation of pixel values is essential to bring the dynamic of the image to values typical of ghost intensities. Simply displaying counts on a log scale is not as good because it still attributes a large part of the color scale to the central part of the centroids. The result of this test was that some values result in significantly lower ghost intensities (about a factor 5 for the brightest ghosts), but it also produces large noisy halos around some ghosts (like in Fig. V.19, positions 4 to 8). This makes the ghosts impossible to avoid while the relative intensity is still too high to completely ignore them.

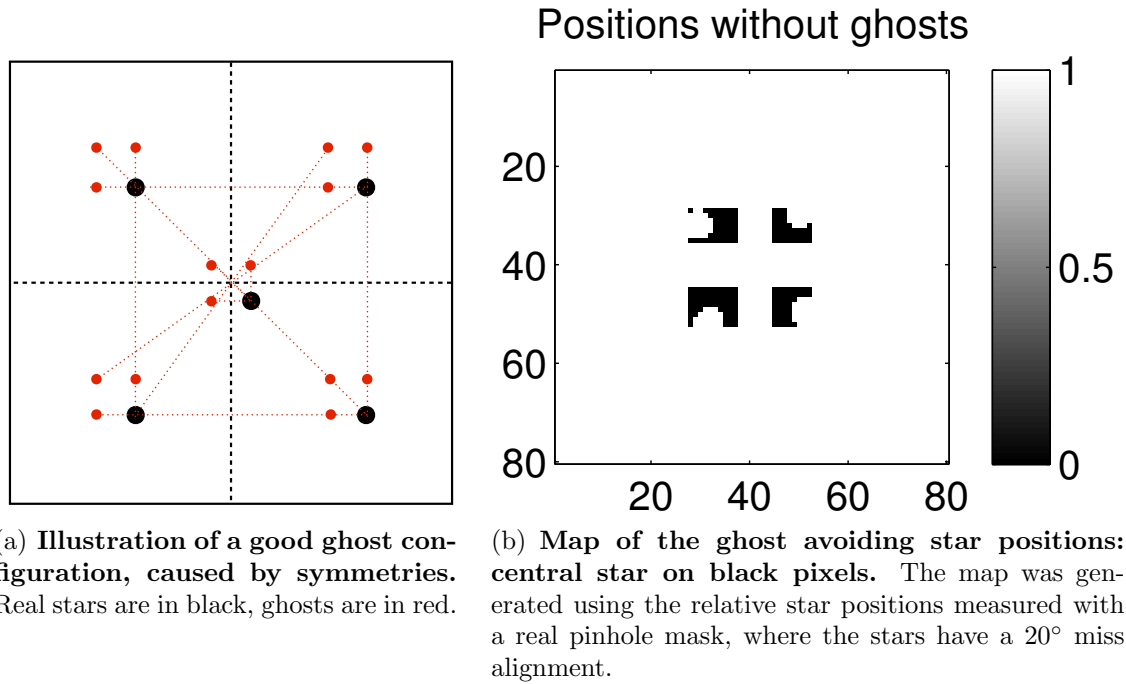
(b) Avoiding the ghosts

To avoid the ghosts, we restrict ourselves to a smaller set of positions. Because the distance between the outer stars is about 40 pixels (the width of one quadrant), avoiding ghosts for one star tends to make ghosts avoided for all stars, by symmetry of the configuration. This is illustrated by Fig. V.21(a): even though there are 15 ghosts and 5 stars on a 80x80 pixels, there are some positions for which no ghost is under a star. In a real configuration, stars are not perfectly aligned with the vertical/horizontal direction (this depends on the mask insertion). If the miss-alignment is too large, the number of available positions decrease. Figure V.21(b) shows a map of the correct pixels for the position of the central star. For all the black pixels, there is no ghost closer to 6 pixels of a star (condition on the euclidean distance between the centers of both ghosts and stars) or closer to 6 pixels from the edge of the CCD.

Thanks to the real time ghost visualization mode, at any time we can in principle check that all the ghosts are visible and not under a centroid, before even taking data. Unfortunately, the pinhole mask was damaged when trying to find a good alignment of the centroids. Multiple optical ghosts are crowding the field and preventing an easy identification of the electronic ones (Fig. V.22). New pinhole masks have been ordered and will solve this problem.

(c) Ghosts: course of action

An early test of centroid accuracy with centroids both CCD voltage controls (“normal” and “low ghosts” voltages), where the centroid where in avoiding ghosts positions did not show any difference any accuracy (accuracy of 1×10^{-3} pixel in both cases). From this test we have concluded that at this stage the ghosts were not the largest error factor.

Figure V.21: **How to avoid ghosts.**

For the time being, the course of action is to use the standard (and supposedly optimal) CCD voltage controls and to only use positions where the ghosts are known to be far from the centroids, as indicated by Fig. V.21(b). This produces ghosts with relative intensities of a few parts per thousand but which are most of the time without large halos. When the new pinhole masks will be available, a better control on the ghosts positions and shapes in real time will be possible.

1.3.2 Quasistatic and dynamic analysis of star positions (-10°C , in vacuum)

On real data, we perform both types of analysis for each setup (quasistatic and dynamic). Each setup produces a data set which consist of several data cubes (one per position of the translation stage). We typically use 2 to 12 different positions, depending on where we allow the centroid to be placed. Because the CCD is only 80 by 80 pixels with 4 quadrants, we have much fewer positions available if we want to avoid putting the central star at the limit between two quadrants or near ghosts and moving from one quadrant to another. The quasistatic analysis only need one data cube (one position) to work, for analysis we simply split the cube into batches. The data set that we present here has 12 positions, 3 on each quadrant. Figure V.23(a) shows where we have put the central star for the 12 measurements. The positions are approximative to about 1 pixel, the position control was done manually by looking at the image of the stars with the quick look utility. A visual fine tuning is needed because the translation stage has asymmetric motion speeds and directions and no position control indicator (open control loop). Figure V.23(b) is an image of the stars for one of the positions.

(a) Quasistatic analysis

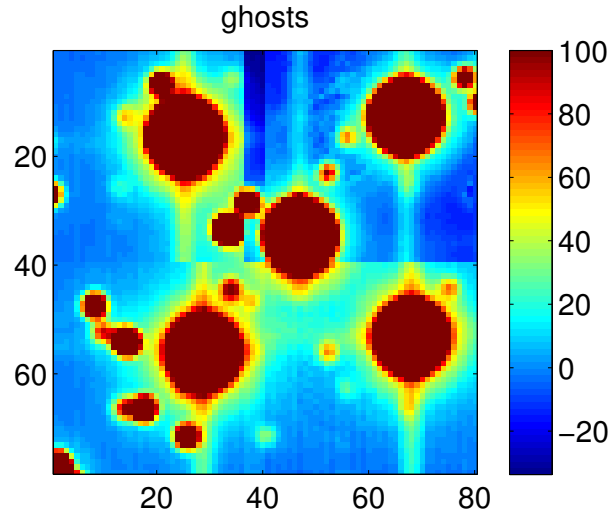
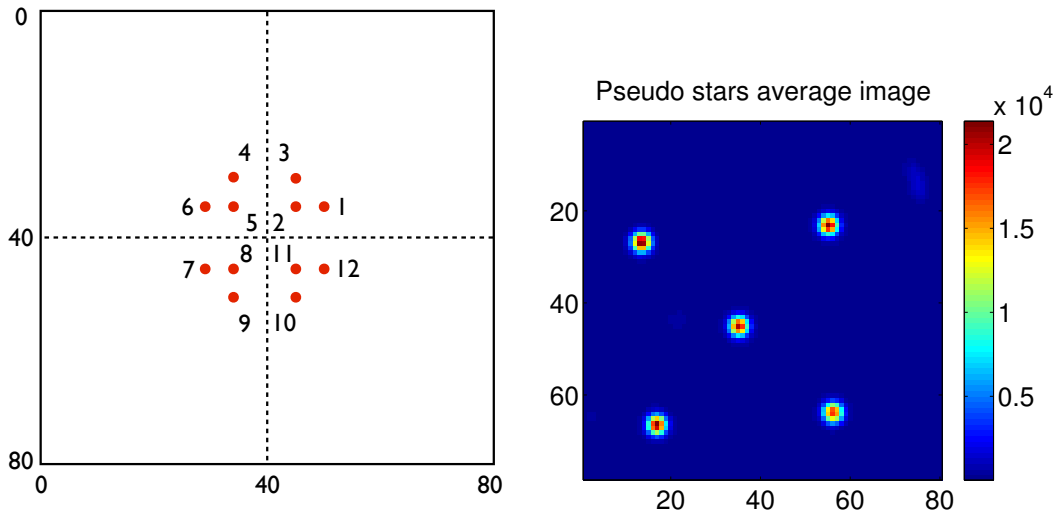


Figure V.22: **Optical ghosts caused by mask damage.** The peak value of the stars is at 20000 counts: the dynamic of the image is limited to 0-0.5%.



(a) The positions used for the differential star position analysis, numbered from 1 to 12.

(b) Images of stars for position 8.

Figure V.23: **Illustration of the pseudo star data set.**

For this analysis the CCD is not moved, the relative apparent motion is caused by vibrations and photon noise. There is an important rule of thumb to keep in mind, derived from the following facts:

- Mechanical stability tests have shown that the positions of star are stable to $\sigma_{\text{motion}} = 3 \times 10^{-3}$ pixels over 100 sec
- The dynamical analysis (next paragraph) shows that even without calibration (of pixels QEs or positions), the differential accuracy when moving over several pixels is better than $\sigma_{\text{centroid}} = 1 \times 10^{-3}$ pixel
- In order to have uncorrelated errors on the centroid, it has to be moved by several pixels

Thus, the differential errors between centroid location should be lower than: $\sigma_{\text{motion}} \times \sigma_{\text{centroid}} = 3 \times 10^{-6}$ pixels (we have taken a safety margin here by considering that errors can become independent for a motion as small as one pixel). This tells us

that the coupling between between pixellation errors (errors caused by pixel QE and offsets) and star oscillations should be lower than photon noise. At the end of the analysis, we expect to find a precision close to the photon noise. Such an outcome would confirm that the detector is well behaved and that the readout noise instabilities we have detected during the CCD characterization are not affecting the measurements.

Figure V.24 shows the variations of the relative positions of each star, each one with respect to the barycenter of all other stars (we call this “barycenter residuals”). Here a single data cube (position number 8) was split into 3 batches of 30000 frames each (1/3rd of the file). Figure V.25 shows the Procrustes residuals.

As the stars are mostly affected by photon noise, plus an eventual common offset between positions, we expect to see no difference in the amplitude of residuals after a simple barycenter and after Procrustes superimposition. We also expect to see amplitudes close to the photon noise limit, which in this case is 1.4×10^{-5} . For entire cubes (3 times larger), the theoretical photon noise limits is thus: 8.2×10^{-6} .

For position 8, the two values are coherent within error bars. This quasistatic analysis has been done on each one of the 12 datacubes/position. The measurements are summarized by table V.1.

Table V.1: Quasistatic residuals for barycenter and Procrustes (unit: 10^{-5} pixel).

Position	Barycenter res.	Procrustes res.
1	2.8	2.2
2	22	13
3	1.4	1.0
4	3.1	1.9
5	2.0	1.1
6	4.0	2.3
7	3.6	1.8
8	2.0	1.8
9	4.0	2.4
10	3.8	2.5
11	4.2	2.6
12	3.5	1.9

No difference between the two metrics (barycenter or Procrustes) was detected on simulated data: when introducing random centroid jitters and averaging over many positions, both metrics are consistent within a few %. On actual data, there are several interesting observations to be made:

- For most positions, the average Procrustes residuals are between 1.8 and 3×10^{-5} pixels, and the barycenter residuals are between 2 and 4×10^{-5} pixels. For most positions the barycenter residuals are larger than the Procrustes residuals by a factor 1.5 to 2.
- The two metrics tend to agree (within the error bars) only when the measured residuals are close to the photon noise (positions 3 and 8).
- Position 2 is an outlier, with an error about an order of magnitude larger than expected (barycenter: 2.19×10^{-4} pixel, Procrustes: 1.32×10^{-4} pixel).

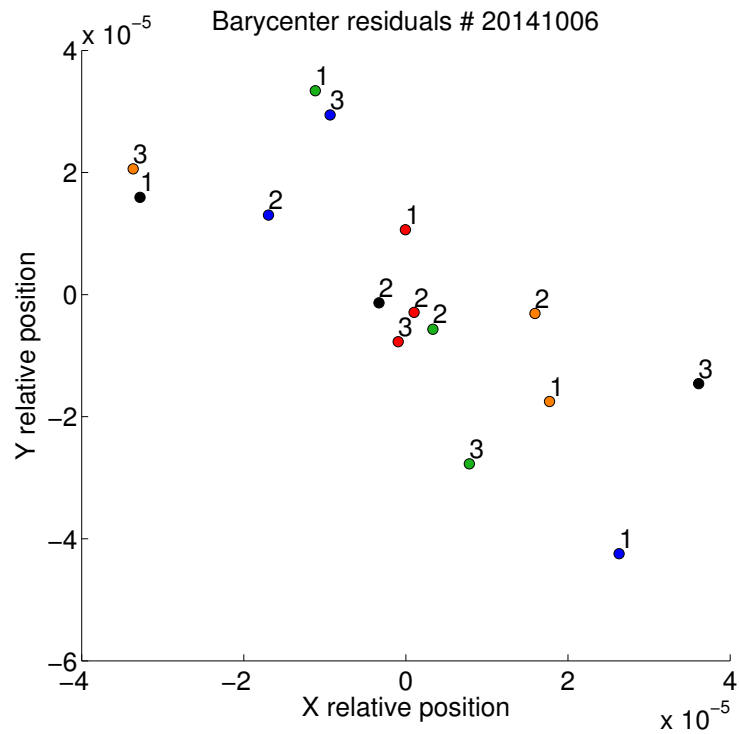


Figure V.24: **Differential motion of each star with respect to the barycenter of all other stars.** The average residual amplitude on this figure is 2.0×10^{-5} pixels.

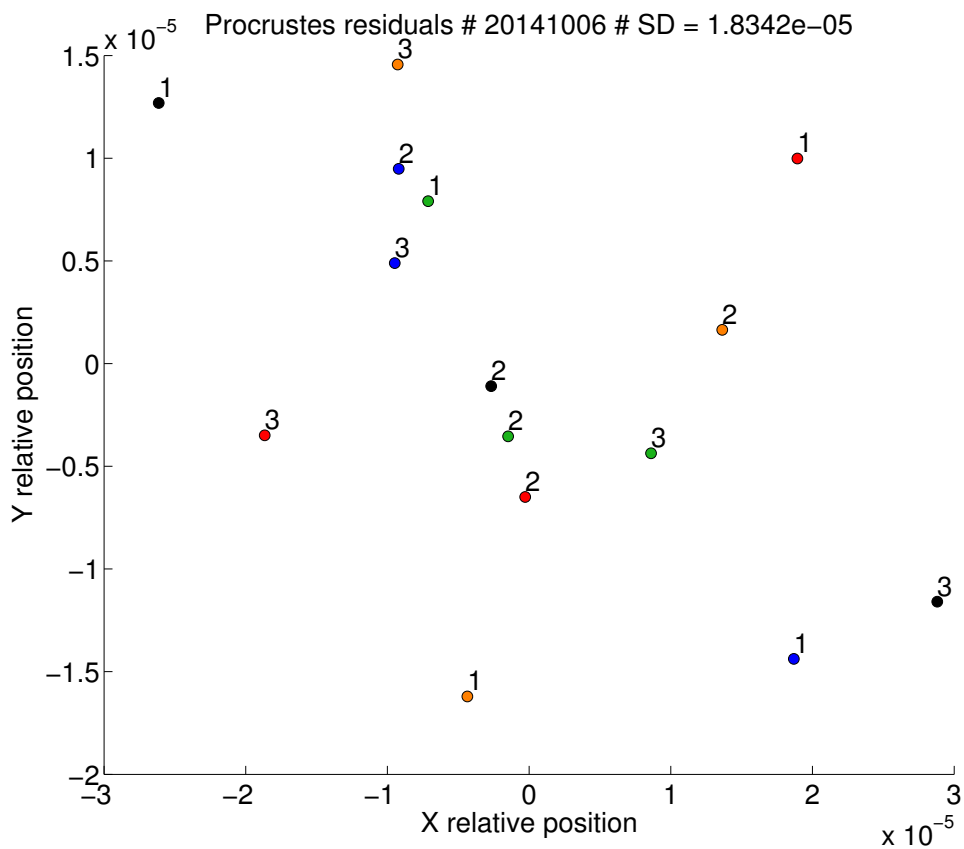


Figure V.25: **Procrustes residuals of the stars with respect to the mean configuration.** The value noted “SD” on the plot is calculated as the average residual amplitude, 1.8×10^{-5} on this figure.

We are unsure of the cause of this observations, it could be linked to an instability of the ghosts or an instability of the readout noise (even at 30 counts the readout noise must be non Gaussian to become significantly larger than photon noise).

(b) Dynamic analysis

For this analysis the stars are moved together by translation of the CCD of about 3 pixels between each position. Figure V.26 shows the Procrustes residuals of the central star, for all 12 positions (without flat field nor metrology calibration). The average residual distance, calculated over all centroids and positions is $1.8 \pm 0.14 \times 10^{-3}$. Figure V.27 shows the Procrustes residuals for all the stars for positions 7 to 9 (without flat field nor metrology calibration). In this case, the average residual distance, calculated over all centroids and positions is $3.6 \pm 0.59 \times 10^{-4}$. For the same positions, with flat field calibration, the accuracy is $2.8 \pm 0.45 \times 10^{-4}$ (Fig. V.28).

One can see that the for the central star (in black), the residuals of the 12 positions are clustering into 4 groups of 3 positions, which corresponds to the central star on the same quadrant. The position of the clusters are symmetric with the relative positions of the quadrants on which the central star was placed. It indicates that a systematic error is introduced when the central star goes from one quadrant to the next. A possible explanation is that there are larger or smaller than average gaps between the pixels at the quadrants limits. Gaps seem to appear in-between quadrants in the maps of measured pixels offsets (see Fig. V.16 in the metrology results).

The error bar on the magnitude of the Procrustes residuals is computed by assuming that the stars are affected by random Gaussian offsets: it takes into account the number of centroids and positions over which the averaged residual distance is obtained. It implicitly assumes that the errors are homogeneous over the CCD. The error is only meaningful as a lower bound, in practice the variation of the estimated accuracy is dominated by what kinds of systematics are introduced into the data, by quadrants and ghosts, which are not (spatially) homogeneous at all. The amplitude of the residuals depends on where the stars are.

The accuracy (estimated as the average amplitude of Procrustes residuals) was determined for each group of 3 positions for which the central star is always on the same quadrant. The best result was obtained for the positions 7, 8 and 9. The accuracies for each set of 3 positions (with flat field calibration only) are:

- Positions 1,2,3: $8.2 \pm 1.3 \times 10^{-4}$
- Positions 4,5,6: $4.0 \pm 0.63 \times 10^{-4}$
- Positions 7,8,9: $2.8 \pm 0.45 \times 10^{-4}$
- Positions 10,11,12: $1.2 \pm 0.19 \times 10^{-3}$

The magnitude of the changes are much larger than the expected random errors for a CCD with homogeneous spatial properties. The large differences are likely to be caused by ghosts positioning. We have used the set of positions 7,8,9 only to test whether the calibrations improve the accuracy. Table V.2 summarizes the results for all configurations (relative to the types of calibrations used).

The conclusion comes easily: the flat calibration improves the accuracy, whereas the metrology does not. It is not surprising given the fact that we have checked the flat

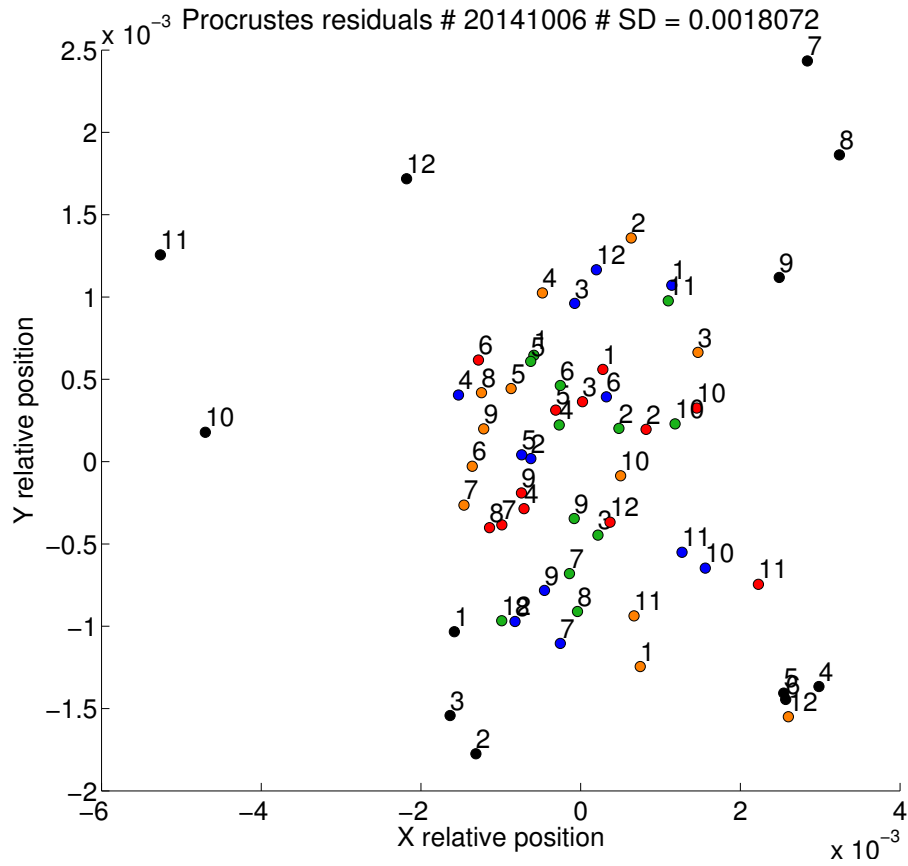


Figure V.26: Procrustes residuals of the stars with respect to the mean configuration (for 12 positions).

Table V.2: Accuracies with different types of calibrations (unit: 10^{-5} pixel).

-	No flat	flat
No metrology	$3.6 \pm 0.59 \times 10^{-4}$	$2.8 \pm 0.45 \times 10^{-4}$
Metrology	$5.9 \pm 0.94 \times 10^{-4}$	$4.3 \pm 0.69 \times 10^{-4}$

field for systematics down to a level of 5×10^{-5} pixels, whereas the metrology could not be verified in the same manner because of hardware issues.

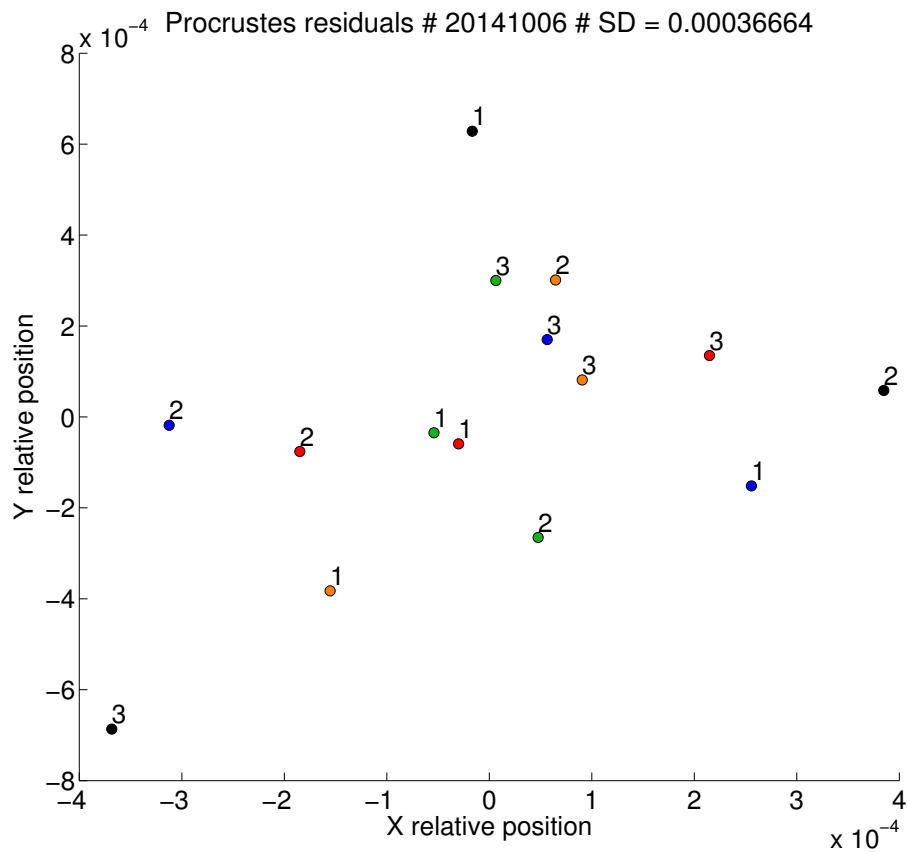


Figure V.27: Procrustes residuals of the stars with respect to the mean configuration (for 3 positions, no calibration).

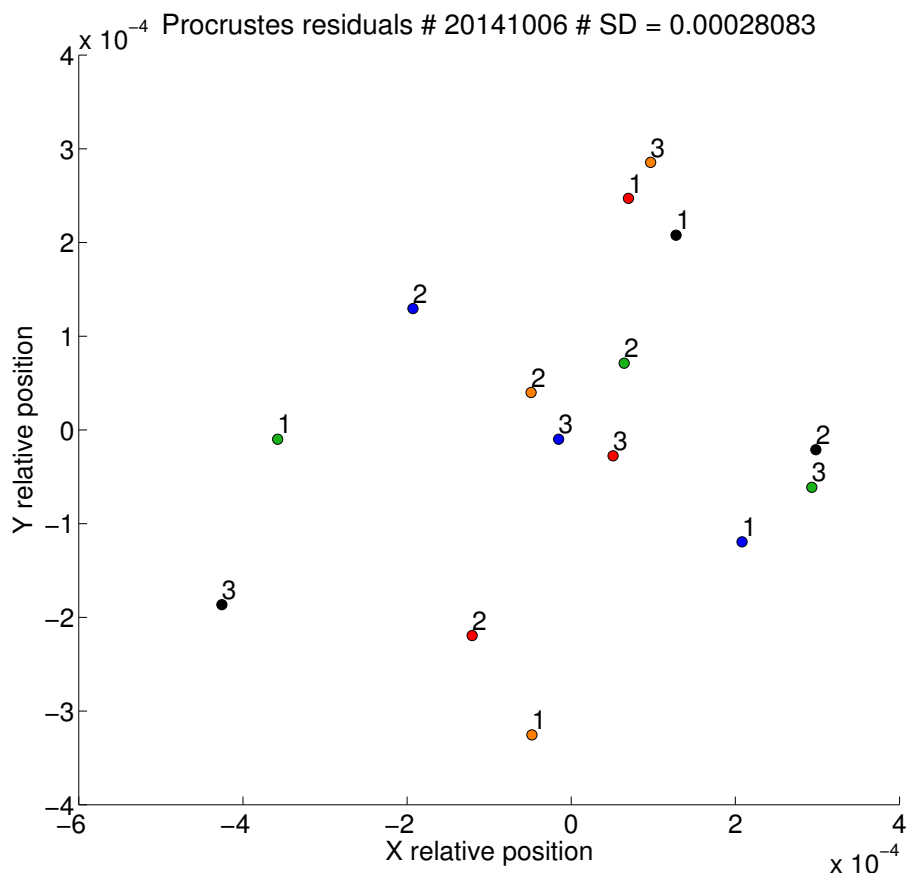


Figure V.28: Procrustes residuals of the stars with respect to the mean configuration (3 positions, flat calibration).

2 Conclusions on the data analysis

2.1 Metrology

The most obvious and disappointing conclusion of our experiment is that correction of pixel offsets from metrology measurements did not work. It seems that we have measured pixel offsets to about a bit better than a percent, but we expect true pixel offsets to have a SD of only 1.5×10^{-3} (from JPL data), so we have in fact measured mostly noise. The cause of these bad metrology measurements is an unidentified source of red noise in metrology data, specific to our testbed. Several observations point to this conclusion:

- Allan deviations of our metrology data become worse when more frames are used.
- The metrology calibration did improve the accuracy for simulated data (down to 10^{-6} pixel) and for data from the VESTA experiment (down to 1.8×10^{-4} pixel).
- Allan deviation on VESTA data is photon limited for the horizontal fringes.

The nature of the red noise in metrology data is unclear, so far we have considered the following possibilities:

Stray light inside the baffle or the vacuum chamber. We have made tests in this direction and observed that when removing the baffle spatial averaging offsets over zones of pixels was less effective. However the effect on individual pixel offsets was not sensible.

Ghost fringes and CCD instabilities. Just like there are ghost images of the stars symmetrical with respect with the quadrants, there may be ghosts fringes at a level of a few parts per thousand. These are much harder to detect because all the CCD is illuminated at once and constantly moving: one can not simply integrate for a long time to see them though photon noise. Attempts to detect systematics from videos of pixel offset residuals (displayed versus time) did not show anything obvious, except for the anomalous quadrant. Simulations have shown that ghosts fringes at a few part per thousand do affect Allan deviation and slightly bias the final pixel offsets, but it does not look like red noise (integrating longer is still beneficial) and the biases are smaller than what we observe on real data.

Damaged fiber tips. Although we have checked visually that all 4 beams for the fiber tips that were used for the metrology data where clean, we still see a stray light pattern on the map of pixel offsets on the X axis which is similar which the patterns obtained with damaged fiber tips.

2.2 Flat fields

A positive point of the experiment is the accuracy of the flat field, for which we have made great progress. The new flat field system provides a very good accuracy, which has been tested for systematics down to a level of 5×10^{-5} (relative errors). This is very close to the specification required to reach the final objective. Because of the

difference between expected and observed errors from flat field (see Fig. V.29), the accuracy of the calibration may already be sufficient.

The most notable improvement was brought by switching from laser light to white light. This is also a positive change from a spectral point of view, the spectrum of the light is more similar to the pseudo stars (although not identical, we have a white LED instead of the tungsten filament). We expect an eventual spectral dependency of the pixel QE to be less visible with the new system. The flat system would be even better with a supercontinuum source with a SMF (to eliminate the possibility of speckles), but with the current results, there is no strong need for a costly supercontinuum source.

Further improvements were visible when upgrading the baffling inside the vacuum chamber. Systematic effects caused by stray light could either be detected directly or by looking at difference between flat fields. Although flat fields were in practice the most successful mode for identifying stray light sources, we have also sometimes used flats from metrology fibers or both. An improvement of data quality for a source of stray light detected with either mode is likely to be beneficial to both systems because all the fibers (multimode and singlemode) are close to each other and are thus likely to be affected by the same stray light sources. Because of this, the conclusions about stray light are presented separately.

2.3 Stray light

With the metrology and the flat field systems, we have identified and taken care of the following stray light reflections:

- On the zerodur bench. We have placed an array made with black paper and razor blades to solve this issue.
- On the piece holding the liquid core fiber (for the pseudo stars). Several razor blades have been placed on this piece to prevent direct reflections from occurring.
- On the edge of baffle vanes. The new vanes made with razor blades have solved this problem (baffle v4).
- Conjugate reflection between the pinhole mask and the CCD, caused by the mirror. A stray light shutter has been installed in front of the mirror.

2.4 Centroids (plus corrections from flat and metrology)

Figure V.29 summarizes the results obtained on simulated and actual data into a single picture, by comparing the relative error levels. The leftmost column shows the relative amplitude of the main sources of errors, estimated from actual testbed data. The values are indicated in accordance to their definitions in table IV.2 (section 3.2), they are either dimensionless or in pixel units). The coefficients of the second column also correspond to the results presented in the former table, they are the results of Monte Carlo simulations on synthetic data. The rightmost column are the accuracies measured for the pseudo stars in different configurations (for actual data).

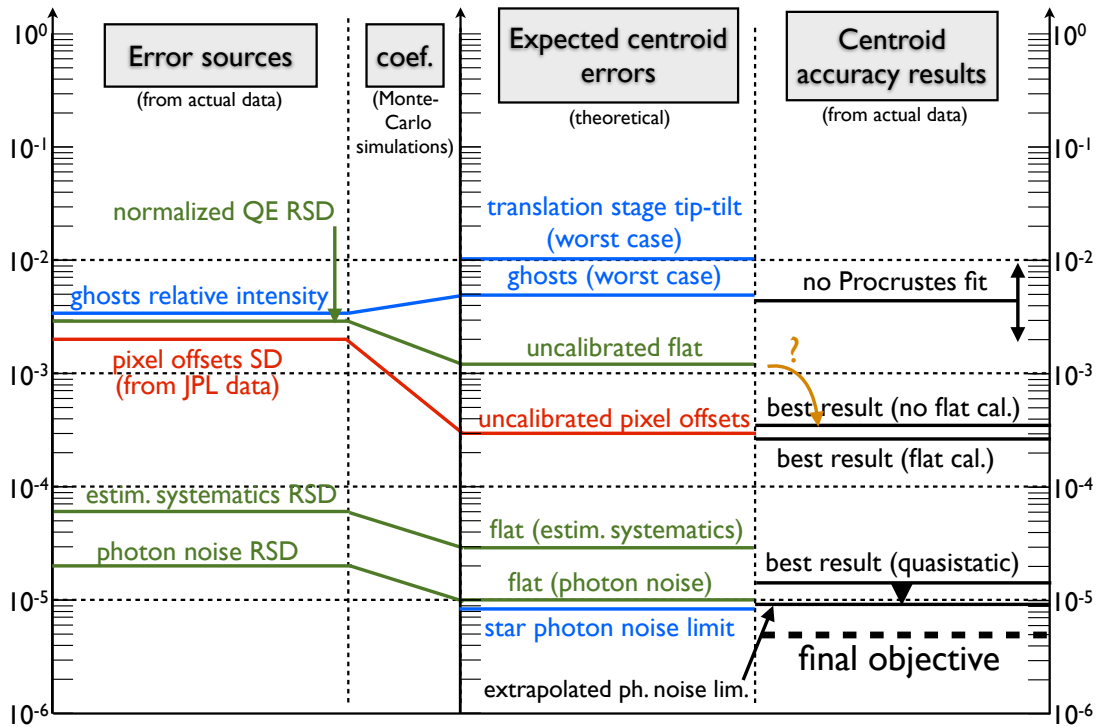


Figure V.29: **Graphic of error levels.** Errors relative to the pseudo stars, flat field and metrology are respectively in blue, green and red. The vertical axis values are either dimensionless or in pixel units, depending on which type of error is considered.

The comparison between the expected errors and the results give us very interesting informations about which errors could be limiting the accuracy. We make the following observations:

1. There seem to be an incoherence in the figure, highlighted by the orange arrow with a question mark: the best (dynamic) accuracy obtained (2×10^{-4}) is about a factor 4 better than the predicted accuracy without flat field. This can be explained by several factors:
 - By trying to avoid bad data sets contaminated by either ghosts or CCD instabilities, we have selected the best result out of 4 sets (of 3 positions each). So we have in fact have cherry picked the final result, this can explain part of the difference (although not a factor 4).
 - Monte-Carlo simulations have been done under the assumption of a white gaussian spatial QE distribution. The real distribution could be different. For example if a small regular gradient is still present in the data, it will increase the apparent RSD, but the differential accuracy of centroid will be unaffected. The few QE drops caused by dust also increase the RSD, but have no effect unless the stars are close to the affected pixels. From the visible locations of the larger dust grains, it seems that stars effectively avoid them.
2. The worst case for the ghosts is way above the best (dynamic) accuracy obtained. It means that we have been successful in avoiding the worst positions where the ghosts are right next to the stars maximums, but that they may be the dominant sources of error for the best result.

3. The best dynamic accuracy fall very close to the level predicted without pixel offset calibration. It is very tempting to conclude that the dominant source of error are the uncalibrated pixel offsets. It may not be the case because:
 - The pixel offsets have not been properly measured in our experiment, the estimation of the QE RSD is actually based on JPL data.
 - Just like for the flat field, the QE spatial distribution may not be white and Gaussian, resulting in a wrong coefficient between the RSD and the expected errors on centroids.

Chapter VI

Conclusions and perspectives

In this chapter I will review the results that have been obtained for both the astrophysical aspect (section 1) and instrumentation aspect (section 2) and I will put them in the broader context of exoplanet research.

Given the current situation with the testbed, the founding of my PhD was extended to the end of 2014 in a last effort to improve the performances. At the date of completion of this manuscript, the new metrology is at last operational on all fibers and new tests will tell if the stray light control has improved the quality of the data or not. However the troublesome issue of ghosts will be hard to workaround in the remaining time. The surest way to deal with the ghost problem would be to change either the CCD and its readout electronics or the translation stage and to use only two centroids on one quadrant. Regretfully, these major changes are not possible within the timeframe of a PhD, which are subject to a rather strict limitation of 3 years in France.

Concerning the astrophysical aspect of the Thesis, which has to do with the NEAT mission concept and its science case, there are also a lot of possibilities that have been left unexplored. The time limit is a strong constraint in this case as well and it has prevented me from doing some interesting refinements. Fortunately, the Theia proposal comes at the right time and in this context I will be able to capitalize on the work already done and expand it a little bit.

1 The NEAT/Theia mission concepts and the science case for μas astrometry

1.1 Results for the science case

Based on the error budget of the NEAT mission¹, which corresponds to a typical differential astrometric accuracy of $0.7 \mu\text{as}\cdot\text{h}^{-0.5}$, I have shown that NEAT is capable of finding dozens of nearby habitable planets. The closest of these would be the best targets for direct imaging and spectroscopic characterization. I have presented a process from which one can:

¹Error budget by Renaud Goullioud, referenced in appendix C

- Create catalogs of target and reference stars for a pointed astrometric mission aiming at detecting nearby exo-Earths
- Acquire various statistics about the reference stars and in particular check if the hypothesis made in the NEAT error budget are correct
- Estimate the science yield of the mission, as a function of mission and telescope parameters, the distribution of the observation time between the targets

1.2 The new mission concept: Theia

The 4th ESA call for M class missions has been made, the deadline for the proposals has been set to January the 15th. The former NEAT consortium will propose a revised version of the NEAT mission called Theia [Malbet et al., 2014].

One of the main critics of the NEAT proposal was relative to the cost estimation. To address the cost issue, the new Theia design will use a slightly downscaled mirror (about 0.6 to 0.8 m of diameter instead of 1 m). Formation flying was also a delicate point and will stay that way. As of now, μ as astrometry with a TMA configuration is not demonstrated and we think that formation flying is still our preferred option (main design). A deployable boom design can still be presented as a backup option.

The exoplanet community is in a delicate situation for this new ESA call, as two transit exoplanet missions have already been selected by ESA (PLATO and CHEOPS), in addition to another one of NASA (TESS). To have a better chance of being positively received, the Theia proposal will set aside more than 70% of its mission time for other objectives than exoplanets, like dark matter study, dynamics of the galaxy, stellar clusters and extreme astrophysical objects, astrometry of Solar System asteroids, measure of relativistic multipolar light deflection around Jupiter.

1.3 Future use of the catalog of targets and references

The work that has been done on the scientific case and the error budget of NEAT has to be updated to assess the exoplanet science case of Theia. With a smaller mirror and about 15 to 30% of the mission time dedicated to exoplanets, which is a drastic reduction compared to NEAT, what science can we do?

To answer this question, we can use a combination of three tools:

The NEAT/Theia catalog of target of references The catalog can be directly reused, the stars have not changed!

The Theia error budget The error budget has to be updated to the new Theia parameters.

A planet population model Here they are several possibilities. We can for example use the planet population model from [Alibert et al., 2013a], the same that was used for the NEAT double blind test. This model is mostly theoretical and based on planet formation and migration simulations. Another possibility is to use a distribution based on the results from the Kepler mission. The first model is interesting because it provides information for a very large space of planet parameters, the second model is expected to be more reliable and

conservative in the number of predicted detections if we restrict the analysis to the actual Kepler detection space and do not extrapolate.

This combination of tools is very powerful. Not only it can answer the initial question, it is possible to go into finer details, like for example:

- For a given mission time how many stars can we survey, at which accuracy?
- What will the exoplanet yield look like (in terms of parameters distribution)?
- Depending on the number of habitable planets we aim to detect, what is the minimal fraction of the mission needed for exoplanets?
- What is the best trade-off between the number of targets searched for exoplanets and the accuracy, relative to the yield?
- Can we optimize the yield by changing the time distribution between the targets?

1.4 Improvements on the catalogs of targets and references and yield simulator

There are numerous improvements possible for the catalogs of targets and references, in some areas very significant simplifications had to be made. Further studies are needed to make progress on some particular points.

Complete the catalog of targets with M stars Very close (early) M stars are interesting to observe with NEAT, exoplanets in their HZ can be detected by astrometry. There is a large overlap with radial velocities in this case, but in some ways it is an advantage: the detection power increase when combining the two methods, which is also a very good way to confirm eventual detections and to better separate the stellar noise from the planetary signals. These few stars would constitute a very valuable case study of how to extract the planet signals from the stellar noise. Habitable exoplanets around these stars could be observed with future giant telescopes. We have realized that quite a few M stars are missing in Fig. 1.9 (for example Barnard star, with a visible magnitude of 9.5, should be visible near the top!). These stars are not in the catalog because the filter used to determine stars that are on the main sequence is too restrictive.

Better way to filter main sequence stars The filter used to select main sequence stars is tricky to define. We have used the following types of regular expressions (here for F stars): `matches(SpType, "^F.*(IV-V|[^I]V)")`. It considers main sequence stars the ones which contain the following string in their Sp-Type columns: "IV-V", "V" or "V" plus some flags before or after it, and of course it excludes "VI". For stars with two components (separated by a "+" sign), we should ideally base the selection on the main component. However, errors will be made if the secondary component only is main sequence: with this regular expression, the star will be included in the list. The problem is that it is not possible to use a "\" sign in the regular expression (it causes an error in Topcat), it is therefore impossible to get the needed escaped "+" in the regular expression. The spectral type of Barnard star indicated by Hipparcos is "sdM4", which explains why it was not in the final catalog. We

have also lost Sirius A (SpType: “A0m...”). Close M stars can also be found in the MEarth catalog [Dittmann et al., 2014], with more suitable spectral types. Another way of filtering the main sequence stars that could be more reliable would be to use their position on the HR diagram.

Update the catalogs with the Gaia survey When the Gaia survey will be released, more precise parallaxes will be known, compared to the Hipparcos ones. This will make a big difference for the reference stars: we will have more information about their true distances. Both the targets and the references stars catalogs could be derived from the Gaia survey. It will also include all the closest M stars that are of interest for our astrometric survey.

Refine the columns calculations The current method to obtain the astrometric signal in HZ is approximative. A number of refinements can be made, such as:

- Using a piecewise power law, instead of simply $L \propto M^{3.8}$. This is important when we consider M stars.
- Updating the HZ inner and outer edges with the latest published results [Kopparapu et al., 2013].

Improve the error estimation for reference stars The photon noise from the reference stars is calculated as a function of the sum of the fluxes of all reference stars. A more realistic estimation has to take into account the geometric configuration of the reference stars. For example if there is only one bright reference star, rotation errors will be larger.

Take into account multiple stars Companions are always counted as valid reference stars. This is an optimistic assumption: for small separations, it could be impossible to obtain accurate measurements of the centroids for each component. In this case the astrometric solution is actually harder than for a single star, the orbital parameters of the close binary have to be subtracted accurately before the planets can be detected.

Improve the integration and automation of the tool The current version relies a lot on Topcat and uses lots of different tools. The consequence is that in order to run a new simulation with different parameters, everything has to be done and checked manually (there are dozens of steps), this is impractical. The issue can be mitigated by exporting the catalogs of targets and references before making all the NEAT new columns. The equivalent reference flux calculation and all remaining columns would then be calculated automatically by a script.

1.5 Near and mid-term perspectives in exoplanetology

Three transit missions, namely TESS, CHEOPS and PLATO have been selected for launch within the next 10 years. These missions will be nicely complemented by Gaia which will find thousands of longer period giant planets (with the best sensitivity for timescales of a few years) and direct imaging for young bodies even further away. This will give us a very rich picture of the distribution of planets and we will have a more comprehensive view of planet formation. We will also have the JWST to do follow-up transit spectroscopy on the most interesting targets and we have a chance of detecting biomarkers with it, for the easiest ones. However

this kind of science will be near the limit of technical capabilities and we will in all likelihood not be able to make a detailed study of an exo-Earth around a Sun-like star with the JWST, unless we get lucky and get a very close habitable transiting planet.

In the meantime, ground-based transits and RV surveys around low mass stars may find very close habitable Earth and super-Earths, which would be prime targets for transit/coronagraphic spectroscopy. It is also interesting to note that in the case of non-transiting habitable planets around M stars, coronagraphic spectroscopy with the next generation of ground-based giant telescopes (ELTs) is more advantageous than in space and should be the first method to obtain spectra of terrestrial habitable planets [Guyon and Martinache, 2013]. The small separations between the stars and the planets and the need to observe in the near infrared result in the need for a very large pupil. It will be interesting to see how much further can the accuracy be pushed for the RV method.

In the longer term, coronagraphs (ground based as well as space born) will offer a higher potential to find and spectroscopically characterize the closest targets because they can be much less sensible to the photon noise from the star (we have explained this in section 1.2.8). So far, astrometry has only played a marginal role in the exoplanet research. Although Gaia will only detect giant exoplanets, when the mission will be completed (around 2019), the number of exoplanets detections by astrometry is expected to be more than all other methods combined [Perryman et al., 2014]. One can hope that it will bring astrometry to the forefront of the research when considering future missions.

2 The NEAT lab demo

2.1 General feedback on the project and teamwork aspects

A lot of people have worked together to make the NEAT lab demo possible and I am very grateful to all of them. I interacted with people from various backgrounds and specialties (researchers, engineers, interns, mechanics, opticians, electricians...), in order to design and build the NEAT testbed. Overall, the teamwork has been an enjoyable and rewarding experience. I have been able to gain in autonomy throughout the process and interact more directly and more effectively with everyone. After the testbed was assembled, I was able to manage the upgrades on the testbed and its operation myself and this was very satisfying.

Another positive aspect of the work is my collaboration with JPL. My first experience at the JPL on the VESTA team, which was composed of Mike Shao, Chengxing Zhai, Bijan Nemati and Inseob Hahn, provided me invaluable experience for our testbed. Our collaboration was very fruitful and is still ongoing. In this context, we have recently exchanged testbed data (in both ways, JPL data to Grenoble and vice versa) and have some teleconferences to discuss the results. Comparative analysis of both data sets will help us to improve the processing and to understand and deal with specific noises in the data. We are also planning a trip to IPAG for Chengxing Zhai at the end of November: we will work together on the NEAT demo testbed during one week.

The project approach has been a good way to put things together rather quickly. We were able to design and assemble the testbed within 2 years: first light on both metrology and pseudo stars was obtained in July 2013, leaving more than one year to work with an operational testbed. Yet the final objective is very ambitious and we had to face unanticipated difficulties which have strongly limited the performances so far. In the next part I will talk about the many kinds of upgrades we can do on the testbed: there are interesting smaller upgrades that can be done before the end of the year.

2.2 Possible improvements for the NEAT lab demo

The final accuracy obtained from the experiment at this stage is not particularly thrilling. We are far from having demonstrated accuracy down to 5×10^{-6} , which would allow detection of exoplanets in habitable zone of nearby stars with the NEAT concept. Our experiment has been impeded by a range of issues, that when combined together, makes it hard to make significant progress. The main dilemma is that we want less pseudo stars to avoid being plagued by electronic ghosts, but we need all 5 stars to correct the tip-tilt of the translation stage. Despite the disappointing results, there are multiple interesting avenues for improvements.

2.2.1 Averaging errors over several detector positions

The first important aspect to mention for the experiment is the possibility to average the systematic errors caused by pixels over several positions. This is very interesting, because the same technique can be applied for an actual mission as well. We have vaguely made a reference to this in chapter 2, where we have said: “Another strategy can be to break each single epoch measurement into several individuals measurements in order to average systematic errors”. In the particular case of errors caused by pixels, the mitigation strategy would be done by taking data on multiple locations on the CCD (for a single epoch). In the case of a space telescope as well as with our experiment, we can apply a common translation to generate in principle as many positions as we want, in practice limited by the size of the detector. The final measure of the relative positions is obtained by averaging over all the detector positions.

For a real instrument, the number of positions that can be averaged per epoch would depend on many parameters. For NEAT, it would be possible to use hundreds of positions, because a single epoch measurement lasts typically several hours and a small tip-tilt of the mirror can be used to apply the common translation motion very quickly (500 Hz feedback loop for the position of the target star). If one accepts the assumption can systematic errors can be averaged efficiently by this technique, the final requirement is relaxed by a factor of 10 (to 5×10^{-5} instead of 5×10^{-6}) if we average over 100 positions. The accuracy currently obtained is not that far from this value !

Even more interesting, we can in theory try to quantify how well this error averaging method works in our experiment: do we obtain the full expected accuracy gain of $1/\sqrt{N_{\text{detector positions}}}$? Instead of looking directly at Procrustes residuals of each position, we can look at Procrustes residuals between the relative stars positions averaged for several detector positions. Unfortunately, with the current setup, we

have access to very few positions (to avoid ghosts) and we had to work with only 3 positions, which make the grouping described above impossible. If we can get to metrology to work properly, it should be possible to compensate for errors seen when the central star change quadrant (if pixel offsets between quadrant are indeed their cause). With 12 positions in a single analysis, we can make 3 groups of 4 positions, thus potentially gaining a factor of 2 in accuracy. However it will be hard push much further, certainly not to 100 positions.

2.2.2 Hardware upgrades

There are numerous improvements that would be very beneficial for the testbed, the first of which is to change the detector and its electronics for a model with only one quadrant and with a stable readout noise. However this change is not realistic to make in the remaining timeframe (the current CCD, its readout took electronics and the related software about 1 year to be developed and installed). I will present small modifications that can be done before the end of the year first, I will talk about more consequent modifications afterwards.

(a) Small upgrades

Bundle of SMF instead of pinhole mask. The current pseudo star system is made from a pinhole mask, back illuminated by a large liquid core multimode fiber. In this configuration, it is not possible to illuminate the stars one at a time (it is all stars or nothing). By replacing this system with a a bundle of SMF it will be possible to control every star independently, at least manually with the fiber connectors. By illuminating the stars one by one, we can check the ghosts much more easily (and even estimate their stability) because we do not have to deal with the signals of other stars on top of it. Having no photon noise to deal with, we can quickly calibrate the ghosts for each position if needed.

Vantablack lining. The current material we are using to cover the interior of the baffle is a black coating called “metal velvet” (acktar[®]). It has a reflectance coefficient of 1% in the visible. We have contacted Surrey Nanosystems which have recently commercialized a new high performance black coating called Vantablack, which a reflectance coefficient of 0.04%, and will soon receive the new sample. The new coating is very expensive though and we will not have enough of it to cover all the baffle interior, this is more for experimentation.

Better stray light control neat the chip. There is a small very bright area around the chip (0.3 cm^2 , see Fig. VI.1), a Zemax stray light model has indicated that it could be by far the dominant contributor to stray light inside the baffle, we are thinking of covering this area with a black material (the Vantablack would be well adapted for this). However the operation is dangerous and the area can not be completely covered because of the CCD bounding.

Installation of a shutter. In order to limit stray light during the flat field and metrology measurements, we will put the stray light shutter in place, like it was supposed to be from the beginning. We had concerns that the conjugate reflection with the mirror would affect the metrology, however a test with a shield on the mirror indicated that it is not the cause for the problematic red

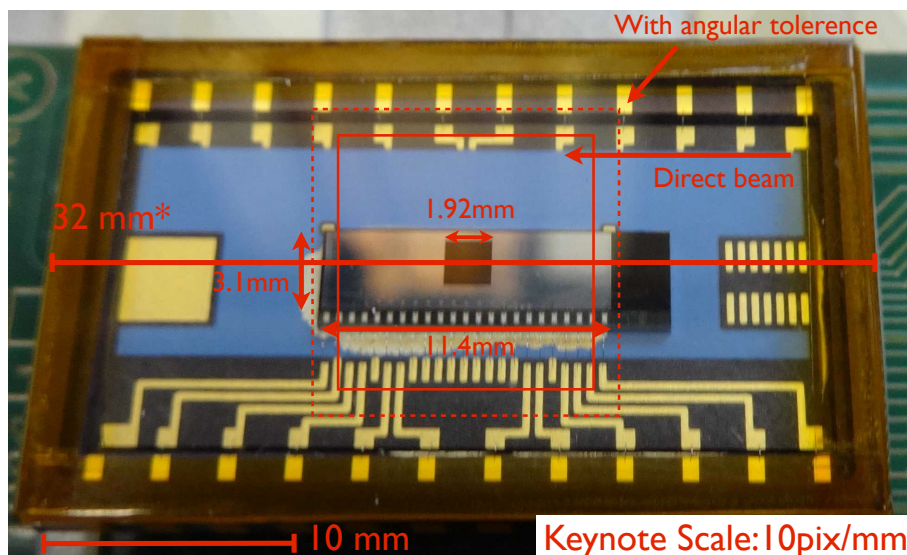


Figure VI.1: Picture of the bright area around the chip.

noise we currently see (no major difference was observed in the Allan deviations with/without the shield). So far the only confirmed effect in on the flat field.

(b) Major upgrades

Translation stage The current translation stage produces large tip-tilt jitter when translating the centroids (it is inherent to its design), this produces plate scale changes between the detector positions. Consequently, it is necessary to have 5 centroids to remove the platescale from the data. With a very stable stage, one would have the option to use only two centroid and look at the distances projected in the X and Y axis. This was done at he JPL, they initially has 3 centroids, but turned off one of them because of electronic ghosts and worked with only two.

Changing the CCD The testbed would benefit greatly from having a CCD with one quadrant only. Data processing would become much easier and several major problems would go away (ghosts, relative quadrant instabilities, anomalous quadrants).

2.2.3 Analysis and software upgrades

There are countless improvement that can be made to the matlab code, here I will only mention the most critical ones in our situation:

1. The analysis of differential centroid accuracy used relative positions only and can be coupled with the old method of measuring position (with Gaussian fits) which give an absolute position in the CCD index frame. This can be useful to plot variations in relative position versus absolute position on the CCD. This function will be useful to check that mechanical vibrations are nominal for all data cubes: for one data cube used in our analysis (pseudo stars at position 2), the precision is far from photon noise. Possible causes are a CCD instability or a mechanical instability.

2. The metrology does not correct for relative quadrant instabilities. There is a worry that the global solution which is over 4 quadrants might be affected. There is a parameter that can absorb large differences of QE between quadrants, but only if they are constant over the duration of one metrology data cube (or baseline). A third set of parameters which depends on both time and quadrant number can be added to correct for this. However we think that this problem is not currently affecting the metrology data because using only one quadrant show identical Allan deviations and because of the successful metrology analysis on JPL data which also has 4 quadrants.

2.3 Lessons learned for the NEAT lab demo

2.3.1 High photon integration speed

To summarize much of our problems in one sentence, I would say that we have been too scared about photon noise and not enough of systematics. We have gone to great lengths to make sure that we could get the needed number of photons within minutes. Our choice of detector (CCD39-01 from E2V) is not innocent in this regard: with its four quadrants, it can be read four times faster. We have also explicitly asked the CEA for readout electronics that can work at 1000 Hz, which is the maximum possible with this model. In parallel we have spent a lot of efforts to develop the photometric tools to ensure that the source can keep up with the CCD. The choice of a pinhole mask over a fiber bundle (like was done at the JPL) for the pseudo stars was for two main reasons: the first one is to allow for precise placement of the centroids on the CCD and the second one is to have more flux per star (the pinhole diameter is larger than a SMF core). Retrospectively, we realize that going for very high photon collecting rate has oriented toward choices that have caused problems afterwards.

2.3.2 Critical systems: detector, translation stage and pseudo stars

If the experiment were to be re-designed from scratch, my main recommendation would be not to use a CCD with several quadrants or at least to check for any information about ghosting. If the choice comes down to it, I would prefer a longer integration time with no quadrants and/or a slightly higher number of pixels and/or a low and stable readout noise.

The second most important aspect would be the specification of the translation stage: a translation stage with small tip-tilt errors would make the Procrustes superimposition optional. The experiment would be more robust, if for whatever reason not all pseudo stars can be used.

Using a SMF bundle instead of a pinhole mask would allow for an easy control of the number of active centroids. This kind of flexibility is very useful to distinguish between optical and eventual electronic ghosts, and to calibrate them if all attempts to suppress them fail.

2.3.3 Metrology

The integrated metrology system, from the source to right before the fiber tips has been working well. Our choice to have everything in integrated polarization maintaining components (i.e. everything is fibered) results in a practical and compact solution. A possible interesting alternative (also with only integrated components) would have been to use circular polarization with fiber stretchers for the phase modulation. The advantages of this configuration over the current one: there is no need to manually align fiber tips axis and the attenuation is lower. Our phase modulators have indeed a rather strong attenuation (6 db), this has lead us towards a high power laser (22 mW). However the most problematic metrology issue we had to solve was with the fiber tip holders. In our case their design is potentially critical (because of the baseline stability requirement) but not trivial. Because the first design was over-specified for stability and used zerodur V-grooves we were unable to clean the fiber tips and the installation was very tricky (it took weeks!). In the end these practical considerations made us change the design.

2.3.4 Real time feedback

On the more positive points, there are things that have been tremendously useful, such as the quick look utility. Having the possibility to investigate and get rid of the most trivial issues in real time was a major advantage and allowed us to solve some problems very quickly. The actual version of the quick-look has a normal (count) display and a temporal noise display, which are both useful. Along the way we have also added a mode to detect ghosts and a remote command that can be used to export a small cube of 25 images into a file. The latter functionality can be used by the user to implement any kind of tricky signal processing on the raw image in quasi real time that would help solve a particular unanticipated issue. In our case we have used it to build an iterative procedure that can reposition the translation stage to an accuracy of 0.01 pixel. I would highly recommend to plan for these functionalities right from the start on any future similar experiment.

2.3.5 System automation

Another positive point was the almost complete automation of the system. Most of the systems are controllable from a single interface, that presents itself as a very convenient Python wrapper. Thanks to the labview remote control interface, the CCD can also be controlled from the same interface. The only system that is not remotely controllable is the flat field source (because it was added at a very late stage), but flats can easily be taken manually at the beginning of the sequence. Unfortunately, various specific concerns prevent us from taking full advantage of the system and running in a completely automated mode, we need to at least be there for some basic checks. The various issues are the stability of the readout noise, the positions and sizes of the ghosts and the stray light shutter which can sometimes get stuck mid position.

2.3.6 Stray light

Stray light proved to be very hard to control. Given our very strict requirement on stray light for coherent metrology light, an integrated approach from the start would have been more effective. In our experiment, many difficulties originated from the small size of the vacuum chamber and our choice to work with a very small off-axis angle to minimize geometrical aberrations on pseudo stars. There are a lot of physical elements near the line of sight between the mirror and the CCD, including the walls of the vacuum chamber.

We were able to significantly improve the situation with a baffle and by shielding the physical elements in the baffle FoV, this was sufficient for the flat field in incoherent white light. However, the stray light effect on the metrology which uses coherent light is larger and is a likely cause for the red noise that limits the accuracy of the pixel offset measurement. In the VESTA experiment, at least one of the metrology baselines has very good properties, which could be the consequence of good stray light control. It would be interesting to understand precisely how this was achieved (I currently have no details about the stray light control on VESTA for this data set).

2.3.7 Numerical simulations

Numerical simulations proved to be an indispensable tool to debug and validate the data analysis process and to refine our understanding of error propagation of all noise sources. We have used stray light simulations very late in the experiment and we have paid a heavy price for it. The integration of simulated data into the analysis process was done in a straightforward manner with a system of option parameters because I was working alone on the code most of the time. However the code is rather complex and the system of option parameters has been pushed to its limits. In the context of a larger project, a better way to organize and document the code would be needed, especially if several people are working together. One student has done an internship on data simulations for the NEAT lab demo and contributed to parts of the code, for example for the simulation of PSFs. I was not able to take full advantage of this work because of the lack of organization and documentation in our respective source codes and our lack of programming experience and best practices.

2.4 Future applications of the NEAT demo experiment

The issues we have encountered are however not fundamental and can be overcome: we have made numerous possible suggestions. There is also the interesting possibility of averaging the residuals calibration errors, which we could not explore also because of the ghosts. Decreasing the calibration requirement by a factor 10 would result in a much easier task. As a matter of fact, an accuracy better than 5×10^{-5} has already been demonstrated at the JPL (priv. comm.²). Short of reaching the ultimate NEAT accuracy, there are other interesting applications for our experiment which have lower requirements.

²More information is available on a two-wheel Kepler white paper by Shao et al. http://keplerscience.arc.nasa.gov/K2/docs/WhitePapers/Shao_et_al_Kepler_2Wheel.pdf

On-board astrometry for spacecraft navigation in the Solar System The concept is to provide a way for a spacecraft navigating in the solar system to autonomously measure its position by performing astrometry on asteroids. The more accurate the astrometry, the more accurate the estimated position. This was the primary goal of the VESTA experiment, the requirement was set at 2×10^{-5} pixel (priv. comm.).

Detector calibration for accurate photometry Astrometry measures the average photon location, whereas photometry is the total number of photons. Correction for the biases caused by the pixel QEs and offsets in the first case also works in the other. There are several transits missions that will fly soon and that could benefit from a ground calibration. Space mission achieve good photometric accuracy by having a very stable pointing, but this does not work on long timescales because of relative star motions (proper motion, parallax, stellar aberration). A fine calibration of the CCD could at least recover most of the photometric accuracy on long time scales and at best relax the requirement for high pointing stability if a full calibration can be relied upon.

Fine characterization of detectors A very wide application is simply the characterization of detectors (CCD and CMOS) in general. Manufacturers are likely to be interested by a method that can accurately measure the properties of their products, as it can give them ways to control or improve them.

3 After my PhD...

One of the key motivations that drove me to work on NEAT is the detection of close habitable worlds. I will follow with great interest how the field evolves in the future and I hope I will have the opportunity to take part in new discoveries by doing a postdoc related to exoplanets. In the current context, there will be many opportunities to work on transit missions or coronagraphy.

Regarding transit missions, one way to contribute would be to assess the benefits of a detector calibration for the accuracy of the mission, based on the results of the NEAT-demo and VESTA experiments. For coronagraphy, experience with detectors and optical simulations will be a useful asset to work on laboratory testbeds. My work with the catalogs of targets/references and the exoplanet yield simulations is also a good starting point to get more deeply involved in the scientific aspects. Another possibility for me is relative to the astrometry on the Gaia mission: I could try to integrate the DPAC (Data Processing and Analysis Consortium).

Appendix A

Animations

This section contains animations relative to some figures. These animations are only compatible with **Adobe® Reader®** which can be downloaded for free [here](#).

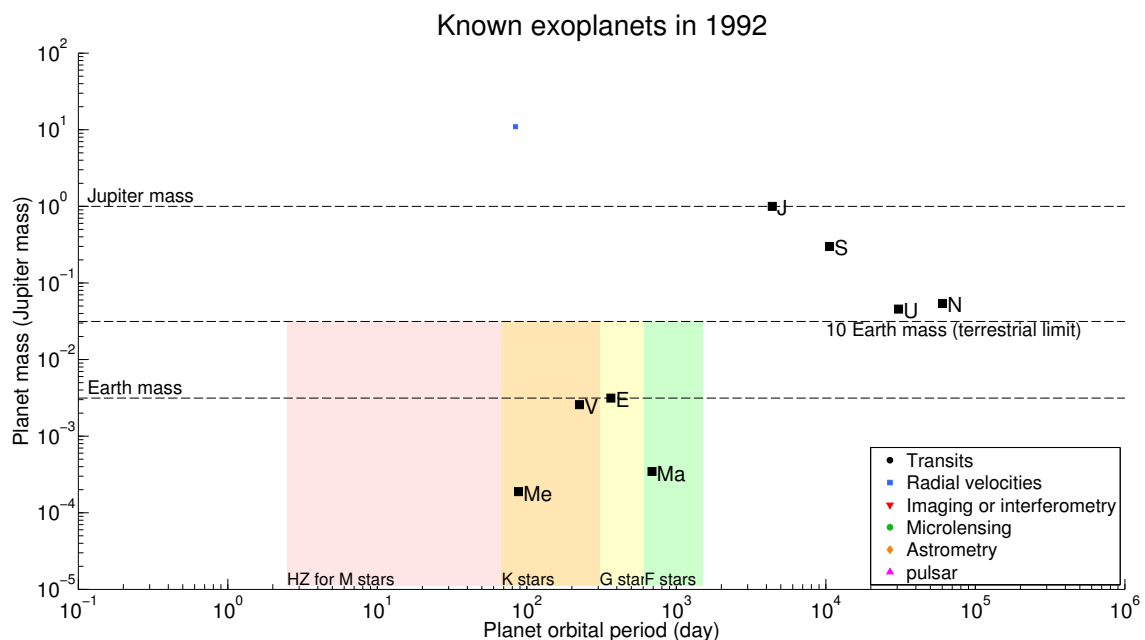


Figure A.1: **Animation showing the exoplanets discoveries year by year on the mass-period diagram, from 1992 to 2013.** As time goes on, one can see that less and less massive planets are discovered: starting from 2004, we find more and more planets with masses below $10M_{\oplus}$, which are likely to be terrestrial. [Go back to figure](#)

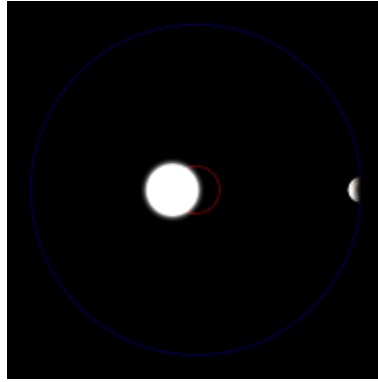


Figure A.2: **Illustration of the star/planet orbital dynamic** (Credit: wikipedia). [Go back to figure](#)

Appendix B

Analysis of JPL data

In the context of our collaboration with the VESTA team at the JPL, they have kindly provided us with their data set from the 02/10/2012, which was the final one used to demonstrate the VESTA performance at a level of 2×10^{-5} pixel accuracy.

The data set includes:

- Two flat fields taken with a superluminous source
- Metrology measurements on a vertical and horizontal baseline, plus associated darks
- Pseudo star measurements for 30 different positions, with a common centroid translation of 3 pixels in the horizontal direction, plus associated darks

1 Flat fields

Figure B.1 shows the difference between the two normalized flat fields (at “step 3”, quadrant and irradiance normalized). Figure B.2 shows the normalized flat field (also quadrant and irradiance normalized). Figure B.3 shows the final flat.

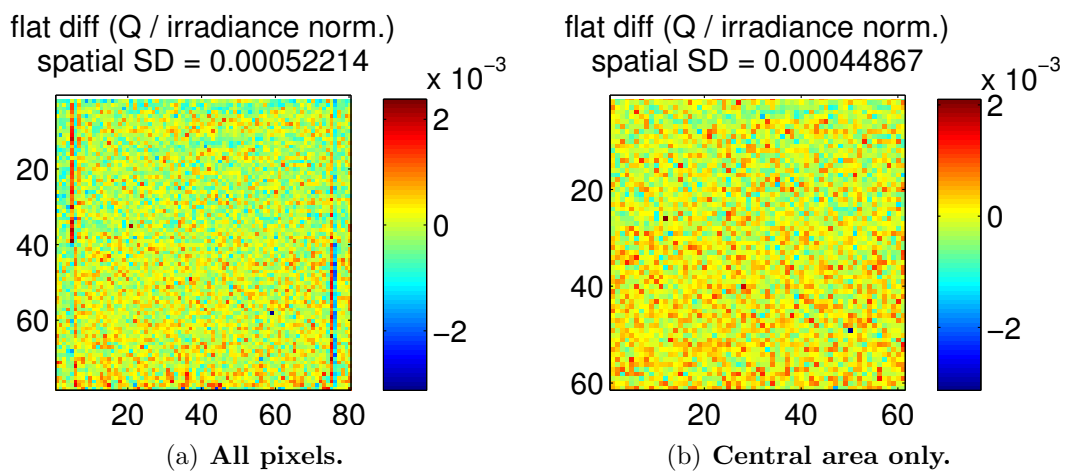


Figure B.1: **Quadrant / irradiance normalized flat field difference.**

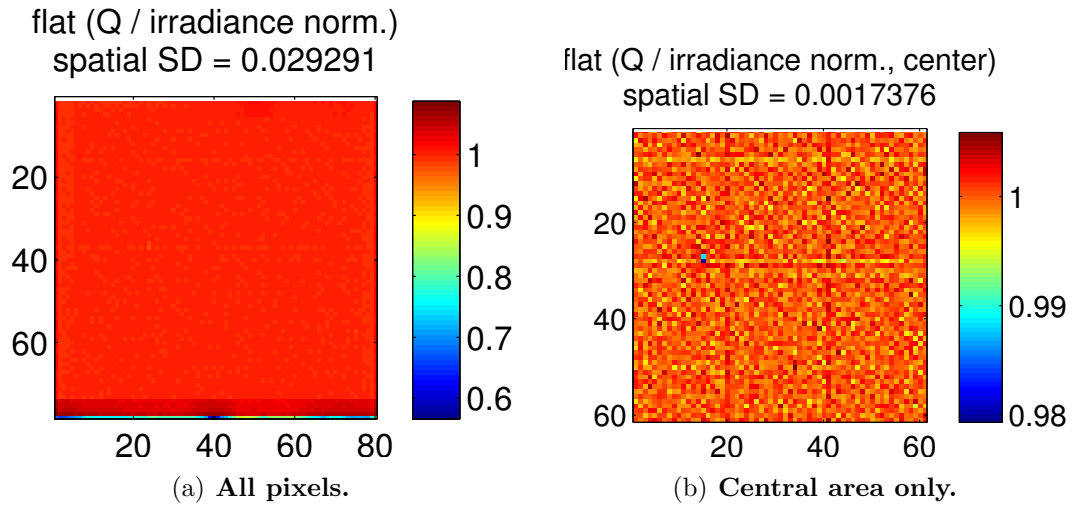


Figure B.2: **Quadrant / irradiance normalized flat field.**

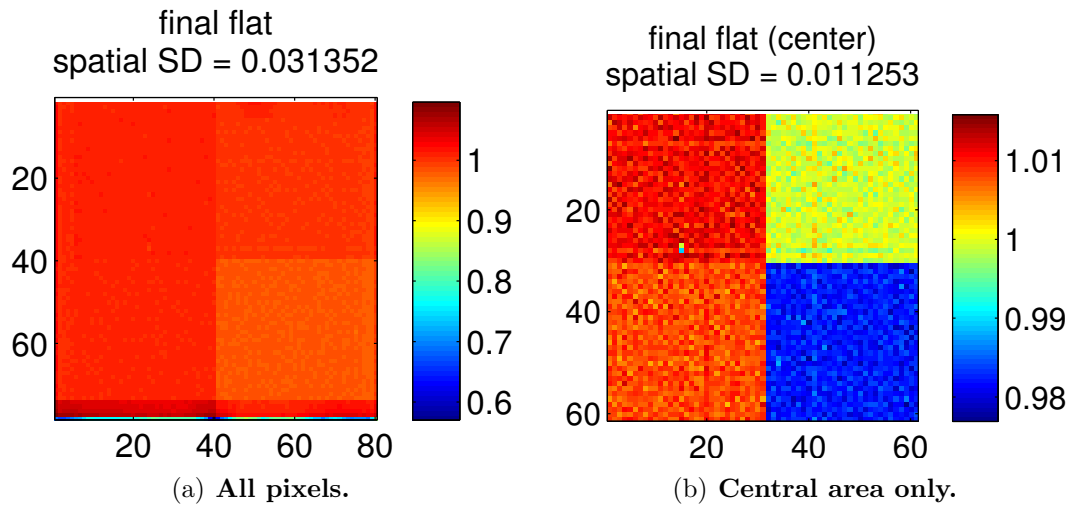


Figure B.3: **Final flat field.**

2 Metrology

Figures B.4 and B.5 show the Allan deviations for respectively the vertical and horizontal directions. Figures B.6 and B.7 show the pixel offsets respectively on the X and Y axis.

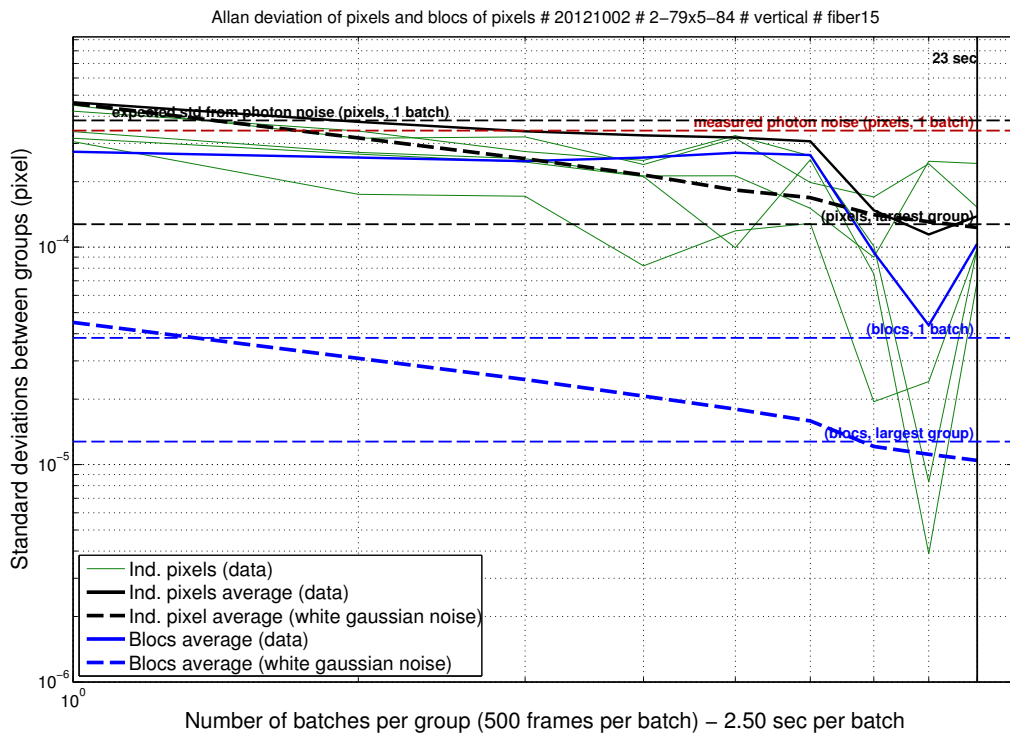


Figure B.4: Allan deviations of pixels and blocs of pixels.

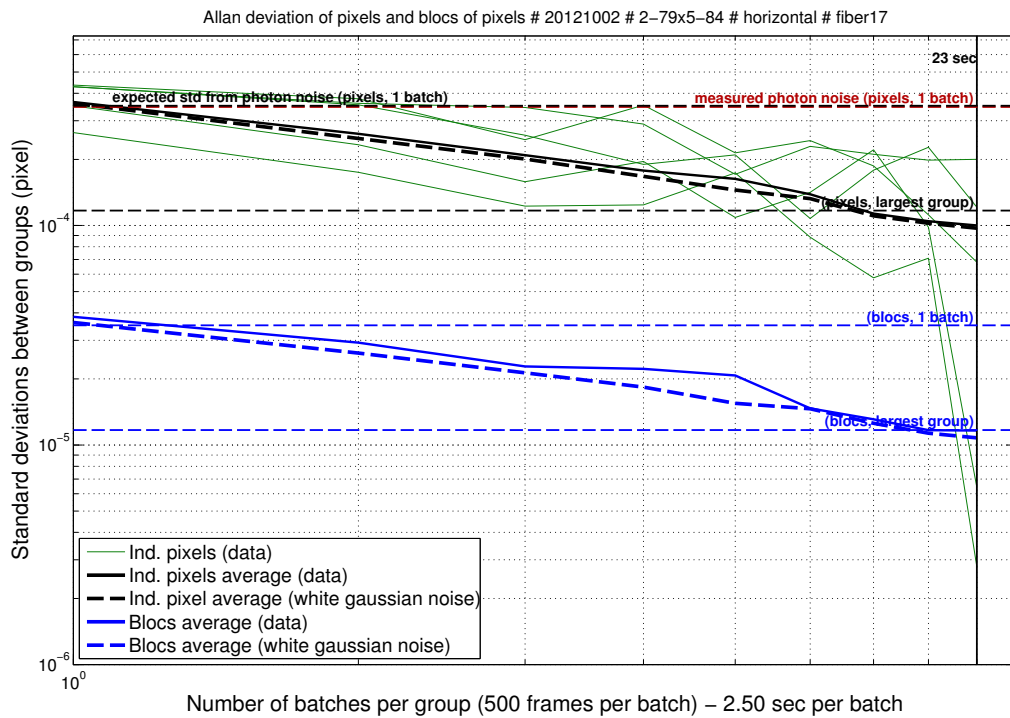


Figure B.5: Allan deviations of pixels and blocs of pixels.

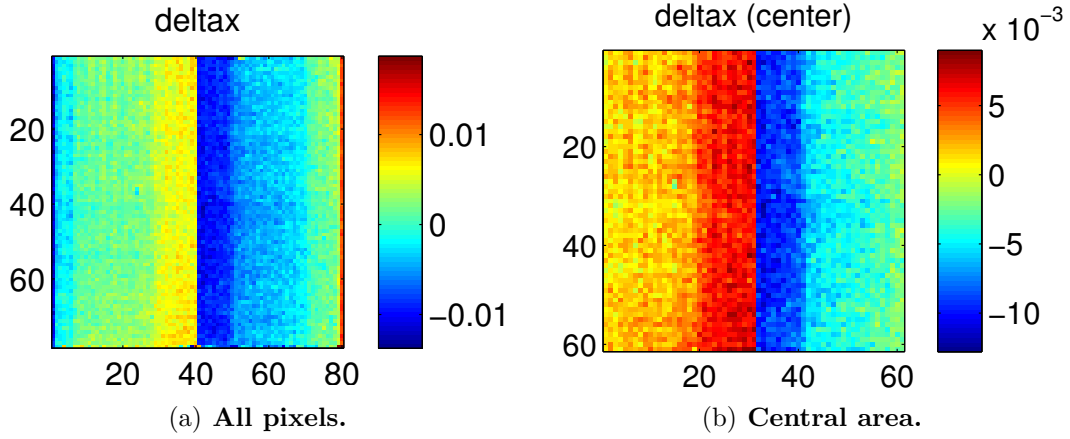


Figure B.6: Measured pixel offsets along the X axis.

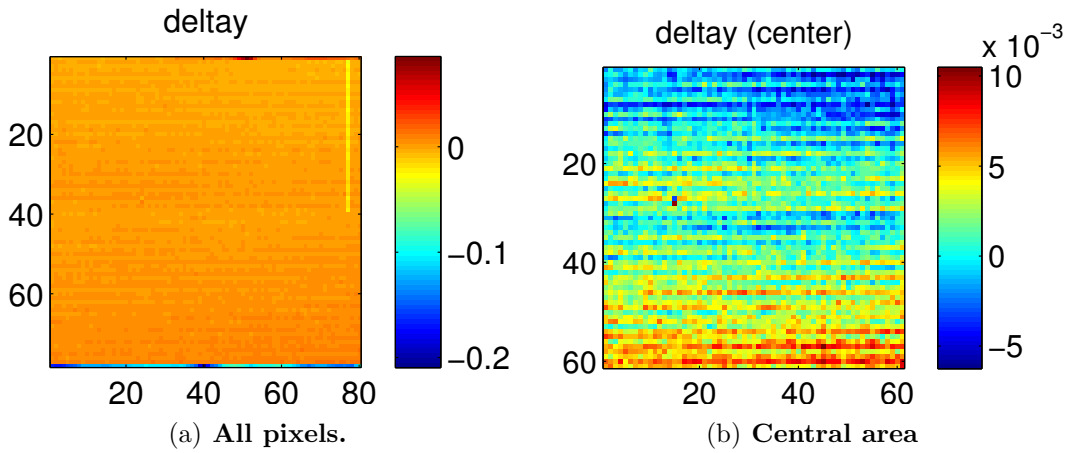


Figure B.7: Measured pixel offsets along the Y axis.

3 Pseudo stars

The quasistatic analysis yielded precisions between 1.5×10^{-4} and 5×10^{-5} (for cubes split into 3 batches, the photon noise extrapolated to the whole cube is about twice as low). This is consistent with the photon noise expected from the number of counts (5×10^{-5} on each star).

For the dynamic analysis, Fig. B.8 shows the variations of the projected distances between the centroids, in the X and Y plane (with flat and metrology corrections active). Table B.1 gives the final accuracy for different calibrations configurations. By grouping of all positions into 3 bins and averaging the centroids positions, the accuracy was increased to 1×10^{-4} .

Table B.1: Accuracies with different types of calibrations.

-	No flat	flat
No metrology	2.99×10^{-4}	1.90×10^{-4}
Metrology	2.82×10^{-4}	1.72×10^{-4}

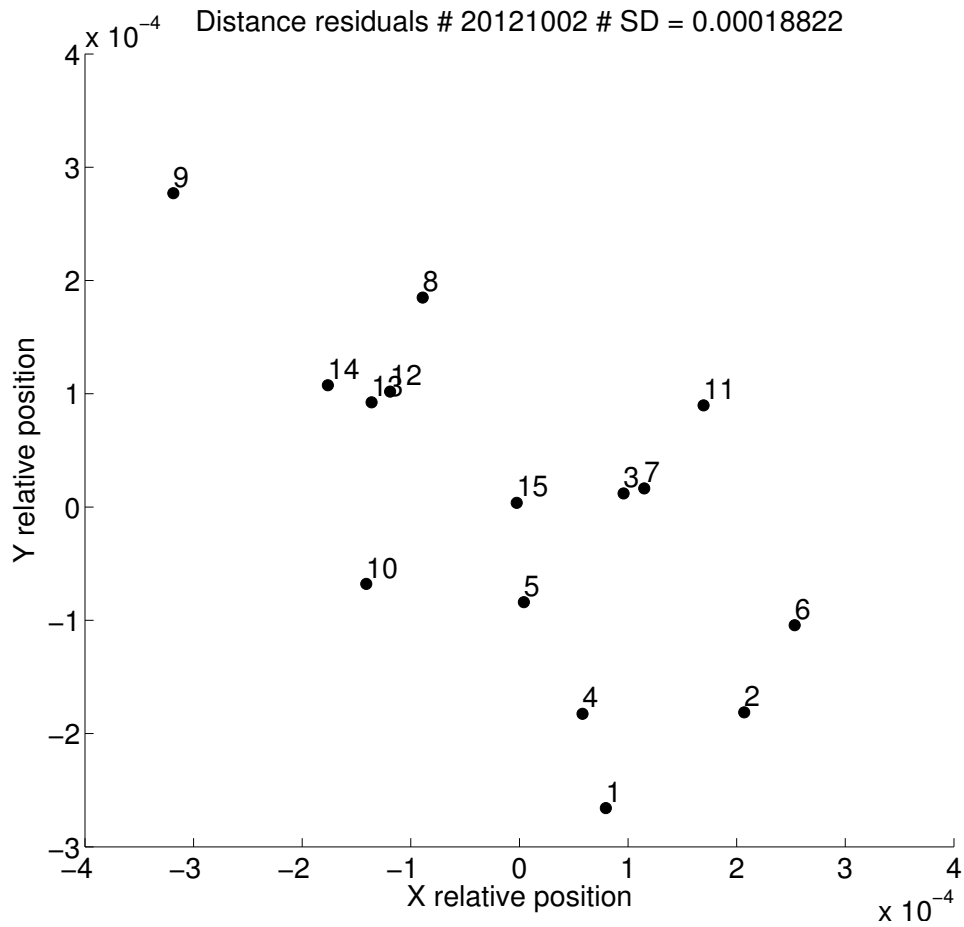


Figure B.8: **Variations of the projected distances between the centroids.** The numbers next to the dots correspond to the number of the star position on the CCD. The value noted “SD” on the plot is calculated as the average residual distance, 1.8×10^{-4} on this figure.

Appendix C

Table of reference documents

Table C.1: Reference documents. The last column “A?” indicates if the document is in the NEAT archive.

Document(s) description	File name (+technical ref. if known)	File type	Responsible or author	A?
NEATRO, NEAT readout system documentation	Description NEATRO (SAP-NEAT-CCa-00xx-12)	pdf	Christophe Cara (CEA)	Y
NEAT proposal of 2010 (call of M3 class missions)	NEAT proposal	pdf	Fabien Malbet (IPAG)	Y
Test and compliance of the zerodur bench by Winlight	Zerodur bench inspection report (PVC1179-A IPAG WO4379)	pdf	Pierre Kern (IPAG)	Y
NEAT-demo mechanical models	-	(Solid Works)	Eric Stadler (IPAG)	N
Optimum number of NEAT visits	Nvisits optimal	xls (spreadsheet)	A. Crouzier (IPAG)	Y
Automatic summary of metrology configuration, based on wiring of fibers	metrology Baselines Configuration v2	xls	A. Crouzier (IPAG)	Y
Photometric budget for the pseudos stars	white source photometric assessment v2	xls	A. Crouzier (IPAG)	Y
Photometric budget for the metrology	metrology photometric assessment v2	xls	A. Crouzier (IPAG)	Y
Error budget for the NEAT mission	AstroFF AEB 1000 v2	xls	Renaud Goullioud (JPL)	Y
Catalog of NEAT targets star	closest MS AFGKM stars topcat	csv	A. Crouzier (IPAG)	Y
Catalog of NEAT references stars	reference stars topcat	csv	A. Crouzier (IPAG)	Y
Topcat session	neat catalog v11	fits	A. Crouzier (IPAG)	Y
Optical error study for NEAT	Etude optique NEAT V1 25 septembre 2014-1 (DCT/SI/OP/2014-15571)	pdf	Jean-Michel Le Duigou (CNES)	Y
Analytic error budget for NEAT lab demo	Bilan Perfo V3 (NEAT-SYS-017)	pdf	Francois Hénauld (IPAG)	Y
Spreadsheet error budget for NEAT lab demo	Bilan Astro V12 (NEAT-SYS-017)	pdf	Francois Hénauld (IPAG)	Y

Appendix D

Components references

Table D.1: Component references.

Sub-system	Component	Manufacturer	Product reference
Metrology	HeNe laser 1.5 mW	Thorlabs	HRS015
	HeNe laser 21 mW	Thorlabs	HNL210L-EC
	Fiber splitter (PM)	Thorlabs	PMC630-50B-APC
	Switch (PM)	Leoni	EOL2x8
	Fiber patch cables (PM)	Thorlabs	P3-630PM-FC
	Modulators	Jenoptik	Integrated Optical Phase Modulator - PM 635
Light detector	CCD	e2v	CCD39-01
	Readout electronics	CEA	custom made
Pseudo stars	Light source: -halogen bulb -power supply -housing -condenser -shutter	Lot-Oriel	-LSB111/5 -LSN111 -LSH102 -LSC111 -LSZ160/161
	Liquid core fiber	Lot-Oriel	LLG210/LLG211
	Pinhole mask	Winlight Optics/FEMTO-ST	custom made
	Diaphragm	IPAG	custom made
Supports	Translation stage: -structure and motors -controlers	-New Focus -New Focus	-9053 -8752/8753
	Zerodur bench	Winlight optics	custom made
Control	Data Acquisition and witch Unit	Agilent	34970A
Environment and temperature control	Pressure gauge	Agilent Varian	AGC-100
	Vacuum chamber	Outillage Mecanique Generale (OMG)	custom made
	Canvas: -structure -air filter	-Faure Automatisme -ADS laminaire	-custom made -custom made
	Peltier: -chip -controler	-TEC Laird Technologies -Keithley	-UT11,12,F2,3030 -2510 TEC SourceMeter
	Water cooler	Thermo scientific	Accel 500 LT
Flat field	Light source: -LED -controler -power supply	Thorlabs	-MWWHF1 -LEDD1B -TPS001
	Multimode optical fibers 200/365 μm	Thorlabs	10230A/10410A
Others	Inverter	Riello UPS	DVR 50/80/110
	Oscilloscope	Agilent	Agilent 1000 Series

Appendix E

NEAT demo user manual

1 Folder naming convention

In order to sort and retrieve files more easily, the raw data, fits cubes and also eventual plots produced from data of a given day are placed in folders with date tags in the following format: “YYYYMMDD” (for example “20140401” if you have acquired data on the first of April in 2014). Every time the “YYYYMMDD” tag appears in this manual, it means “the actual date tag corresponding to the data”.

2 The work environment

Lab environment

Figure E.1 is a simplified plan (roughly scaled) to help you identify the physical elements and devices that are mentioned throughout this manual and it tells where they are located in the lab. Here we only shown the most important (high level) ones. In particular we do not list what is installed on the instrumentation rack. Almost any device that isn't mentioned on the plan is on the rack, but there are quite easy to identify.

Electrical wiring

Electrical devices are split into groups A and B for security reasons, as shown by fig. E.2. The group A can be protected behind a circuit breaker when the short circuit switch is open. This allows for safe operation at CCD cold temperature: it the even of a pressure or power loss, all electric devices of group A are powered off (see section 6.3). Power will not come back at the same time than the mains, it has to be re-established manually. The experiment is thus put in a stable state until we make sure it can be safely resumed. The group B is protected by the inverter, which will maintain power for about 15 minutes in the event of a power loss. This will give time to shut down computers properly.

Network spaces and architecture

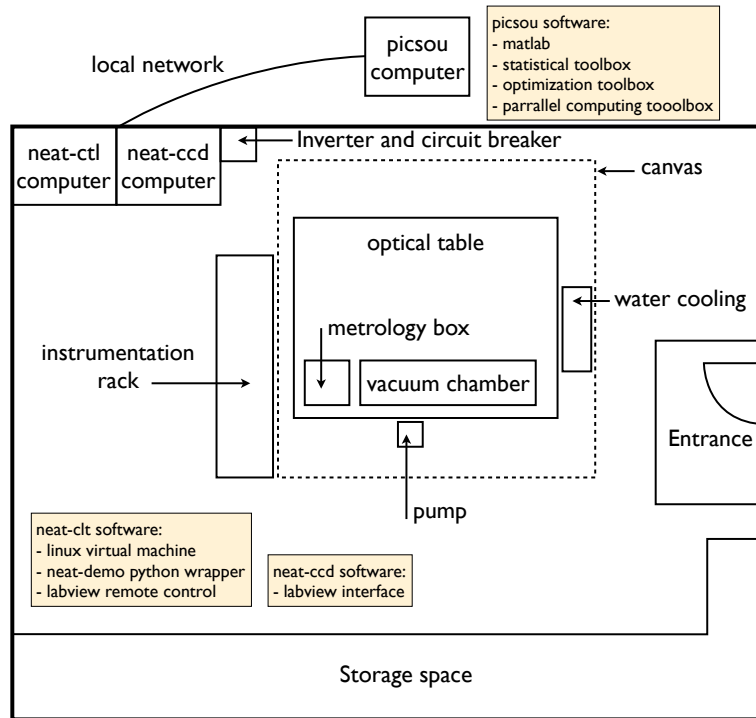


Figure E.1: **Simplified plan of setup inside the neat-demo laboratory.** The plan also show what kind of software utilities each computer has.

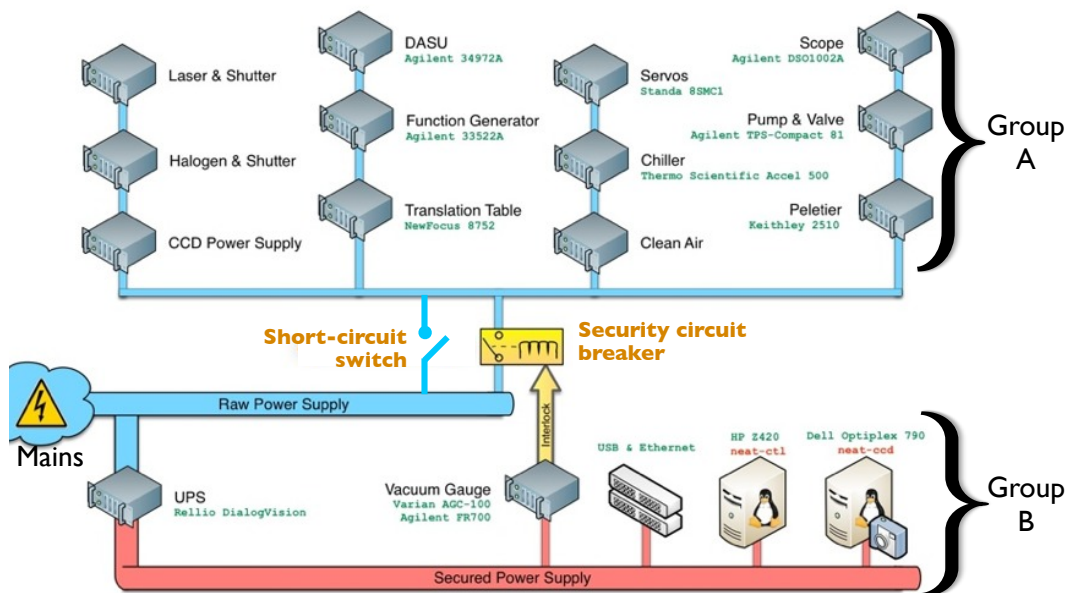


Figure E.2: **Electrical wiring of the neat-demo experiment** Electrical devices are split into two groups: group A is behind the security circuit breaker (or directly plugged to the mains if the short circuit switch is activated), group B is behind the inverter. Instead of using the short-cut switch the pump and valve can be plugged directly into the main as vacuum is not dangerous for the CCD (only the cold is).

A lot of different network resources have been used in addition to the 3 computers already mentioned. The multiplicity of the tools has created an working environment that is rather disintegrated (as in the opposite of integrated). In order to create a unique and functional archive most of the important files and documents have been gathered into the so called “neat-demo archive”. However, the archive is not completely exhaustive and it can be advantageous to access some resources directly. All the existing resources are listed below.

Neat-demo Twiki pages A subset of the Twiki pages for NEAT are exclusively for Neat-demo:

<http://ipag.osug.fr/twiki/bin/view/Ipag/Projets/Neat/LabDemo/WebHome>.

This resource has been used for project management as it offers many different functions, such as maintaining lists of actions, sharing meetings reports, attaching documentation files... Of particular interest is the logbook page:

<http://ipag.osug.fr/twiki/bin/view/Ipag/Projets/Neat/LabDemo/CahierDeManip>.

It contains detailed reports of what was modified on the neat testbed and what kind of data has been acquired (with the CCD39) on a daily basis. This space being properly backed-up and web based, it is not copied in the Neat-demo archive. An IPAG ID is needed to access the resource.

Neat-demo workspace This is a disk space of a size of 500 GB available via the IPAG local network (not backed-up). It was used to share large files between Neat-demo crew members. Access to this space also requires an IPAG ID and can be a bit tricky (see tutorial 6).

Personal workspace Everyone at IPAG has about 15 GB of personal workspace (backed-up on a weekly basis). Workspaces can be accessed from almost any machine: my personal workspace was used to host the matlab scripts which are executed by picsou. The final version of the code has been copied in the Neat-demo archive.

Picsou hard drive Picsou has been equipped with 3 hard drives in a RAID5 configuration (not backed-up). The volume of available data is 2TB. Raw data files are first transferred to picsou and fits cube are generated. Data security is assured because the fits can be rebuild from the raw data files conserved on neat-ccd.

forge.osug.fr SVN repository includes Documentation wiki pages <http://forge.osug.fr/trac/IPAG-neat>. The repository was also used to host the matlab scripts and allow users to share source files (for example with the interns). However the space has reached maximal capacity and I am now working alone so the code is not up to date.

3 Reminder: list of operations


□ Foreword

This section contains the list of operations needed to acquire data, in different cases. We have defined 4 possible modes to operate the CCD (see section 6.3), they are reminded here:


1. In air, ambient temperature. Although far from ideal, it is possible to operate

in air with no cooling at all. Operating the CCD will heat it slightly, to around 25°C. In this mode, the equilibrium temperature of the CCD will be high and unstable, dark current and read noise may be high and variable. This is useful if one want to have images very quickly.

2. In air, cool temperature ($T_{\text{CCD}} = 17^{\circ}\text{C}$)
3. In vacuum, cool temperature ($T_{\text{CCD}} = 17^{\circ}\text{C}$)
4. In vacuum, cold temperature ($T_{\text{CCD}} = -10^{\circ}\text{C}$). This setup is expected to give the best performances: the CCD is specified for operation at this temperature.


 Cold operation in air is not possible because of possible formation of dew or ice on the CCD.


In addition to this, there is a remote control system that makes it possible to control the labview interface via a python script: to enable this remote control, execute the corresponding step.


The list of operations below is the most complete one, corresponding to mode number 4 with the remote control. Some operations are optional as they depend on the chosen mode: they are noted with a  icon.


List of operations

1. Pump the vacuum chamber down to 0.2 mbar



- Seal the vacuum chamber
- Plug the electric power supplies of the vacuum pump and the valve directly on the mains
- Wait until the pressure has decreased to at least 0.2 mbar (this will take about 4 hours)
- Unplug the pump and the valve
-  Engage the circuit breaker and then switch off the short circuit: group A is now protected by the circuit breaker (needed only for cold temperature)

 The valve is normally closed: it will stay open when powered and will automatically close if the pull is plugged or if the power goes out.

 The pump should always be off while taking data to avoid vibration and increase stability. The vacuum sealing is good enough to retain proper vacuum ($P < 0.5$ mbar) for about a day.

 The **circuit breaker** is a protection against a loss of pressure and must always be used when operating the CCD at low temperatures ($T < 17^{\circ}\text{C}$). In the event of a loss of vacuum (i.e. quick pressure increase), cooling must be stopped immediately to let the CCD warm up. If the CCD is kept cool under high atmospheric pressure, dew and/or ice will form on the chip and could damage it. The circuit breaker can only be engaged when the pressure is less than 0.2 mbar and will automatically cut power off if pressure increase to more than 0.5 mbar. Details about this issue are explained in section 6.3.

2. Turn on all devices

-  Water cooler (set $T=18^{\circ}\text{C}/8^{\circ}\text{C}$)
-  Peltier controller (set $T=17^{\circ}\text{C}/-10^{\circ}\text{C}$)

- HeNe laser
- Function generator
- Oscilloscope
- Halogen lamp
- Halogen source shutter

i Start the water cooler and Peltier first to save time: the temperature will take about 10 minutes to stabilize to either 17°C or -10°C.

i After immediate shut down of the cooling, for a water temperature of 8°C, the CCD will take less than 1 minute to warm up above 0°C, thus avoiding the worst (the ice) in case of a loss of pressure.

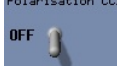
i The HeNe laser can be advantageously left turned-on for weeks at a time (avoiding on/off cycles will extend its lifetime).

i The life time of the halogen lamp is only about 100 hours, it should only be turned-on when taking data.

3. Start the CCD and its acquisition software:

- Turn on the CCD/readout electronics power supply (red button)
- When voltage indicators lights are all green, push the “output” button on the top right (the CCD is now powered)
- Start labview: Applications > National instruments > Labview 2012 > NEATConfig_v10.vi, then click the “⇒” arrow (top left)

- Switch on the labview remote control: 

- Apply CCD polarizations with the switch button: 

- Choose a sequencer:  Each sequencer is for a different frame rate. The numerous choices span from 50 to 977 Hz.

- Go to “Quick Look” tab. Activate automatic refresh view: 

i The CCD quantum well is 300000 e-, the gain is about 10 e-/count, the bias is about 9000 counts. So as a rule of thumb, proper operation of the CCD in the linear regime is from 9000 to 30000 counts. Above this threshold, non linear effects will start to increase above 0.2% (result from linearity calibration). Increase the frame rate or attenuate the light source in this case.

4. Turn on the logger and the neat-demo wrapper

- Turn-on the linux virtual machine (installed with VirtualBox, there is a shortcut on the desk of the neat-ctl computer)
- Log in (ID: neat, Password: same as the default on ESO machines)
- Execute bash command: `start.sh`
- Execute bash command: `python`
- In python, load the neat-demo wrapper with: `from neatCore import *`

i The VM default folder is `/home/neat`

i Executing the command `start.sh` will start the logger: all housekeeping variables, such as errors generated by the software, state of the compo-

nents, pressure inside the chamber and temperatures (by 3 different probes) are recorded in a time tagged folder on the VM: `home/neat/YYYY-MM-DD_HH/MM/SS`.


i If the remote control has been switched on in labview before executing `start.sh`, the remote control is now active.

i Labview remote control and neat-demo python wrappers are grouped into the neatCore python library, the documentation can be found at the following address:

<https://forge.osug.fr/trac/IPAG-neat>. A python file of command examples can be found in the virtual machine default folder or in the appendix 5.

i For better usability, once the VM has started, you can access it from an ssh connection: `ssh -X neat@neat-ctl.obs.ujf-grenoble.fr -p 2222`. This can be useful if for example you want to work on python script files with your favorite text editor.

5. Record data

- Turn on/off the relevant hardware to have either a flat, metrology or stars images
- For each data cube: chose a duration and click: 
- Organize all the data and put it in a folder named YYYYMMDD
- **Or:** use the remote interface to acquire data



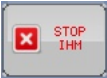
i By default data is created on the neat-ccd machine in the folder: `/mnt/s-db/PCIEData`.

i It is strongly advised to create one folder per data cube/acquisition (see fits generation in section 4).

i The flat field source is not included with the neat-demo wrapper, the broadband white LED has to be turned on and off manually. If you want to have a flat field in an automated sequence, take it manually at the beginning or the end of it.

i To validate a new acquisition duration, you have to type a new number **and then push ENTER**.

6. Power CCD off and shut down labview

- Switch off the CCD polarisations: 
- Shut down the remote control if active:
 - Switch off the python remote control client first: `neatCore.controlCamera("P", "")`
 - Switch off the remote control in labview last: 
- Exit labview: . This will also stop the C acquisition process.

i Switching off the CCD polarisations can also be done via the remote control.

! Do not forget to switch off the CCD polarisation before closing labview. You should be able cut the power off to the CCD without damage, but the safest process is to switch off polarisations first.


7. **Exit the neat-demo wrapper, save logs and turn off the logger**

- Exit python with: `quit()`
- Execute bash command: `stop.sh`
- Enter your login and password (this is needed to save logs)


8. **Return to ambient temperature**


- Shut the Peltier controller off
- Shut the water cooler off

9. **Return to atmospheric pressure**

-  Before proceeding further, check that the temperature has returned above 17°C
- Disengage the circuit breaker and switch the power outlet of group A from the circuit breaker to mains
- Plug the valve to open it
- Use the nitrogen pressurized bottle when starting to fill the vacuum chamber
- Complete with air to 1 bar


10. **Shut down all remaining devices**

 Of course, in case other acquisitions are planned in the near future some devices can safely be left powered or in sleep mode, such as the laser, computers or even the virtual machine.

 Don't ever forget to turn off the halogen lamp ! If you leave it on over the week end you are good to replace it with a new one (experience speaking here).


11. **Transfer the data to picsou**

- execute bash command: `ssh -X picsou`
- execute bash command:
`rsync -rv neat@neat-ccd.obs.ujf-grenoble.fr: '/mnt/sdb/PCIeDATA/YYYYMMDD' /picsou/SHARED/dataNEAT/rawDataCCD39`. This command will synchronize the picsou folder and add new data in case previous data was already taken and transferred.

 It is easier to execute the data transfer form picsou, network rules at IPAG might prevent it if attempted from another machine.

12. **Generate the fits data cubes**

- if not already done, execute bash command: `ssh -X picsou`
- execute bash command: `matlab&`
- open script file: `createFitsCubes.m`
- update the variable `directory` with actual date tag (YYYYMMDD)
- execute the script

 Information about the generation of the fits and what kind of issues may arise is found in section 4.

□ Conclusion

Although the complete list of operation is long, depending on the needs of the user, a lot of operations can be skipped or swapped, in particular for tests (when not in vacuum and cold). The critical points to remember are:

- Never operate at cold temperature if not below 0.5 mbar, use circuit breaker when CCD is cold
- However the chamber can be safely left in vacuum and with the pump on at any time (cold is dangerous, not vacuum)
- Switch off CCD polarisation before closing labview
- If a bug or crash occurs, always restart the software in the same order as presented
- Do not leave the halogen lamp on overnight

Happy experimentation !

4 The data cube creation routine: from row data to fits files

4.1 Introduction

The acquisition system made by the CEA generates two data files labeled V3 and V4, each one containing multiplexed data from two quadrants. Before having usable images, the data has to be extracted from these two files (called “raw data files”), checked, reorganized and stored in a proper data cube which consists of stacked frames. Dimensions 1 and 2 of the cube are pixel rows and columns and the third dimension is time. This process is taken care of by a matlab script called “create-FitsCubes.m”. This section describe every step of the process, it contains important practical information related to the creation of these cubes and to the acquisition system. Such information will be needed if problems arise with the acquisition system for any reason, most likely if new versions are developed. There were a lot of issues with the early versions of the acquisitions system and there are still some minor issues left. In any case **it is advisable that anyone acquiring data and producing fits from them reads this information at least once to have a basic understanding of what is happening and what the caveats are.** For extensive information about the acquisition system, refer to the NEATRO documentation (doc ref.: SAp-NEAT-CCa-00xx-12).

First a word about the rationale behind the acquisition system: the CCD reading electronics have been developed specifically to enable a very high frame-rate. That is why the data comes-in through two separate channels, referred to as V3 and V4. Each channel corresponds to 2 CCD quadrants, the CCD being split into 4 different quadrants. At the end of an acquisition, two “raw data files” (one per channel) are saved on the hard drive. The file corresponding to the channel V3 contains the quadrants 1 and 2, the file corresponding to the channel V4 contains the quadrants 3 and 4 (see Fig. E.3).

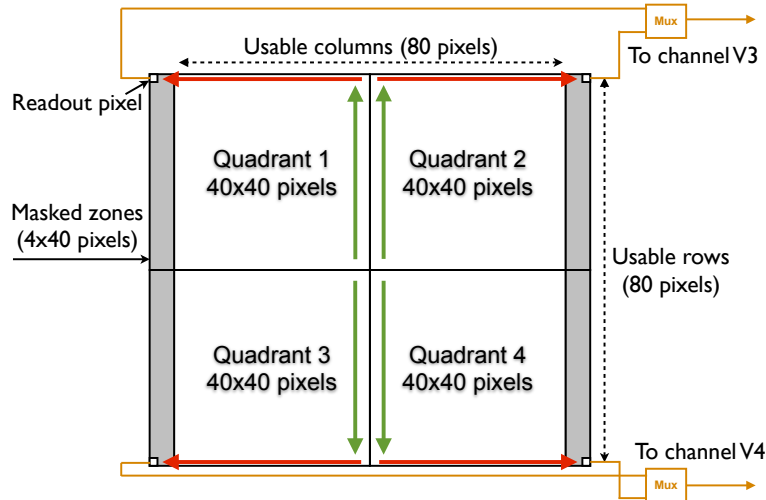


Figure E.3: **Schematic of the CCD quadrants and their relation to the data in V3 and V4 files.** Quadrants and reading directions of the CCD39. In each quadrant the reading occurs row by row. The outer row is read (red arrows) and then all the columns of the quadrant are shifted (green arrow). The process is repeated until all the quadrant has been read. The pixels of quadrants (1,2) and (3,4) are multiplexed and sent respectively into channels V3 and V4.

Important remark: the result presented by Fig. E.3 was deduced by reconstructing the “potato” (see Fig. E.5). It is in contradiction with the information given by the NEATRO documentation (Fig. 13, “construction des trames”): quadrant 3 and 4 are swapped. It is possible to reconstruct an image where quadrants 3 and 4 are flipped and swapped, but this breaks the potato and the potato cannot lie...

The usage of the “createFitsCubes.m” script is quite simple: one simply needs to update the variable `directory` to match the name of the folder containing the new raw data before executing it. It is implicitly assumed that all the raw data to be processed has been stored and sorted within a folder named in the following format: “YYYYMMDD”. At first the script will recursively search for all pairs of raw data file within the folder and its sub-folders and memorize their paths. It will then attempt to process each pair, and if successful, a .fits data cube will be created at the same location than the pair. The name of the fits is derived from common part in the names of the pairs, which is a time tag. It is strongly recommended to place each raw data file pair into a separate folder with a more explicit name in order to facilitate ulterior access to data when loading files for “science” analysis. The function “loadFitsCube” can be used to load a data cube automatically without the need to know its complete name with the cumbersome time tag. It relies on the folder name (given as argument) and extension name (known to be .fits), but it can only work properly if there is a unique fits cube into the folder.

4.2 createFitsCubes.m: list of operations

□ Find the pairs of V3/V4 raw data files

The “raw data files” are named in the following pattern:

Year_Month_Day_Hour_Min_Sec_Mode_Channel.bin

They should be put into subdirectories, sorted by acquisition-pairs (V3/V4 pairs) by the user. The program first task is to identify and list the pairs of files to be processed. The following operations are done on each pair separately.

□ Drop the first 50 frames

On one of the channels, one of the first 50 half frames is often incomplete, the reason of this is linked to the acquisition starting phase but the precise cause has not been found, so to workaround this problem we simply get rid of the first 50 frames of each raw data file.

□ Check the file structure

Given the high speed of the transfer, it is possible that some frames are incomplete, for example if there was a buffer overflow caused by a lack of CPU time during the acquisition. So we check the size of all the half frames inside the file. This function has also been very useful to debug the system. The structure of the half frames is described by Fig. E.4.

Octet			
#1	#2	#3	#4
Target logical address (0x20)	PID (0x01)	Instruction (0x64)	Key (0x00)
Initiator logical address (SpW#1 : 0x40 SpW#2 : 0x50)	Transaction ID (MS)	Transaction ID (LS)	Extended address (0x00)
Address (MS) (0x00)	Address (0x00)	Address (0x00)	Address (LS) (0x00)
Data length (MS) (0x00)	Data length (0x00)	Data length (LS) (0x00)	Header CRC
Frame number (MS)	Frame number	Frame number	Frame number (LS)
Flag (MS) (0xAA)	Flag (0x55)	Flag (0xAA)	Flag (LS) (0x55)
Data1 ADC1 (MS)	Data1 ADC1 (LS)	Data1 ADC2 (MS)	Data1 ADC2 (LS)
Data2 ADC1 (MS)	Data2 ADC1 (LS)	Data2 ADC2 (MS)	Data2 ADC2 (LS)
...
Padding (0xCE)	Padding (0xAC)	Padding (0xEA)	Data CRC
EOP			

Figure E.4: **Structure of a half-frame (2 multiplexed quadrants) in the raw data files.** The expected size of one half-frame is $2 \times 40 \times 44$ uint16, i.e. $3520 \times 2 = 7040$ bytes plus a header of 24 bytes and a trailer of 4 bytes. So its total size is 7068B. The last byte visible on the figure is suppressed by the acquisition card. Credit: CEA, Description NEATRO.

In case an abnormal frame is encountered, i.e. the length between the headers is not right, the program will only save the frames before the abnormal one and a warning will be generated. One recurrent issue that has not been resolved is the following: when processing large data cubes ($\gtrsim 2.5$ GB), an abnormal frame is always encountered near the end of the file. In practice files larger than 2.5 GB can not be created because of this, although the original specification was a maximum size of 4GB. The cause of this problem has never been found.

□ Synchronise the frames between V3 and V4

When the files are saved, the OS can introduce some delay (a few milliseconds) between channels V3 and V4. It means that for each (V3,V4) pair of files there is

a shift of a few frames between the two. Each half frame has a header in which is stored an identification number (the “Frame number”, see Fig. E.4). So we use this information to resynchronize V3 and V4.

□ Demultiplex the data into two quadrants

The data in each raw file are half frames of two multiplexed quadrants. We demux the data into two arrays of size 44x40. Although this is not clear on Fig. E.3, masked zones are parts of the quadrant. The data in the masked areas is simply discarded before scientific use, for which the effective size is 40x40.

□ Reorganize the quadrant orientations

We now have 4 arrays representing the quadrants, to assemble them we have to take into account the readout order to have a spatially consistent image. To verify that this step is correctly implemented we took some data with an irregular paper hole placed in front of the chip. We obtain a spot roughly shaped like a potato (see Fig. E.5): when the “potato” is reconstructed we know that we have correctly oriented each quadrant array.

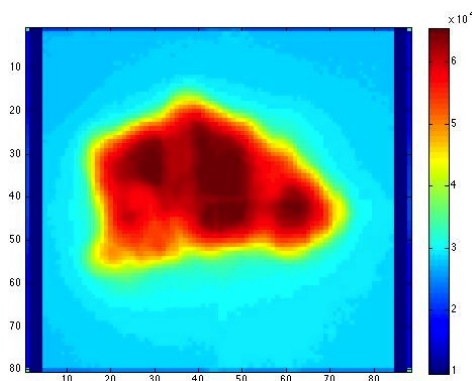


Figure E.5: Image of the correctly reconstructed “potato”, an irregular paper hole placed in front of the chip.

□ Save the cubes in a .fits format

We have now reconstructed clean data cubes of size $80 \times 88 \times N_{\text{frames}}$, we can save them in a .fits file format for later use. The original data is in “big endian” uint16, but the fits format doesn’t allow for unit16 format, so we use a manual conversion to int16. This is important because the total volume of data will be significant (a single data cube can in theory be up to 4GB), so we cannot afford to use int32 (doubles the volume) or even worse, floats (volume x4). To convert from uint16 to int16 we subtract 32768 to the data. Upon loading, we simply have to add 32768 back.

5 Python example command file

```
from neatCore import *
```

```

# camera commands (labview remote controle)
neatCore.controlCamera("P", "") # Read acquisition card status (test:
    camera responds?)
neatCore.controlCamera("F", "") # get free disk space
neatCore.controlCamera("Q", "once") # save small dataCube
neatCore.controlCamera("D", "/20140219/testFolder")
neatCore.controlCamera("A", "on") # star acq
neatCore.controlCamera("A", "off") # stop acq
neatCore.controlCamera("K", "") # stop remote control camera session.
    Needed before stopping remote control

# start modulators
neatCore.outputModulatorSignal("1", "T", 0.1, 10, 0, 0)
neatCore.outputModulatorSignal("2", "T", 0.1, 10, 0, 180)

# translation stage
neatCore.moveAligner("X", "T", 1000, 1000, 1000) # move centroids to the
    TOP
neatCore.moveAligner("Y", "T", 1000, 1000, 1000) # move centroids to the
    LEFT (default: to bottom left)
neatCore.moveAligner("X", "R", 1000, 1000, 1000) # move baffle pupil to
    the LEFT
neatCore.moveAligner("Y", "R", 1000, 1000, 1000) # move baffle pupil to
    the bottom

# to reset virtual stops
neatCore.moveAligner("X", "h", 1000, 1000, 1000)
neatCore.moveAligner("Y", "h", 1000, 1000, 1000)

# square move sequence
neatCore.moveAligner("X", "T", 12000, 1000, 1000)
neatCore.moveAligner("Y", "T", -18000, 1000, 1000)
neatCore.moveAligner("X", "T", -18000, 1000, 1000)
neatCore.moveAligner("Y", "T", 18000, 1000, 1000)

# L move sequence (for with 3 centroids only)
neatCore.moveAligner("Y", "T", -18000, 1000, 1000)
neatCore.moveAligner("X", "T", 3000, 1000, 1000)
neatCore.moveAligner("X", "T", -6000, 1000, 1000)
neatCore.moveAligner("Y", "T", 18000, 1000, 1000)

# peltier setting:
neatCore.setTemperature(17)
neatCore.setTemperature(-10)

# switch control
neatCore.setSwitchChannels(0,0) # shut off all light
neatCore.setSwitchChannels(1,2) # fiber 1 and 2 on lanes 1 and 2

# examples / doc
neatCore.outputModulatorSignal("1", "T", 0.1, 10, 0, 0) # channel,
    waveform, freq, ampl, offset, phase (deg)

```

```
neatCore.moveAligner("Y", "R", 10000, 1000, 1000) # axis, T/R, Nsteps,  
           motor acc, motor speed
```

6 Tutorial: mounting directories with SSH tunnel manager and Macfusion

In this tutorial we ssh tunnel to jupiter and mount the neat workspace locally. But the same method can be applied to all network spaces accessible through an ssh tunnel.

1. Connect manually to the ssh to verify that you have the access rights

- if login from outside the lab, connect to janus first:

```
ssh -X @janus.obs.ujf-grenoble.fr
```

- connection to the neat space with:

```
ssh -X @jupiter.obs.ujf-grenoble.fr
```

2. Creation of your public key

This will avoid having to enter your password everytime you connect, follow the instructions here:

<http://ipag.osug.fr/twiki/bin/view/Trash/Intranet/InfoDocAgentSsh>

3. SSH Tunnel manager

Download link: <http://www.macupdate.com/app/mac/10128/ssh-tunnel-manager>

Configuration:

- Click on the button configuration
- Create a new profile

- Nom: NEAT demo
- Hôte: `janus.obs.ujf-grenoble.fr`
- Port: 22
- Redirections locales: Port: 2022, Hôte distant: `jupiter.obs.ujf-grenoble.fr`, Port: 22

- Go into "Options" and select: Connection automatique / Gérer l'authentification / Activer la compression

4. Mac fusion

If not already installed, install macfuse first:

download link for macfuse: <http://code.google.com/p/macfuse/>

download link for macfusion: <http://macfusionapp.org/>

Configuration:

- click on "+" to create a new SSHFS mount point
- click on edit:

- SSH:
 - Host: localhost
 - User name: *your username*

- Password: *your password*
- Path: */data/neat/*

- SSH Advanced:
 - Port: 2022
 - Enable Compression: Yes
 - Follow Symbolic Links: Yes
 - Extra options: `-o idmap=user -o uid=yourUID -o gid=yourGID`

- Mac fusion:
 - Mount Point: `/Users/username/dirname` (example)
 - Volume Name: `dirname` (example)

7 Metrology switch configuration

The fibers are separated into two groups: 4 are vertically aligned and 4 are horizontally aligned (see Fig. E.6). As we do not use diagonal baselines, we want to max out the number of accessible baselines within each group. For this we have to connect 2 fibers from each “sub-switch” (1x4) to each group of 4 fibers. Within each group, we will have 4 baselines available, over a total of 6 (number of 2-combinaisons among the 4 fiber tips) that would have been possible with a truly 2x8 switch. The other possibilities are obviously less interesting, if instead of 2/2 we go with a 3/1 or 4/0 mixing between the switch and the groups, we end up with respectively 3 or 0 available baselines within the groups.

When doing a 2/2 mixing, we have in principle 24 possible cabling configurations (4!) for each group, but only 6 of them are non equivalent (they will change which baselines are available in the end), a lot of them are redundant and will only result in a permutation of switch command. The easiest way to think about it is the following: for each group of 4 fibers one has to select a first impossible baseline (2 fibers tips among 4). These two fibers are set to come from the same sub-switch and the corresponding baseline is eliminated. The other two fibers of the same group also are coming from the same sub-witch and are also eliminated. The 4 remaining combinations are all accessible.

7. Metrology switch configuration

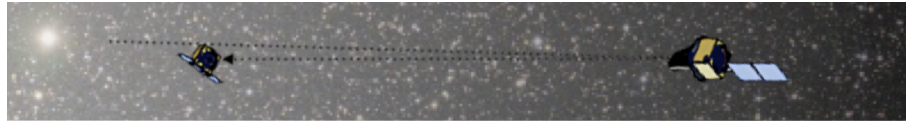
This file contains the current metrology baseline configuration, this includes both the set of connections after the switch and in the vacuum chamber
 Possible upgrade: switch 4 with 3 and 5 with 6 between the switch and the plug
 switch command: setSwitchChannel(Ti,Si)
 Inputs: Outputs:



Figure E.6: **Metrology configuration spreadsheet.** It summarize all the practical information needed about the current metrology configuration: how the connectors/fibers are paired between the switch and the vacuum plug, after the vacuum plug inside the vacuum chamber, what are the final baselines interfringe distances and what are the corresponding switch commands.

Appendix F

NEAT memo: Creation and exploitation of the NEAT catalog



NEAT Memo

NEAT-sci-001

Orig. : *A. Crouzier*
 Dest. : NEAT consortium
 Date : 16-09-2014
 Version : v4

Subject : **Creation and exploitation of the NEAT catalogs**

Memo version history

- 25-Jan-2012 (v1): initial writing
- 29-May-2012 (v2): addition of the section for HZ calculation
- 01-Jun-2012 (v3): reorganization of the sections
- 16-09-2014 (v4): major update, change of main sequence selection criteria (broader tolerances), addition of observational strategies

Scope

The targets of the NEAT mission are the Sun-like stars in our close neighborhood. They correspond more precisely to the main sequence stars of spectral types A, F, G, K and M that are located at a distance of less than 20 pc from the Sun.

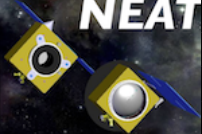
The goal of this memo is to describe the sequence of commands I used to create the **NEAT catalog of targets** with the program Topcat. This catalog is defined as the A, F, G, K and M main sequence stars, located at less than 20 pc from the Sun, in the Hipparcos catalog. We will also define the **NEAT catalog of references** stars from the **NEAT catalog of targets**. Other sections will show how one can use Topcat and the newly defined NEAT catalogs to check for sample completeness and to obtain statistics about the target and reference stars.

Topcat is a spreadsheet application for astronomical catalogs, developed by Mark Taylor. It offers the possibility to define catalog subsets and has a nice set of visualization tools. It can be downloaded for free from this webpage: <http://www.star.bris.ac.uk/~mbt/topcat/>.

Acronyms

BC Bolometric Correction

Appendix F - NEAT Memo: Creation and exploitation of the NEAT catalog

	Nearby Earth Astrometric Telescope	Ref: NEAT-sci-001 Version : v4
	<i>Creation and exploitation of the NEAT catalogs</i>	Date : 16-09-2014 Page : 2 / 34

HZ Habitable zone

NEAT Nearby Earth Astrometric Telescope

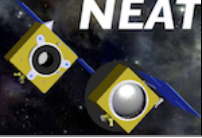
SciDAVis Scientific Data Analysis and Visualization

SNR Signal to Noise Ratio

TOPCAT Tool for OPerations on Catalogues And Tables

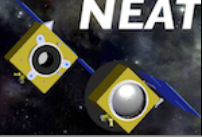
Reference documents, files, catalogs and papers

- NEAT: a spatial telescope to detect nearby exoplanets using astrometry (PhD manuscript of Antoine Crouzier)
- NEAT Proposal of 2010
- TOPCAT Reference manual
- Hiparcos catalog - available on Vizier
- Tycho2 catalog - available on Vizier
- The exoplanet catalog of “The Extrasolar Planets Encyclopaedia”
- Transformations from Theoretical Hertzsprung-Russell Diagrams to Color-Magnitude Diagrams: Effective Temperatures, B-V Colors, and Bolometric Corrections (Flower, 1996)
- The B-V / BC / Teff relation for main sequence stars, subgiants, and giants (Flower, 1996) - available on Vizier
- Target star catalogue for Darwin Nearby Stellar sample for a search for terrestrial planets (Kaltenegger et al., 2010).
- Habitable Zones around Main Sequence Stars (Kasting et al., 1993)
- Physical Parameters of the Stars (Schmidt-Kaler, 1982)
- NEAT error budget (Renaud Goullioud, priv comm.)
- Spreadsheet for calculation of NEAT photon noise limit: `neat_photon_limit.xls`
- Planet population synthesis model (Alibert et al., 2013).
- List of synthetic exoplanet systems: `CD2133_1tev.dat`.
- Matlab script (calculation of exoplanet yields): `observational_strategy_yields.m`
- Python script (calculation of reference equivalent magnitude): `process_ref_stars.py`

	Nearby Earth Astrometric Telescope	Ref: NEAT-sci-001
	<i>Creation and exploitation of the NEAT catalogs</i>	Version : v4 Date : 16-09-2014 Page : 3 / 34

Contents

1	Creation of the NEAT catalogs of target and reference stars	4
1.1	Extraction of the NEAT catalog of targets from the Hipparcos catalog	4
1.2	Creation of the catalog of reference stars.	5
1.3	Availability of the reference stars	7
1.4	Calculation of the reference star total flux	8
2	Creation of the NEAT columns	9
2.1	Determination of the astrometric signal in HZ	9
2.2	Time allocation schemes and science yields	14
2.3	Astrometric signal in HZ versus stellar mass	22
2.4	Crossmatch with "The Extrasolar Planets Encyclopaedia"	23
2.5	Checking the sample completeness	27
A	Summary of the Topcat operations	30
B	List of the NEAT columns	30
C	Python script for summing reference stars flux: source code	32

	Nearby Earth Astrometric Telescope	Ref: NEAT-sci-001 Version : v4
	<i>Creation and exploitation of the NEAT catalogs</i>	Date : 16-09-2014 Page : 4 / 34

1 – Creation of the NEAT catalogs of target and reference stars

1.1 – Extraction of the NEAT catalog of targets from the Hipparcos catalog

The **NEAT catalog of targets** will consist of all the main sequence stars of spectral types A, F, G, K and M located at a distance of less than 20 pc from the sun (see Fig. 1). What I call the **final list of targets** will be a sub sample of this pre selection, relative to the exercise of observation time allocation. The final selection will prioritize the targets with the highest astrometric signals, so depending on the observational strategy, a fraction of the stars is likely to be excluded.

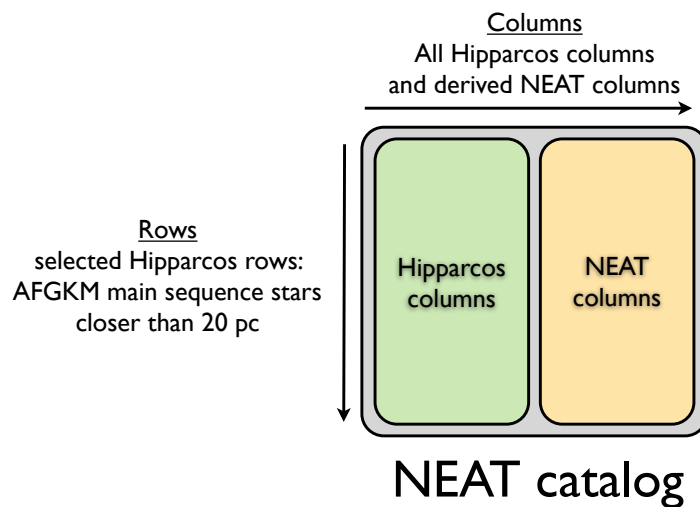


Figure 1: *Schematic view of the NEAT catalog of target stars. The NEAT targets are selected within the Hipparcos catalog. The part called NEAT columns are computed values from the Hipparcos original columns.*

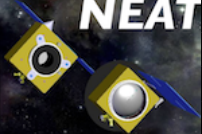
Unfortunately Topcat does not offer the possibility to save a list of commands. Instead the full session, including all the Hipparcos data, has to be saved in a fits-plus file, which can have a substantial size (hundreds of mega bytes in our case), this constraint limits the possibility to share the Topcat sessions. To mitigate this problem, I will describe in details the commands I used to define the NEAT catalog.

To begin, the NEAT catalog is created from a subset of stars from the Hipparcos catalog. In order to manipulate the data more easily, several subsets will be defined. Additionally, we have to download the Hipparcos catalog from the vizier portal because we need to add RA2000 and DEC2000 columns.

This is done with the following sequence of actions:

- Search for the Hipparcos catalog in Vizier.
- In the catalog list select **All** (so you will be also downloading the tycho catalog, which is the last table).
- On the **Preferences** window on the left, tick **All columns**, set max to **unlimited**, set the format to **VOTable** and verify that the J2000 box is active in the **Compute** menu.

Appendix F - NEAT Memo: Creation and exploitation of the NEAT catalog

	Nearby Earth Astrometric Telescope	Ref: NEAT-sci-001
	<i>Creation and exploitation of the NEAT catalogs</i>	Version : v4 Date : 16-09-2014 Page : 5 / 34

- Click **Query selected Tables** and save the tables on the hard drive.
- In Topcat, open the **Load New Table** dialog box via the menu **File > Load table**.
- Click on the **System Browser** icon and load the catalogs.
- Select the Hipparcos main catalog: 1/239/hip_main (it is the first table in the **Table List**).
- Click the tool **Display row subsets**.
- Click the tool **Define a new subset...** in the window showing the list of subsets
- Type a condition in the column **Algebraic expression**

The last two actions are repeated for each new subset. Each subset is defined by its own algebraic expression. Here is the list of all the subsets I chose to create:

- A first subset named `closest_stars` containing all the Hipparcos stars closer than 20 pc, using the following expression: `Plx > 50`
- One subset for each sun-like spectral type (A, F, G, K and M), among the closest stars. For example, for the main sequence F stars, the subset name is: `closest_MS_F_stars` and the expression is:
`_2 && matches(SpType, "^F.*(IV-V|[^I]V)")`
- One subset named `closest_MS_FGK_stars`, this is the union of the three subsets above. The expression is:
`_2 && (matches(SpType, "^F.*(IV-V|[^I]V)") || matches(SpType, "^G.*(IV-V|[^I]V)") || matches(SpType, "^K.*(IV-V|[^I]V)")`
- One subset named `closest_MS_AFGKM_stars` with the A,F,G,K and M main sequence stars closer than 20 pc. This is the NEAT catalog of targets. The expression is:
`_2 && (matches(SpType, "^A.*(IV-V|[^I]V)") || matches(SpType, "^F.*(IV-V|[^I]V)") || matches(SpType, "^G.*(IV-V|[^I]V)") || matches(SpType, "^K.*(IV-V|[^I]V)") || matches(SpType, "^M.*(IV-V|[^I]V)")`

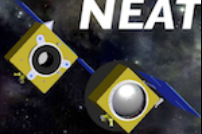
The `(IV-V|[^I]V)` part in the regular expression mean that we accept selected all main sequence stars (or between main sequence and sub-giant). For stars with two components (separated by a “+” sign), we should ideally base the selection on the main component. However, errors will be made if the secondary component only is main sequence: with this regular expression, the star will be included in the list. The problem is that it is not possible to use a “\” sign in the regular expression (it causes an error in Topcat), it this therefore impossible to get the needed escaped “+” in the regex.

“`_2`” refers to the second subset (“`_1`” is referring to the full Hipparcos catalog itself). By doing this, each spectral class can be easily manipulated. You should now have 351 stars in the `closest_MS_FGK_stars` subset and 455 in the `closest_MS_AFGKM_stars` subset.

1.2 – Creation of the catalog of reference stars.

One strong requirement of NEAT is the availability of the reference stars. The field of view of NEAT is limited to about 0.6° because of the aberrations. For each target star, NEAT needs at least 6 reference stars of $V_{\text{mag}} < 11$ in the field of view to reach its specified accuracy. The reference stars are ideally quiet and immobile stars, used for differential astrometry measurements. In practice they are mostly K giants at long distances. Ideally, the reference stars should fill the following list of conditions:

Appendix F - NEAT Memo: Creation and exploitation of the NEAT catalog

	Nearby Earth Astrometric Telescope	Ref: NEAT-sci-001 Version : v4
	<i>Creation and exploitation of the NEAT catalogs</i>	Date : 16-09-2014 Page : 6 / 34

- Magnitude lower than 11
- Not too noisy...

Stars too close, too active or with giant planets could show excessive noise and be unsuitable to be used as references. In practice, we only have knowledge about the magnitude in Tycho and some targets critically lack reference stars. It is important to keep all we can find¹. Also, the shape of the NEAT detector is square, which authorizes the use of some reference stars located between 0.6° and 0.84° ². So we will use the whole Tycho catalog, with a threshold of either 0.6 or 0.84° . We will also calculate a magnitude equivalent to the sum of the flux from the reference stars to estimate the reference star photon noise for each target (some targets might have a lot of references stars but only faint ones).

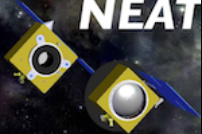
The reference stars are found by cross-matching the NEAT catalog (`closest_MS_AFGKM_stars` subset) with the Tycho catalog. The list of conditions above can be applied to filter out all the stars that are unsuitable (for example to reject stars with $V_{\text{mag}} < 13$). It is necessary to apply at least the condition `!NULL_Vmag`: some stars have unknown/null magnitudes and will crash the script (section 1.4) unless they are filtered out. Here is the list of the corresponding operations in Topcat:

- Select the Tycho catalog ("`1/239/tyc_main`").
- Create a "reference_stars" subset of the Tycho catalog with the conditions of your choice (for example `Vmag < 13 && !NULL_Vmag`).
- Crossmatch the NEAT catalog ("`closest_MS_AFGKM_stars`" subset) with the "reference_stars" subset. Use the following parameters:
 - **Max Error** 0.3 or 0.42°
 - **Table 1**: Hipparcos main catalog
 - **RA column** (for Table 1): `_RAJ2000` - degrees
 - **Dec column** (for Table 1): `_RAJ2000` - degrees
 - **Table 2**: Tycho main catalog
 - **RA column** (for Table 2): `_RAJ2000` - degrees
 - **Dec column** (for Table 2): `_RAJ2000`- degrees
 - **Match selection**: Best match for each Table 2 row
 - **Join type**: 1 and 2
- Eventually plot the results on a sphere (to visually verify the RAs and DEC)s)

You should obtain a crossmatch table containing 6466 reference stars (for 0.84° FoV and with $V_{\text{mag}} < 13$). Click on the tool **Display Table Metadata** and in front of the raw **Name**,

¹Tycho is magnitude limited to about $V_{\text{mag}} = 12 - 13$. It is not complete after $V_{\text{mag}} = 11$, but still have a lot of stars between 11 and 13. These stars will be our backup reference is we lack brighter one and we will not be flooded with stars too faint to be useful.

²With only 0.6° of FoV, the first result indicated that a significant proportion of target have few reference stars (4 or less). Using 0.84° improves the result quite dramatically for some stars. We will overestimate the number of available references stars in some rare cases (not all references close to 0.84° can be used). But seeing how to best place a square FoV can not be solved with Topcat, it would require tricky programming instead.

	Nearby Earth Astrometric Telescope	Ref: NEAT-sci-001
	<i>Creation and exploitation of the NEAT catalogs</i>	Version : v4 Date : 16-09-2014 Page : 7 / 34

change the value `Joined to Tycho reference stars crossmatch`. This will help distinguish all the different crossmatches.

The current method used to select the reference stars is very crude. For a real mission, other criteria should be used to filter out unsuitable reference stars. A minimum distance (for example 1 kpc) and a condition on the activity of the stars could be added. The parallax of the Tycho catalog can not be used as the errors are typically several dozen of mas (as a result, distances of more than one hundred parsec are not measured properly). An alternative to estimate the distance would be to use the H-R diagram... or to wait for Gaia. The statistics we will obtain are close to a best case scenario for the number of reference stars because Tycho is 99% complete to magnitude 11.

1.3 – Availability of the reference stars

Now that we have a catalog of the reference stars, we want to know **the distribution of the size of the groups of reference stars**, each group being all the reference stars associated with one NEAT target. This is a bit tricky to do this with Topcat: using directly the information of the column `count` in the crossmatch results to plot an histogram doesn't yield correct results. This is because for a group of n stars, each reference star will contribute one count. Consequently, in the final distribution, a group of size n will be counted n times.

To tackle this problem, do the following sequence of actions:


- Open the menu **Joins > Internal match..**
- Select the reference stars crossmatch in **Table**.
- Chose the option **Eliminate all but first of each group**.
- Leave all the other options unchanged and click ok.
- Change the name of the new crossmatch table to:
`Histogram group size reference stars`

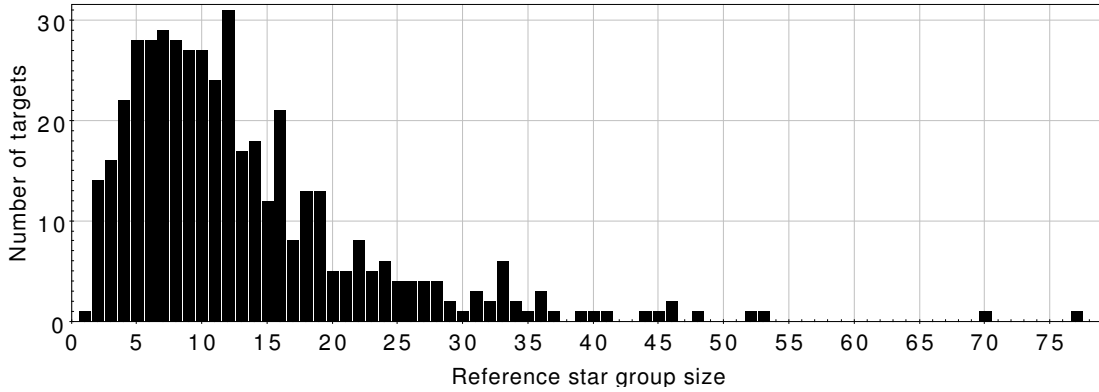
Now you can plot the histogram of the distribution of the number of reference stars for each NEAT target stars. Click on the **Histogram** tool, then change the X-axis to **GroupSize-1**. The -1 eliminates the target stars from the group (it was counted with the reference stars). The result is shown in the fig. 2.

Remark: The internal match discards the stars that are not in groups, i.e. for which no reference star is available. They do not appear in Fig. 2. By doing an internal match with the option **Eliminate All Grouped Rows** you will find how many targets are without reference (0 for 0.84° FoV and with $V_{\text{mag}} < 13$).

Conclusions

Though in average the number of reference is good, there is a significant fraction of the NEAT targets (about 100 of 340) that have only 4 available references stars or less (with a field of 0.6° and a V_{mag} limit of 11). This could affect the ability of NEAT to find planets around these stars.

	Nearby Earth Astrometric Telescope	Ref: NEAT-sci-001
	<i>Creation and exploitation of the NEAT catalogs</i>	Version : v4 Date : 16-09-2014 Page : 8 / 34

Figure 2: *Distribution of the number of reference stars per NEAT target star.*

1.4 – Calculation of the reference star total flux

The total flux of the reference stars is useful to estimate the integration time requirement for each target star and for a given astrometric signal and mass detection threshold.

It is not straightforward to obtain this quantity with Topcat: we have a catalog of the reference stars, which are organized in groups that also include the target star. We have the visible magnitude of all the stars of each group and we want to “sum” the magnitudes to find an equivalent magnitude which flux corresponds to the sum of the flux of the reference stars. The problem is that Topcat does not provide a way to perform this specific operation. So we will export the catalogs of the reference stars and the target stars as .csv files and run a python script through them. The catalog of the reference stars is called `reference_stars_topcat.csv` and the catalog of the subset of main sequence AFGKM NEAT targets is called `closest_MS_AFGKM_stars_topcat.csv`. To create these files, select the appropriate table and subset, then use the menu **File > Save Table(s)/Session**, select the .csv format, enter the name and hit save.

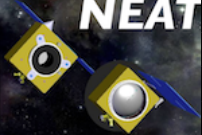
The operations applied in the python script is summarised here:

- Get all the targets’ hipparcos IDs from the catalog of targets
- Loop though the catalog of references and identify the targets stars among them
- Loop though the catalog of reference stars, sum the flux of all the reference stars (excluding the targets) and calculate the equivalent magnitudes
- Add the equivalent magnitudes into the catalog of targets

The equivalent magnitude is the magnitude of a star which flux would be the sum of the reference star flux. We note F_0 the reference star flux for the visible magnitude. We have:

$$M = -2.5 \log (F/F_0) \Leftrightarrow F = F_0 \times 10^{-M/2.5}$$

$$\Rightarrow \sum_i F_i = F_0 \sum_i 10^{-M_i/2.5} \Rightarrow M_{eq} = -2.5 \log \left(\sum_i 10^{-M_i/2.5} \right)$$

	Nearby Earth Astrometric Telescope	Ref: NEAT-sci-001 Version : v4
	<i>Creation and exploitation of the NEAT catalogs</i>	Date : 16-09-2014 Page : 9 / 34

After running the script a new csv file is created: `closest_MS_AFGKM_targets_topcat_out.csv`. Import the file back into the list of table via the menu **File > Load**. The new column `EqRefMag` has been added.

Figure 3 is an histogram of the equivalent magnitudes. The NEAT error budget assumed 6 stars of magnitude 11 (equivalent magnitude of 9.05). The histogram confirms that this is a sound assumption: nearly all the target have enough bright reference stars to verify “equivalent” $V_{\text{mag}} < 9.05$.

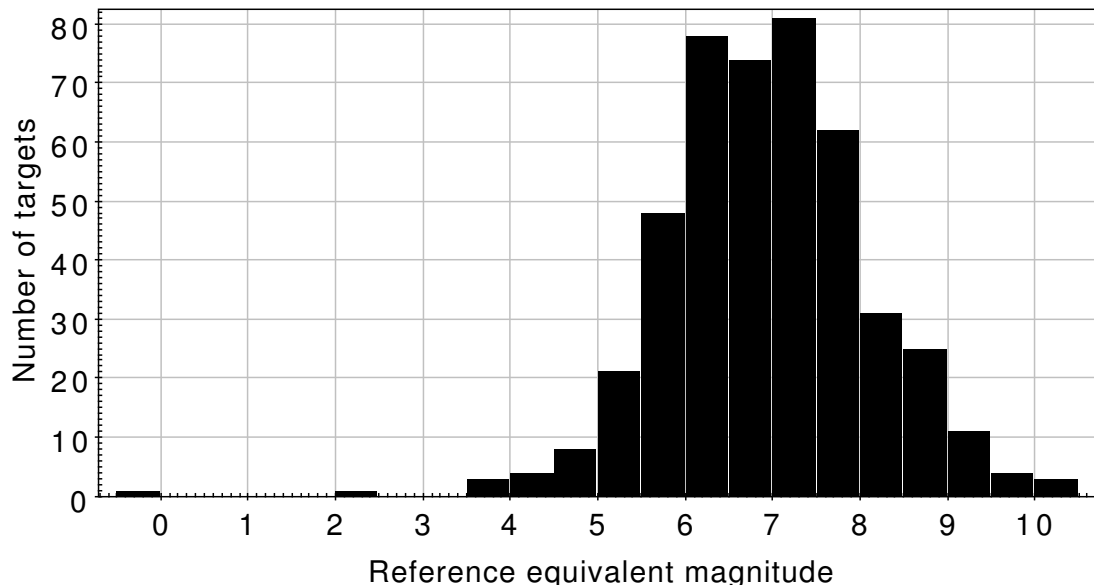


Figure 3: *Distribution of the equivalent magnitudes of groups of reference stars (one group per target).*

2 – Creation of the NEAT columns


In this second part we will add a lot of NEAT columns to the catalog of targets. Some of them can in principle be added before the column `eq_ref_mag` has been added. But the latter is integrated into a new table (`closest_MS_AFGKM_targets_topcat_out.csv`, different from the original Hipparcos subset). So any column created before has to be created again, or a crossmatch much be performed to merge the two tables. The simplest way to avoid the problem is to create the `closest_MS_AFGKM_targets_topcat_out.csv` table first (with the `eq_ref_mag` column), and to create all other NEAT columns later.

2.1 – Determination of the astrometric signal in HZ

2.1.1 – Introduction

The goal of this subsection is to add a new column specifying the astrometric signal of an Earth mass planet in the HZ of the target stars. The amplitude of the astrometric signal

Appendix F - NEAT Memo: Creation and exploitation of the NEAT catalog

	Nearby Earth Astrometric Telescope	Ref: NEAT-sci-001
	<i>Creation and exploitation of the NEAT catalogs</i>	Version : v4 Date : 16-09-2014 Page : 10 / 34

yielded by an exoplanet at a distance D , of mass M_{Planet} , with a semi major axis R around a star of mass M_{Star} is given by:

$$A = 3\mu\text{as} \times \frac{M_{\text{Planet}}}{M_{\text{Earth}}} \times \left(\frac{M_{\text{Star}}}{M_{\text{Sun}}}\right)^{-1} \times \frac{R(\text{AU})}{1\text{AU}} \times \left(\frac{D(\text{pc})}{1\text{pc}}\right)^{-1} \quad (1)$$

From that formula one can see that a star mass increase will have the following effects on the signal:

- Greater star/planet mass ratio (decreases the signal)
- Greater star luminosity \Rightarrow further away HZ \Rightarrow greater semi major axis (increases the signal)

Note that the mass and the spectral type are strongly correlated, so changes in the stars emission spectrum have to be taken into account. The additional effects, implicit in the formula above, that happen when the mass increase are listed below:

- Blue shifted spectrum \Rightarrow Greater normalized solar flux factor \Rightarrow closer HZ \Rightarrow smaller semi major axis (decreases the signal).
- Greater semi major axis \Rightarrow Period increase
- Increase of the target stellar flux.

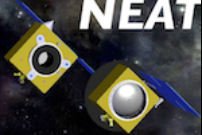
The normalized solar flux factor is a coefficient taking into account the overlap of the stellar emission and the planetary albedo. The values of this coefficient for different spectral types are found in the literature (Kasting et al., 1993). The overall effect is a moderate negative feedback on the variation of the HZ location with the mass: for more blue and luminous stars, the albedo is higher, so the net energy input is a bit smaller than expected.

The period also has an influence on the detection threshold. Because of the nature of the mission, for periods longer than the mission duration the minimum planet mass required for detection increases, despite an increasing astrometric signal: in this case only a portion of the orbit will be sampled so a larger SNR is required. But in our case study this parameter doesn't matter much: even for F stars the planet period at the HZ outer edge barely exceed 5 years.

Finally, if the stellar flux is larger, the precision of the astrometric measurements will increase more rapidly with the integration time (noted T): the location error on the measured centroid of the target will be $\sigma_{\text{measure}} \propto \frac{1}{\sqrt{TF_{\text{star}}}}$. However in the case of NEAT which is differential astrometry, the photon noise of the much fainter reference stars dominates in most cases. This means that the final precision will be almost insensitive of the target star flux, but will depend on: the astrometric signal, the photon noise of the reference stars and the integration time.

The overall effect of the host star mass on the astrometric signal in HZ is a bit tricky to determine. The result is that the astrometric signal increase with the stellar mass, see section 2.3 for details.

Another important parameter I haven't mentioned yet is the distance, but it is easily derived from the Hipparcos parallax. The last parameter, the planet mass, can not be known before the observations. We will normalize by the Earth mass: the signal for any mass is easily obtained by scaling by the ratio: $\frac{M_{\text{planet}}}{M_{\text{Earth}}}$.

	Nearby Earth Astrometric Telescope	Ref: NEAT-sci-001 Version : v4
	<i>Creation and exploitation of the NEAT catalogs</i>	Date : 16-09-2014 Page : 11 / 34

2.1.2 – Determination of Dist, L, HZin, HZout, and Mass

To determine the astrometric signal in habitable zone, we will determine the following intermediate quantities: the distance, the bolometric luminosity, the HZ inner and outer boundaries, and the star mass for each NEAT target star (respectively noted Dist, L, HZin, HZout, and Mass). Figure 4 shows how L, HZin, HZout, and Mass are derived. The detailed descriptions of the process for each quantity are presented below.

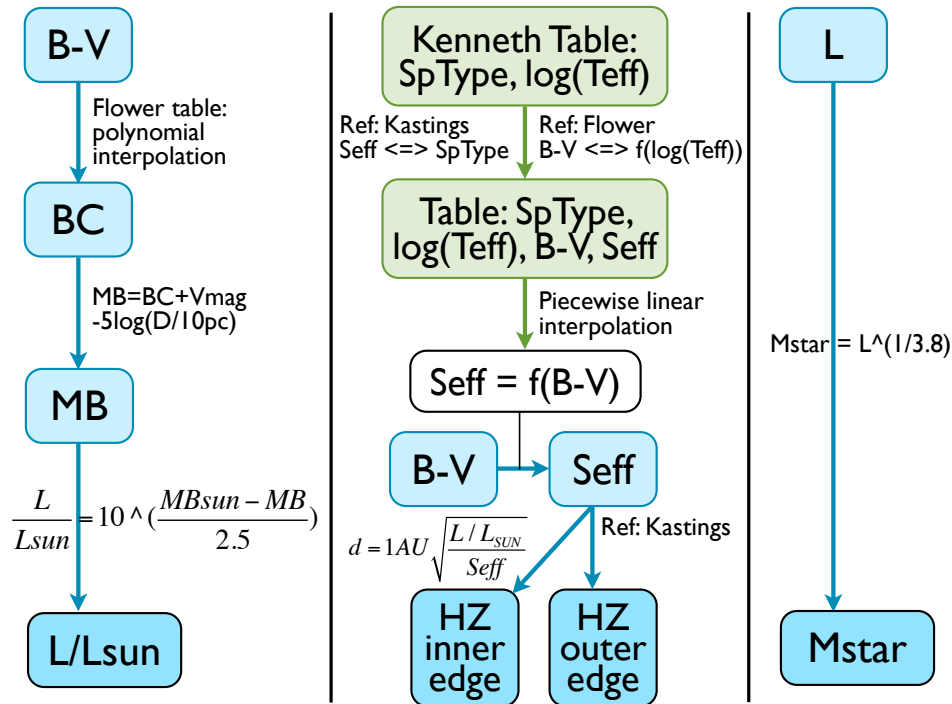


Figure 4: **How the luminosity, HZ boundaries and the stellar mass are derived.** The blue boxes represent added columns to the catalogues and the green boxes represent data tables.


□ How to obtain the distance

The distance is obtained directly from the hipparcos parallax. Add a new column for the distance by doing the following actions in Topcat:

- Select the Hipparcos main catalog (1 239 hip main, closest_stars_AFGKM subset) OR closest_MS_AFGKM_targets_topcat_out.csv in the Table List.
- Click the tool **Display column metadata**
- Click the tool **Add a new column**
- Name it Dist and enter the following expression: $1000/P1x$

□ How to obtain the luminosity

Appendix F - NEAT Memo: Creation and exploitation of the NEAT catalog

	Nearby Earth Astrometric Telescope	Ref: NEAT-sci-001
	<i>Creation and exploitation of the NEAT catalogs</i>	Version : v4 Date : 16-09-2014 Page : 12 / 34

This work is based mostly on the following publication: Transformations from Theoretical Hertzsprung-Russell Diagrams to Color-Magnitude Diagrams: Effective Temperatures, B-V Colors, and Bolometric Corrections (Flower, 1996). In order to complete the first step, download the main sequence "Teff, B-V and BC" table from the same author (the data is accessible via Vizier). It is necessary to download the data and perform an interpolation manually because the $BC = P(B-V)$ relation doesn't exist in the publication (it only gives the $\log(\text{Teff}) = P(B-V)$ and the $\log(\text{Teff}) = P(BC)$ polynomial relations).

I downloaded the data in a csv format and loaded it in SciDAVis (a free application for Scientific Data Analysis and Visualization). I performed with the latter a polynomial interpolation (order 10 i.e. 11 DoF). The resulting fit looks very good, the χ^2 value of the fit is 0.0004. The table 1 gives the coefficients of the polynomial ($P = a_0 + a_1X + a_2X^2 + \dots$).

Coefficient	Value	Error
a0	-0,1784538504862980	0,0040439753600725
a1	2,9023636120332208	0,0358593758682318
a2	-12,3188141929402839	0,1468192147338562
a3	20,9310264552908833	0,7901640483937037
a4	-22,5026837177971153	1,7789678865741207
a5	63,6149604337794230	3,6915037287900767
a6	-177,5417213564442136	11,9138718837156965
a7	249,9150285256258428	16,1324092451378540
a8	-182,6519997569876352	11,0043353138590163
a9	67,4220567552053751	3,7755649838561576
a10	-9,9870014580361062	0,5193285281379360

Table 1: *Polynomial coefficients of the relation $BC = P(B - V)$.*

With these coefficients I can now complete the first step and add a BC column to the AFGKM subset:

```
BC -0.1784538+2.9023636*$39-12.318814*pow($39,2)+20.931026*pow($39,3)
-22.50268371*pow($39,4)+63.6149604*pow($39,5)-177.541721356*pow($39,6)
+249.915028525*pow($39,7)-182.6519997*pow($39,8)+67.42205675*pow($39,9)
-9.98700145*pow($39,10)
```


In the above expression, \$39 refers to the B-V column. It is required that one addresses this column by its ID because it has a "-" in its name.

One last thing to do is to verify that all the targets have a B-V index in the interpolated range. This can be done by creating a new subset with the following expression: `_8 && $39 < 1.8 && $39 > -0.35` and noting that the number of rows is unchanged (_8 is the FGKM subset). From this point, it is very straightforward to obtain the luminosity in solar units, by creating two other columns:

```
MB Vmag+BC-5*ln(100/Plx)/ln(10)
```

```
L pow(10, (4.75-MB)/2.5)
```

Remark: The value of 4.75 in the formula above is the solar absolute bolometric magnitude.

	Nearby Earth Astrometric Telescope	Ref: NEAT-sci-001
	<i>Creation and exploitation of the NEAT catalogs</i>	Version : v4 Date : 16-09-2014 Page : 13 / 34

□ How to obtain the boundaries of the habitable zone

First of all I extract some data from a table (Schmidt-Kaler, 1982). I need only the rows F0, G2 and M0 and the following columns: spectral type and log(Teff). Then I add the following columns: B-V, Seff IN, Seff OUT. All this is done manually by feeding the values in a spreadsheet (the final table size is only 3 rows by 7 columns). The table is shown on Fig. 5.

NOTE: B-V = a + b*log(Teff)+c(log(Teff))^2+... Coefficients 3,979145 -0,654499 1,74069 -4,608815 6,7926 -5,39691 2,19297 -0,359496	Maximum greenhouse and runaway greenhouse limits						
	Spectral type	Teff	log(Teff)	B-V (poly)	Seff IN	Seff OUT	B-V (graphic)
	F0	7194,48978	3,857	-685,6903264	1,90	0,46	0,29
	G2	5861,38165	3,768	-550,8516149	1,41	0,36	0,62
	M0	3845,91782	3,585	-342,7309295	1,05	0,27	1,59
	Line coefficient	A IN	A OUT	B IN	B OUT		
	1	-1,4848485	-0,3030303	2,330606061	0,54787879		
	2	-0,371134	-0,0927835	1,640103093	0,41752577		
	Early Mars and recent Venus limits						
	Spectral type	Teff	log(Teff)	B-V (poly)	Seff IN	Seff OUT	B-V (graphic)
	F0	7194,48978	3,857	-685,6903264	2,00	0,41	0,29
	G2	5861,38165	3,768	-550,8516149	1,76	0,32	0,62
	M0	3845,91782	3,585	-342,7309295	1,60	0,24	1,59
	Line coefficient	A IN	A OUT	B IN	B OUT		
	1	-0,7272727	-0,2727273	2,210909091	0,48909091		
	2	-0,1649485	-0,0824742	1,862268041	0,37113402		

Figure 5: **The Seff versus B-V table.** The spreadsheet also gives the values of the A and B coefficients of the $S_{eff}^{IN/OUT} = A_{1/2}^{IN/OUT} \times (B - V) + B_{1/2}^{IN/OUT}$ relations.

The values in the B-V column are found by using the relation $B-V = P(\log(\text{Teff}))$ (Flower, 1996). Since there is obviously a problem when using the polynomial coefficients from the paper, I simply used the plots of the publication to graphically obtain the B-V values.

The values in the Seff columns are found in a publication from Kastings (Kasting et al., 1993). They performed climate simulations to determine the width and the locations of the HZ. Note that the concept of HZ remains very fuzzy, as it depends strongly on which model and hypothesis one relies. Here we use two sets of limits: the runaway greenhouse/maximum greenhouse limits and the recent venus/early mars ones.


These limits were calculated for F0, G2 and M0 spectra and should be updated for all spectral sub classes (Kaltenegger, Segura and Kasting in prep). So when more values for Seff will become available, it will be possible to add rows to the table and perform a polynomial interpolation. In the meantime, with only 3 data points available to calibrate the relation $(\text{Seff IN, Seff OUT}) = f(B-V)$ I chose to use a piecewise linear function ($Seff = A \times (B - V) + B$).

Assuming the following notations for Seff IN in the table:

B-V	Seff IN
x_1	y_1
x_2	y_2
x_3	y_3

the coefficients A et B are given by: $A_1 = (y_2 - y_1)/(x_2 - x_1)$ and $B_1 = (y_1 x_2 - y_2 x_1)/(x_2 - x_1)$, for the first segment. Similarly we have $A_2 = (y_3 - y_2)/(x_3 - x_2)$ and $B_2 = (y_2 x_3 - y_3 x_2)/(x_3 - x_2)$ for the 2nd segment. The coefficient for Seff OUT are calculated in the same way. After replacing $A_{1/2}$ and $B_{1/2}$ by their numerical values (see Fig. 5), we obtain the following expressions:

Appendix F - NEAT Memo: Creation and exploitation of the NEAT catalog

	Nearby Earth Astrometric Telescope	Ref: NEAT-sci-001 Version : v4
	<i>Creation and exploitation of the NEAT catalogs</i>	Date : 16-09-2014 Page : 14 / 34

SeffIn1 $\$39 < 0.62?$ $-1.484 * \$39 + 2.330$: $-0.371 * \$39 + 1.640$

SeffOut2 $\$39 < 0.62?$ $-0.273 * \$39 + 0.489$: $-0.082 * \$39 + 0.371$

SeffIn1 $\$39 < 0.62?$ $-1.484 * \$39 + 2.330$: $-0.371 * \$39 + 1.640$

SeffOut2 $\$39 < 0.62?$ $-0.273 * \$39 + 0.489$: $-0.082 * \$39 + 0.371$

The columns indexes 1 and 2 are for different types of habitable zone limits (they are not related to A1/A2 B1/B2 which simply results from the piecewise nature of the fits). For all the columns related to the HZ, the index 1 is for the runaway greenhouse/maximum greenhouse limits whereas the index 2 is for the recent venus/early mars limits ((Kasting et al., 1993)).

Finally the inner and outer edges of the habitable zones are given by the following formula (Kasting et al., 1993):

$$d = 1AU \times \left(\frac{L/L_{\odot}}{S_{\text{eff}}} \right)^{0.5} \quad (2)$$

So the expression for the edges of the HZ columns will be:

HZIn1 $\text{pow}(L/\text{SeffIn1}, 0.5)$

HZIn2 $\text{pow}(L/\text{SeffIn2}, 0.5)$

HZOut1 $\text{pow}(L/\text{SeffOut1}, 0.5)$

HZOut2 $\text{pow}(L/\text{SeffOut2}, 0.5)$

□ How to obtain the star mass


The star mass can be obtained in at least two ways: the first way is to use the information contained on the exoplanet encyclopedia. The drawback of this method is that the mass will only be available for the NEAT target stars that have already known exoplanets around them (92 stars out of 385). The other method is to use the relation $L = M^{3.8}$. The problem with this second method is that its very approximative. It is nevertheless necessary to estimate the mass of all the target stars in order to know how much integration time must be allocated to reach the habitable zone. The column is created as follows:

Mass $\text{pow}(L, 1.0/3.8)$

We know have all the columns needed to derive the astrometric signal at the HZ boundaries and the Earth flux equivalent position, the inner working angles of the respective circular orbits and their orbital periods. All columns are listed in appendix B. Only the astrometric signals are useful for the next section (observation strategy and science yields), but the other columns can be useful to explore various aspect by plotting the data, such as inner working angle for direct imaging or deriving RV amplitude signals.

2.2 – Time allocation schemes and science yields

In this section we explore different ways of distributing the observation time between the targets and the effect on the science yield of the mission.

	Nearby Earth Astrometric Telescope	Ref: NEAT-sci-001
	<i>Creation and exploitation of the NEAT catalogs</i>	Version : v4 Date : 16-09-2014 Page : 15 / 34

2.2.1 – Relation between minimum detectable signal and integration time

In order to carry on our analysis we need a relation between the minimum astrometric signal detectable (A_{\min}) and the integration time (T) for each target. We will need the relation in both ways:

- With $T = f(A_{\min})$: we can rank the targets by order of increasing “difficulty”. The difficulty is defined as the integration time required to detect a terrestrial mass planet at the inner edge of the habitable zone.
- With $A_{\min} = f(T)$: for a given integration time, we know the detection limit. For any pair of target star/simulated planetary system, we can easily determine which planets would be detected.

An error model for NEAT, with the knowledge of the visible magnitude of the target star and the magnitude equivalent to the sum of associated reference stars allows us to find for each target a relation between its observation time and the minimum detectable signal. The model is mainly based on the photon noise limit of the NEAT instrument. The photon noise limit can be estimated with a spreadsheet, using fundamental laws (see reference document: `neat_photon_limit.xls`). The steps used to estimate the photon limit are:


1. The total visible photon flux of the Sun ($\text{photon.s}^{-1}.\text{m}^{-2}$) is calculated. This is done using the plank function and a numerical integration among 41 wavelength channels, from 400 to 810 nm. After the stellar spectral irradiances (W.m^{-1}) are converted into a photon flux for each channel, the sum of all channels gives the total photon flux.
2. The photon flux is expressed as a function of distance (in pc) from the Sun and the mirror size.
3. The flux is converted into a photo-electron flux (e.s^{-1}).
4. The fundamental limit on the (angular) accuracy of the centroid is given by: $\frac{0.42\lambda_{\text{eff}}}{D\sqrt{N_e}}$. The factor 0.42 is the standard deviation of the best Gaussian fit to an Airy spot central lobe (this is an optimistic assumption, we ignore the wings). In practice the PSF is polychromatic: longer wavelengths have larger standard deviations and vice versa. The photon budget per channel indicates that red channels have more photons. To safely take into account out these effects we use the maximum wavelength (810 nm) as a reference.

To verify the method, I have used the same star brightness than the NEAT error budget: I assume a G2 target star of $V_{\text{mag}} = 6$ and 6 references stars of $V_{\text{mag}} = 11$. The reference stars total flux is equivalent of one star of $V_{\text{mag}} = 9.05$. As a common reference I also assume an integration time of one hour. I find that the photon noise of the target star (σ_{target}) and the reference stars (σ_{ref}) are respectively $0.09 \mu\text{as.h}^{-0.5}$ and $0.36 \mu\text{as.h}^{-0.5}$.

There are significant differences with the NEAT error budget, they can explain why the photon noise limits we find are smaller. Indeed, the error budget yields: $\sigma_{\text{target}} = 0.12 \mu\text{as.h}^{-0.5}$, $\sigma_{\text{ref}} = 0.61 \mu\text{as.h}^{-0.5}$ for references, plus $\sigma_{\text{systematics}} = 0.44 \mu\text{as.h}^{-0.5}$ for instrument systematics. The notable differences are:

- K0 stars (target and references) are used instead of G2

Appendix F - NEAT Memo: Creation and exploitation of the NEAT catalog

	Nearby Earth Astrometric Telescope	Ref: NEAT-sci-001
	<i>Creation and exploitation of the NEAT catalogs</i>	Version : v4 Date : 16-09-2014 Page : 16 / 34

- Wavelength integration is over 8 channels, from 450 to 950 nm
- CCD quantum efficiency is specified per channel, not only averaged
- A lot of other error sources are taken into account, instrumental and astrophysical errors like metrology calibration, stellar aberration...
- The method to derive the centroid accuracy from the number of collected photon is different

For our purposes, we will use the more conservative values of the NEAT error budget. We will adjust the multi epoch accuracy σ_f for the brightness of target (baseline flux F_{target}^0) and reference stars (baseline flux F_{ref}^0) and for the integration time T (in hours) in the following way:

$$\sigma_f^2 = \left[\sigma_{\text{target}}^2 \frac{F_{\text{target}}^0}{F_{\text{target}}} + \sigma_{\text{ref}}^2 \frac{F_{\text{ref}}^0}{F_{\text{ref}}} + \sigma_{\text{systematics}}^2 \right] \times \frac{1}{T} = \sigma_{\text{target/h}}^2 \frac{1}{T} \quad (3)$$

The fundamental point is the square root increase of the accuracy with the number of collected photons, either because we have more flux or we integrate longer. Moreover, we consider that most systematics can be averaged out by taking many data points, eventually several per epoch. We can now determine for each target the sum of errors $\sigma_{\text{target/h}}$, normalized for a one hour integration. In Eq. 3: the value of $\sigma_{\text{target/h}}$ as a function of the target and reference equivalent magnitudes is:

$$\sigma_{\text{target/h}} = \sqrt{10^{\frac{V_{\text{mag,target}}-6}{2.5}} \sigma_{\text{target}}^2 + 10^{\frac{V_{\text{mag,ref}}-9.05}{2.5}} \sigma_{\text{ref}}^2 + \sigma_{\text{systematics}}^2} \quad (4)$$

The column is created as follows:

```
SigmaH pow(0.0144*pow(10, (Vmag-6)/2.5)+0.372*pow(10, (EqRefMag-9.05)/2.5)+0.194,0.5)
```

The minimum detectable astrometric signal is for an SNR of 6:

$$A_{\text{min}} = 6\sigma_f = 6\sigma_{\text{target/h}} \sqrt{\frac{1}{T}} \quad (5)$$


The inverse relation is:

$$T = 36 \frac{\sigma_{\text{target/h}}^2}{A_{\text{min}}^2} \quad (6)$$

The column for the target “difficulty” (integration time needed for an exo-Earth at the inner edge of HZ) is created with:

```
TexoEarth 36*pow(SigmaH,2)/pow(AIn1,2)
```

Note that I have made implicit assumptions to obtain this simple result. I have forgotten the complex considerations about how to optimize the number of visits, their duration and the number of slews required (these are addressed in the manuscript). I retain only the total time of effective observation per target (excluding slew time from this total). The approximation can be made because the number of epochs per target, number of data points per epoch or integration time per data point all increase the accuracy roughly as the power 0.5 when the number of independent measurements is larger than the number of free parameters. Concerning systematic errors, we assume that we have enough epochs per target and data points per epoch to verify the number given by the error budget. There are a lot of possible caveats to this simplistic approach, here is a list of important ones I can think of:


	Nearby Earth Astrometric Telescope	Ref: NEAT-sci-001
	<i>Creation and exploitation of the NEAT catalogs</i>	Version : v4 Date : 16-09-2014 Page : 17 / 34

- We assume that systematic errors are averaged by having many epochs. On a real instrument, this will not be the case for all kinds of systematics.
- The NEAT error budget assumes the same number of visits for every target. In a real mission, the number of visits could be different for each target and could also depend on the number of planet detected before the end of the mission. If we find a very interesting system, no doubt we will come back more often before the mission is over. Moreover, in the manuscript we have determined that the optimal number of visits depends on the final accuracy desired.
- We have not considered the impact of giant exoplanets ($M > M_{\text{Jupiter}}$) around reference stars. They would increase the total number of parameters on the global solution. There is also the option of removing noisy reference stars from the global solution (in this case the reference equivalent magnitude increases). We expect to find giant planets around about 10% of stars, so depending on the rejection criteria, the number of useful reference stars might be slightly lower than expected and/or some reference stars will be more noisy.

2.2.2 – Impact of the time allocation scheme

Having decoupled the total integration time from the number and durations of visits, from now on I only consider the total effective observing time (slew time not included). Based on the content of the NEAT proposal, I fix the total effective observation time at $T_{\text{tot}} = 20000$ hours (subtracting about 10% of the total time from the proposal to account for slew time). I analyze different scenarios for the time allocation scheme. This is done via a matlab script: `observational_strategy_yield.m`.

1. All NEAT catalog targets (455 stars) are selected. The observation time is distributed equally.
2. The 200 easiest stars are selected. The observation time is distributed equally.
3. The 100 easiest stars are selected. The observation time is distributed equally.
4. Time allocated equal to TexoEarth: more observation time is allocated for harder targets. Cumulative time stops at T_{tot} .
5. The observation time is distributed to reach specific mass detection thresholds in habitable zone. Several categories are defined manually. For the closest stars, a threshold of $M_{\text{lim}} = 0.5 M_{\oplus}$ at the inner edge of the HZ is used to calculate the time allocated. When the time needed becomes too large, the threshold is changed to $1 M_{\oplus}$ (2nd category). Same thing for the last category ($M_{\text{lim}} = 5 M_{\oplus}$). The boundaries between the categories are placed so that all the observation time is used after at least 400 targets.
6. Time allocated equal to $\frac{C_1}{T_{\text{ExoEarth}}^\alpha}$, with a maximum time threshold of $\frac{T_{\text{tot}}}{C_2}$. So slightly more time is allocated for easier targets. The constant C_1 determines at which target we stop allocating a constant fraction of time and we start to decrease. The constant C_2 determines the maximum time threshold for easy targets. The constant α determines the speed at which we decrease the allocated time with increasing difficulty. The numerical values are: $C_1 = 957$, $C_2 = 250$ and $\alpha = 0.5$.

	Nearby Earth Astrometric Telescope	Ref: NEAT-sci-001 Version : v4
	<i>Creation and exploitation of the NEAT catalogs</i>	Date : 16-09-2014 Page : 18 / 34

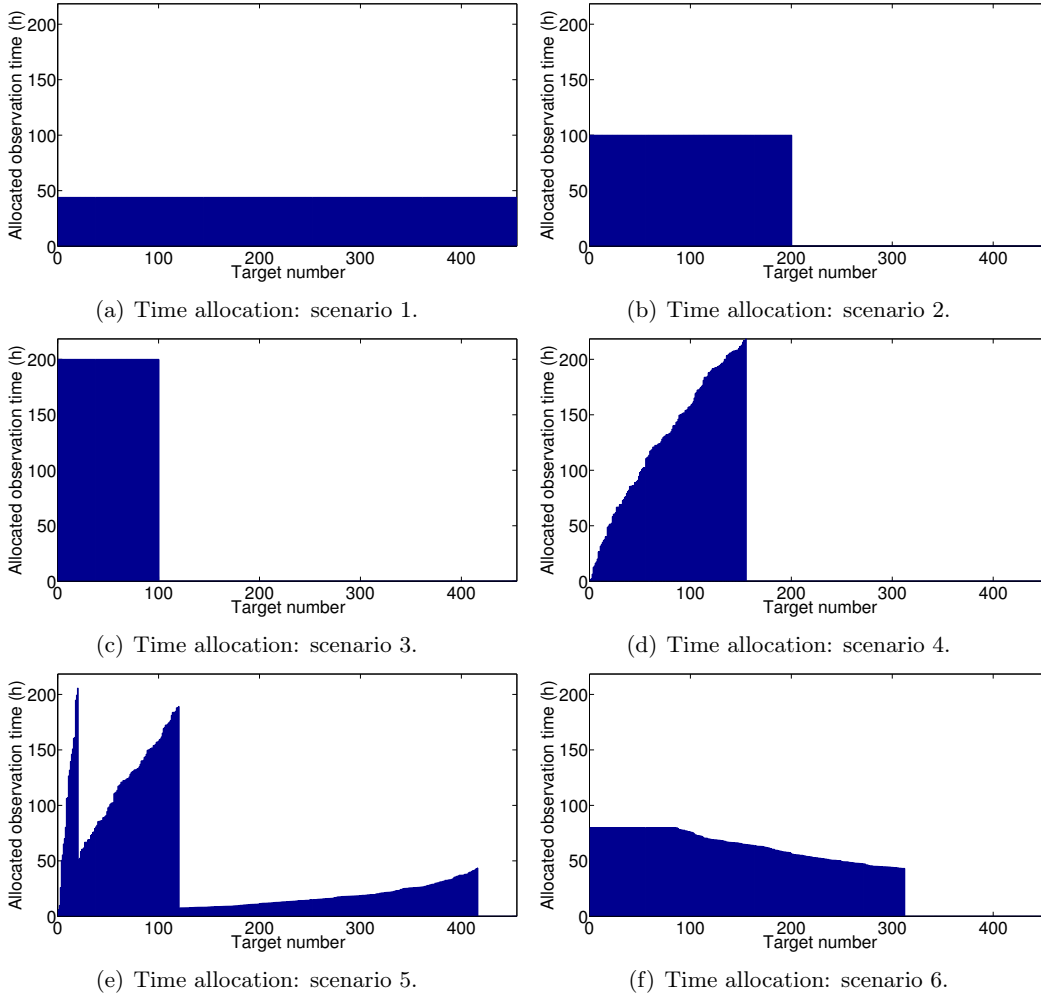


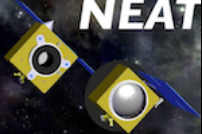
Figure 6: *Time distribution per target for 6 different time allocation schemes.*

Figure 6 shows the time distribution corresponding to each scenario.

Figures 7 and 8 are bar graphs of predicted exoplanet yields. The yield simulation is based on a list of 344 synthesized planetary systems kindly provided by Yann Alibert, they were originally generated for the NEAT double blind test (for non-blind test runs). For detailed informations about the population synthesis model, refer to (Alibert et al., 2013). The fundamental assumptions of the planet synthesis model are:

- Maximum of 10 planets per system
- Star mass of $1M_{\odot}$
- Alpha disk model (1+1D model, azimuthal symmetry, $\alpha = 2 \times 10^{-3}$)
- Migration model based on (Mordasini et al., 2011) and (Dittkrist et al., 2014)
- Disk properties (mass and lifetime) should be similar to observations

The yields are obtained by averaging 100 random permutations. With only one permutation the results vary too much (by several percents for a yield of about 8% for terrestrial planet in HZ, for example). The variability is introduced when we randomly assign the planetary

	Nearby Earth Astrometric Telescope	Ref: NEAT-sci-001 Version : v4
	<i>Creation and exploitation of the NEAT catalogs</i>	Date : 16-09-2014 Page : 19 / 34

systems to the target stars: the permutation will be more favorable if more planets/more interesting planets end-up around easy/close stars). With 100 permutations, the deviation between two runs is less than 0.1%.

The 6 bar plots highlight the trade-offs between the allocation schemes. The difference between **1**, **2** and **3** is that we increasingly concentrate more time on easy targets. **1** yields more giant planets than **2**, but slightly less terrestrial ones. However when we reduce the number of targets too much (**3**), we obtain less giant but also less terrestrial planets. In this case we have already spent a fair amount of time on the easy targets in **2**, so the additional observation time around these do not compensate for the planet loss of the “medium” targets (ranked 100 to 200).


The idea behind schemes **4**, **5** and **6** is too see whether having an unequal distribution time can yield better results. We test several possibilities:

- In **4**, I choose to spend more time on hard targets, by having for each star an observation time that allows the detection of an Earth at the inner edge of the habitable zone. The advantage is that we avoid using more time than necessary on easy targets. But this also causes the allocation time to increase very quickly (see Fig. 6(d)) and I run out of time around the target number 160. The overall result is not very good compared to **5**.
- In **5** the approach is similar, but I mitigate the problems encountered in **4** by having several mass detection thresholds. When the allocated time has become too large, the threshold is changed to a higher mass value. The final yield difference with **4** is sensible. However if we look at the distribution of allocated time, the jumps when we change threshold feel unnatural: we are using a lot of time for targets just before the peak and not enough for targets just after, which are only slightly harder. This approach (**5**) was the one used in the NEAT proposal.
- In **6**, the idea is to mainly spend more time on easy targets, but with some caps to avoid wasting too much time. The first time cap is flat, the second one is equal to the time needed to detect a $0.5 M_{\oplus}$ planet in HZ. In practice the second cap make almost no difference (very few targets concerned), so I ignore it and only apply the first one. For harder targets, the time spent is proportional to $\frac{1}{T_{exoEarth}^{\alpha}}$. Around harder targets, we reduce the time spent: we only hope to detect massive super-Earth and giant planets.

In the end the simulation indicates that **6** finds the most terrestrial exoplanets. It seems to be a good compromise for splitting time between easy and hard targets, because a significant fraction of the giant planets are detected (55%), not very far from the maximum obtained with **1** (75%). Figure 9 is a mass/period diagram of the detected exoplanets for scenario 6. The plot is obtained for a single permutation (to avoid having fractions of planets !).

In the case of the new ESA call for proposals (M4, 2015), the former NEAT consortium will propose a new mission called Theia, with revisited science objectives. What was called the main science program in NEAT will shrink to a smaller portion of the total available telescope time and more alternative science programs will be proposed. Also, the previous goal of detecting gas giants, down to about $10 M_{\oplus}$ (so called mini-Neptunes), and up to 20pc, has become less interesting as the number of known exoplanets has increased to more than 2000 and other missions already in preparation will detect a lot of these planets. The critical point remains the exo-Earths (and habitable super Earths) around nearby stars, especially for stars latter than M. This yield simulator will be very useful to determine to which extent the observation time can be reduced (for a given objective in number of detections) and what is the best way to distribute the observation time among the targets.

Appendix F - NEAT Memo: Creation and exploitation of the NEAT catalog

	Nearby Earth Astrometric Telescope	Ref: NEAT-sci-001 Version : v4
	<i>Creation and exploitation of the NEAT catalogs</i>	Date : 16-09-2014 Page : 20 / 34

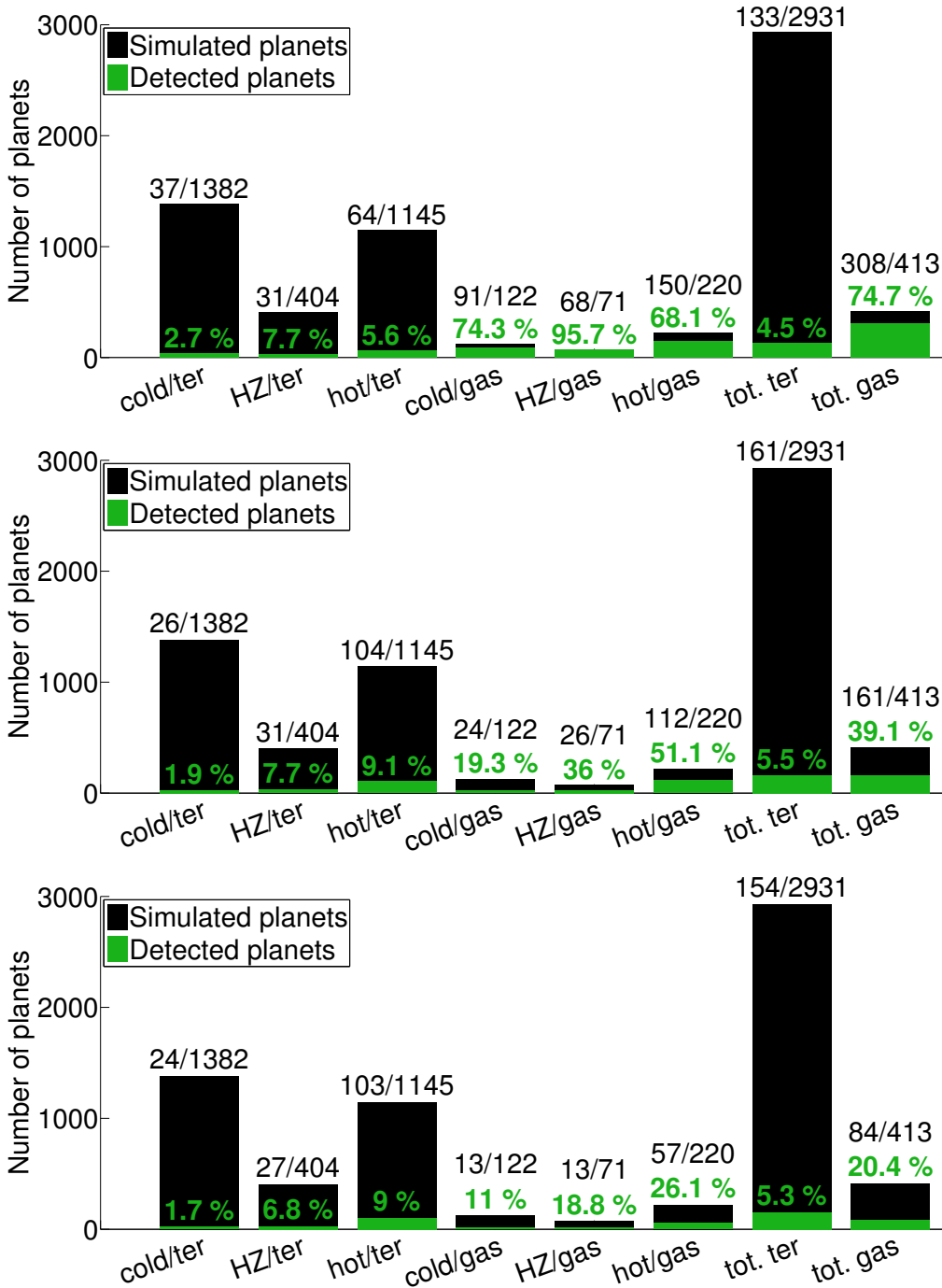
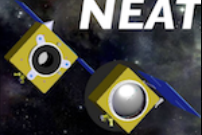


Figure 7: Exoplanet yields for allocation schemes 1, 2 and 3 (from top to bottom).

	Nearby Earth Astrometric Telescope	Ref: NEAT-sci-001 Version : v4
	<i>Creation and exploitation of the NEAT catalogs</i>	Date : 16-09-2014 Page : 21 / 34

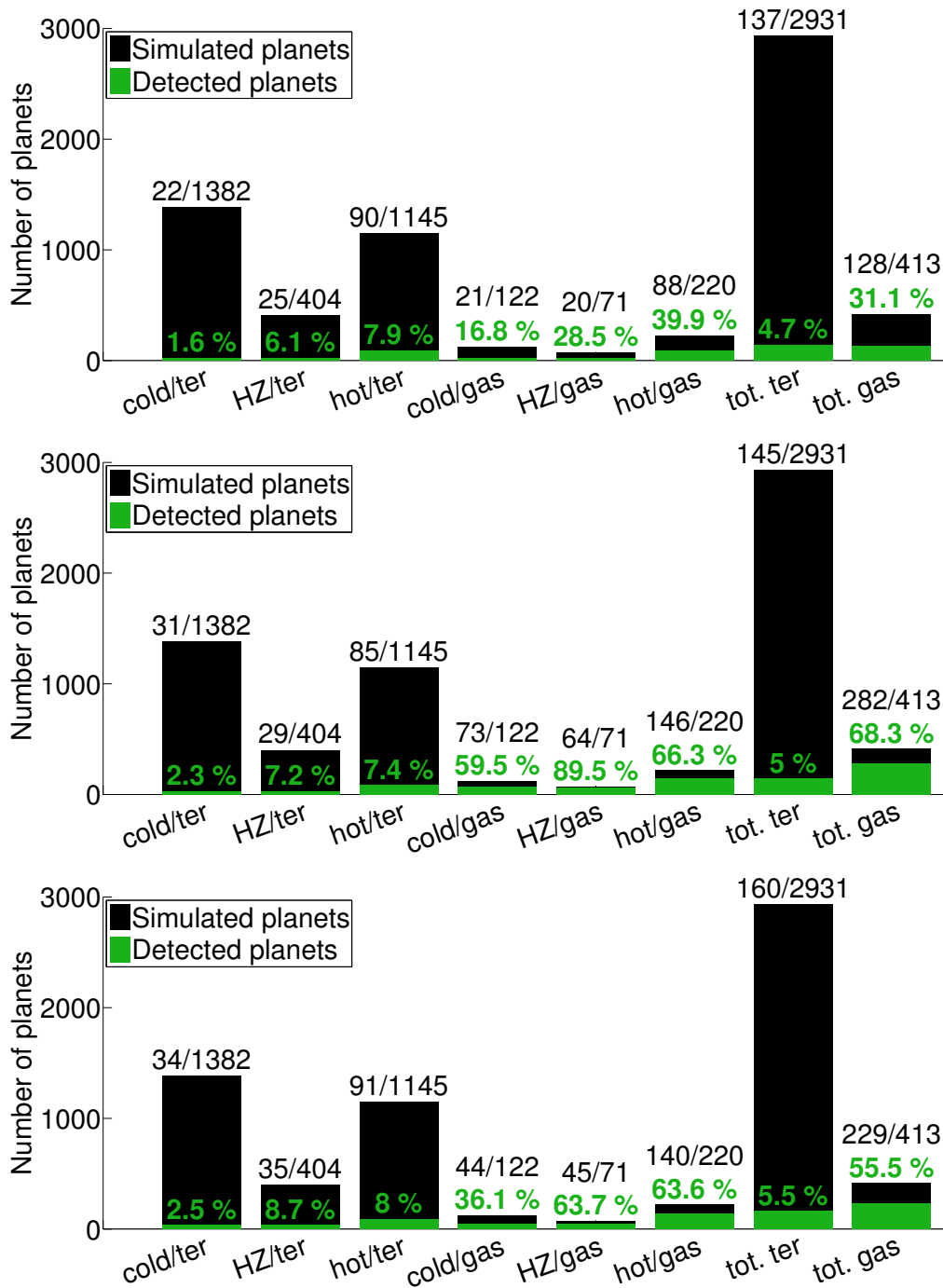
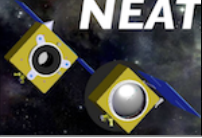


Figure 8: Exoplanet yields for allocation schemes 4, 5 and 6 (from top to bottom).

	Nearby Earth Astrometric Telescope	Ref: NEAT-sci-001 Version : v4
	<i>Creation and exploitation of the NEAT catalogs</i>	Date : 16-09-2014 Page : 22 / 34

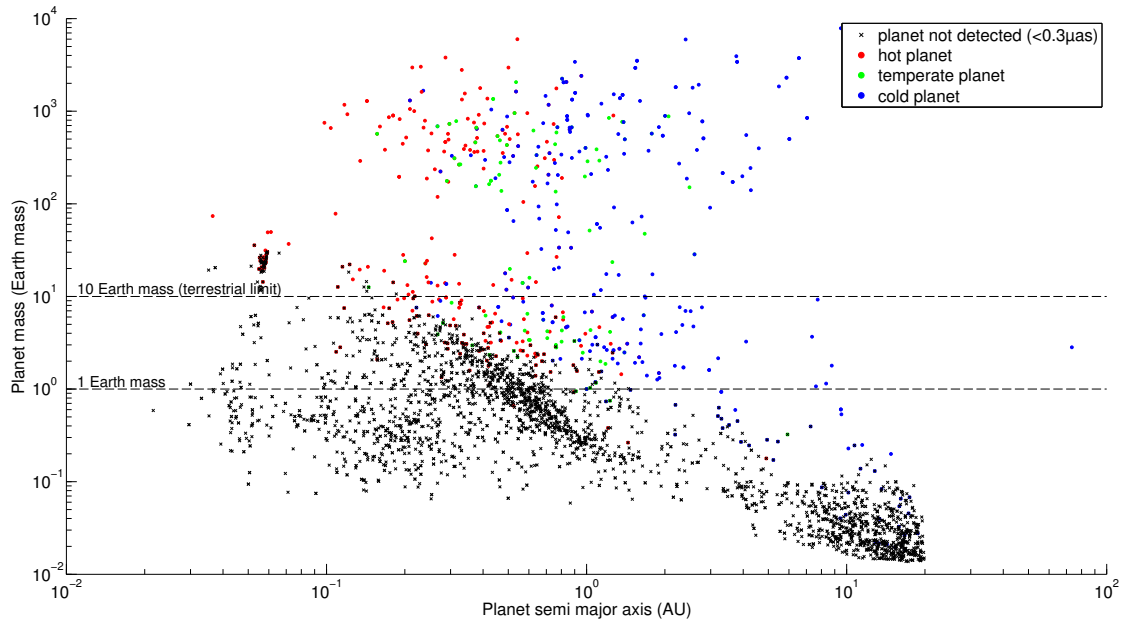


Figure 9: *Mass period diagram of the NEAT mission simulated exoplanet yield.*

2.3 – Astrometric signal in HZ versus stellar mass

Overall, the astrometric signal (A) in HZ increases with the host stellar mass (M). This is the result of several competing effects:

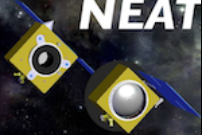
1. The star luminosity increase with the mass: $L \propto M^{3.8}$
2. The orbital distance of the HZ increase with the luminosity: $R(\text{HZ}) \propto L^{0.5}$
3. The albedo of the planet is higher for bluer light (it moves the HZ slightly closer to the star)
4. The ratio $\frac{M_{\text{planet}}}{M_{\text{star}}}$ is smaller

The net effect of 1 and 2 is an increase of the astrometric signal ($A \propto M^{1.9}$). This is somewhat attenuated by 3 (but it is a weak effect). We can take the albedo into account by defining an effective luminosity $L_{\text{eff}} \approx L^{-\alpha}$ and we obtain for 1, 2 and 3: $A \propto M^{1.9-\alpha/2}$. The effect of 4 is to subtract 1 to the total power. So we finally obtain: $A \propto M^{0.9-\alpha/2}$. This relation is approximative, as we have used several approximated power laws: the $L = f(M)$ relationship breaks down for M stars (the limit is around $0.43 M_{\odot}$) and the albedo effect is in our case modeled by a piecewise linear function. In reality the exact albedo effect will be non linear and specific to each planet.

Figure 10 shows the astrometric signal in HZ versus the stellar mass. In order to separate the effects of the distance and the stellar mass, Fig. 11 shows the astrometric signal in HZ (μas) multiplied by the distance to the Sun (pc) versus the stellar mass. This is equivalent to moving all the targets at a distance of 1 pc from the Sun.

Figure 11 confirms that the spectral effect is weak and that the astrometric signal in HZ increase with stellar mass, roughly as $M^{0.63}$ ($\Rightarrow \alpha = 0.54$)³. This result is important, it tells

³Extrapolating from the following data points: ($M=0.42$, $A=2.0$) and ($M=2.0$, $A=6.0$).

	Nearby Earth Astrometric Telescope	Ref: NEAT-sci-001 Version : v4
	<i>Creation and exploitation of the NEAT catalogs</i>	Date : 16-09-2014 Page : 23 / 34

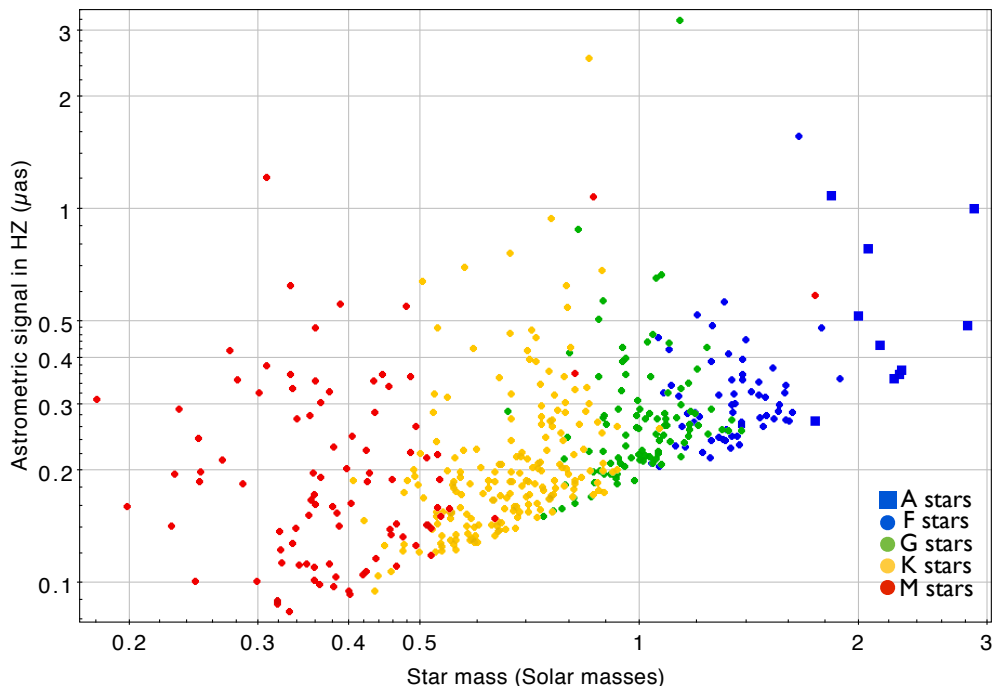


Figure 10: *Astrometric signal in HZ versus star mass for the NEAT targets, by spectral type.* The different areas corresponding to spectral type from M to A are easily distinguishable. The bottom line is for stars close to 20 pc, the vertical dispersion is caused by the distance. Low hanging fruits (and their spectral types) are easy to spot on this plot. The two stars at the very top (G and K) are the Alpha Centauri system. A few blatant spectral miss classifications (for example 2 M stars with $M > 0.8M_{\odot}$) are visible on the plot.

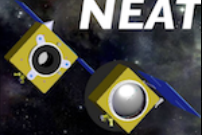
us that astrometry is complementary with radial velocities when searching for planets in the habitable zone. Indeed, for radial velocities, exoplanet detection in HZ becomes harder when the stellar mass increases. There is an important caveat that must be noted here: the increase in astrometric signal with stellar mass goes with a period increase. The temporal baseline must be larger than the period to fully take advantage of the increased signal amplitude. For stars later than A, the orbital period at the inner edge of the HZ becomes larger than 5 years (the nominal duration of the NEAT mission).

2.4 – Crossmatch with “The Extrasolar Planets Encyclopaedia”

Now we will load the “Interactive Extra-solar Planets Catalog”, from this website: <http://www.exoplanet.eu/>. This catalog contains all the known exoplanet candidates, we will use it to perform a crossmatch with the NEAT catalog and pinpoint which NEAT targets already have exoplanet candidates.

- Go to the website, then to the “All catalogs” page, then click on the “All fields” link
- Download the data as a **VOTABLE**
- Open the **Load New Table** dialog box via the menu **File > Load table**
- Click on the **System Browser** icon and load the table
- Create a subset `closest_exoplanets` with the condition: `star_distance < 20`

Appendix F - NEAT Memo: Creation and exploitation of the NEAT catalog

	Nearby Earth Astrometric Telescope	Ref: NEAT-sci-001 Version : v4
	<i>Creation and exploitation of the NEAT catalogs</i>	Date : 16-09-2014 Page : 24 / 34

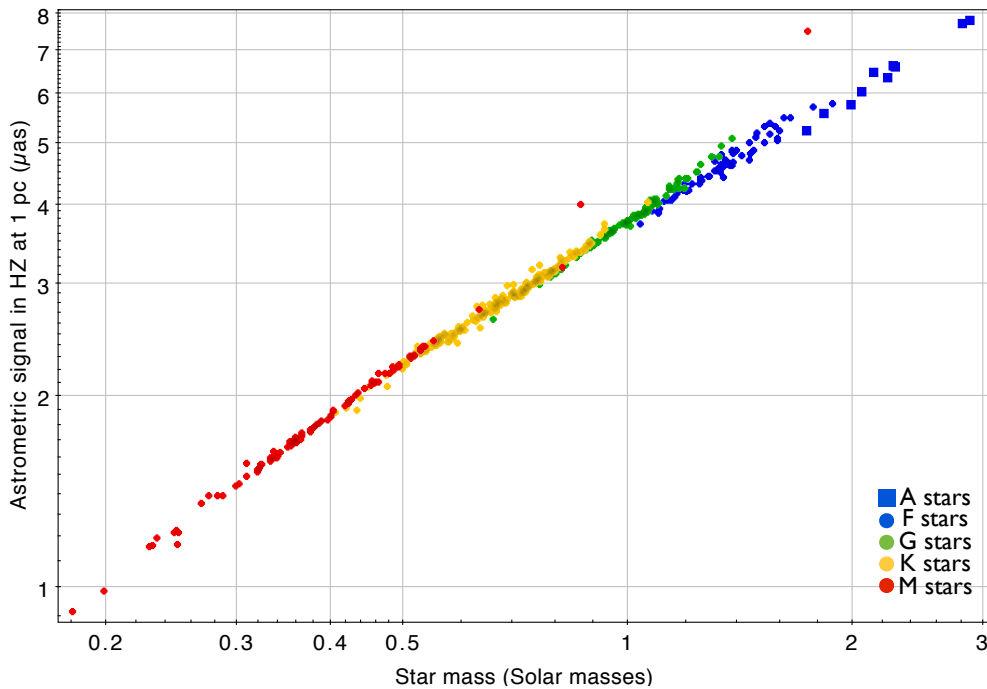
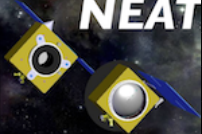


Figure 11: *Astrometric signal in HZ times distance versus star mass for the NEAT targets, by spectral type.* Multiplying by the distance has normalized the astrometric signal to the signal seen at a distance of 1 pc.

- Select the `closest_exoplanets` subset in the exoplanets catalog.
- Select the `closest_stars` subset in the Hipparcos main catalog.
- Crossmatch the catalogs via the menu **Joins > Pair Match**, using the following parameters:
 - **Max Error** of 1 arcmin.
 - **Table 1**: Hipparcos main catalog
 - **RA column** (for Table 1): RA(ICRS) - degrees
 - **Dec column** (for Table 1): DE(ICRS) - degrees
 - **Table 2**: Exoplanet catalog
 - **RA column** (for Table 2): St_Right_Asc - degrees
 - **Dec column** (for Table 2): St_Decl - degrees
 - **Match selection**: Best match for Table 2 row
 - **Join type**: 1 and 2
- Call the table `Exoplanet.eu closest stars crossmatch`

BEFORE performing the crossmatch, make sure you have selected the `closest_stars` and `closest_exoplanets` subsets in their respective catalogs in the **Table List**. The result of the crossmatch are the exoplanets closer then 20 pc that orbit nearby stars of the Hipparcos catalog. The crossmatch result has only 113 rows instead of the 126 expected most likely

Appendix F - NEAT Memo: Creation and exploitation of the NEAT catalog

	Nearby Earth Astrometric Telescope	Ref: NEAT-sci-001
	<i>Creation and exploitation of the NEAT catalogs</i>	Version : v4 Date : 16-09-2014 Page : 25 / 34

because some host stars are absent of the Hipparcos catalog (which is not complete up to 20 pc for K and M stars).

Repeat the crossmatch operation with the hipparcos `closest_stars_AFGKM` subset and name the new table `Exoplanet.eu closest MS AFGKM stars crossmatch`.

Tip: if you change the **Match selection** parameter to "Best match for Table 1 row", you will obtain the number of stars with known exoplanets candidates in the subset (instead of the number of exoplanets candidates around stars of the subset). Table 2 sums up the row counts in all the cases.

Table 2: *Number of stars with known exoplanets (updated 02/09/2014)*. Two different stars subset are compared: the first one is all Hipparcos stars closer than 20 pc (934 stars) and the second one is the NEAT catalog of targets (455 stars). The "Exoplanet count" tells how many exoplanets have been successfully associated with a Hipparcos host star, the "Star counts" tells how many Hipparcos stars host at least one known exoplanet. There is a small fraction of exoplanets for which no host star is found, they are most likely M stars that are too faint for Hipparcos.

Hipparcos subset	Exoplanet count	Exoplanet count (%)	Star count	Star count (%)
All stars < 20 pc	113/126	90%	64/934	6.9%
Main sequence AFGKM stars < 20 pc	74/126	59%	39/455	8.6%

Remark: apparently the RA and DEC coordinates are from different epochs for each catalog, hence the very wide tolerance used for the crossmatch. This could be another explanation for missing rows. Nevertheless, the results are visually satisfying.


Table 2 tells several interesting facts:

- Among the 1821 exoplanets candidates, only 113 are located at less than 20 pc.
- The fraction of main sequence stars that have known exoplanets is not significantly higher than the fraction for all stars. We have not put a particularly strong emphasis on main sequence stars in past surveys.
- We expect on average several planets per star: many more exoplanets are yet to be discovered in our solar neighborhood.

We will now create a 3D map of the stars and planets, by matching the angular and radial positions the of objects with their real positions in space.

Remark: the following step works best with Topcat version V3. On later version, the 3D plot with spherical grid has been removed.

To plot the data, click the tool **Spherical polar scatter plot**. Select the Hipparcos main catalog in the **Table** field. Chose a style for each subset (each spectral type), add a radial axis and enter the value **1000/Plx**: as the Hipparcos Plx value is the parallax in mas, this will yield the distance of the star in parsecs. Click on the **Add a new data set** button, select the result of the crossmatch with all the stars and process it in a similar way. For the radial value, you can directly enter the distance column: **star_distance**. You should also deactivate the fog option. The resulting plot is shown in Fig. 12.

	Nearby Earth Astrometric Telescope	Ref: NEAT-sci-001 Version : v4
	<i>Creation and exploitation of the NEAT catalogs</i>	Date : 16-09-2014 Page : 26 / 34

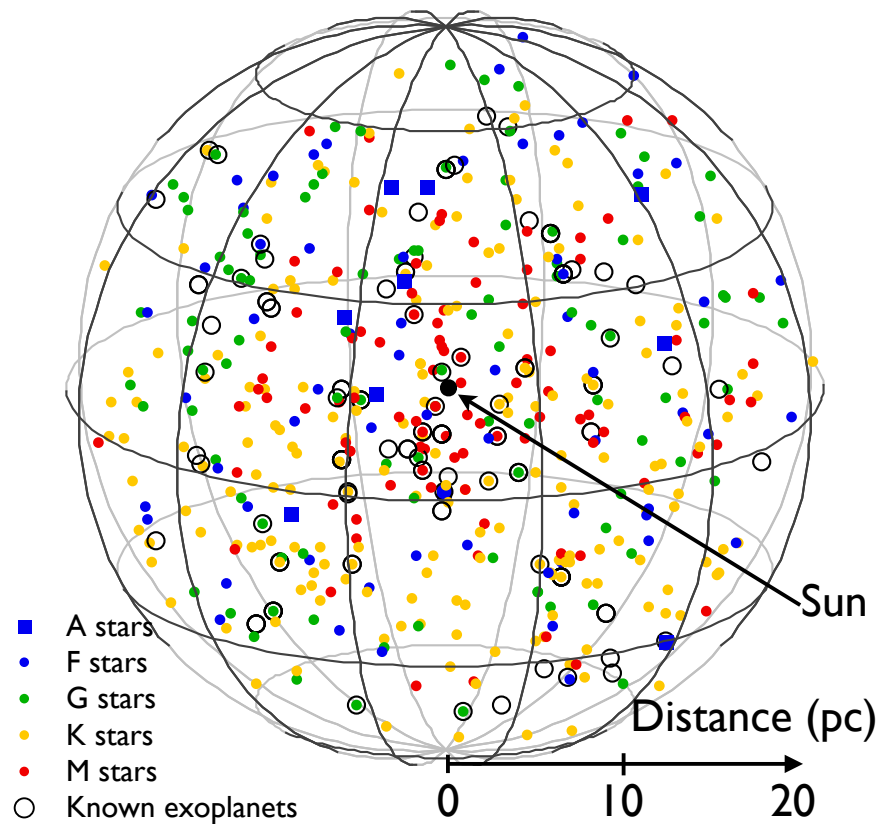
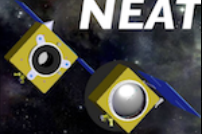


Figure 12: *3D representation of the catalog of the NEAT catalog of targets, by spectral type (updated 02/09/2014)*. The stars are crossmatched with the list of known exoplanets, the ones with at least one known exoplanet in orbit are circled. There are 10 A, 62 F, 97 G, 192 K and 94 M stars.

As expected, only a small fraction of the stars are circled. Notice that they are also some circles without star. These are exoplanets around star that are absent of the Hipparcos catalog or they are crossmatch errors.

If you haven't already done it, I advise you to save the full session now: use the menu **File** > **Save Table(s)/Session**. Make sure to select the tab **Session** and the format **fits-plus** as the output format to save the whole session.

WARNING: tough saving the full session in a fits-plus format will save the subsets, the algebraic expressions defining each subset will be discarded upon loading of the session. The plots will be lost as well, so you should export them as images before you close Topcat.

	Nearby Earth Astrometric Telescope	Ref: NEAT-sci-001 Version : v4
	<i>Creation and exploitation of the NEAT catalogs</i>	Date : 16-09-2014 Page : 27 / 34

2.5 – Checking the sample completeness

By looking at the 3D representation of the NEAT catalog, it is clear that the M stars are not evenly distributed. They are mostly located within 10 pc of the sun. There is obviously a problem of completeness for the M stars: the most distant M stars seems to be absent of the Hipparcos catalog because their magnitudes are too high.

So I ask the following: are all the F, G and K stars closer than 20 pc present in the Hipparcos catalog ? To answer this, one can simply plot the histogram of the number of stars versus the distance.

Add new subsets of main sequence F,G,K and M stars closer than 100 pc in the main Hipparcos table. For example for F stars:

-name: `close_MS_F_stars`

-condition: `P1x > 10 && matches(SpType, "^F.*(IV-V|[I]V)")`

Assuming an homogeneous distribution of the stars in the solar neighbourhood, the number of stars in a radius r is: $n = \alpha \times 4/3\pi r^3$, where α is the mean density of stars, thus: $dn = \alpha \times 4\pi r^2 dr$. An histogram of the stars count versus the distance (in log axis) is in fact a representation of $\log \frac{dn}{dr}$ versus $\log r$. Since we have: $\log \frac{dn}{dr} = 2 \log r + 2 \log 4\pi\alpha$, we expect to see a slope of 2 for the short distances, where the Hipparcos catalog is complete. The breakpoint in the slope indicate where the catalog is not complete anymore.

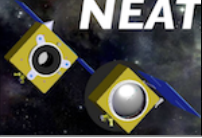
In order to see the breakpoints, other subsets are defined. The procedure is the same than the one that was used to define the NEAT catalog, expect that the distance is limited to 1kpc (as a result almost all the Hipparcos stars are included). The final histograms are shown in Fig. 13 and 14

□ Conclusion

One can assume near completeness of the Hipparcos catalog for the FGK main sequence stars (the completeness breakpoints are all well further than 20 pc). The same is not true for M stars, because they are much fainter. These results are consistent with the existing literature, a completeness study was performed to assess the completeness of the Darwin catalog (which was also build from the Hipparcos catalog): “Excluding the M stars from the estimate leads to a high completeness at 20 pc and 30 pc of 97% and 76% respectively, based on the estimated number of stars per volume using the 10 pc RECONS data set.” (Kaltenegger et al., 2010).

The incompleteness issue is of little practical importance for the main science program because Hipparcos is 99.9% complete to magnitude 10, and measures around fainter stars would be strongly impaired by high photon noise (it becomes larger than reference photon noise). To summarize: the NEAT catalog is volume limited for F,G and K stars at 20 pc, and magnitude limited for M stars (around $V_{\text{mag}} = 10$).

Appendix F - NEAT Memo: Creation and exploitation of the NEAT catalog

	Nearby Earth Astrometric Telescope	Ref: NEAT-sci-001 Version : v4
	<i>Creation and exploitation of the NEAT catalogs</i>	Date : 16-09-2014 Page : 28 / 34

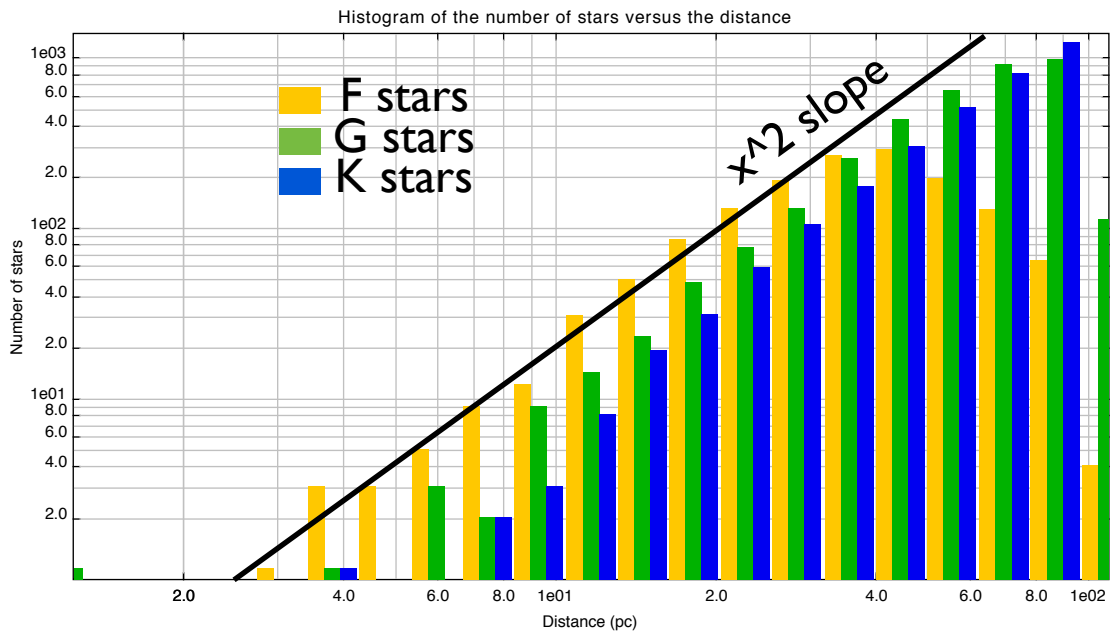


Figure 13: *Histogram of the distribution of the F, G and K stars versus the distance. We can see that the completeness breakpoint locations are different for each spectral type: 40 pc for K stars, 60 pc for G stars and further away for F stars. This pattern was expected since the hotter a star is, the larger it's luminosity is. The values for distances less than 10 pc can be ignored (the number of stars in these beans is too small).*

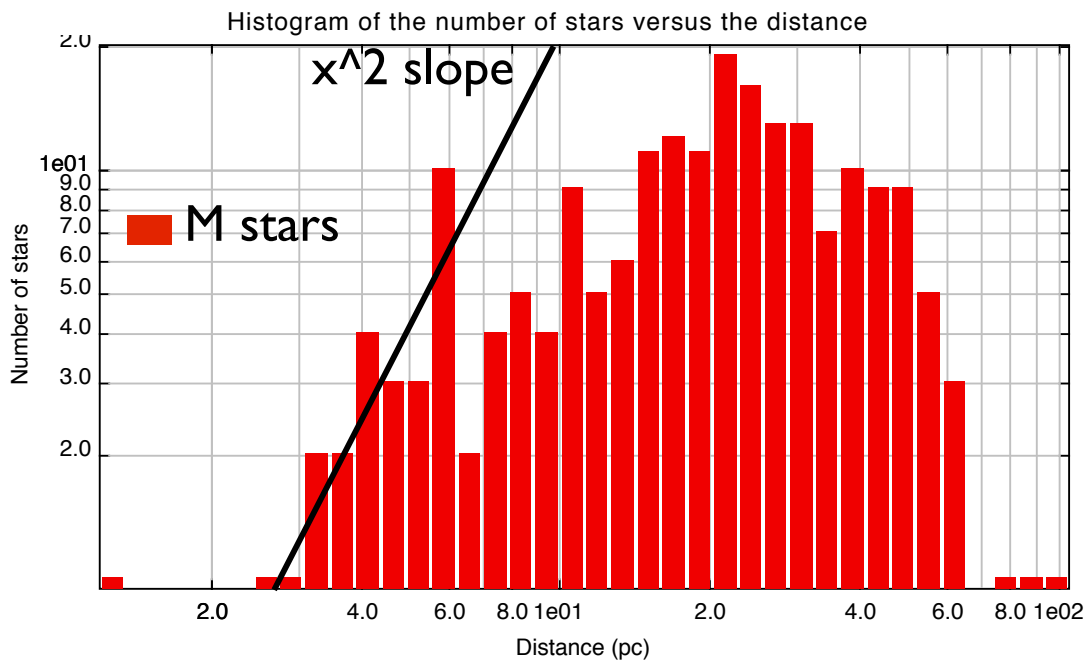
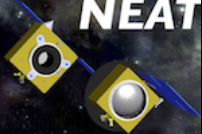
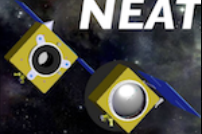


Figure 14: *Histogram of the distribution of the M stars versus the distance. The sample is quite small (75 stars). One can see that the slope is less than 2 for this histogram: although there is an upward trend for distances less than 20 pc, the sample is clearly incomplete (not even at 10 pc!).*

	Nearby Earth Astrometric Telescope	Ref: NEAT-sci-001 Version : v4
	<i>Creation and exploitation of the NEAT catalogs</i>	Date : 16-09-2014 Page : 29 / 34

References

- Alibert, Y., Carron, F., Fortier, A., Pfyffer, S., Benz, W., Mordasini, C., and Swoboda, D.: 2013, *Astronomy and Astrophysics* **558**, A109
- Dittkrist, K.-M., Mordasini, C., Klahr, H., Alibert, Y., and Henning, T.: 2014, *Astronomy and Astrophysics* **567**, A121
- Flower, P. J.: 1996, *APJ* **469**, 355
- Kaltenegger, L., Eiroa, C., and Fridlund, C. V. M.: 2010, *APSS* **326**, 233
- Kasting, J. F., Whitmire, D. P., and Reynolds, R. T.: 1993, *Icarus* **101**, 108
- Mordasini, C., Dittkrist, K.-M., Alibert, Y., Klahr, H., Benz, W., and Henning, T.: 2011, in A. Sozzetti, M. G. Lattanzi, and A. P. Boss (eds.), *IAU Symposium*, Vol. 276 of *IAU Symposium*, pp 72–75
- Schmidt-Kaler: 1982, in Astronomy and Astrophysics (eds.), *Stars and star clusters*, Vol. 2b, SpringerMaterials

	Nearby Earth Astrometric Telescope	Ref: NEAT-sci-001 Version : v4
	<i>Creation and exploitation of the NEAT catalogs</i>	Date : 16-09-2014 Page : 30 / 34

A – Summary of the Topcat operations

- Load the hipparcos and tycho catalog (all the tables), with the computed J2000 coordinates in a VOTable format
- In the main Hipparcos table, define the following subsets
 - closest_stars: `Plx > 50`
 - closest_MS_A_stars: `_2 && matches(SpType, "^A.*V$")`
 - closest_MS_F_stars: `_2 && matches(SpType, "^F.*V$")`
 - closest_MS_G_stars: `_2 && matches(SpType, "^G.*V$")`
 - closest_MS_K_stars: `_2 && matches(SpType, "^K.*V$")`
 - closest_MS_M_stars: `_2 && matches(SpType, "^M.*V$")`
 - closest_MS_FGK_stars:


```
_2 && (matches(SpType, "^F.*V$")
||matches(SpType, "^G.*V$") ||matches(SpType, "^K.*V$"))
```
 - closest_MS_AFGKM_stars:


```
_2 && (matches(SpType, "^A.*V$")
||matches(SpType, "^F.*V$") ||matches(SpType, "^G.*V$") ||
matches(SpType, "^K.*V$") ||matches(SpType, "^M.*V$"))
```
- Select the Tycho table and perform a crossmatch with Hipparcos to find the reference stars.
Change table name to: **Tycho reference stars crossmatch**
Export table as: **reference_stars_topcat.csv**
- Export the closest_MS_AFGKM_stars subset as **closest_MS_AFGKM_stars_topcat.csv**, run the script and import the new table with the new magnitude column.
- Select the closest_MS_AFGKM_stars subset and create all the "NEAT" columns (see the list in section B)
- For completeness only: create the close main sequence F, G, K and M stars subsets in the main Hipparcos table (stars closer than 100 pc).
- Re create the A, F, G, K and M main sequence stars subsets in the **closest_MS_AFGKM_stars_topcat.cs** table.

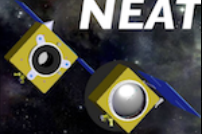
B – List of the NEAT columns

□ Columns prior to sum of reference stars flux (by script) .

These columns can be created either before or after the equivalent reference star magnitude is added.

Dist 1000/Plx

Appendix F - NEAT Memo: Creation and exploitation of the NEAT catalog

	Nearby Earth Astrometric Telescope	Ref: NEAT-sci-001 Version : v4
	<i>Creation and exploitation of the NEAT catalogs</i>	Date : 16-09-2014 Page : 31 / 34

```

BC -0.1784538+2.9023636*$39-12.318814*pow($39,2)+20.931026*pow($39,3)
-22.50268371*pow($39,4)+63.6149604*pow($39,5)-177.541721356*pow($39,6)
+249.915028525*pow($39,7)-182.6519997*pow($39,8)+67.42205675*pow($39,9)
-9.98700145*pow($39,10)
MB Vmag+BC-5*ln(100/Plx)/ln(10)
L pow(10,(4.75-MB)/2.5)
Mass pow(L,1.0/3.8)
SeffIn1 $39<0.62? -1.484*$39+2.330 : -0.371*$39+1.640
SeffOut1 $39<0.62? -0.303*$39+0.547 : -0.092*$39+0.417
SeffIn2 $39<0.62? -0.727*$39+2.211: -0.165*$39+1.862
SeffOut2 $39<0.62? -0.273*$39+0.489 : -0.082*$39+0.371
HZIn1 pow(L/SeffIn1,0.5)
HZIn2 pow(L/SeffIn2,0.5)
HZOut1 pow(L/SeffOut1,0.5)
HZOut2 pow(L/SeffOut2,0.5)
AIn1 3/Mass*HZIn1/Dist
AIn2 3/Mass*HZIn2/Dist
AOut1 3/Mass*HZOut1/Dist
AOut2 3/Mass*HZOut2/Dist
AEarthFlux 3/Mass*pow(L,0.5)/Dist
AMid1 (AIn1+AOut1)/2
AMid2 (AIn2+AOut2)/2
IWAIn1 HZIn1/Dist
IWAIn2 HZIn2/Dist
IWAOut1 HZOut1/Dist
IWAOut2 HZOut2/Dist
IWAEarthFlux pow(L,0.5)/Dist
IWAMid1 (IWAIn1+IWAOut1)/2
IWAMid2 (IWAIn2+IWAOut2)/2
TIn1 pow(pow(HZIn1,3)/Mass,0.5)
Tin2 pow(pow(HZIn2,3)/Mass,0.5)
TOut1 pow(pow(HZOut1,3)/Mass,0.5)
TOut2 pow(pow(HZOut2,3)/Mass,0.5)

```


Columns after sum of reference stars flux (by script) .

These columns can only be created after the equivalent reference star magnitude is added.

```

SigmaH pow(0.0144*pow(10,(Vmag-6)/2.5)+0.372*pow(10,(EqRefMag-9.05)/2.5)+0.194,0.5)
TexoEarth 36*pow(SigmaH,2)/pow(AIn1,2)

```

	Nearby Earth Astrometric Telescope	Ref: NEAT-sci-001
	<i>Creation and exploitation of the NEAT catalogs</i>	Version : v4 Date : 16-09-2014 Page : 32 / 34

C – Python script for summing reference stars flux: source code

```

import sys
print "\n" + "PYTHON VERSION: " + sys.version + "\n"

from math import sin, cos, atan2, pi, sqrt, log

# The path to the include directories has to be added manually...
sys.path.append("/Library/Frameworks/Python.framework/Versions/2.7/lib/python2.7/site-packages")
sys.path.append("/opt/local/Library/Frameworks/Python.framework/Versions/2.7/lib/python2.7/site-pa

import pylab as pl
import scipy as sp
import scipy.integrate as integ
from scipy import optimize
import numpy as np
import matplotlib.pyplot as plt # the tidy way
import matplotlib.mlab as mlab
import matplotlib as mp

# this script processes the target and reference stars from topcat imported csv
# data files. The goal is to compute for each target stars, the flux of each ref
# star and the total flux of the ref stars

import csv
from decimal import Decimal

print "SCRIPT START"

print "Step 1: retrieve magnitudes and IDs of target stars"

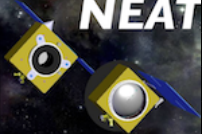
target = csv.reader(open('closest_FGK_targets_topcat.csv'))
#data = csv.DictReader(open('test.csv'))

ref = csv.reader(open('reference_stars_topcat.csv'))
fields = ref.next()
# the columns of interest are:
# - 0: RA (HIP)
# - 1: DEC (HIP)
# - 3: HIP ID
# - 81:

# TODO: add a way to find/print the selected columns, to check the correctness of
# the calculations
hip_ids = []
ra_targets = []
dec_targets = []

# retrieve hipparcos ids, RA and DEC coordinates of neat targets
for raw in target:
    ra_targets.append(raw[0])

```

	Nearby Earth Astrometric Telescope	Ref: NEAT-sci-001 Version : v4
	<i>Creation and exploitation of the NEAT catalogs</i>	Date : 16-09-2014 Page : 33 / 34

```

        dec_targets.append(raw[1])
        hip_ids.append(raw[3])

ra_targets.pop(0)
dec_targets.pop(0)
hip_ids.pop(0)

print('hip_ids = ')
print(hip_ids)

print "Step 2: find which tychos stars are the targets"
# finds which entry in the tychos ref stars is the target
tyc_ids = [0]*len(hip_ids)
ref_star_mageq = [99]*len(hip_ids) # equivalent magnitude of ref stars

counts = 0

for i in range(len(hip_ids)):
    dist = 3600.0**2
    ref = csv.reader(open('reference_stars_topcat.csv'))
    ref.next()
    for raw in (ref):
        # print('hip_id = ' + hip_ids[i])
        # print('raw = ' + raw[3])
        # print(' ')

        if int(raw[3]) == int(hip_ids[i]):
            counts = counts + 1
            new_dist = (float(raw[81])-float(ra_targets[i]))**2 +
                (float(raw[82])-float(dec_targets[i]))**2
            if new_dist < dist:
                tyc_ids[i] = raw[84]
                dist = new_dist

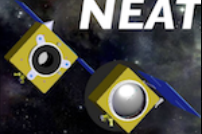
print('counts = ')
print(counts)
print('tyc_ids = ')
print(tyc_ids)

print('size tyc_ids = ')
print(len(tyc_ids))

vmag_hip = []
vmag_tyc = []
sep = []
print "Step 3: verification of the matching between the hipparcos targets and the
    tychos matches found "
# TODO: add a verification step: verify that the parameters for the identified
    hipparcos targets in the list of references have the same hipparcos/tychos
    parameters. Count the good matches. Plot the values of hip params VS tyc params
for i in range(len(tyc_ids)):
    ref = csv.reader(open('reference_stars_topcat.csv'))
    ref.next()
    for raw in ref:
        if raw[84] == tyc_ids[i]:

```

Appendix F - NEAT Memo: Creation and exploitation of the NEAT catalog

	Nearby Earth Astrometric Telescope	Ref: NEAT-sci-001 Version : v4
	<i>Creation and exploitation of the NEAT catalogs</i>	Date : 16-09-2014 Page : 34 / 34

```

        vmag_hip.append(float(raw[7]))
        vmag_tyc.append(float(raw[88]))
        sep.append(float(raw[142]))

#TODO: switch loop imbrication to speed up, with a counter on the neat targets
      (works only if the neat targets are in the same order than in the reference
      stars file)s
vmag_hip_arr = np.array(vmag_hip)
vmag_tyc_arr = np.array(vmag_tyc)
pl.figure(1)
plt.scatter(vmag_hip_arr,vmag_tyc_arr)
for ids, maghip, magtyc in zip(hip_ids, vmag_hip, vmag_tyc):
    plt.annotate(ids, xy = (maghip, magtyc), xytext = (-20, 20),textcoords =
        'offset points', ha = 'right', va = 'bottom',
        bbox = dict(boxstyle = 'round,pad=0.5', fc = 'yellow', alpha = 0.5))
#arrowprops = dict(arrowstyle = '->', connectionstyle = 'arc3,rad=0') adding arrow
option => crash
plt.show()
pl.figure(2)
plt.scatter(sep,vmag_hip_arr-vmag_tyc_arr)
plt.show()
pl.figure(3)
plt.scatter(sep,vmag_hip_arr)

print "Step 4: calculate the sums of the reference stars flux for each target"
# calculate the sums of the reference stars flux for each target
for i in range(len(hip_ids)):
    ref = csv.reader(open('reference_stars_topcat.csv'))
    ref.next()
    for raw in ref:
        if raw[3] == hip_ids[i]:
            if raw[84] != tyc_ids[i]:
                ref_star_mageq[i] =
                    -2.5/log(10)*log(10**(-ref_star_mageq[i]/2.5) +
                    10**(-float(raw[88])/2.5))

print(ref_star_mageq)

target_out = csv.writer(open('closest_FGK_targets_topcat_out.csv', 'wb'))

target = csv.reader(open('closest_FGK_targets_topcat.csv'))
fields = target.next()

fields.append('eq_ref_mag')
print(fields)

target_out.writerow(fields)

i=0
for row in target:
    row.append(ref_star_mageq[i])
    target_out.writerow(row)
    i = i + 1

print "SCRIPT ENDS"

```

Appendix G

Tests on individual components

Table G.1: Test report Table.

Component tested	Laser HeNe 1.5mW
Test Name / Test number	Intensity stability / 1
Supplier name / Product ref.	Thorlabs / HRS015
Test date - Performed by	15/02/13 - Antoine Crouzier
Compliance	Yes
Specification / Result	1×10^{-3} / 9.5×10^{-5}

- Description:
Measure of the relative intensity stability
- Hardware used:
Thorlab Photo-diode
- Method:
The laser is turned on, in frequency-stabilized mode, the injection lens is removed and the room is darkened (negligible dark current). A photo-diode is placed in the path of the beam. The intensity is recorded versus the time. Sampling frequency: 1 Hz. Duration: 1000 s.
- Results:
Figure G.1 shows measured intensity versus the time.

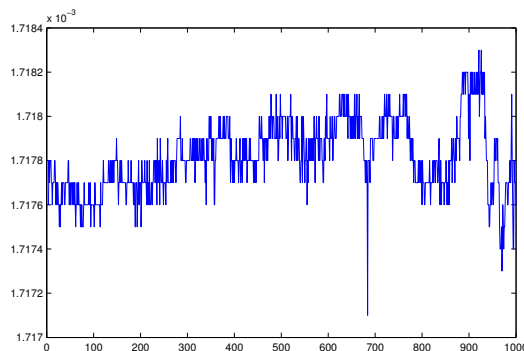


Figure G.1: Intensity (mW) vs time (s).

- Remarks:
 $I_{\text{dark}} = 0 \text{ nW}$
- Conclusion:
 For a duration of 1000 sec, with a 1 Hz sampling: $\text{RSD}(\text{intensity}) = 9.5 \times 10^{-5}$

 Table G.2: **Test report Table.**

Component tested	Laser HeNe 1.5mW
Test Name / Test number	Polarization linearity / 2
Supplier name / Product ref.	Thorlabs / HRS015
Test date - Performed by	15/02/13 - Antoine Crouzier
Compliance	Yes
Specification / Result	1000:1 / 5400:1

- Description:
 Measure of the linearity of the polarization at the laser output. The linearity R_{pol} is defined as the following ratio: $\frac{\text{intensity of straight polarization}}{\text{intensity of circular polarization}}$.
- Hardware used:
 Two polarizers: Glan–Thompson crystals, theoretical rejection ratio of 100 000:1. Thorlab Photo-diode.
- Method:
 The laser is on and in frequency-stabilized mode, the injection lens is removed. The room is darkened (negligible dark current).
 1. The laser beam is blocked and the resulting “dark intensity” is noted I_{dark} .
 2. The polariser extinction ratio is measured by placing the two polarizers in the path of the laser beam. The first polarizer is aligned with the laser main axis (by searching the maximum). The second polarizer is also aligned with the polarization (same method) and I_{para} is measured. The angle of the second polariser is changed by 90° (by searching the minimum) and I_{perp} is measured. The ratio between the intensity of each case (after dark subtraction) gives the rejection ratio. It gives the maximum value of R_{pol} that can be obtained by this measure.

$$\text{Rejection ratio} = \frac{I_{\text{para}} - I_{\text{dark}}}{I_{\text{perp}} - I_{\text{dark}}}$$
 3. The second polarizer is removed (only one is left in front of the laser). The angle of the polariser is tuned to find the maximum of intensity I_{max} . The angle of the polarizer is tuned to find the minimum of intensity I_{min} . We obtain $R_{\text{pol}} = \frac{I_{\text{max}} - I_{\text{dark}}}{I_{\text{min}} - I_{\text{dark}}}$.
- Results:
 Read noise photo-detector (no light): $\pm 3\text{nW}$
 $I_{\text{dark}} < 1 \text{ nW}$
 $I_{\text{para}} = 1.337 \text{ mW}$
 $I_{\text{perp}} = 45 \pm 3 \text{ nW}$
 $\Rightarrow \text{Rejection ratio} > 3.0 \times 10^4 \pm 10\%$
 $I_{\text{max}} = 1.371\text{mW}$
 $I_{\text{min}} = 248 \pm 3 \text{ nW}$
 $\Rightarrow R_{\text{pol}} = 5400 : 1 \pm 1\%$

- Remarks:

After using a sheet of paper to block the part of the beam visible on the left of the photo-detector (outside of the integrating area): $I_{\text{perp}} = 10$ nW. Some internal reflections or alignment problems inside the polarizers are creating stray light on the photo-detector. The pattern of these off-axis reflections changes with the alignment. We conclude that we have only obtained a lower bound of the rejection ratio, however the value is sufficiently high for our purposes (Rejection ratio $\gg R_{\text{pol}}$).

- Conclusion:

Polarization ratio = 5400 : 1 \pm 1%.

Table G.3: **Test report Table.**

Component tested	Laser HeNe 1.5mW
Test Name / Test number	Polarisation angular stability / 3
Supplier name / Product ref.	Thorlabs / HRS015
Test date - Performed by	15/02/13 - Antoine Cruzier
Compliance	NS
Specification / Result	NS / [0.038; 0.24] $^{\circ}$

- Description:

Measure of the angular stability of the polarization versus time

- Hardware used:

One polarizer: Glan–Thompson crystal, theoretical rejection ratio of 100 000:1. Thorlab Photo-diode.

- Method:

The laser is on and in frequency-stabilized mode, the injection lens is removed. The room is darkened (negligible dark current).

1. The beam is blocked and the “dark intensity” is noted I_{dark}
2. The intensity is measured after the linear polarizer placed in front of the laser output. The polarizer is set with an angle of 90° between the laser polarization and the transmitting axis by searching the minimum of transmission. The value of the intensity $I(t)$ is recorded versus the time. Sampling rate = 1 Hz. Duration = 100 s.
3. The intensity is measured after the linear polarizer placed in front of the laser output. The polarizer is set with an angle of 0° between the laser polarization and the transmitting axis by searching the maximum of transmission. The value of the intensity $I'(t)$ is recorded versus the time. Sampling rate = 1 Hz. Duration = 100 s.

Is it quite troublesome to get back to the variation of the polarization angle from only this intensity measurement. The contributions from the circularity of the laser polarization and the miss-alignment angle of the polarizer have to be separated. Here we consider a model where the polarization is (slightly) elliptical and constant with time. The electric field after the polarizer is the sum of the projections of the minor and major axis (with are out of phase by 180°) along the polarizer transmitting axis:

$$\vec{E} = E_x \cos(t) \cos(d\theta(t) + \phi) \vec{u}_x + E_y \sin(t) \sin(d\theta(t) + \phi) \vec{u}_y$$

where:

- E_x is the electric field amplitude along the minor polarization axis of the laser
- E_y is the electric field amplitude along the major polarization axis of the laser
- ϕ is the static miss-alignment between the polarizer transmitting axis and the laser major axis
- $d\theta(t)$ is the random variation of the laser polarization angle at a time t .

Let us define $\Phi = d\theta(t) + \phi$. Given the setup and the previous results, we can safely assume $\Phi \lesssim 0.02$ rad, so we can write: $I(t) \approx Ex^2(1 - \Phi^2)^2 + Ey^2\Phi^2$. The intensity $I(t)$ is minimum when $\Phi = 0$. The variations of $I(t)$ are in first approximation caused by the change in the projection of E_y because: $E_y^2 \gg E_x^2$ (from previous tests, we have already determined $Ex^2 = I_{\min}$ and $Ey^2 = I_{\max}$).

Assuming that the miss-alignment angle is small ($d\theta(t) \gg \phi$):

$$I(t) \approx I_{\min} + I_{\max} (d\theta(t))^2 \approx I(t)_{\min} + I_{\max} (d\theta(t))^2 \quad (\text{G.1})$$

$$\Rightarrow |d\theta(t)| = \sqrt{\frac{I(t) - I(t)_{\min}}{I_{\max}}} \quad (\text{G.2})$$

Assuming that the miss-alignment angle is large ($d\theta(t) \leq \phi$):

$$I(t) \approx I_{\min} + I_{\max}\phi^2 + I_{\max} (2d\theta(t)\phi) \approx I(t)_{\text{mean}} + I_{\max} (2d\theta(t)\phi) \quad (\text{G.3})$$

$$\Rightarrow d\theta(t) = \frac{I(t) - I(t)_{\text{mean}}}{2\phi I_{\max}} \quad (\text{G.4})$$

In our setup we feed the laser into two modulators that select a linear polarization. So what we are really interested in is the level of intensity fluctuations after selecting the main polarization ($I'(t)$). Then the fluctuations can be compared to laser intensity fluctuations and we can simply assess how much polarization instability contributes into overall intensity fluctuations. In fact $I'(t)$ gives us the stability of the intensity and the polarization combined.

- Results:

Figure G.2 shows $I(t)$. Figure G.3 shows $d\theta(t)$. Figure G.4 shows $I'(t)$.

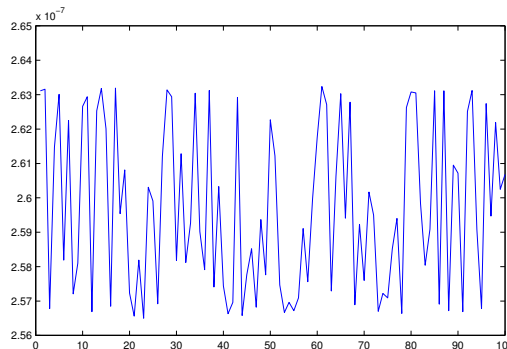


Figure G.2: $I(t)$ (W) vs time (s). These points are used to calculate $d\theta(t)$.

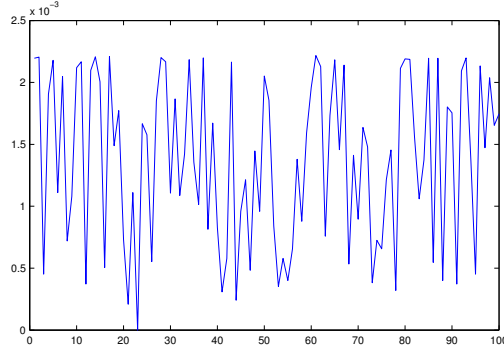


Figure G.3: $\sqrt{\frac{I(t) - I(t)_{\min}}{I_{\max}}}$ vs time(s).

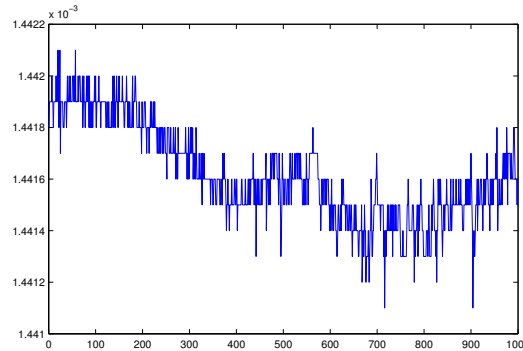


Figure G.4: $I'(t)$ (W) versus time (s).

For a duration of 100 sec, with a sampling of 1 Hz:

- $\text{RSD}(I(t)) = 9.3 \times 10^{-3}$.
- $\text{RSD}(I'(t)) = 1.3 \times 10^{-4}$
- If $d\theta(t) \gg \phi$: $\text{RSD}(|d\theta(t)|) = 6.7 \times 10^{-4} \text{rad} = 0.038^\circ$
- If $d\theta(t) \leq \phi$, the worst case is when we assume $\phi = 8 \times 10^{-3} \text{rad}$, because we find

$$\text{SD}[d\theta(t)] = \frac{\text{RSD}[I(t)]\text{Mean}[I(t)]}{2\phi I_{\max}} = 4.3 \times 10^{-3} \text{rad} = 0.24^\circ \quad (\text{G.5})$$

We know this to be the worst case because if assume lower values for ϕ , we quickly obtain $d\theta(t) \geq \phi$, which contradicts the hypothesis.

- Remarks:

$$I_{\text{dark}} = 0$$

$$I_{\max} = 1.371 \text{mW (known from other tests)}$$

- Conclusion:

The intensity variations observed after the polarizer are dominated by intensity variation only (the RSD of the intensity before and after selection of the main axis with a polarizer are respectively 9.5×10^{-5} and 1.3×10^{-4} , the difference is not significant and could be simply due to changes in the amplitude of thermal fluctuations between the two measures.

The angle of the polarization is fairly stable, for a duration of 100 sec: $\text{STD}(d\theta) < 0.24^\circ$

Test report:Table G.4: **Test report Table.**

Component tested	Laser HeNe 1.5mW
Test Name / Test number	Stabilization time / 4
Supplier name / Product ref.	Thorlabs / HRS015
Test date - Performed by	13/02/13 - Antoine Crouzier
Compliance	No
Specification / Result	30 min / 60-70 min

- Description:
Measure of the stabilization time
- Hardware used:
Clock
- Method:
The laser is turned on and the time after which the LED stops blinking is noted.
- Results:
The laser stabilized between 60 and 70 minutes after being turned on.
- Remarks:
- Conclusion:
The laser can take longer than the time given by the constructor to stabilize (not critical).

Test report:Table G.5: **Test report Table.**

Component tested	Laser HeNe 1.5mW
Test Name / Test number	Wavelength stability / 5
Supplier name / Product ref.	Thorlabs / HRS015
Test date - Performed by	18/02/13 - Antoine Crouzier
Compliance	No
Specification / Result	2×10^{-9} / 1.5×10^{-8}

- Description:
Measure of the wavelength stability
- Hardware used:
HiFinesse spectrometer: <http://www.highfinesse.com/en/wavelengthmeter/ws6.php>
Theoretical resolution: better than 1×10^{-6}
- Method:
The laser is turned ON, in frequency-stabilized mode and injected into a (non PM) fiber. The fiber is fed into a lambda meter. The wavelength is recorded versus the time. Sampling rate: 10 Hz. Lambda meter integration time: 100 ms. Duration = 3000 seconds.

- Results:

A wavelength of -4 on the data log indicates that the laser was saturated, this happens because the intensity is not stable and the exposure time becomes too high. Only the first part of the data (before saturation) is shown below. The deviation is greater for longer time scales: slow drifts occur. This can be due to thermal variations.

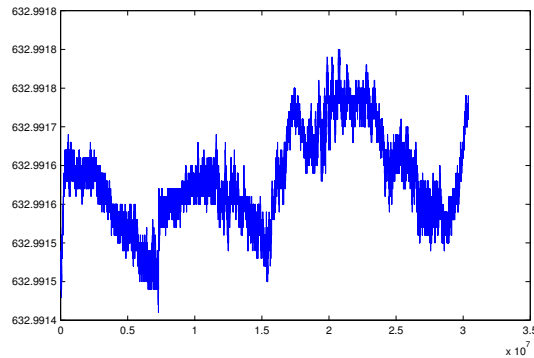


Figure G.5: **Wavelength (nm) vs time (ms)**. There are 30000 points on this plot, at a sampling rate of 10Hz, the total duration is 3000 seconds. Relative STD = 9.5×10^{-8} .

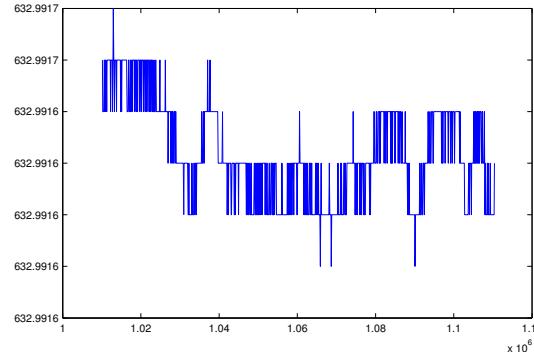


Figure G.6: **Figure 2: Wavelength (nm) vs time (ms)**. There are 1000 points on this plot, at a sampling rate of 10Hz, the total duration is 100 seconds. Wavelength RSD: 1.5×10^{-8} . The deviation is smaller because it was dominated by large variations in large time scales in the previous set of data points: on short time scale the laser is more stable.

- Remarks:

- Conclusion:

For a duration of 100 sec, $RSD(\text{wavelength}) = 1.5 \times 10^{-8}$. Although the final values found are not compatible with the constructor specification, this could be caused by the resolution of the spectrometer used. The measured wavelength stability should however be enough for our application.

Table G.6: **Test report Table.**

Component tested	Liquid core fiber
Test Name / Test number	Plug interface leakage / 6
Supplier name / Product ref.	Oriel / Liquid light guides - LLG210/LLG211
Test date - Performed by	18/02/13 - Antoine Crouzier and Eric Stadler
Compliance	Yes
Specification / Result	Air tight / Air tight

- Description:
Air Leakage inside the fiber when interfaced with a vacuum plug
- Hardware used:
Leakage detector. Plug.
- Method:
The fiber is inserted into the plug, the plug is connected to the leakage detector, the vacuum is made and the leakage rate is tested with helium.
- Results:
No significant leakage was detected ($< 1 \times 10^{-10}$ mBar on the leakage manometer).
- Remarks:
The joint had to be maintained in place manually, so the leakage has been tested reliably only for a short time (a few seconds).
- Conclusion:
No significant leakage was detected inside the fiber. The fiber still works after the operation.

Table G.7: **Test report Table.**

Component tested	Liquid core fiber
Test Name / Test number	Degassing / 7
Supplier name / Product ref.	Oriel / Liquid light guides - LLG210/LLG211
Test date - Performed by	21/12/12 - Antoine Crouzier
Compliance	Yes
Specification / Result	Air tight / Air tight

- Description:
Behavior of the fiber into vacuum, degassing .
- Hardware used:
Vacuum stove
- Method:
The fiber is put into vacuum, its integrity and transmission are checked after passage into vacuum. The quantity of gas released by the fiber is measured coarsely.

The fiber is first placed into vacuum for several days to be cleaned. After that the pump of the vacuum stove is stopped and the pressure increase is measured versus the time. This pressure increase correspond to the leaks of the stove plus the residual degassing of the fiber.

Because the vacuum stove is not airtight, additional actions are taken:

- the valve between the stove and the pump is closed before stopping the pump
 - the pressure increase is also measured without the fiber
- Results:

Measure 1: With fiber, after 3 days + 14 hours of vacuum cleaning:

T (min)	0	0,5	1,5	2,5	3	4	4,5	5	35	177
P (mbar)	6	7	8	9	10	11	12	13	54	285

Leaking rates:

$$F(5 \text{ min}) = 1.5 \text{ mbar/min}$$

$$F(35 \text{ min}) = 1.37 \text{ mbar/min}$$

$$F(177 \text{ min}) = 1.57 \text{ mba/min}$$

Measure 2: Without fiber

T (min)	0	0,3	0,6	0,8	1	1,5	2	2,5	3	4	5	98
P (mbar)	14	15	16	17	18	20	22	25	27	32	36	780

Leaking rates:

$$F(5 \text{ min}) = 4.4 \text{ mbar/min}$$

$$F(98 \text{ min}) = 7.81 \text{ mbar/min}$$

Measure 3: Without fiber

T (min)	0	0,5	1	1,5	2	2,5	3	3,5	4	4,5	5	121
P (mbar)	7	8	9	10	11	11	12	13	14	15	16	147

Leaking rates:

$$F(5 \text{ min}) = 1.8 \text{ mbar/min}$$

$$F(121 \text{ min}) = 1.16 \text{ mbar/min}$$

- Remarks:

For the measure 2 the door was first pressed against the frame before locking. This apparently resulted in a much higher leaking rate. The leaking rate changes with time, it seems to decrease first and increase afterwards. The leak was 1 mbar/sec at the end of the measure 2.

- Conclusion:

The fiber still works after being put into vacuum, a visual inspection shows no damages and it still transmits light properly (the change in transmission is not noticeable to the naked eye).

The deviation on the leaking rate of the door (at 5 minutes) is 1.83 mbar/min. It is greater than the leaking rate measured with the fiber inside. The degassing rate can be anywhere between 0 and 1.5 mbar/min. Assuming a volume of 200 L, we can only say that the degassing rate is less than 0.3 L/min. A cryostat is needed to obtain a useful measure.

Table G.8: **Test report Table.**

Component tested	Integrated-optical phase modulators
Test Name / Test number	Attenuation / 8
Supplier name / Product ref.	Jenoptik / PM 635
Test date - Performed by	06/03/13 - Antoine Crouzier
Compliance	Yes
Specification / Result	6 db / 5.94 db

- **Description:**
Measure of the intensity attenuation.
 - **Hardware used:**
Laser source. Fibers and connectors. Photo-diode.
 - **Method:**
The light is fed from the fibered HeNe laser into the photodiode, the intensity levels are compared when the modulator is out (I_{ref}) and in ($I_{\text{modulator}}$) the chain. The transmission is $T = \frac{I_{\text{modulator}}}{I_{\text{ref}}}$. The attenuation is: $A(\text{db}) = 10 \log(-T)$. Because no fiber was available, the splitter was used between the laser and the photo-diode/the modulator.
 - **Results:**
 $I_{\text{ref}} = 255 \pm 5 \text{ nW}$
 $I_{\text{modulator}} = 65 \pm 2 \text{ nW}$
 $\Rightarrow T = 0.255$
 $\Rightarrow A = 5.94 \text{ db}$
- With the modulator plugged, the intensity was varying between 0 nW and a maximum of about 65 nW when the fiber was moved. This is consistent with a modulator that selects only a linear polarization: the flux is maximum when the polarization at the end of the fiber is (by chance) aligned with the transmitting axis.
- **Remarks:**
 - **Conclusion:**
A=5.94 db. It May be advantageous to use a PM fiber between the laser and the splitter, it can reduce the difficulty of obtaining a configuration with the main polarization axis aligned with each modulator. To avoid having a bad and/or variable visibility, we must insure that after the separation in the splitter, the polarization in both lanes is aligned with each respective modulator and that the setup is stable mechanically and thermally.

 Table G.9: **Test report Table.**

Component tested	Halogen light sources
Test Name / Test number	White light source stability / 9
Supplier name / Product ref.	Lot-Oriel / LSB111/5
Test date - Performed by	15/02/13 - Antoine Crouzier and Jan Dupont
Compliance	NS
Specification / Result	NS / 8%

- Description:
Measure of the power output and intensity stability after coupling into the liquid core fibers.
- Hardware used:
Thorlab photo-diode. Liquid core fibers.
- Method:
 1. The white source is injected into the liquid core fiber, the extremity of the fiber is placed a few millimeters in front of the photo-diode. The intensity $I(t)$ is measured versus time.
 2. We add the “optical filter” provided with the lamp. The maximum output level is measured, then we place a second liquid core fiber in front of the first fiber. We measure again the intensity.
- Results:
At the output of the first fiber: $I_{\max} = 8.25$ mW, at the output of the second fiber $I_{\max} = 5.17$ mW.

Figure G.7 shows the measured intensity versus time.

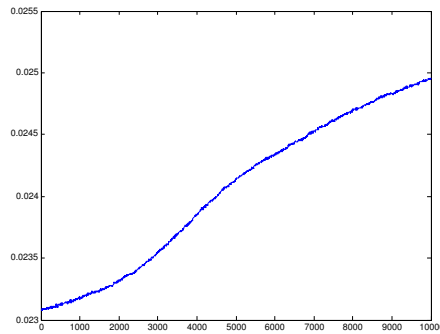


Figure G.7: **Intensity (W) vs time (s).**

- Remarks:
- Conclusion:
The intensity of the light steadily increased by 8% during the first 1000 seconds after turning on the lamp. The short scale fluctuation amplitude is about 0.2% of the total intensity.

The total power collected after filtering and coupling into one liquid fiber is 8.25 W. The coupling ratio between the two liquid fibers is 63%.

Appendix H

Size of the diffraction spot and Nyquist sampling

The aim of this appendix is to determine the size of the diffraction spot in the NEAT demo optical configuration (“real object”/“real image”). We will use the notion of “equivalent focal”. Figure H.1 shows an equivalent optical set-up, where the mirror is replaced with two thin lenses of focal lengths $f_1 = F_1O_1$ and $f_2 = O_2F_2$ (with $1/f_1 + 1/f_2 = 1/f$) and an intermediary stop aperture between them.

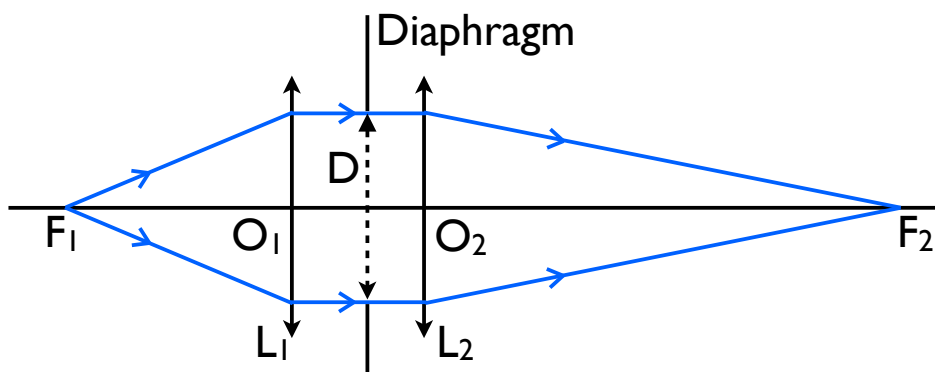


Figure H.1: **Equivalent optical set up.**

Let be A the location of the pseudo star objects, A' the location of their image. We have the relation $1/OA + 1/OA' = 1/f$. By choosing $f_1 = OA$ and $f_2 = OA'$, we have the artificial stars at the focus of the first lens of the equivalent system. A collimated beam of light is sent by the lens L_1 unto the diaphragm. So the diffraction pattern at infinity (before L_2) is an Airy pattern, which is imaged at the focus of lens L_2 . The light distribution at the detector plane is:

$$I(\theta) \propto I_0 \left(\frac{J_1 \left[\frac{\pi D r}{L \lambda} \right]}{\frac{\pi D r}{L \lambda}} \right)^2$$

With r the distance to the optical axis in cylindrical coordinates. The maximum spatial frequency of this Airy pattern is $\frac{\lambda L}{D}$ (and the first zero is at $r = 1.22 \frac{\lambda L}{D}$). So compared to a configuration with real stars at infinity, we have simply replaced f

by the “equivalent focal” L and the Nyquist sampling condition is:

$$2e \leq \frac{L\lambda_{\min}}{D} \quad (\text{H.1})$$

Appendix I

Coherent and incoherent stray light

In the case of incoherent light, we have: $\text{SNR} \propto \frac{I_0}{I_1}$, where I_0 is the light intensity from the source we want to observe (direct path) and I_1 is the stray light intensity, i.e. after reflection(s) inside the vacuum chamber or the baffle.

The stray light is a much more sensitive issue when the light is coherent: consider the fringe pattern created by two beams of respective intensities I_0 and I_1 , the resulting intensity can be written as:

$$I_0 + I_1 + 2\sqrt{I_0 I_1} \cos(2\pi\delta_{12}(M))$$

Here $\delta_{12}(M)$ is the path-length difference between the beams 1 and 2 and the point M. Now we place ourselves in the case $I_0 \gg I_1$, where I_0 is the main beam and I_1 is the stray light (the intensity, after (multiple) reflection(s), on the CCD).

In this case we have $\text{SNR} = \frac{I_0}{2\sqrt{I_0 I_1}} = \frac{1}{2}\sqrt{\frac{I_0}{I_1}}$: I_0 is the intensity created by the main beam and $2\sqrt{I_0 I_1}$ is the secondary fringe pattern created by the stray light. This means that this kind of stray light must be taken care off very minutely.

Glossary

M_{\oplus} Unit of mass equal to the mass of the Earth ($M_{\oplus} = 5.97219 \times 10^{24}$ kg). 9, 230

M_{\odot} Unit of mass equal to the mass of the Sun ($M_{\odot} = 1.988 \times 10^{30}$ kg). 230

R_{\oplus} Unit of length equal to the radius of the Earth ($R_{\oplus} = 6.371$ m). 9, 19, 230

R_{\odot} Unit of length equal to the radius of the Sun ($R_{\odot} = 6.955 \times 10^5$ m). 230

arcmin The arcminute (arcmin/amin) is a unit of angle commonly used by astronomers, it is equal to $1/60^{\text{th}}$ of a degree. It can also be noted with a single prime symbol: $1' = 1$ arcmin. 25, 230

as The arcsecond (arcsec/as) is a unit of angle commonly used by astronomers, it is equal to $1/3600^{\text{th}}$ of a degree. It can also be noted with a double prime symbol: $1'' = 1$ as. 13, 230

bolometric luminosity The bolometric luminosity of a star is a logarithmic measure of its total energy emission, integrated over all wavelengths. 49, 230

confirmed exoplanet Exoplanet detection is delicate. Very often, the data available is only indicative of a planet, but not sufficient to be sure of its existence. This happens if the detection threshold barely exceeds the noise, or if the possibility of another physical explanation cannot be excluded. Both cases can lead to false detections: the literature is full of examples of retracted planets. A standard practice is to classify detections into exoplanet candidates and confirmed exoplanets. Typically, we consider that an exoplanet is confirmed when we estimate that the probability of a false detection is below 1%, otherwise it is only a candidate. In order to confirm a candidate, one can try to acquire more accurate data or detect the same planet with a different method. 10, 230

exo-Earth An exo-Earth is using in this manuscript to designate an habitable Earth-like planet around a sun like star. More precisely this means a similar planetary mass, orbital distance and ellipticity and that the host star has a mass similar to the sun. 9, 12, 230

exoplanet An exoplanet (portmanteau of extrasolar planet), is a planet outside of the Solar System. 8, 230

exoplanet candidate see confirmed exoplanet 19, 20, 230

inclination The inclination of an orbit is the angle between the vector normal to the orbital plane and a reference. In the case of radial velocities, the reference is the direction of the observer. 12, 230

main sequence The main sequence is the state in which stars spend most of their time during their life cycle. The simplified life cycle for a Sun-like star is: formation (by collapse of a gas cloud), pre-main sequence stage (at this stage the star is contracting and mainly powered by gravitational collapse), main sequence (hydrogen fusion maintain the star is quasi-equilibrium), giant phase

(fusion of heavier elements) and finally ejection of the outer layer and formation of a dense stellar remnant. The Sun is in the middle of its main sequence. 8, 230

pc The parsec (pc) is a distance unit commonly used by astronomers. One pc is the distance at which one astronomical unit (distance Earth to Sun) has an apparent angle of 1 arc second, i.e. $1/3600^{\text{th}}$ of a degree. $1 \text{ pc} = 3.08567758 \times 10^{16} \text{ m} = 3.26 \text{ light years}$. 8, 13, 230

pulsar A pulsar (portmanteau of pulsating star) is a highly magnetized, rapidly rotating neutron star. A neutron star is a type of very dense stellar remnant that can result from the death of a massive star, it is almost entirely composed of neutrons. 8, 230

spectral type The spectral type of a star is related to its surface temperature (Harvard classification). Star surface temperatures are strongly correlated to their mass and luminosities. In first approximation, spectral types can be directly mapped onto mass/luminosity/temperature ranges. The more massive the stars, the hotter and the more luminous they are. 10, 230

super Earth An exoplanet of a mass between $1 M_{\oplus}$ and $10 M_{\oplus}$. 20, 230

Acronyms:

AU: Astronomical Unit. The AU is a distance unit commonly used by astronomers. One astronomical unit is $1.495978707 \times 10^{11} \text{ m}$, roughly the average distance between the Earth and the sun.

CCD: Charged-Coupled Device. CCDs are microelectronic devices that are sensitive to light. They operate by shifting charges between each sensitive element, called pixel. They are widely used in digital cameras.

CEA: Commissariat à l'Énergie Atomique et aux Énergies Alternatives. CEA is a french public research organism in the fields of energy, defense, information technology, health sciences. Its current annual budget is about 4.7 billion euros (2012).

CNES: Centre National d'Études Spatiales. CNES is the French Space Agency. Established in 1961 and headquartered in Paris, its current annual budget is about 1.9 billion euros (2012).

COROT: COncvection ROtation et Transits Planétaires. COROT is a space mission of CNES (2006-2011) with contributions from ESA and the German Aerospace Center (DLR). COROT has done precise photometry on stars, for stellar seismology and for detecting transiting exoplanets.

EELT: European Extremely Large Telescope. The E-ELT is a planned ground-based extremely large telescope for the optical/near-infrared range, to be completed by 2022 by ESO on a mountain top in Cerro Armazones, Chile. The primary mirror will have a diameter of 39 meters, fragmented into 798 hexagonal segments, each of them 1.45 meters wide.

EPICS: Exoplanet Imaging Camera and Spectrograph. EPICS is a proposed instrument for the European ELT, dedicated to the detection and characterization of Exoplanets using direct imaging, spectroscopy and polarimetry.

ESA: European Space Agency. ESA is an intergovernmental organization dedicated to the exploration of space, with 20 member states (all in Europe). Established in 1975 and headquartered in Paris, it currently has an annual budget of about 4.28 billion euros (2013).

ESO: European Southern Observatory. ESO is an intergovernmental research organization for astronomy. Since its creation in 1962, ESO provides astronomers access to the southern sky with state-of-the-art observatories located in northern Chile. The annual member state contributions to ESO are approximately 130 million euros (2013).

Gaia: Global Astrometric Interferometer for Astrophysics. Gaia is a scientific mission of ESA launched in december 2013, for a planned duration of 5 years. It is expected to measure the position of 1 billion objects with an accuracy going from 7 micro arcseconds (for magnitude $V=10$) to hundreds of micro arcseconds ($V=20$). Gaia works by direct imaging: although it was first planned as an interferometer, this design was abandoned but the name was kept.

HARPS: High Accuracy Radial Velocity Planet Searcher. HARPS is a high-precision echelle spectrograph installed in 2002 on ESO's 3.6 m telescope at La Silla Observatory in Chile. Its state of the art precision of 1m/s allows to detect habitable super-Earth by radial velocities.

HST: Hubble Space Telescope. The HST is a space telescope (diameter of 2.4 m) that was launched in 1990 and is still in operation today.

HZ: Habitable Zone. The habitable zone (around a given star) is the range of orbital distances (or periods) where planets can have liquid water on their surface. We consider that this condition is the best proxy for "favorable to life as we know it on Earth".

Hipparcos: High Precision PARallax Collecting Satellite. Hipparcos was a scientific mission of ESA (1989-1993). It was the first space mission devoted to precision astrometry, it measured the parallaxes of 100,000 close and bright stars with an accuracy of 1mas. The name of the mission is an obvious reference to the ancient Greek astronomer Hipparchus.

IAS: Institut d'Astrophysique Spatiale.

IPAG: Institut de Planetologie et d'Astrophysique de Grenoble.

JPL: Jet Propulsion laboratory. JPL is a federally funded research and development center and NASA field center located in La Canada Flintridge, California, United States.

JWST: James-Webb Space Telescope. The James-Webb space telescope is an underway NASA project, with contribution from ESA and CSA (Canadian Space Agency), planned for launch in 2018. The telescope is a scientific successor to the Hubble Space Telescope and the Spitzer Space Telescope. The design is optimized

for observations in the infrared with passive cooling. Its diameter of 6.5m will make it the largest infrared observatory ever sent into orbit: it will have an unprecedented resolution and sensitivity from visible red to mid-infrared.

MMF: Multi Mode Fiber.

NASA: National Aeronautics and Space Administration. NASA is the agency of the United States government that is responsible for the nation's civilian space program and for aeronautics and aerospace research. Established in 1958 and headquartered in Washington D.C., its current annual budget is about 18 billion US dollars (2013).

NEAT: Nearby Earth Astrometric Telescope. NEAT is a concept of M class space mission proposed to ESA in 2010. The concept is a space telescope to detect nearby exoplanets by astrometric detection of the wobble of the host star.

PLATO: Planetary Transits and Oscillations of stars. PLATO is a space mission of ESA planned for 2024 which will survey up to a million star to find transiting rocky exoplanets, down to the Earth size.

PRF: Pixel Response function. A PRF is a function representing a pixel sensitivity to light (or quantum efficiency) in the CCD plane.

PSF: Point Spread Function. The PSF of an imaging instrument (for instance a telescope) is the light distribution pattern at its focal plane when exposed to a point source. In practice stars are quasi-perfect point sources because their apparent diameter is well below the resolution of any current telescope.

RSD: Relative Standard Deviation. The RSD is the absolute value of the coefficient of variation. The latter is defined as the ratio of the standard deviation to the mean.

RSS: Root of Sum of Squares. RSS is a mathematical formula, in statistics it can be used to calculate the deviation of a sum of independent random variables of known deviations. When making error budgets, it is used to add several independent sources of errors.

SD: Standard Deviation.

SMF: Single Mode Fiber.

SNR: Signal to noise ratio. The SNR gives information about the amplitude of a signal, relative to the noise level.

STEP: Search for Terrestrial Extrasolar Planets. STEP is a mission of CAS (Chinese Academy of Science) / NSSC (National Space Science Center) selected as part of the advanced research project in the Chinese Strategic Pioneer Program (SPP) on Space Science. STEP is a pointed astrometric mission similar to NEAT but it uses a compact configuration with several mirrors. If approved to enter phase B around 2015, STEP should be planned for launch in 2020.

VESTA: Validation Experiment for Solar-system STaring Astrometry. VESTA is a

high accuracy astrometry testbed that was operated at the JPL, it was very similar to and preceded the NEAT lab demonstration.

VLT: Very Large Telescope. The VLT is a telescope operated since 1998 by the European Southern Observatory on Cerro Paranal in the Atacama Desert of northern Chile. It consists of four individual telescopes, each with a primary mirror 8.2 m in diameter, which can be used either separately or together as an interferometer to achieve very high angular resolution.

Bibliography

- A. Aaboe. Scientific Astronomy in Antiquity. Philosophical Transactions of the Royal Society, 276, 1974. doi: 10.1098/rsta.1974.0007.
- Asger H. Aaboe. Episodes from the Early History of Astronomy. Springer, 2001. ISBN 9780387951362.
- R. L. Akeson, X. Chen, D. Ciardi, M. Crane, J. Good, M. Harbut, E. Jackson, S. R. Kane, A. C. Laity, S. Leifer, M. Lynn, D. L. McElroy, M. Papin, P. Plavchan, S. V. Ramírez, R. Rey, K. von Braun, M. Wittman, M. Abajian, B. Ali, C. Beichman, A. Beekley, G. B. Berriman, S. Berukoff, G. Bryden, B. Chan, S. Groom, C. Lau, A. N. Payne, M. Regelson, M. Saucedo, M. Schmitz, J. Stauffer, P. Wyatt, and A. Zhang. The nasa exoplanet archive: Data and tools for exoplanet research. Publications of the Astronomical Society of the Pacific, 125:989–999, August 2013.
- Y. Alibert, F. Carron, A. Fortier, S. Pfyffer, W. Benz, C. Mordasini, and D. Swo-boda. Theoretical models of planetary system formation: mass vs. semi-major axis. Astronomy and Astrophysics, 558:A109, October 2013a.
- Y. Alibert, F. Carron, A. Fortier, S. Pfyffer, W. Benz, C. Mordasini, and D. Swo-boda. Theoretical models of planetary system formation: mass vs. semi-major axis. Astronomy and Astrophysics, 558:A109, October 2013b. doi: 10.1051/0004-6361/201321690.
- M. Auvergne, P. Bodin, L. Boissard, J.-T. Buey, S. Chaintreuil, G. Epstein, M. Joutet, T. Lam-Trong, P. Levacher, A. Magnan, R. Perez, P. Plasson, J. Plessier, G. Peter, M. Steller, D. Tiphène, A. Baglin, P. Agogué, T. Appourchaux, D. Barbet, T. Beaufort, R. Bellenger, R. Berlin, P. Bernardi, D. Blouin, P. Boumier, F. Bonneau, R. Briet, B. Butler, R. Cautain, F. Chiavassa, V. Costes, J. Cuvilho, V. Cunha-Parro, F. de Oliveira Fialho, M. Decaudin, J.-M. Defise, S. Djalal, A. Docclo, R. Drummond, O. Dupuis, G. Exil, C. Fauré, A. Gaboriau, P. Gamet, P. Gavalda, E. Grolleau, L. Gueguen, V. Guivarc’h, P. Guterman, J. Hasiba, G. Huntzinger, H. Hustaix, C. Imbert, G. Jeanville, B. Johlander, L. Jorda, P. Journoud, F. Karioty, L. Kerjean, L. Lafond, V. Lapeyrere, P. Landiech, T. Larqué, P. Laudet, J. Le Merrer, L. Leporati, B. Leruyet, B. Levieuge, A. Llebaria, L. Martin, E. Mazy, J.-M. Mesnager, J.-P. Michel, J.-P. Moalic, W. Monjoin, D. Naudet, S. Neukirchner, K. Nguyen-Kim, M. Olivier, J.-L. Orcesi, H. Ottacher, A. Oulali, J. Parisot, S. Perruchot, A. Piacentino, L. Pinheiro da Silva, J. Platzer, B. Pontet, A. Pradines, C. Quentin, U. Rohbeck, G. Rolland, F. Rollenhagen, R. Romagnan, N. Russ, R. Samadi, R. Schmidt, N. Schwartz, I. Sebbag, H. Smit, W. Sunter, M. Tello, P. Toulouse, B. Ulmer, O. Vandermarcq, E. Vergnault, R. Wallner, G. Waultier, and P. Zanatta.

- The CoRoT satellite in flight: description and performance. *Astronomy and Astrophysics*, 506:411–424, October 2009.
- R.R. Bate, D.D. Mueller, and J.E. White. *Fundamentals of Astrodynamics*. Dover Books on Aeronautical Engineering Series. Dover Publications, 1971. ISBN 9780486600611.
- C. A. Beichman, N. J. Woolf, and C. A. Lindensmith. *The Terrestrial Planet Finder (TPF): a NASA Origins Program to search for habitable planets*. 1999.
- A. R. Belu, F. Selsis, J.-C. Morales, I. Ribas, C. Cossou, and H. Rauer. Primary and secondary eclipse spectroscopy with JWST: exploring the exoplanet parameter space. *Astronomy and Astrophysics*, 525:A83, January 2011. doi: 10.1051/0004-6361/201014995.
- Z. K. Berta, D. Charbonneau, J. Irwin, C. Burke, J. Dittman, E. Falco, E. Newton, P. Nutzman, A. A. West, and M. Zastrow. The MEarth Project: Characterizing the Nearest M Dwarfs while Searching for Transiting, Habitable Exoplanets. In *American Astronomical Society Meeting Abstracts 218*, page 306.03, May 2011.
- F. W. Bessel. Bestimmung der Entfernung des 61sten Sterns des Schwans. *Astronomische Nachrichten*, 16, 1838. doi: 10.1002/asna.18390160502.
- J.-L. Beuzit, M. Feldt, K. Dohlen, D. Mouillet, P. Puget, F. Wildi, L. Abe, J. Antichi, A. Baruffolo, P. Baudoz, A. Boccaletti, M. Carillet, J. Charton, R. Claudi, M. Downing, C. Fabron, P. Feautrier, E. Fedrigo, T. Fusco, J.-L. Gach, R. Gratton, T. Henning, N. Hubin, F. Joos, M. Kasper, M. Langlois, R. Lenzen, C. Moutou, A. Pavlov, C. Petit, J. Pragt, P. Rabou, F. Rigal, R. Roelfsema, G. Rousset, M. Saisse, H.-M. Schmid, E. Stadler, C. Thalmann, M. Turatto, S. Udry, F. Vakili, and R. Waters. SPHERE: a planet finder instrument for the VLT. In *Society of Photo-Optical Instrumentation Engineers (SPIE) Conference Series*, volume 7014 of *Society of Photo-Optical Instrumentation Engineers (SPIE) Conference Series*, August 2008.
- A. Boccaletti, P. Baudoz, J. Baudrand, J. M. Reess, and D. Rouan. Imaging exoplanets with the coronagraph of JWST/MIRI. *Advances in Space Research*, 36: 1099–1106, 2005.
- X. Bonfils, X. Delfosse, S. Udry, T. Forveille, M. Mayor, C. Perrier, F. Bouchy, M. Gillon, C. Lovis, F. Pepe, D. Queloz, N. C. Santos, D. Ségransan, and J.-L. Bertaux. The HARPS search for southern extra-solar planets. XXXI. The M-dwarf sample. *Astronomy and Astrophysics*, 549:A109, January 2013.
- Alan Boss. *The Crowded Universe : The Search for Living Planets*. Basic Books, 2009. ISBN 0-465-00936-0.
- James Bradley. A Letter from the Reverend Mr. James Bradley Savilian Professor of Astronomy at Oxford, and F.R.S to Dr. Edmond Halley, Astronom. Reg. &c. giving an account of a new discovered motion of the Fix'd Stars. *Philosophical Transactions of the Royal Society*, 35:637–661, 1727.
- James Bradley. A Letter to the Right Honourable George Earl of Macclesfield concerning an Apparent Motion Observed in Some of the Fixed Stars. *Philosophical Transactions of the Royal Society*, 1753.

- C. Broeg, A. Fortier, D. Ehrenreich, Y. Alibert, W. Baumjohann, W. Benz, M. Deleuil, M. Gillon, A. Ivanov, R. Liseau, M. Meyer, G. Oloffson, I. Pagano, G. Piotto, D. Pollacco, D. Queloz, R. Ragazzoni, E. Renotte, M. Steller, and N. Thomas. CHEOPS: A transit photometry mission for ESA small mission programme. In European Physical Journal Web of Conferences, volume 47 of European Physical Journal Web of Conferences, page 3005, April 2013.
- D. Chen. STEP mission: high-precision space astrometry to search for terrestrial exoplanets. Journal of Instrumentation, 9:C04040, April 2014.
- M. Clampin. Status of the James Webb Space Telescope (JWST). In Society of Photo-Optical Instrumentation Engineers (SPIE) Conference Series, volume 7010 of Society of Photo-Optical Instrumentation Engineers (SPIE) Conference Series, August 2008.
- C. S. Cockell, A. Léger, M. Fridlund, T. M. Herbst, L. Kaltenegger, O. Absil, C. Beichman, W. Benz, M. Blanc, A. Brack, A. Chelli, L. Colangeli, H. Cottin, V. Coudé du Foresto, W. C. Danchi, D. Defrère, J.-W. den Herder, C. Eiroa, J. Greaves, T. Henning, K. J. Johnston, H. Jones, L. Labadie, H. Lammer, R. Launhardt, P. Lawson, O. P. Lay, J.-M. LeDuigou, R. Liseau, F. Malbet, S. R. Martin, D. Mawet, D. Mourard, C. Moutou, L. M. Mugnier, M. Ollivier, F. Paresce, A. Quirrenbach, Y. D. Rabbia, J. A. Raven, H. J. A. Rottgering, D. Rouan, N. C. Santos, F. Selsis, E. Serabyn, H. Shibai, M. Tamura, E. Thiébaud, F. Westall, and G. J. White. Darwin-A Mission to Detect and Search for Life on Extrasolar Planets. Astrobiology, 9:1–22, February 2009. doi: 10.1089/ast.2007.0227.
- M. M. Colavita, J. K. Wallace, B. E. Hines, Y. Gursel, F. Malbet, D. L. Palmer, X. P. Pan, M. Shao, J. W. Yu, A. F. Boden, P. J. Dumont, J. Gubler, C. D. Koresko, S. R. Kulkarni, B. F. Lane, D. W. Mobley, and G. T. van Belle. The Palomar Testbed Interferometer. The Astrophysical Journal, 510:505–521, January 1999. doi: 10.1086/306579.
- T. Currie, J. Debes, T. J. Rodigas, A. Burrows, Y. Itoh, M. Fukagawa, S. J. Kenyon, M. Kuchner, and S. Matsumura. Direct Imaging Confirmation and Characterization of a Dust-enshrouded Candidate Exoplanet Orbiting Fomalhaut. The Astrophysical Journal Letters, 760:L32, December 2012.
- M. B. Davies, F. C. Adams, P. Armitage, J. Chambers, E. Ford, A. Morbidelli, S. N. Raymond, and D. Veras. The long-term dynamical evolution of planetary systems. ArXiv e-prints, November 2013.
- D. Deming, S. Seager, J. Winn, E. Miller-Ricci, M. Clampin, D. Lindler, T. Greene, D. Charbonneau, G. Laughlin, G. Ricker, D. Latham, and K. Ennico. Discovery and Characterization of Transiting Super Earths Using an All-Sky Transit Survey and Follow-up by the James Webb Space Telescope. Publications of the Astronomical Society of the Pacific, 121:952–967, September 2009. doi: 10.1086/605913.
- K.-M. Dittkrist, C. Mordasini, H. Klahr, Y. Alibert, and T. Henning. Impacts of planet migration models on planetary populations. Effects of saturation, cooling and stellar irradiation. Astronomy and Astrophysics, 567:A121, July 2014.

- J. A. Dittmann, J. M. Irwin, D. Charbonneau, and Z. K. Berta-Thompson. Trigonometric Parallaxes for 1507 Nearby Mid-to-late M Dwarfs. The Astrophysical Journal, 784:156, April 2014.
- Christian Doppler. On the coloured light of the binary stars and some other stars of the heavens. 1842.
- X. Dumusque. Radial Velocity Stellar Noise and Impact for the Detection of Other Earths. In Astronomy of Exoplanets with Precise Radial Velocities, page 11, August 2010.
- X. Dumusque, F. Pepe, C. Lovis, D. Ségransan, J. Sahlmann, W. Benz, F. Bouchy, M. Mayor, D. Queloz, N. Santos, and S. Udry. An Earth-mass planet orbiting Alpha Centauri B. Nature, 491:207–211, November 2012.
- P. J. Flower. Transformations from Theoretical Hertzsprung-Russell Diagrams to Color-Magnitude Diagrams: Effective Temperatures, B-V Colors, and Bolometric Corrections. APJ, 469:355, September 1996. doi: 10.1086/177785.
- Galileo Galilei. Sidereus Nuncius (The Sidereal Messenger). Thomas Baglioni, 1610.
- B. S. Gaudi. Microlensing Surveys for Exoplanets. Annual Review of Earth and Planetary Sciences, 50:411–453, September 2012.
- W. Gliese. Dichte, Hertzsprung-Russell-Diagramm und Geschwindigkeitsverteilung der Sterne innerhalb 20 Parsec. Zeitschrift für Astrophysik, 39:1–35, 1956.
- R. Goullioud. SIM Lite Instrument Description, Operation, and Performance. In V. Coudé du Foresto, D. M. Gelino, and I. Ribas, editors, Pathways Towards Habitable Planets, volume 430 of Astronomical Society of the Pacific Conference Series, page 450, October 2010.
- R. Goullioud. Neat error budget. Private communication, 2010.
- O. Guyon and F. Martinache. How Extremely Large Telescopes (ELTs) will Acquire the First Spectra of Rocky Habitable Planets. In American Astronomical Society Meeting Abstracts, volume 221 of American Astronomical Society Meeting Abstracts, page 419.05, January 2013.
- O. Guyon, E. A. Pluzhnik, M. J. Kuchner, B. Collins, and S. T. Ridgway. Theoretical Limits on Extrasolar Terrestrial Planet Detection with Coronagraphs. Astrophysical Journal Supplement Series, 167:81–99, November 2006. doi: 10.1086/507630.
- O. Guyon, E. Bendek, S. M. Ammons, M. Shao, S. Shaklan, R. A. Woodruff, R. Belikov, and T. Milster. Characterization of habitable exoplanets with simultaneous coronagraphy and astrometry with a single aperture telescope. In Society of Photo-Optical Instrumentation Engineers (SPIE) Conference Series, volume 8442 of Society of Photo-Optical Instrumentation Engineers (SPIE) Conference Series, September 2012. doi: 10.1117/12.927196.
- O. Guyon, J. A. Eisner, R. Angel, N. J. Woolf, E. A. Bendek, T. D. Milster, S. M. Ammons, M. Shao, S. Shaklan, M. Levine, B. Nematy, F. Martinache, J. Pitman, R. A. Woodruff, and R. Belikov. Simultaneous Exoplanet Characterization and Deep Wide-field Imaging with a Diffractive Pupil Telescope. The Astrophysical Journal, 767:11, April 2013.

- A. P. Hatzes. The Radial Velocity Detection of Earth-mass Planets in the Presence of Activity Noise: The Case of Alpha Centauri Bb. The Astrophysical Journal, 770:133, June 2013.
- Robert Hirsch. Seizing the Light: A History of Photography. McGraw-Hill, 1999.
- K. W. Hodapp, R. Suzuki, M. Tamura, L. Abe, H. Suto, R. Kandori, J. Morino, T. Nishimura, H. Takami, O. Guyon, S. Jacobson, V. Stahlberger, H. Yamada, R. Shelton, J. Hashimoto, A. Tavrov, J. Nishikawa, N. Ukita, H. Izumiura, M. Hayashi, T. Nakajima, T. Yamada, and T. Usuda. HiCIAO: the Subaru Telescope's new high-contrast coronagraphic imager for adaptive optics. In Society of Photo-Optical Instrumentation Engineers (SPIE) Conference Series, volume 7014 of Society of Photo-Optical Instrumentation Engineers (SPIE) Conference Series, July 2008. doi: 10.1117/12.788088.
- M. J. Holman and N. W. Murray. The Use of Transit Timing to Detect Terrestrial-Mass Extrasolar Planets. Science, 307:1288–1291, February 2005.
- A. W. Howard, G. W. Marcy, S. T. Bryson, J. M. Jenkins, J. F. Rowe, N. M. Batalha, W. J. Borucki, D. G. Koch, E. W. Dunham, T. N. Gautier, III, J. Van Cleve, W. D. Cochran, D. W. Latham, J. J. Lissauer, G. Torres, T. M. Brown, R. L. Gilliland, L. A. Buchhave, D. A. Caldwell, J. Christensen-Dalsgaard, D. Ciardi, F. Fressin, M. R. Haas, S. B. Howell, H. Kjeldsen, S. Seager, L. Rogers, D. D. Sasselov, J. H. Steffen, G. S. Basri, D. Charbonneau, J. Christiansen, B. Clarke, A. Dupree, D. C. Fabrycky, D. A. Fischer, E. B. Ford, J. J. Fortney, J. Tarter, F. R. Girouard, M. J. Holman, J. A. Johnson, T. C. Klaus, P. Machalek, A. V. Moorhead, R. C. Morehead, D. Ragozzine, P. Tenenbaum, J. D. Twicken, S. N. Quinn, H. Isaacson, A. Shporer, P. W. Lucas, L. M. Walkowicz, W. F. Welsh, A. Boss, E. Devore, A. Gould, J. C. Smith, R. L. Morris, A. Prsa, T. D. Morton, M. Still, S. E. Thompson, F. Mullally, M. Endl, and P. J. MacQueen. Planet Occurrence within 0.25 AU of Solar-type Stars from Kepler. The Astrophysical Journal Supplement, 201:15, August 2012.
- James R Johnson. Comprehending the Cosmos, a Macro View of the Universe. Thomas Baglioni, 2013. ISBN 978-1-477-64969-5.
- M. Kasper, J.-L. Beuzit, C. Verinaud, R. G. Gratton, F. Kerber, N. Yaitskova, A. Boccaletti, N. Thatte, H. M. Schmid, C. Keller, P. Baudoz, L. Abe, E. Allart-Carpentier, J. Antichi, M. Bonavita, K. Dohlen, E. Fedrigo, H. Hanenburg, N. Hubin, R. Jager, V. Korkiakoski, P. Martinez, D. Mesa, O. Preis, P. Rabou, R. Roelfsema, G. Salter, M. Tecza, and L. Venema. EPICS: direct imaging of exoplanets with the E-ELT. In Society of Photo-Optical Instrumentation Engineers (SPIE) Conference Series, volume 7735 of Society of Photo-Optical Instrumentation Engineers (SPIE) Conference Series, July 2010.
- J. F. Kasting, D. P. Whitmire, and R. T. Reynolds. Habitable Zones around Main Sequence Stars. Icarus, 101:108–128, January 1993. doi: 10.1006/icar.1993.1010.
- D. G. Koch, W. J. Borucki, G. Basri, N. M. Batalha, T. M. Brown, D. Caldwell, J. Christensen-Dalsgaard, W. D. Cochran, E. DeVore, E. W. Dunham, T. N. Gautier, III, J. C. Geary, R. L. Gilliland, A. Gould, J. Jenkins, Y. Kondo, D. W. Latham, J. J. Lissauer, G. Marcy, D. Monet, D. Sasselov, A. Boss, D. Brownlee, J. Caldwell, A. K. Dupree, S. B. Howell, H. Kjeldsen, S. Meibom, D. Morrison,

- T. Owen, H. Reitsema, J. Tarter, S. T. Bryson, J. L. Dotson, P. Gazis, M. R. Haas, J. Kolodziejczak, J. F. Rowe, J. E. Van Cleve, C. Allen, H. Chandrasekaran, B. D. Clarke, J. Li, E. V. Quintana, P. Tenenbaum, J. D. Twicken, and H. Wu. Kepler Mission Design, Realized Photometric Performance, and Early Science. The Astrophysical Journal Letters, 713:L79, April 2010.
- R. K. Kopparapu, R. Ramirez, J. F. Kasting, V. Eymet, T. D. Robinson, S. Mahadevan, R. C. Terrien, S. Domagal-Goldman, V. Meadows, and R. Deshpande. Habitable Zones around Main-sequence Stars: New Estimates. The Astrophysical Journal, 765:131, March 2013. doi: 10.1088/0004-637X/765/2/131.
- Jean Kovalevsky and P. Kenneth Seidelmann. Fundamentals of astrometry. Cambridge University Press, 2001. ISBN 0521642167.
- L. R. Kump, S. L. Brantley, and M. A. Arthur. Chemical Weathering, Atmospheric CO₂, and Climate. Annual Review of Earth and Planetary Sciences, 28:611–667, 2000. doi: 10.1146/annurev.earth.28.1.611.
- A.-M. Lagrange, M. Bonnefoy, G. Chauvin, D. Apai, D. Ehrenreich, A. Boccaletti, D. Gratadour, D. Rouan, D. Mouillet, S. Lacour, and M. Kasper. A Giant Planet Imaged in the Disk of the Young Star Beta Pictoris. Science, 329:57–, July 2010.
- A.-M. Lagrange, N. Meunier, M. Desort, and F. Malbet. Using the Sun to estimate Earth-like planets detection capabilities . III. Impact of spots and plages on astrometric detection. AAP, 528:L9, April 2011. doi: 10.1051/0004-6361/201016354.
- H. Lammer, J. F. Kasting, E. Chassefière, R. E. Johnson, Y. N. Kulikov, and F. Tian. Atmospheric Escape and Evolution of Terrestrial Planets and Satellites. Space Science Reviews, 139:399–436, August 2008.
- John Lankford. History of astronomy: an encyclopedia. Taylor & Francis, 1997. ISBN 081530322X.
- D. W. Latham, R. P. Stefanik, T. Mazeh, M. Mayor, and G. Burki. The unseen companion of HD114762 - A probable brown dwarf. Nature, 339:38–40, May 1989. doi: 10.1038/339038a0.
- P. F. Lazorenko. Differential image motion at non-Kolmogorov distortions of the turbulent wave-front. Astronomy and Astrophysics, 382:1125–1137, February 2002. doi: 10.1051/0004-6361:20011671.
- P. F. Lazorenko, M. Mayor, M. Dominik, F. Pepe, D. Segransan, and S. Udry. Precision multi-epoch astrometry with VLT cameras FORS1/2. Astronomy and Astrophysics, 505:903–918, October 2009.
- R. Lenzen, M. Hartung, W. Brandner, G. Finger, N. N. Hubin, F. Lacombe, A.-M. Lagrange, M. D. Lehnert, A. F. M. Moorwood, and D. Mouillet. NAOS-CONICA first on sky results in a variety of observing modes. In M. Iye and A. F. M. Moorwood, editors, Instrument Design and Performance for Optical/Infrared Ground-based Telescopes, volume 4841 of Society of Photo-Optical Instrumentation Engineers (SPIE) Conference Series, pages 944–952, March 2003.
- L. Lindegren. Atmospheric limitations of narrow-field optical astrometry. Astronomy and Astrophysics, 89:41–47, September 1980.

- L. Lindgren, C. Babusiaux, C. Bailer-Jones, U. Bastian, A. G. A. Brown, M. Cropper, E. Høg, C. Jordi, D. Katz, F. van Leeuwen, X. Luri, F. Mignard, J. H. J. de Bruijne, and T. Prusti. The Gaia mission: science, organization and present status. In W. J. Jin, I. Platais, and M. A. C. Perryman, editors, IAU Symposium, volume 248 of IAU Symposium, pages 217–223, July 2008.
- B. A. Macintosh, J. R. Graham, D. W. Palmer, R. Doyon, J. Dunn, D. T. Gavel, J. Larkin, B. Oppenheimer, L. Saddlemyer, A. Sivaramakrishnan, J. K. Wallace, B. Bauman, D. A. Erickson, C. Marois, L. A. Poyneer, and R. Soummer. The Gemini Planet Imager: from science to design to construction. In Society of Photo-Optical Instrumentation Engineers (SPIE) Conference Series, volume 7015 of Society of Photo-Optical Instrumentation Engineers (SPIE) Conference Series, July 2008.
- V. V. Makarov, D. Parker, and R. K. Ulrich. Astrometric Jitter of the Sun as a Star. ApJ, 717:1202–1205, July 2010. doi: 10.1088/0004-637X/717/2/1202.
- F. Malbet, A. Sozzetti, P. Lazorenko, R. Launhardt, D. Ségransan, F. Delplancke, N. Elias, M. W. Muterspaugh, A. Quirrenbach, S. Reffert, and G. van Belle. Review from the Blue Dots Astrometry Working Group. In V. Coudé du Foresto, D. M. Gelino, and I. Ribas, editors, Pathways Towards Habitable Planets, volume 430 of Astronomical Society of the Pacific Conference Series, page 84, October 2010.
- F. Malbet, R. Goullioud, P. Lagage, A. Léger, M. Shao, A. Crouzier, and consortium NEAT. Neat: a space born astrometric mission for the detection and characterization of nearby habitable planetary systems. Proc. of SPIE, 8442, 2012.
- F. Malbet, A. Léger, M. Shao, R. Goullioud, P.-O. Lagage, A. G. A. Brown, C. Cara, G. Durand, C. Eiroa, P. Feautrier, B. Jakobsson, E. Hinglais, L. Kaltenegger, L. Labadie, A.-M. Lagrange, J. Laskar, R. Liseau, J. Lunine, J. Maldonado, M. Mercier, C. Mordasini, D. Queloz, A. Quirrenbach, A. Sozzetti, W. Traub, O. Absil, Y. Alibert, A. H. Andrei, F. Arenou, C. Beichman, A. Chelli, C. S. Cockell, G. Duvert, T. Forveille, P. J. V. Garcia, D. Hobbs, A. Krone-Martins, H. Lammer, N. Meunier, S. Minardi, A. Moitinho de Almeida, N. Rambaux, S. Raymond, H. J. A. Röttgering, J. Sahlmann, P. A. Schuller, D. Ségransan, F. Selsis, J. Surdej, E. Villaver, G. J. White, and H. Zinnecker. High precision astrometry mission for the detection and characterization of nearby habitable planetary systems with the Nearby Earth Astrometric Telescope (NEAT). Experimental Astronomy, 34: 385–413, October 2012.
- F. Malbet, A. Crouzier, A. Léger, M. Shao, and R. Goullioud. NEAT: ultra-precise differential astrometry to characterize planetary systems with Earth-mass exoplanets in the vicinity of our Sun. In Society of Photo-Optical Instrumentation Engineers (SPIE) Conference Series, volume 9143 of Society of Photo-Optical Instrumentation Engineers (SPIE) Conference Series, August 2014.
- C. Marois, B. Zuckerman, Q. M. Konopacky, B. Macintosh, and T. Barman. Images of a fourth planet orbiting HR 8799. Nature, 468:1080–1083, December 2010. doi: 10.1038/nature09684.
- D. N. Matsakis, J. H. Taylor, and T. M. Eubanks. A statistic for describing pulsar and clock stabilities. Astronomy and Astrophysics, 326:924–928, October 1997.

- M. Mayor and D. Queloz. A Jupiter-mass companion to a solar-type star. Nature, 378:355–359, November 1995. doi: 10.1038/378355a0.
- M. Mayor, F. Pepe, D. Queloz, F. Bouchy, G. Rupperecht, G. Lo Curto, G. Avila, W. Benz, J.-L. Bertaux, X. Bonfils, T. Dall, H. Dekker, B. Delabre, W. Eckert, M. Fleury, A. Gilliotte, D. Gojak, J. C. Guzman, D. Kohler, J.-L. Lizon, A. Longinotti, C. Lovis, D. Megevand, L. Pasquini, J. Reyes, J.-P. Sivan, D. Sosnowska, R. Soto, S. Udry, A. van Kesteren, L. Weber, and U. Weilenmann. Setting New Standards with HARPS. The Messenger, 114:20–24, December 2003.
- I. S. McLean, E. E. Becklin, O. Bendiksen, G. Brims, J. Canfield, D. F. Figer, J. R. Graham, J. Hare, F. Lacayanga, J. E. Larkin, S. B. Larson, N. Levenson, N. Magnone, H. Teplitz, and W. Wong. Design and development of NIRSPEC: a near-infrared echelle spectrograph for the Keck II telescope. In A. M. Fowler, editor, Infrared Astronomical Instrumentation, volume 3354 of Society of Photo-Optical Instrumentation Engineers (SPIE) Conference Series, pages 566–578, August 1998.
- C. Mordasini, H. Klahr, Y. Alibert, W. Benz, and K.-M. Dittkrist. Theory of planet formation. ArXiv e-prints, December 2010.
- C. Mordasini, K.-M. Dittkrist, Y. Alibert, H. Klahr, W. Benz, and T. Henning. Application of recent results on the orbital migration of low mass planets: convergence zones. In A. Sozzetti, M. G. Lattanzi, and A. P. Boss, editors, IAU Symposium, volume 276 of IAU Symposium, pages 72–75, November 2011.
- B. R. Oppenheimer and S. Hinkley. High-Contrast Observations in Optical and Infrared Astronomy. Annual Review of Astronomy and Astrophysics, 47:253–289, September 2009. doi: 10.1146/annurev-astro-082708-101717.
- F. Pepe, P. Molaro, S. Cristiani, R. Rebolo, N. C. Santos, H. Dekker, D. Mégevand, F. M. Zerbi, A. Cabral, P. Di Marcantonio, M. Abreu, M. Affolter, M. Aliverti, C. Allende Prieto, M. Amate, G. Avila, V. Baldini, P. Bristow, C. Broeg, R. Cirami, J. Coelho, P. Conconi, I. Coretti, G. Cupani, V. D’Odorico, V. De Caprio, B. Delabre, R. Dorn, P. Figueira, A. Fragoso, S. Galeotta, L. Genolet, R. Gomes, J. I. González Hernández, I. Hughes, O. Iwert, F. Kerber, M. Landoni, J.-L. Lizon, C. Lovis, C. Maire, M. Manna, C. Martins, M. Monteiro, A. Oliveira, E. Poretti, J. L. Rasilla, M. Riva, S. Santana Tschudi, P. Santos, D. Sosnowska, S. Sousa, P. Spanó, F. Tenegi, G. Toso, E. Vanzella, M. Viel, and M. R. Zapatero Osorio. ESPRESSO: The next European exoplanet hunter. Astronomische Nachrichten, 335:8, January 2014.
- M. Perryman, J. Hartman, G. Á. Bakos, and L. Lindgren. Astrometric Exoplanet Detection with Gaia. The Astrophysical Journal, 797:14, December 2014. doi: 10.1088/0004-637X/797/1/14.
- M. A. C. Perryman. Extra-solar planets. Reports on Progress in Physics, 63:1209–1272, August 2000.
- M. A. C. Perryman and ESA, editors. The HIPPARCOS and TYCHO catalogues. Astrometric and photometric star catalogues derived from the ESA HIPPARCOS Space Astrometry Mission, volume 1200 of ESA Special Publication, 1997.

- E. A. Petigura, A. W. Howard, and G. W. Marcy. Prevalence of Earth-size planets orbiting Sun-like stars. Proceedings of the National Academy of Science, 110: 19273–19278, November 2013.
- M. R. Rampino and K. Caldeira. The Goldilocks Problem: Climatic Evolution and Long-Term Habitability of Terrestrial Planets. Annual Review of Earth and Planetary Sciences, 32:83–114, 1994.
- H. Rauer, C. Catala, C. Aerts, T. Appourchaux, W. Benz, A. Brandeker, J. Christensen-Dalsgaard, M. Deleuil, L. Gizon, M.-J. Goupil, M. Güdel, E. Janot-Pacheco, M. Mas-Hesse, I. Pagano, G. Piotto, D. Pollacco, N. C. Santos, A. Smith, J. C., Suarez, R. Szabo, S. Udry, V. Adibekyan, Y. Alibert, J.-M. Almenara, P. Amaro-Seoane, M. Ammler-von Eiff, M. Asplund, E. Antonello, W. Ball, S. Barnes, F. Baudin, K. Belkacem, M. Bergemann, G. Bihain, A. C. Birch, X. Bonfils, I. Boisse, A. S. Bonomo, F. Borsa, I. M. Brandao, E. Brocato, S. Brun, M. Burleigh, R. Burston, J. Cabrera, S. Cassisi, W. Chaplin, S. Charpinet, C. Chiappini, R. P. Church, S. Csizmadia, M. Cunha, M. Damasso, M. B. Davies, H. J. Deeg, R. F. Dlaz, S. Dreizler, C. Dreyer, P. Eggenberger, D. Ehrenreich, P. Eigmüller, A. Erikson, R. Farmer, S. Feltzing, F. de Oliveira Fialho, P. Figueira, T. Forveille, M. Fridlund, R. A. Garcia, P. Giommi, G. Giuffrida, M. Godolt, J. Gomes da Silva, T. Granzer, J. L. Grenfell, A. Grottsch-Noels, E. Günther, C. A. Haswell, A. P. Hatzes, G. Hébrard, S. Hekker, R. Helled, K. Heng, J. M. Jenkins, A. Johansen, M. L. Khodachenko, K. G. Kislyakova, W. Kley, U. Kolb, N. Krivova, F. Kupka, H. Lammer, A. F. Lanza, Y. Lebreton, D. Magrin, P. Marcos-Arenal, P. M. Marrese, J. P. Marques, J. Martins, S. Mathis, S. Mathur, S. Messina, A. Miglio, J. Montalbán, M. Montalto, M. J. P. F. G. Monteiro, H. Moradi, E. Moravveji, C. Mordasini, T. Morel, A. Mortier, V. Nascimbene, R. P. Nelson, M. B. Nielsen, L. Noack, A. J. Norton, A. Ofir, M. Oshagh, R.-M. Ouazzani, P. Pápics, V. C. Parro, P. Petit, B. Plez, E. Poretti, A. Quirrenbach, R. Ragazzoni, G. Raimondo, M. Rainer, D. R. Reese, R. Redmer, S. Reffert, B. Rojas-Ayala, I. W. Roxburgh, S. Salmon, A. Santerne, J. Schneider, J. Schou, S. Schuh, H. Schunker, A. Silva-Valio, R. Silvotti, I. Skillen, I. Snellen, F. Sohl, S. G. Sousa, A. Sozzetti, D. Stello, K. G. Strassmeier, M. Svanda, G. M. Szabo, A. Tkachenko, D. Valencia, V. van Grootel, S. D. Vauclair, P. Ventura, F. W. Wagner, N. A. Walton, J. Weingrill, S. C. Werner, P. J. Wheatley, and K. Zwintz. The PLATO 2.0 Mission. ArXiv e-prints, October 2013.
- S. N. Raymond, T. Quinn, and J. I. Lunine. High-Resolution Simulations of The Final Assembly of Earth-Like Planets. 2. Water Delivery And Planetary Habitability. Astrobiology, 7:66–84, March 2007. doi: 10.1089/ast.2006.06-0126.
- G. R. Ricker, D. W. Latham, R. K. Vanderspek, K. A. Ennico, G. Bakos, T. M. Brown, A. J. Burgasser, D. Charbonneau, M. Clampin, L. D. Deming, J. P. Doty, E. W. Dunham, J. L. Elliot, M. J. Holman, S. Ida, J. M. Jenkins, J. G. Jernigan, N. Kawai, G. P. Laughlin, J. J. Lissauer, F. Martel, D. D. Sasselov, R. H. Schingler, S. Seager, G. Torres, S. Udry, J. N. Villaseñor, J. N. Winn, and S. P. Worden. Transiting Exoplanet Survey Satellite (TESS). In American Astronomical Society Meeting Abstracts #215, volume 42 of Bulletin of the American Astronomical Society, page 450.06, January 2010.
- E. J. Rivera, J. J. Lissauer, R. P. Butler, G. W. Marcy, S. S. Vogt, D. A. Fischer, T. M. Brown, G. Laughlin, and G. W. Henry. A 7.5 Earth Planet Orbiting the

- Nearby Star, GJ 876. The Astrophysical Journal, 634:625–640, November 2005. doi: 10.1086/491669.
- J. F. Rowe, S. T. Bryson, G. W. Marcy, J. J. Lissauer, D. Jontof-Hutter, F. Mul-lally, R. L. Gilliland, H. Issacson, E. Ford, S. B. Howell, W. J. Borucki, M. Haas, D. Huber, J. H. Steffen, S. E. Thompson, E. Quintana, T. Barclay, M. Still, J. Fortney, T. N. Gautier, III, R. Hunter, D. A. Caldwell, D. R. Ciardi, E. De-vore, W. Cochran, J. Jenkins, E. Agol, J. A. Carter, and J. Geary. Validation of Kepler’s Multiple Planet Candidates. III. Light Curve Analysis and Announce-ment of Hundreds of New Multi-planet Systems. The Astrophysical Journal, 784: 45, March 2014.
- J. Sahlmann, P. F. Lazorenko, A. Mérand, D. Queloz, D. Ségransan, and J. Woillez. Astrometric detection of exoplanets from the ground. In Society of Photo-Optical Instrumentation Engineers (SPIE) Conference Series, volume 8864 of Society of Photo-Optical Instrumentation Engineers (SPIE) Conference Series, September 2013a.
- J. Sahlmann, P. F. Lazorenko, A. Mérand, D. Queloz, D. Ségransan, and J. Woillez. Astrometric detection of exoplanets from the ground. In Society of Photo-Optical Instrumentation Engineers (SPIE) Conference Series, volume 8864 of Society of Photo-Optical Instrumentation Engineers (SPIE) Conference Series, September 2013b. doi: 10.1117/12.2023929.
- J. Sahlmann, P. F. Lazorenko, D. Ségransan, E. L. Martín, D. Queloz, M. Mayor, and S. Udry. Astrometric orbit of a low-mass companion to an ultracool dwarf. Astronomy and Astrophysics, 556:A133, August 2013c.
- J. Schneider, C. Dedieu, P. Le Sidaner, R. Savalle, and I. Zolotukhin. Defining and cataloging exoplanets: the exoplanet.eu database. Astronomy and Astrophysics, 532:A79, August 2011.
- M. Shao, R. Goulliard, J. Marr, B. nemati, C. Zhai, J. Catanzarite, and X. Pan. Astrometric Detection Exo-Earths with a Small Telescope. In American Astronomical Society Meeting Abstracts 217, volume 43 of Bulletin of the American Astronomical Society, page 425.01, January 2011.
- I. A. G. Snellen, R. Stuik, R. Navarro, F. Bettonvil, M. Kenworthy, E. de Mooij, G. Otten, R. ter Horst, and R. le Poole. Ground-based search for the brightest transiting planets with the Multi-site All-Sky CAmERA: MASCARA. In Society of Photo-Optical Instrumentation Engineers (SPIE) Conference Series, volume 8444 of Society of Photo-Optical Instrumentation Engineers (SPIE) Conference Series, September 2012. doi: 10.1117/12.925178.
- D. Spergel, N. Gehrels, J. Breckinridge, M. Donahue, A. Dressler, B. S. Gaudi, T. Greene, O. Guyon, C. Hirata, J. Kalirai, N. J. Kasdin, W. Moos, S. Perlmutter, M. Postman, B. Rauscher, J. Rhodes, Y. Wang, D. Weinberg, J. Centrella, W. Traub, C. Baltay, J. Colbert, D. Bennett, A. Kiessling, B. Macintosh, J. Merten, M. Mortonson, M. Penny, E. Rozo, D. Savransky, K. Stapelfeldt, Y. Zu, C. Baker, E. Cheng, D. Content, J. Dooley, M. Foote, R. Goullioud, K. Grady, C. Jackson, J. Kruk, M. Levine, M. Melton, C. Peddie, J. Ruffa, and S. Shaklan. WFIRST-2.4: What Every Astronomer Should Know. ArXiv e-prints, May 2013.

- B. Swinyard, T. Nakagawa, P. Merken, P. Royer, T. Souverijns, B. Vandenbussche, C. Waelkens, P. Davis, J. Di Francesco, M. Halpern, M. Houde, D. Johnstone, G. Joncas, D. Naylor, R. Plume, D. Scott, A. Abergel, S. Bensammar, J. Braine, V. Buat, D. Burgarella, P. Cais, H. Dole, L. Duband, D. Elbaz, M. Gerin, M. Girard, J. Goicoechea, C. Joblin, A. Jones, J. P. Kneib, G. Lagache, S. Madden, R. Pons, F. Pajot, D. Rambaud, L. Ravera, I. Ristorcelli, L. Rodriguez, S. Vives, A. Zavagno, N. Geis, O. Krause, D. Lutz, A. Poglitsch, W. Raab, J. Stegmaier, E. Sturm, R. Tuffs, H. M. Lee, B.-C. Koo, M. Im, S. Pak, W. Han, J.-H. Park, U.-W. Nam, H. Jin, D.-H. Lee, I.-S. Yuk, S. Lee, Y. Aikawa, N. Arimoto, Y. Doi, K. Enya, M. Fukagawa, R. Furusho, S. Hasegawa, M. Hayashi, M. Honda Kanagawa, S. Ida, Imanishi, Masatoshi, S.-i. Inutsuka, H. Izumiura, H. Kamaya, H. Kaneda, T. Kasuga, H. Kataza, K. Kawabata, M. Kawada, H. Kawakita, T. Kii, J. Koda, T. Kodama, E. Kokubo, Keiji Komatsu, H. Matsuhara, T. Matsumoto, S. Matsuura, T. Miyata, M. Miyata, Hiroshi, H. Nagata, T. Nagata, T. Nakajima, K. Naoto, R. Nishi, A. Noda, A. Okamoto, Y. K. Okamoto, K. Omukai, T. Onaka, T. Ootsubo, M. Ouchi, H. Saito, Y. Sato, S. Sako, T. Sekiguchi, H. Shibai, H. Sugita, K. Sugitani, H. Susa, T.-s. Pyo, M. Tamura, Y. Ueda, M. Ueno, T. Wada, J. Watanabe, T. Yamada, I. Yamamura, N. Yoshida, K. Yoshimi, Y. Yui, M. Benedettini, R. Cerulli, A. Di Giorgio, S. Molinari, R. Orfei, S. Pezzuto, L. Piazzo, P. Saraceno, L. Spinoglio, T. de Graauw, P. de Korte, F. Helmich, H. Hoovers, R. Huisman, R. Shipman, F. van der Tak, P. van der Werf, W. Wild, J. Acosta-Pulido, J. Cernicharo, J. Herreros, J. Martin-Pintado, F. Najarro, I. Perez-Fourmon, J. Ramon Pardo, F. Gomez, N. Castro Rodriguez, P. Ade, M. Barlow, D. Clements, M. Ferlet, H. Fraser, D. Griffin, M. Griffin, P. Hargrave, K. Isaak, R. Ivison, M. Mansour, J. Laniresse, P. Maukopf, D. Morozov, S. Oliver, A. Orlando, M. Page, C. Popescu, S. Serjeant, R. Sudiwala, D. Rigopoulou, I. Walker, G. White, S. Viti, B. Winter, J. Bock, M. Bradford, M. Harwit, and W. Holmes. The space infrared telescope for cosmology and astrophysics: SPICA A joint mission between JAXA and ESA. *Experimental Astronomy*, 23:193–219, March 2009.
- G. Tinetti, J. P. Beaulieu, T. Henning, M. Meyer, G. Micela, I. Ribas, D. Stam, M. Swain, O. Krause, M. Ollivier, E. Pace, B. Swinyard, A. Aylward, R. van Boekel, A. Coradini, T. Encrenaz, I. Snellen, M. R. Zapatero-Osorio, J. Bouwman, J. Y.-K. Cho, V. Coudé de Foresto, T. Guillot, M. Lopez-Morales, I. Mueller-Wodarg, E. Palle, F. Selsis, A. Sozzetti, P. A. R. Ade, N. Achilleos, A. Adriani, C. B. Agnor, C. Afonso, C. Allende Prieto, G. Bakos, R. J. Barber, M. Barlow, V. Batista, P. Bernath, B. Bézard, P. Bordé, L. R. Brown, A. Cassan, C. Cavarroc, A. Ciaravella, C. Cockell, A. Coustenis, C. Danielski, L. Decin, R. De Kok, O. Demangeon, P. Deroo, P. Doel, P. Drossart, L. N. Fletcher, M. Focardi, F. Forget, S. Fossey, P. Fouqué, J. Frith, M. Galand, P. Gaulme, J. I. G. Hernández, O. Grasset, D. Grassi, J. L. Grenfell, M. J. Griffin, C. A. Griffith, U. Grözinger, M. Guedel, P. Guio, O. Hainaut, R. Hargreaves, P. H. Hauschildt, K. Heng, D. Heyrovsky, R. Hueso, P. Irwin, L. Kaltenegger, P. Kervella, D. Kipping, T. T. Koskinen, G. Kovács, A. La Barbera, H. Lammer, E. Lellouch, G. Leto, M. Lopez Morales, M. A. Lopez Valverde, M. Lopez-Puertas, C. Lovis, A. Maggio, J. P. Maillard, J. Maldonado Prado, J. B. Marquette, F. J. Martin-Torres, P. Maxted, S. Miller, S. Molinari, D. Montes, A. Moro-Martin, J. I. Moses, O. Mousis, N. Nguyen Tuong, R. Nelson, G. S. Orton, E. Pantin, E. Pascale, S. Pezzuto, D. Pinfield, E. Poretti, R. Prinja, L. Prisinzano, J. M. Rees, A. Reiners, B. Samuel, A. Sánchez-Lavega, J. S. Forcada, D. Sasselov, G. Savini, B. Sicardy, A. Smith, L. Stixrude,

- G. Strazzulla, J. Tennyson, M. Tessenyi, G. Vasisht, S. Vinatier, S. Viti, I. Waldmann, G. J. White, T. Widemann, R. Wordsworth, R. Yelle, Y. Yung, and S. N. Yurchenko. EChO. Exoplanet characterisation observatory. Experimental Astronomy, 34:311–353, October 2012. doi: 10.1007/s10686-012-9303-4.
- W. Traub, E. Ford, G. Laughlin, H. Levison, D. Lin, S. Raymond, V. Makarov, S. Casertano, D. Fischer, J. Kasdin, M. Muterspaugh, M. Shao, C. Beichman, A. Boss, A. Gould, and J. Marr. Overview of the sim-rv double-blind simulation to detect earths in multi-planet systems. In American Astronomical Society Meeting Abstracts #213, volume 41 of Bulletin of the American Astronomical Society, page #300.01, Jan 2009.
- S. Udry and N. C. Santos. Statistical Properties of Exoplanets. Annual Review of Astronomy and Astrophysics, 45:397–439, September 2007. doi: 10.1146/annurev.astro.45.051806.110529.
- S. Udry, X. Bonfils, X. Delfosse, T. Forveille, M. Mayor, C. Perrier, F. Bouchy, C. Lovis, F. Pepe, D. Queloz, and J.-L. Bertaux. The HARPS search for southern extra-solar planets. XI. Super-Earths (5 and 8 Mearth) in a 3-planet system. Astronomy and Astrophysics, 469:L43–L47, July 2007. doi: 10.1051/0004-6361:20077612.
- G. T. van Belle, J. Sahlmann, R. Abuter, M. Accardo, L. Andolfato, S. Brilliant, J. de Jong, F. Derie, F. Delplancke, T. P. Duc, C. Dupuy, B. Gilli, P. Gitton, P. Haguenaue, L. Jocou, A. Jost, N. di Lieto, R. Frahm, S. Ménardi, S. Morel, J.-M. Moresmau, R. Palsa, D. Popovic, E. Pozna, F. Puech, S. Lévêque, A. Ramirez, N. Schuhler, F. Somboli, S. Wehner, and Espri Consortium. The VLTI PRIMA Facility. The Messenger, 134:6–11, December 2008.
- F. van Leeuwen. The HIPPARCOS Mission. Space Science Reviews, 81:201–409, August 1997.
- P. J. Wheatley, D. L. Pollacco, D. Queloz, H. Rauer, C. A. Watson, R. G. West, B. Chazelas, T. M. Loudon, S. Walker, N. Bannister, J. Bento, M. Burleigh, J. Cabrera, P. Eigmüller, A. Erikson, L. Genolet, M. Goad, A. Grange, A. Jordán, K. Lawrie, J. McCormac, and M. Neveu. The Next Generation Transit Survey (NGTS). In European Physical Journal Web of Conferences, volume 47 of European Physical Journal Web of Conferences, page 13002, April 2013. doi: 10.1051/epjconf/20134713002.
- J. N. Winn. Transits and Occultations. ArXiv e-prints, January 2010.
- A. Wolfgang and G. Laughlin. Combining Kepler and HARPS Exoplanet Occurrence Rates to Infer the Period-Mass-Radius Distribution of Super-Earths/Sub-Neptunes. AGU Fall Meeting Abstracts, page F6, December 2011.
- A. Wolszczan and D. A. Frail. A planetary system around the millisecond pulsar PSR1257 + 12. Nature, 355:145–147, January 1992. doi: 10.1038/355145a0.
- Neville Woolf and J. Roger Angel. ASTRONOMICAL SEARCHES FOR EARTH-LIKE PLANETS AND SIGNS OF LIFE. Annual Review of Astronomy and Astrophysics, 36:507–537, September 1998. doi: 10.1146/annurev.astro.36.1.507.

- JasonT. Wright and B.Scott Gaudi. Exoplanet detection methods. In TerryD. Oswalt, LindaM. French, and Paul Kalas, editors, Planets, Stars and Stellar Systems, pages 489–540. Springer Netherlands, 2013. ISBN 978-94-007-5605-2. doi: 10.1007/978-94-007-5606-9_10.
- C. Zhai, M. Shao, R. Goullioud, and B. Nemati. Micro-pixel accuracy centroid displacement estimation and detector calibration. Royal Society of London Proceedings Series A, 467:3550–3569, 2011.